Fakultät für Medizin

Technische Universität München

Functional states shape the spatio-temporal features of stimulus processing, effective connectivity, and spontaneous neuronal activity in the mouse cortex

Silviu-Vasile Bodea

Vollständiger Abdruck der von der Fakultät für Medizin der Technischen Universität München zur Erlangung des akademischen Grades eines

Doctor of Philosophy (Ph.D.)

genehmigten Dissertation.

Vorsitzende: TUM Junior Fellow Dr. Maike Buchner-Mayr

Betreuer: Prof. Dr. Gil G. Westmeyer

Prüfer der Dissertation:

1. Prof. Dr. Albrecht Stroh

2. Prof. Dr. Simon N. Jacob

Die Dissertation wurde am 08.07.2022 bei der Fakultät für Medizin der Technischen Universität München eingereicht und durch die Fakultät für Medizin am 25.09.2022 angenommen.

Abstract

In order to function in highly dynamic environmental conditions, mammals must integrate sensations, memories, projections of the future, and motor commands. Recent studies in humans and rodents have shown that neural activity and behavior resulting from the presentation of identical stimuli are highly heterogeneous. The ability of the brain to process sensory information is contingent on the functional state of cortical networks yet, the governing principles of the relationship are insufficiently understood.

This work is dedicated to exploring spontaneous cortical activity, cortical responses to stimulation as well as effective connectivity as a function of the brain state. Sedation, surgical-level anesthesia, and dissociation-unconsciousness are induced in a reproducible manner with the use of medetomidine, isoflurane, and ketamine. In these experimental conditions, compartmentalized functional cortical activity termed "persistent" state as well as activity dominated by propagating waves of cortical activation, termed "slow-wave" brain state can be observed. Combinations of global pharmacological intervention, sensory and optogenetic stimulations reveal how spontaneous activity, stimulus processing, and effective connectivity are influenced by the functional state of the cortical network.

A wide-field fluorescence microscope was developed for the purpose of recording cortical activity in transgenic mice expressing GCaMP6s in pyramidal neurons. This instrument can access spatio-temporal and frequency domains that bridge the gap between electroencephalography (EEG) and functional magnetic resonance imaging (fMRI). As a point of contrast to these methods, optical imaging enables genetic control over the neuronal populations that are being recorded and stimulated.

Spontaneous brain activity is not random, rather it is comprised of internally generated computational streams, execution of housekeeping tasks, and fluctuations that reflect brain network architecture. A metric called Brain Pattern Dimensionality (BPD) was developed to quantify functional cortical network segregation levels and classify functional brain states.

The transition from isoflurane sedation to surgical-level anesthesia was induced by a stepwise increase in isoflurane concentration and led to a dose-dependent loss of functional segregation. Global changes in cortical excitability underlie the gradual transition between sedation and surgical-level anesthesia. These quantitative findings correspond to the transition from compartmentalized spontaneous activity, the persistent functional state, to activity dominated by propagating waves of activation, the slow-wave functional state.

Cortical sensory information processing is essential to generating behavior. Visual and hind paw simulations were used to study how sensory information processing is modulated by functional brain states. The responses to stimulation were assessed using topological complexity. Functional state transitions from the persistent state to slow-wave activity led to a decrease in the topological complexity of cortical responses to both visual and hind paw stimulation. During the persistent state, we could differentiate between visual and hind paw stimulations, visual stimulations showing greater topological complexity. During recordings with prominent slow-wave activity, brain responses to stimulation became stereotypical and global and could not be differentiated based on the neuronal networks that were targeted with specific stimuli.

To study cortical information integration, effective connectivity was characterized with a perturbational approach using optogenetic stimulation of the red-shifted opsin ChrimsonR in parallel with GCaMP6s imaging. This implementation enables effective connectivity to be assessed from genetically tagged neuronal populations with the perturb-and-measure approach and quantified with a metric called perturbational complexity index (PCI-ST).

The transition from the compartmentalized persistent state to slow-wave activity led to a progressive decrease in both functional segregation (BPD) and the complexity of effective connectivity responses (PCI-ST). In contrast, ketamine-induced dissociation-unconsciousness exhibits high levels of functional segregation as well as stereotypical responses to optogenetic stimulation. These findings coupled with the observation of a distinctive 1-3Hz rhythm in the retrosplenial cortex under ketamine provide evidence that dissociation-unconsciousness represents a functional state that is distinct from the persistent and slow-wave states.

The trends described above were consistent regardless of the neuronal network stimulated (somatosensory or visual), indicating that the functional brain state determines the complexity of cortical information processing.

Conclusively, the work presented here demonstrates that spontaneous activity, stimulus representations, and effective connectivity are strongly dependent on the functional state of cortical pyramidal neuron networks. These results call for brain state-informed assessment

of spontaneous activity recordings as well as task-based studies in animal models and in humans. The experimental and computational strategies presented here will help ensure greater consistency in neuroimaging findings and expose cell-type-specific, systems-level processes relevant to healthy brain function and disease.

Zusammenfassung

Um unter hochdynamischen Umweltbedingungen operieren zu können, müssen Säugetiere Empfindungen, Erinnerungen, Zukunftsprojektionen und motorische Befehle integrieren. Jüngste Studien an Menschen und Nagetieren haben gezeigt, dass die neuronale Aktivität und das Verhalten bei der Darbietung identischer Reize sehr heterogen sind. Die Fähigkeit des Gehirns, sensorische Informationen zu verarbeiten, hängt vom Funktionszustand der kortikalen Netzwerke ab, doch sind die grundlegenden Prinzipien dieser Beziehung nur unzureichend bekannt.

Diese Arbeit widmet sich der Erforschung der spontanen kortikalen Aktivität, der kortikalen Reaktionen auf Stimulation sowie der effektiven Konnektivität als Funktion des Gehirnzustands. Sedierung, Narkose und Dissoziation werden in reproduzierbarer Weise mit Medetomidin, Isofluran und Ketamin induziert. Unter diesen experimentellen Bedingungen können sowohl eine kompartimentierte funktionelle Aktivität, die als "persistenter" Zustand bezeichnet wird, als auch eine Aktivität, die von sich ausbreitenden Wellen kortikaler Aktivierung dominiert wird und als *"Slow-Wave"*-Gehirnzustand bezeichnet wird, beobachtet werden. Kombinationen aus globalen pharmakologischen Interventionen, sensorischen und optogenetischen Stimulationen zeigen, wie spontane Aktivität, Reizverarbeitung und effektive Konnektivität vom funktionellen Zustand des kortikalen Netzwerks beeinflusst werden.

Ein Fluoreszenzmikroskop wurde konzipiert, um die kortikale Aktivität von transgenen Mäusen aufzuzeichnen, die GCaMP6s in pyramidalen Neuronen exprimieren. Dieses Instrument ermöglicht den Zugang zu räumlich-zeitlichen und Frequenzbereichen, die die Lücke zwischen Elektroenzephalographie (EEG) und funktioneller Magnetresonanztomographie (fMRI) schließen. Im Gegensatz zu diesen Methoden ermöglicht die optische Bildgebung die genetische Kontrolle über die aufgezeichneten und stimulierten Neuronenpopulationen.

Spontane Hirnaktivität ist nicht zufällig, sondern setzt sich aus intern generierten Rechen-

strömen, der Ausführung von Routineaufgaben und Fluktuationen zusammen, die die Netzwerkarchitektur des Gehirns widerspiegeln. Es wurde eine Metrik namens *Brain Pattern Dimensionality* (BPD) entwickelt, um das Niveau der funktionellen kortikalen Netzwerksegregation zu quantifizieren und funktionelle Gehirnzustände zu klassifizieren. Der Übergang von der Isofluran-Sedierung zur chirurgischen Anästhesie wurde durch eine schrittweise Erhöhung der Isofluran-Konzentration induziert und führte zu einem dosisabhängigen Verlust der Segregation der funktionellen Netzwerken. Globale Veränderungen der kortikalen Erregbarkeit liegen dem allmählichen Übergang zwischen Sedierung und chirurgischer Anästhesie zugrunde. Diese quantitativen Ergebnisse entsprechen dem Übergang von komplexer Spontanaktivität, dem persistenten Funktionszustand, zu einer Aktivität, die von langsamen Wellen dominiert wird, dem *slow-wave* Funktionszustand.

Die kortikale Verarbeitung sensorischer Informationen ist für die Entstehung von Verhalten unerlässlich. Mit Hilfe von visuellen Reizen und Reizen an der Hinterpfote wurde untersucht, wie die Verarbeitung sensorischer Informationen durch funktionelle Hirnzustände moduliert wird. Die Reaktionen auf die Stimulation wurden anhand der topologischen Komplexität bewertet. Funktionelle Zustandsübergänge vom persistenten Zustand zur *Slow-Wave*-Aktivität führten zu einer Abnahme der topologischen Komplexität der kortikalen Reaktionen auf visuelle und Hinterpfoten-Stimulation. Während des persistierenden Zustands konnte zwischen visuellen und Hinterpfoten-Stimulationen unterschieden werden, wobei die visuellen Stimulationen eine größere topologische Komplexität aufwiesen. Während der Aufzeichnungen mit ausgeprägter *Slow-Wave*-Aktivität wurden die Reaktionen des Gehirns auf die Stimulation stereotyp und global und konnten nicht anhand der neuronalen Netzwerke unterschieden werden, auf die die spezifischen Stimuli abzielten.

Um die kortikale Informationsintegration zu untersuchen, wurde die effektive Konnektivität mit einem perturbatorischen Ansatz charakterisiert, der optogenetische Stimulation mit Hilfe des rotverschobenen Opsins ChrimsonR parallel zur GCaMP6s-Bildgebung verwendet. Diese Implementierung ermöglicht es, die effektive Konnektivität von genetisch markierten neuronalen Populationen mit dem Perturbations- und Messansatz zu bewerten und mit einer Metrik namens Perturbationskomplexitätsindex (PCI-ST) zu quantifizieren.

Der Übergang vom persistierenden Zustand zur *Slow-Wave*-Aktivität führte zu einer progressiven Abnahme sowohl der funktionellen Segregation (BPD) als auch der Komplexität der effektiven Konnektivität (PCI-ST). Im Gegensatz dazu weist die ketamininduzierte Dissoziation ein hohes Maß an funktioneller Segregation sowie stereotype Reaktionen auf optogenetische Stimulation auf. Diese Befunde sowie die Beobachtung eines ausgeprägten 1-3Hz-Rhythmus im retrosplenialen Kortex unter Ketamin belegen, dass Dissoziation einen funktionellen Zustand darstellt, der sich von den persistierenden und *Slow-Wave*-Zuständenunterscheidet.

Die oben beschriebenen Tendenzen waren unabhängig von dem stimulierten neuronalen Netzwerk (somatosensorisch oder visuell) konsistent, was darauf hindeutet, dass der funktionelle Zustand des Gehirns die Komplexität der kortikalen Informationsverarbeitung mitbestimmt.

Zusammenfassend zeigt die vorgestellte Arbeit, dass spontane Aktivität, Stimulusrepräsentationen und effektive Konnektivität stark vom funktionellen Zustand kortikaler pyramidaler Neuronennetzwerke abhängig sind. Diese Ergebnisse erfordern eine hirnzustandsbezogene Bewertung der Spontanaktivität sowie aufgabenbasierte Studien in Tiermodellen und beim Menschen. Die hier vorgestellten experimentellen und computergestützten Strategien werden dazu beitragen, eine größere Konsistenz der neuronalen Bildgebungs-Ergebnissen zu gewährleisten und zelltypspezifische Prozesse auf Systemebene aufzudecken, die für die Funktion des gesunden Gehirns und für Krankheiten relevant sind.

Contents

List of abbreviations

2D	two-dimnsional
3D	three-dimensional
AAV	adeno-associated virus
ANOVA	analysis of variance
AP	action potential
ATP	adenozin-triphosphate
BBB	blood-brain-barrier
BOLD	Blood-oxygen-level-dependent
BPD	Brain Pattern Dimensionality
Ca	calcium
CamKII	calmodulin-dependent protein kinase II
CBV	cerebral blood volume
CMRO	cerebral metabolic rate of O2
cre	clization recombinase
DMD	Dynamic mode decomposition
DMN	default mode network
DNA	deoxyribonucleic acid
EEG	electroencephalography
eGFP	enhanced green fluorescence protein
emCCD	electron multiplier charge-coupled devices
FC	functional connectivity
FLASH	fast low angle shot
fMRI	functional magnetic resonance imaging
FWE	family-wise error
GABA	gamma-Aminobutyric acid
GCaMP	Green fluoresecnce protein Calmodulin-M13 Peptide
GE EPI	Gradient Echo-Planar Imaging
GECI	genetically-encoded calcium indicator

GIFT	Group ICA of fMRI Toolbox
GLM	General linear model
GMP	Guanosinmonophosphat
HbO	oxygenated hemoglobin
HbR	deoxygenated hemoglobin
HbT	total hemoglobin
HRF	hemodynamic response function
ICA	independent components anlysis
ICG	Indocyanine green
IHC	immunohistochemistry
IIT	information integration theory
iso.	isoflurane
K	pottasium
ket.	ketamine
LED	light-emitting diodes
LEiDA	leading eigenvector dynamics analysis
LPF	local field potentials
med.	medetomidine
Na	Natrium
nAChR	nicotinic acetylcholine receptors
NIR	near infrared
nm	nanometer
NMDA	N-methyl-D-aspartate
OIS	optical intrinsic imaging
PCA	principal components analysis
PCI	perturbation complexity index
PCI-ST	perturbation complexity index - state transitions
POD	proper orthogonal decomposition
RARE	rapid imaging with refocused echoes
REM	rappid aye movement
RNA	ribonucleic acid
ROI	region of interest
sCMOS	scientific complementary metal-oxide-semiconductor
SD	standard deviation
SNR	signal-to-noise ratio
SPM	Statistical Parametric Mapping

tetO	tetracycline operator
TMS	Transcranial Magnetic Stimulation
TRPC	transient receptor potential type C
tTA	tetracycline transactivator
UMAP	Uniform Manifold Approximation and Projection
WBES	Wavelet-based Event Separation processing pipeline

List of Figures

1

Introduction

1.1 Functional states of the mammalian brain and their relevance to neuroscience and medicine

The brain is a convoluted mass of cells, nerve fibers, vasculature, and connective tissue encased in permanent darkness in the protective bony structure of our skull, yet it allows us to probe and understand the fundamental laws of nature as well as our daily lives. Ever since it was realized that the brain is the destination of most sensory pathways and the origin of most motor signals, the bewildering informational output produced by this organ has puzzled philosophers and neuroscientists alike. Tremendous progress in the field of neuroscience has recently been guided by materialist philosophical principles which hold that the brain is a complex information processing system. Behavior, cognition, and memory formation, amongst others, are explained by ever-changing informational structures that have a physical substrate in our interconnected neural network [1].

The overwhelming complexity of the brain results from the billions of neurons and their even greater number of connections which are tightly integrated into a compact and efficient machine. To make sense of this intricate organ, neuroscientists have found it useful to think about the brain as a network where each neuron represents a node that is connected to other neurons by edges. This geometric abstraction is referred to as the brain connectome [2,3]. The structural connectome refers to the neurons and their wiring i.e. dendrites and axons while functional connectivity (FC) concerns the analysis of correlated patterns of neuronal firing.

The study of FC revealed that the brain exhibits a large variety of preferred functional configurations known as brain states. These brain states govern the way mammals process information and behave in the environment. Brain states can be thought of as points in a high-dimensional space where the dimensions are represented by neurons, groups of neurons, or brain regions, and the coordinates of the brain state are indicated by the levels of activation along the above-mentioned dimensions. If observed for extended periods, single points in this parameter space form trajectories of preferential brain configurations which cluster together to form more general functional states such as those during wakefulness, sleep, quiescence, etc. [4]. It is important to differentiate between states of vigilance and functional brain states because changes in the brain state do not always translate into observable behavioral changes.

Some of the most general functional brain states include the persistent state present also during sedation, in which complex mesoscopic network fluctuations give rise to compartmentalized network configurations[5], and the slow-wave state, during anesthesia and deep sleep, in which propagating patterns of global activation dominate cortical activity [6].

Not all possible configurations in this parameter space represent healthy brain states, for example, a state exhibiting multiband fast activity with suppression of lower frequencies and high levels of synchronization describes an epileptic seizure [7].

Neurodegenerative and psychiatric diseases lead to wide-ranging alterations in functional connectivity on a systems-level [8]. Finding efficient therapies for these conditions will require reverse-engineering the brain and finding interventions that will force the transition from pathological to healthy functional brain states. Such interventions are already available for certain conditions, for example, deep brain stimulation for Parkinson's disease [9] or inhibition of epileptic seizures in animal models with the use of optogenetics [10].

These therapies are driven by experimentation rather than a precise theoretical model of the brain network. Taking inspiration from methodology applied in physics i.e. finding the essential elements of a network and perturbing them to reveal underlying dynamics has been proposed as a more systematic strategy for making progress in characterizing brain states [11].

1.2 Functional and effective connectivity in the study of functional brain states

Two key concepts guiding strategies for the study of brain states are functional integration and segregation. There is wide consensus in the neuroscience community that high-level brain activity necessitates the integration of processing streams from functionally specialized brain regions [12]. On the other hand, specific tasks have to be processed within spatially-defined brain regions without interference from neighboring areas, i.e segregation. The study of brain states has been done traditionally by observing the baseline activity of the brain, spontaneous activity [11,13].

Functional connectivity is defined as "the temporal coincidence of spatially segregated neurophysiological events which can be as short as one millisecond" [14]. FC is based on correlations between spatially segregated brain regions and can be visualized in the form of a network graph. In this framework we can make use of purely observational data i.e. spontaneous activity measurements and the application of information theory allows for measures of segregation and integration to be derived [15,16].

Effective connectivity (EC) refers to "the capacity of a set of neuronal groups to causally affect the activity of other neuronal groups within the wider network" [14,17]. One way to estimate EC is to directly activate a brain region and observe the effect of this activation on the extended network [18].

Understanding how brain states influence cortical information processing will require a more perturbational approach in which a processing task is presented to the brain in order to infer its structure and interactions. The application of this idea to the study of brain states is known as the “perturb and measure” approach [18] and can be used as a surrogate measurement to estimate EC. This allows us to move beyond statistical dependencies and rule out more trivial sources of integration such as common drivers of brain activation. Using this approach cortical representations of stimuli can be described as a function of the respective brain state. Additionally, local responses to stimulation suggest a lack of integration while global stereotypical responses point to a loss of segregation [19].

As suggested in the previous section, inducing functional state transitions is essential for understanding how interventions could be used for the treatment of neuropsychiatric diseases. The level of arousal is easy to control with the use of anesthetics. While most studies deal with binary states such as wakefulness versus anesthesia, here, transitional states like sedation will be investigated so, naturally, a quantitative approach is needed to accurately describe these less than obvious functional brain configurations.

1.3 Motivation for using wide-field optical imaging in mouse models for the study of brain states

As detailed above, the development of accurate theoretical brain models will depend on precise functional and structural experimental data. Most of the insights into brain states and their transitions come from electroencephalography (EEG) and functional magnetic resonance imaging (fMRI) studies in humans. EEG features millisecond temporal resolution, as it records electrical potentials from populations of neurons while spatial resolution is limited to around 150 electrodes. fMRI, on the other hand, is only capable of recording one brain volume per second while also imaging deep neuronal structures to produce 3-dimensional (3D) high-resolution activation maps. Both these modalities, however, lack information about the neuronal populations that are being recorded.

Wide-field optical imaging of fluorescent calcium indicators enables in principle cellular resolution two-dimensional (2D) images to be acquired at a temporal resolution of about 20 frames per second [20]. Consequently, it is possible for wide-field imaging to access brain activation streams that are more relevant for active information processing while retaining high spatial resolution. Crucially wide-field fluorescence microscopy can be combined with the imaging of transgenic reporter animals which gives certainty as to the genetic identity of the neuronal population being investigated. Consequently, Wide-field fluorescence imaging could play an important role in bridging the gap between electrophysiology and fMRI and provide valuable insights into brain states.

This work will focus on mice. Mouse genetics are well characterized and mice represent the most versatile mammal species for genetic manipulation and for modeling human disease currently available to biomedicine [21]. With respect to primates, mouse brains share the same broad regions, e.g., a cortex divided into two hemispheres, cerebellum, hippocampi, thalami, basal ganglia, brain stem, etc. "Mice have a similar hierarchical organization to primates based on largely reciprocal feedforward and feedback connections and similar connectivity distance rules" [22], however, mouse cortices have fewer functional areas and their modular parcellation and microarchitecture are different from those of primates [22]. Notwithstanding these differences in size and complexity, studying the mouse brain has been at the forefront of neuroscientific discoveries and has led to breakthrough treatments in human brain pathologies [23].

1.4 Goal and objectives

The goal of this work is to study functional brain states relevant to neuroscience and medicine in mouse models. The brain states under investigation are those present in drug-induced sedation, dissociation-unconsciousness, and anesthesia. As presented above, achieving new insights in this field will require innovations in imaging data acquisition, genetic manipulation of the model organism, and the development of novel computational techniques.

To achieve this goal, the objectives of this project can be formulated as follows:

- Design and assemble an optical instrument suited for acquiring fluorescence imaging data from the whole mouse cortex
- Develop a computational method to quantify functional brain states based only on imaging data
- Investigate how spontaneous brain activity is influenced by sedation-unconsciousness, dissociation-unconsciousness, and anesthesia
- Develop a strategy for the coexpression of a fluorescent calcium indicator and an optogenetic actuator in excitatory cortical neurons
- Investigate how somatosensory, visual and optogenetic cortical responses to stimulation are influenced by the functional state of cortical networks

1.5 Relevance and translational value

This work has been done for the purpose of furthering knowledge about the brain and its function. The insights and methods that derive from this study have an intrinsic value for the neuroscience community in the context of basic scientific research. Methodological advances from this study will aid in the standardization of imaging neuroscience experiments, particularly in the field of FC and sensory perception. Novel scientific insights from this work will inform researchers working in the fields of sensory perception, pharmacology, anesthesia, psychiatry as well as computational neuroscience.

Additionally, all experiments have been done in the mouse, a model organism for human brain function in health and disease, and thus hold high translational value. All brain states investigated have great relevance for human medicine. Millions of people receive medical care in anesthetized or sedated states each year and dissociation is a prominent feature of numerous psychiatric conditions. Some of the substances used in this study are also used illegally as drugs of abuse so, understanding the cerebral mechanisms underlying their effects holds the potential of informing novel treatments for addiction.

As outlined above the raw imaging data in itself can be used for refining existing models of brain states and transitions. Such future models will allow researchers to carry out experiments *in silico* and efficiently test interventions which will lead to novel treatments for systems-level manifestations of brain disease.

2

State of the art: wide-field fluorescence microscopy in the study of brain states

2.1 From action potentials to pixels - reporters of neuronal activity

2.1.1 Calcium sensors

Electrical activity has traditionally been used to characterize the molecular, cellular, and system-wide neurophysiological events that form the basis of cerebral information processing. The action potential (AP) represents the primary means of communication in the nervous system. The role of electrical signals as information carriers was first demonstrated by Galvani in 1791 who was able to trigger muscle contraction in frogs after introducing an electrical pulse to nerve fibers [24]. The AP was described in the middle of the 20th century by Hodgkin and Huxley who discovered that voltage-gated ion channels in the giant axon of squid neurons were responsible for the propagation of electrical potentials [25]. The AP is initiated in the segment of the axon that is adjacent to the soma [26] and propagates to the presynaptic terminals where the electrical signal is transduced into a chemical message by way of neurotransmitter release into the synaptic cleft.

Electrophysiology with implantable electrodes is used to characterize neuronal electrical activity at the finest spatial and temporal scales. However, the precise identification of the neuronal subtype being recorded remains challenging when using electrophysiology alone. The genetic identification of neuronal cells and their contribution to complex behavior is essential to modern neuroscience and fluorescent calcium sensors have been developed for this application.

Intracellular calcium signaling is essential for the homeostasis, gene transcription, and life cycle regulation of neuronal cells. This second messenger is also central to neuronal information processing and signal propagation to connected neurons. Owing to the complex morphology of neurons, Ca^{2+} transients can be localized to subcellular compartments and act locally to induce exocytosis of neurotransmitter vesicles in presynaptic terminals and cause activity-dependent synaptic plasticity in dendritic spines while nuclear Ca^{2+} concentrations contribute to gene transcription [27].

This plethora of functions has led to complex cellular machinery for regulating free Ca^{2+} concentrations, as only free Ca^{2+} ions are biologically active. Baseline calcium concentrations in neuronal bodies are 53 - 100 nM [28] while extracellular levels reach 1.5 to 2.0 mM [29,30]. Ion channels involved in regulating membrane passage of Ca^{2+} include voltage-gated calcium channels, nicotinic acetylcholine receptors (nAChR), ionotropic glutamate receptors, and transient receptor potential type C (TRPC) channels [27]. Internal Ca^{2+} buffering proteins like parvalbumin, calbindin-D28k, and calretinin have numerous Ca^{2+} binding sites and together with the endoplasmatic reticulum (the most important source of intracellular calcium) regulate cytoplasmatic free Ca^{2+} levels [31]. Apart from buffering in the cytoplasm, Ca^{2+} concentrations can be brought down by membrane channels like plasma membrane calcium ATPase and the sodium-calcium exchanger [31,32].

Action potentials are followed by fast changes in free intracellular calcium concentrations [33–36] which increase by 43 ± 14 nM after a single action potential [28]. During intense electrical activity, intracellular concentrations can rise as much as 100 times relative to baseline levels [32]. Simultaneous electrical recordings and imaging studies after intracellular injection of calcium-sensitive dyes revealed a strong correlation between APs and calcium transients [37–40]. It is for this reason that Ca^{2+} signals are used as a proxy for measuring neuronal electrical potentials. Calcium sensors are localized in the cytoplasm which provides a large compartment for indicators to accumulate whereas voltage sensors are confined to the limited surface of plasma membranes [31,41,42], additionally, the magnitude of the Ca^{2+} transients after action potentials effectively acts as an AP signal amplifier [32].

It is for these reasons that research into Ca^{2+} sensors has been taken up by a large bioengineering community that has produced a myriad of synthetic and genetically encoded Ca^{2+} sensors spanning much of the visible spectrum and displaying a wide range of kinetic properties.

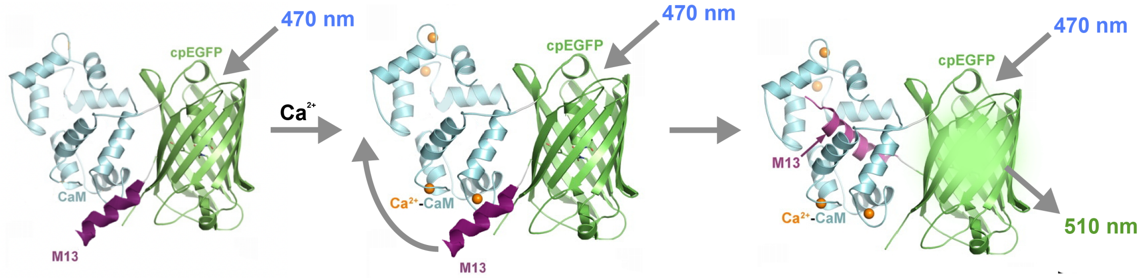

Figure 2.1: GCaMP6s - fluorescence generation mechanism. After binding to calmodulin, calcium induces a conformational change of the GCaMP protein and fluorescence with a peak at 510nm is produced as a result.

The earliest calcium sensors were found in marine invertebrates like the jellyfish aequorea victoria. The bioluminescent protein named aequorin consists of an apoprotein attached to a chromophore which upon calcium binding to one of three binding sites emits a 470nm photon [43]. The construct had to be loaded with pipettes and light emission to take place, coelenterazine had to be co-expressed. Even in the presence of these preconditions photon yield was low which limited the use of this calcium-sensing protein [44]. A significant breakthrough in Ca^{2+} sensor technology came with the engineering of fura-2 which is a combination of a Ca^{2+} chelator and a chromophore [45,46]. This is a synthetic fluorescent dye that, when illuminated with ultraviolet light and bound to Ca^{2+} emits 505 to 520nm photons. Fura2 can be used for quantitative measurements of intracellular Ca^{2+} concentrations and the high quantum yield made it attractive for in vivo recordings [47]. Progres in synthetic calcium dyes was closely matched by advances in two-photon microscope imaging technology and for this application, Oregon Green 488 Bapta-1 AM-ester was preferred because of its superior behavior in vivo.

Genetically encoded calcium indicators (GECI) represent an attractive alternative to synthetic dyes because they can be genetically expressed in target cells, thus enabling the recording of genetically defined neuronal populations. Two major classes of GECI can be discerned based on their mechanism of fluorescent light generation: FRET-based (Fluorescence Resonance Energy Transfer) indicators and single-fluorophore constructs [27].

The FRET mechanism necessitates a more complicated design encompassing a donor and an acceptor fluorophore. When Ca^{2+} is not present emission is dominated by the donor while upon Ca^{2+} binding the receiver fluorophore emits more light thus, calcium levels are expressed as a ratio between donor and acceptor signals [48].

Single fluorophore constructs have been preferred by the neuroscience community because of their simpler design and versatility in terms of kinetics, excitation/emission wavelength, and brightness. This design strategy has led to the development of the GCaMP calcium indicator family which presently includes around 19 versions. At the core of the GCaMP structure lies the enhanced green fluorescent protein (eGFP) beta-barrel to the sides of which calmodulin (a Ca^{2+} binding protein) and calmodulin-binding peptide M13 are attached [49,50]. When Ca^{2+} attaches to calmodulin-M13 conformational changes in the eGFP fluorophore lead to an increase in fluorescence. These probes feature dissociation constants ranging from 46 nM (jGCaMP8s) [51] to 6.12 µM (Fast-GCaMP-EF20) [52], dynamic ranges from 4.5 $\Delta F/F0$ (GCaMP1)[50] to 145,5 $\Delta F/F0$ (GCaMP7c)[53] and with responses as fast as 25 ms time to peak after action potentials [51].

In particular, the GCaMP6s and GCaMP6f versions have been widely adopted by the neuroscience community [40]. GCamp6s has lower background fluorescence, 74% of GCaMP3 levels, and 11 fold higher SNR after 1 AP as compared to GCaMP3. The time to peak after 10 AP is longer than for GCaMP6f, 480ms vs. 80ms and the decay of fluorescence signal after 10 AP is also longer as compared to GCaMP6f, 1796ms vs 400ms. GCaMP6s is preferred for integration in mouse genomes because it is considered that its slower dynamics lower its calcium buffering effects in neurons in vivo and thus preserves neuronal homeostasis in vivo.

Substantial efforts were also invested in shifting GECI absorption and emission spectra to the red [54] and near-infrared [55] wavelengths. Having these red-shifted sensors allows for more robust multiplexing with other indicators of neuronal activity or optogenetic tools and may also enable imaging with short-wave-infra-red [56] and optoacoustic systems [57]. A comprehensive review covering the multitude of GECI variants can be found in [58].

Despite the rapid progress in calcium sensors, this technology has limitations when compared to voltage sensing. Notably, calcium imaging fails to capture hyperpolarisation and sub-threshold depolarization events [42]. Millisecond timescales relevant for capturing aspects of neuronal information processing and for studying fast-spiking cells such as interneurons are difficult to record with calcium imaging [39,59]. Computational methods for spike inference from calcium recordings have been put forward and validated under slower neuronal firing conditions [60–64].

Notwithstanding these shortcomings, calcium sensors are well-matched in terms of signal-to-noise ratio and acquisition timescales to modern single and multiphoton imaging devices. The wide palette of bright sensors covering numerous excitation wavelengths and exhibiting fast kinetics have helped establish calcium reporters of neuronal activity as the workhorse sensors of optical brain imaging.

2.1.2 Imaging brain hemodynamics

Normal brain function necessitates high amounts of energy substrate, estimated at 4.81 x 10^9 ATP/spike/neuron while neurons consume 9.20 x 10^8 ATP/neuron/s during quiescence [65]. The brain uses 20% of the total O_2 intake making it the most energy-expensive tissue per unit mass [66]. Most of this energy is spent on synaptic activity and restoring baseline membrane potentials after an AP [67]. The brain, however, does not possess significant stores of oxygen and glucose. Intense brain tissue activity leads to a localized increase in cerebral blood flow which covers higher energetic demands [68]. The coupling of the blood flow to neuronal activity is known as the neurovascular coupling and was first proposed by Roy and Sherrington [69].

The precise mechanisms behind the neuro-vascular coupling are still being investigated, however, consensus has been building around the central role of nitric oxide in the regulation of this phenomenon. Nitric oxide stimulates the nitric oxide receptor which in turn leads to the production of cGMP (Guanosinmonophosphat) and cGMP-dependent kinase signaling resulting in vasodilation [70,71]. Additionally, Ca^{2+} is released in astrocytic terminals triggering vasodilation [72]. These two pathways work together to cause vasodilation at different levels: the nitric oxide mechanism, triggered by neurons seems to act on arterioles while the astrocytic mechanism involving Ca^{2+} signaling increases capillary volume [70].

These mechanisms which are critical for maintaining the homeostasis and efficient operation of the brain can be leveraged for inferring brain activity. Hemoglobin is universally found in mammals as oxygen fearing molecule and because it is naturally occurring, imaging neurovascular dynamics can be achieved non-invasively without the need for further chemical or genetic manipulation of the investigated organism. Neuronal firing has to be inferred from hemodynamic recordings and for this, various mathematical models have been put forward.

These models are subsumed under the umbrella term of hemodynamic response functions (HRF) and describe how localized increases in neuronal activity affect cerebral blood flow changes [73]. The main parameters which are included in the modeling of the hemodynamic response function are the time-to-peak, amplitude, and response duration of the hemodynamic signals. Mathematical models have been created for describing hemodynamic effects in different parts of the human brain [74], in subjects spanning all ages [75], and across a multitude of pathological conditions [76,77]. In preclinical research, great effort has been invested in characterizing the HRF in rats [78] and mice [79,80] as well as standardizing experimental protocols for the generation of reproducible experimental results [80].

Despite the progress in our understanding of the metabolic pathways underlying the neurovascular coupling, deriving precise causal relationships between neuronal firing and hemodynamic signals remains a difficult proposition [81]. The complexity and variation in the shape of vascular responses reflect the intricate nature of the pathways underlying the coupling of neuronal and vascular activity. Strong evidence suggests that energy-intensive synaptic events could contribute more to increases in cerebral blood flow than neuronal action potentials [81]. Energy is being expended in inhibitory and excitatory synapses and excitatory vs. inhibitory activity cannot be differentiated based on neurovascular responses [82]. Furthermore, the vascular response itself includes influences from blood flow, blood oxygenation levels, blood volume, and hematocrit and varies based on the imaging technology used for acquisition [83].

Notwithstanding these limitations, brain hemodynamic responses have been extensively used in clinical and preclinical studies to report brain activity in different physiological and pathological brain states and to infer brain circuit dynamics involved in task performance. Imaging of hemodynamic parameters can be performed with a large number of imaging instruments including functional MRI, optical intrinsic imaging (OIS), functional ultrasound, photoacoustics, and short-wave infrared imaging. Some of these imaging devices have fields of view that span the entire brain and can be employed in small animal models as well as in human subjects. It is for these reasons that imaging brain hemodynamics occupies an important role in modern neuroscience research.

Hemodynamic signal changes can be detected by MRI because relaxation rates of protons in a given imaging voxel are modulated by the concentration and oxygenation state of hemoglobin. This so-called Blood-Oxygenation-Level-Dependent contrast (BOLD)[84,85] is sensitive to changes in vasodilation and has been used in fMRI to create functional connectivity maps in humans and animals.

The abundance of hemoglobin in the rodent brain, around 6.3 mg/ml[86], compensates for low fMRI sensitivity. Notwithstanding, the BOLD effect remains incompletely characterized with contributions from cerebral blood volume, cerebral blood flow, and cerebral metabolic rate of O_2 (CMRO) being discussed[87]. As a result, multimodal imaging systems where fMRI data is co-recorded with PET[88], EEG[89], NIRS[90] and calcium fluorescence [91,92] have been employed to independently validate and increase the specificity of fMRI imaging findings.

fMRI in preclinical research is usually limited to experiments that can be carried out in general anesthesia although procedures for awake measurements in mice [93], rats [94], and non-human primates [95] have been proposed. Conventional fMRI sequences are limited in their temporal resolution to 1 brain image/sec, though using lower spatial resolution allows for data acquisition at 10-20 Hz[96,97].

The relatively low signal-to-noise ratio is overcome by averaging multiple trials although learning and anticipating stimuli means that these trials are likely to lead to qualitatively and quantitatively different activation patterns[98].

2.1.3 Contrast agent delivery methods

Intravenous contrast agent delivery, for functional imaging, can have the goal of bringing a contrast agent to the bloodstream. In this case, we are dealing with so-called ‘blood pool agents’ such as superparamagnetic iron oxide nanoparticles [99] or dyes [100]. For optical imaging, contrast agents should ideally have the peak absorption in the NIR window, far away from the strong absorbance from hemoglobin. Long circulation time is desired for hemodynamic imaging which often benefits from contrast agent accumulation in biological structures of interest.

Suppose contrast agent delivery to neurons after intravenous administration is desired. In that case, the contrast agents should ideally have high blood-brain barrier (BBB) permeability, and size preferably below 1nm [101,102]. If these conditions are not satisfied, the BBB can also be transiently opened with focused ultrasound [103].

Interstitial delivery via intracranial injection is a convenient way of circumventing the BBB. Only small volumes (1-2 microL) can be administered in this way and have to be injected at very slow rates (0.1 microL/min) to compensate for slow contrast agent diffusion in brain tissue [104].

Synthetic contrast agents can benefit from the entire spectrum of chemical and biological synthesis strategies available for in vitro production. Selective synthetic agents for biological structures of interest are difficult to produce and, once delivered to the target tissue, often get degraded over time and are difficult to replenish.

To address these challenges, genetically encoded contrast agents have been proposed. DNA encoding the contrast agent has to be integrated into genetically defined cells which then go on to produce the contrast agent usually without the need for external intervention. Transduction, i.e. the modification of the cell’s DNA can be achieved by hereditary mechanisms or via the administration of viral [105] or non-viral [106] DNA delivery vehicles.

Promoters are DNA sequences that act as ‘begin’ instructions for transcription. The promoter represents the binding site for RNA polymerase and ancillary transcription factors and also indicates the direction and DNA strand to be transcribed. The selective use of gene promoters ensures that a large collection of neuronal or glial cell types can be addressed [107]. After transduction, the foreign DNA sequence can either be integrated into the host genome [108] or persist as an episome in the nucleus [109]. Neuronal cells are stable over time and do not multiply so this enables the long-term expression of the genetically encoded contrast agents in the brain.

Viral injections are usually employed for *in vivo* experiments [104] or alternatively, the increasingly popular method of intravenous AAV9 administration can be used [110–112]. The AAV9 serotype has been further developed into two variants PHP.B and PHP.eB and which have been reported to deliver fluorescent signals similar to Ai93 and Ai94 mice if administered to the bloodstream 4 weeks before imaging [113].

2.1.4 Transgenic mouse reporter lines for calcium brain imaging

The first germline-competent transgenic mouse line dates back 4 decades [114] since then, transgenic mouse models have become a powerful tool for modeling human and animal diseases and numerous mouse reporter lines have been generated for neuroscience applications. DNA fragments of interest are typically injected into the pronucleus of a zygote and multiple copies of the transgenes integrate into the host genome[115]. This technology is conducive to the transfer of small DNA fragments which are usually based on plasmids as well as large DNA fragments such as bacterial artificial chromosomes [116]. Foreign DNA integration can occur at random [117] or at specifically chosen sites that have been shown to enable large expression levels in numerous neuronal subtypes [117,118]. Transgenic mouse lines have to be examined for expression levels as well as successful propagation of the foreign gene to offspring.

The use of transgenic mouse lines as reporters for neuroimaging studies has been made possible by the development of genetically encoded reporters [119]. Mouse genetics are well characterized and mice are the most common mammal model for studying brain physiology thus transgenic mouse lines have been used in neuronal tracing as well as for functional brain imaging studies. In transgenic mouse lines, long-term neuronal sensor expression can be achieved over large areas of the brain. Furthermore, expression levels are more consistent compared to bulk injections and viral transfection [120].

Progress in mouse genetics and sensors for neuronal activity was closely matched by the engineering of advanced imaging systems such as the two-photon microscope. Fluorescence imaging routinely relies on calcium sensors as reporters of neuronal activity, this combination allowing single-cell measurements at high signal-to-noise ratios and high temporal resolution [35,121–123]. The preferred calcium sensors for the generation of transgenic mouse lines come from the GCaMP6 family. In applications requiring high signal-to-noise ratios, and subcellular imaging, GCaMP6s is preferred while for fast neuronal dynamics GCaMP6f is the sensor of choice [40].

For cell-type-specific targeting, genetic reporters of neuronal activity can be expressed in neuronal subtypes under specific promoters. The most straightforward strategy involves the use of the Thy1 promoter which results in a single gene transgenic mouse. Alternatively, crossing two mouse lines is necessary for sensor expression under the control of the tetracycline transactivator (tTA) protein in conjunction with the tetracycline operator (tetO) or the crossing of 3 mouse lines for cre-recombinase and tTA control [113].

The combination of fast and slow calcium sensors and cell-type-specific promoters has led to the development of several transgenic mouse lines. The simplest design involves the expression of GCAMP6s in excitatory neurons under Thy1 control [123]. While this mouse line does not require the breeding of multiple mouse lines for its generation, this reporter variant does not yield strong fluorescence signals [113].

To address this issue mouse lines expressing both GCaMP6f (Ai93) and 6s (Ai94) under the control of cre and tTA and the CamKII (calmodulin-dependent protein kinase II) promoter have been proposed [118]. A popular transgenic GCaMP6s mouse line under the control of the tTA protein, tetO, and the CamKII promoter (Camk2a-tTA;tetO-GCaMP6s) [124] requires the crossing of two mouse lines compared to the three crossings necessary for Ai93 and Ai94 while showing only marginally lower Ca^{2+} fluorescence responses compared to these latter strains [113].

All calcium sensors also act as Ca^{2+} buffers, consequently, reporters with high affinity and fast binding kinetics are likely to alter neuronal Ca^{2+} homeostasis. The consequences of this are difficult to assess and the methods employed for these determinations rely on comparing the electrophysiology and connectivity structure of mouse reporter lines to wild-type strains. One easily measurable functional anomaly, which may hint at an underlying pathological burden on the transgenic animals is represented by ictal spikes. This pathological activity was observed in the Ai93 and Ai94 mouse strains while generalized seizures were only observed in the Ai93 mouse line. The significance of ictal spikes is unclear as mice did not show behavioral changes during these events, however generalized seizures could hint at possible cre or tTA-related toxicity. GCaMP6s expression during development could also be to blame and it was shown that doxycycline-induced inhibition of GCaMP expression before 7 weeks of age was successful in preventing seizures in most Ai93 mice [120].

Notably, no aberrant activity was reported in the Camk2a-tTA;tetO-GCaMP6s mouse line [124] which seems to represent an attractive choice of transgenic model given that the fluorescent GCaMP signal in these mice approaches that recorded in Ai94 mice. The Camk2a-tTA;tetO-GCaMP6s mouse line exhibits high levels of fluorescence and no abnormal neuronal activity and was consequently used in this study.

2.2 Wide-field optical brain imaging

Wide-field optical imaging broadly refers to an optical imaging system that records 2D images of specific areas or the entire cortex of the mouse over a series of time steps, essentially generating movies of brain activity. Depending on the molecular sensors leveraged by the imaging apparatus we can distinguish between wide-field imaging of voltage sensors, calcium sensors, and blood pool agents (hemoglobin or blood-soluble dyes).

Wide-field imaging was first used for imaging synthetic voltage sensors in the rat brain [125]. This served as a proof of principle that optical imaging could be used to record complex brain dynamics in vivo. Voltage-sensitive dyes, however, are difficult to inject into broad areas of the cortex and produced increases in fluorescence less than 0.5% of baseline and their fast on/off dynamics were difficult to capture by camera technology [25]. Because of this, the combination of synthetic voltage-sensitive dyes and wide-field imaging systems found its use in a limited number of experimental settings. To address these limitations, genetically encoded voltage indicators were developed and enabled highly detailed spatial maps of activation of the barrel cortex after whisker stimulation. However, in vivo signals only increased by 0.1% over baseline after whisker stimulation [126,127].

The lower signal-to-noise ratio of genetically encoded voltage indicators stems from the fact that these sensors are situated in neuronal membranes and are thus limited in the maximal concentration achievable. While noise sources are manageable in vitro, motion and hemodynamic effects play an important role in vivo and still hamper modern wide-field imaging with genetically encoded voltage sensors [126,128].

Soon after the first wide-field imaging experiments with voltage sensors, it became clear that changes in reflectance of the exposed cortex contained useful functional information. This imaging method was termed intrinsic signal imaging because it takes advantage of an endogenous reporter of neuronal activity, namely hemoglobin [129]. As detailed in the section on neurovascular coupling, neuronal activation is accompanied by changes in blood volume, blood flow, and hemoglobin oxygenation levels in the activated areas. It was shown that hemoglobin exhibits intricate light absorption properties depending on the wavelength of light used for imaging and the oxygenation level of the protein [130].

The illumination wavelengths are specifically chosen to leverage the light absorption characteristics of oxygenated and deoxygenated hemoglobin (Fig. 2.1). Red, green, and blue illumination is required for calculating the concentrations of total hemoglobin, oxygenated hemoglobin (ΔHbO2), and deoxygenated hemoglobin (ΔHb). At 470 nm illumination hemoglobin absorption is large regardless of the oxygenation state while 530 nm and 590 nm represent so-called isosbestic wavelengths i.e. wavelengths at which oxygenated and deoxygenated hemoglobin absorption is similar. Finally, at 625 nm light absorption is dominated by deoxygenated Hb [131,132]. Molar concentrations of Hb and HbO2 can be calculated from 530 and 625 nm, see Fig. 2.2.

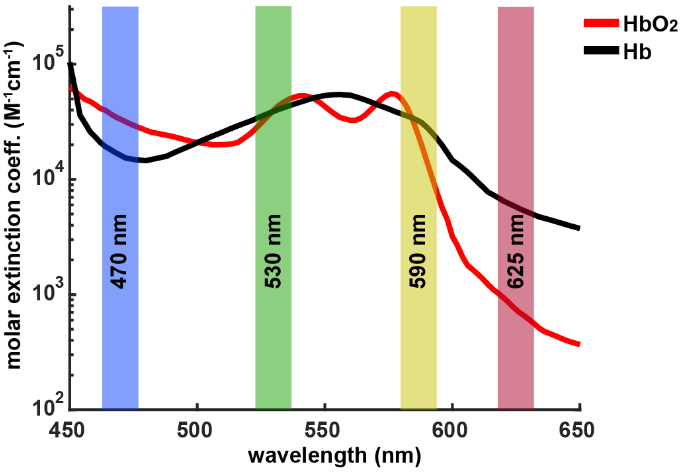

Figure 2.2: Illumination wavelengths used in intrinsic signal imaging. The determination of oxygenated and deoxygenated Hb concentration requires imaging at isosbestic wavelengths (530nm and 590nm) as well as wavelengths where absorption differs between oxygenated and deoxygenated Hb (470nm and 625 nm).

As discussed in the chapter on hemodynamic imaging, using the neurovascular coupling does not allow for neuronal events to be imaged directly. An alternative implementation of wide-field imaging records fluorescence signals in transgenic mice which express genetically encoded calcium sensors in cortical neurons. This approach can access neuronal activity directly at high signal-to-noise ratios and high frame rates

Generally, wide-field optical imaging systems consist of a camera-lens assembly and one or more artificial light sources which provide illumination. In terms of camera technology, either electron multiplier charge-coupled devices (emCCD) or scientific complementary metal-oxide-semiconductor (sCMOS) microcircuits can be used as recording devices. In emCCDs pixels are read out sequentially in a register while for sCMOS the readout mechanism is localized in each pixel element. For this reason, readout noise is higher for sCMOS than the emCCD. In practice, the higher the frame rate the higher the noise in the emCCD readout, and added to that the electron multiplication process also adds noise so that low light sensitivity in sCMOS and emCCD sensors is comparable [133]. To further lower the noise, both emCCD and sCMOS sensors are electronically cooled to between 0 and -20 °C which enables higher frame rates [134].

In terms of light sources, light-emitting diodes (LED) are preferred because of their lower costs and availability of colors covering the UV to infra-red spectrum. LEDs lack the spectral precision of lasers and light generated by these sources has to be optically filtered to precisely select the wavelengths needed for illumination. In the absence of such filters, the highly sensitive camera sensors easily pick up unwanted light leading to an artificially high background signal.

2.2.1 Wide-field calcium sensor fluorescence imaging

Calcium sensors mainly report neuronal spiking activity while achieving high signal-to-noise ratios and exhibiting slower kinetics than voltage sensors. These properties are well-matched to scientific camera sensitivity, resolution, and achievable exposure times. In particular, the development of the GCaMP class of calcium sensors was closely synchronized with advances in single-photon and multiphoton imaging systems. Advances in transgenic mouse reporter lines enable imaging of the dorsal cortex over long periods while allowing access to genetically defined subpopulations of neurons.

Typically the imaging system consists of a scientific camera and multiple LEDs which are used for excitation of the fluorescent reporter and the correction of physiological noise. The brain must be illuminated at the excitation wavelength of the fluorophore (which for GCaMP is around 460±25 nm) while emission light must be filtered to remove unwanted background illumination (for GCaMP 525 ±25 nm). The emission light will always have lower energy and a longer wavelength than the excitation light.

Wide-field calcium imaging systems routinely cover fields-of-view of up to 1 cm2 with a spatial resolution of 10-100 µm/pixel and temporal resolution of up to 100 frames/sec [135]. The imaging depth that can be achieved is dependent on the intensity of the sensor that is being used as well as the intensity of the excitation light and the geometric distribution of sources inside the tissue. If all sources are situated at higher depths, fluorescence may still be recorded even if heavily blurred due to tissue scattering. If fluorescent sources are situated in both superficial and deep layers images will more strongly reflect the dynamic activity of the superficial sources [136].

Fluorescence intensity is reported as the percentage change at time point t relative to a prior time point t0 or relative to a baseline. Fluorophore fluorescence is dependent on illumination homogeneity, time-dependent confounding factors such as absorption by hemoglobin, and dark signal arising from intrinsic camera noise as well as ambient light [132,136]. Illumination uniformity can be improved by using collimated LEDs equipped with diffusers while effects of dark signals can be subtracted on a per-image basis if dark frames were acquired at the end of the experiment.

An important technical consideration for wide-field calcium imaging is the need to correct

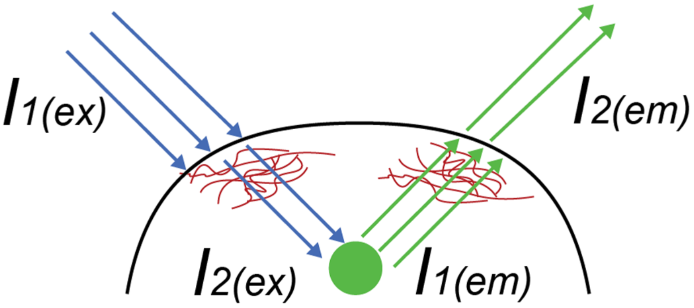

Figure 2.3: Hemodynamic parameter fluctuations affect calcium fluorescence imaging. A fraction of the blue excitation light $I1(ex)$ is absorbed by blood before reaching the fluorophore so that the actual intensity of the excitation light will be $I2(ex)$. Similarly, a part of the emission light $I1(em)$ is blocked by hemoglobin before exiting the brain with intensity $I2(em)$.

fluorescence data that is contaminated with physiological noise which mainly arises from motion due to breathing and hemodynamic fluctuations. Excitation light has to travel through the tissue before reaching the fluorophore and once light is emitted this travels through brain tissue and air before reaching the camera-lens assembly. The brain is a well-perfused organ and hemoglobin absorption is heavily dependent on the wavelength of incoming light as well as the blood oxygenation. If perfusion and blood oxygenation were constant the effects of bran perfusion on wide-field GCaMP images would be null [132]. However, as described in the section on neurovascular coupling, increases in brain activity cause hyperemia [87] in the activated areas leading to time-varying changes in light absorption.

Several strategies have been proposed for the removal of unwanted hemodynamic effects from the fluorescence data:

- Division of GCaMP imaging data by single-wavelength reflectance data at the emission wavelength (510nm) corrects for confounding hemodynamic effects by removing the time-varying absorption effects in the 510nm dataset. Diffuse-reflectance measurements give us an approximation of the absorption by hemoglobin, provided that it is measured at the emission wavelength. Recording sequential GCaMP images and reflectance images at the emission wavelength is useful for correcting unwanted hemodynamic effects in the recorded GCaMP fluorescence data. For this method, the approximation is made that the pathlength of excitation light (488 nm) is the same as that of the emission light (510 nm), additionally, the pathlength of the diffuse 510 nm reflection light is assumed to be equal to the sum of the excitation and emission pathlengths. In this case, contamination removal can be done by the simple division of the fluorescence ratio by the reflectance ratio[136].

- Regression of single-wavelength reflectance data at an isosbestic hemoglobin absorption wavelength represents an alternative to the method above. For this strategy, correction is being done by using reflectance imaging at 390 - 410 nm wavelength that also has the property of exhibiting equal absorption for oxygenated and deoxygenated hemoglobin. At these wavelengths, any fluorescence emission from GCaMP is calcium-independent [137–139]. This type of reflectance imaging estimates changes in global blood volume in the tissue being imaged. Computationally, linear regression is done on a pixel-by-pixel basis to remove trends found in the 390-410 nm channel from the GCaMP fluorescence data [132].

- Using estimated excitation and emission attenuation. GCaMP excitation and emission attenuation can be used to correct unwanted hemodynamic effects. Practically it is very difficult to estimate the attenuation at the excitation wavelength of the fluorophore without using a filter wheel or a second camera for acquisition. It was proposed instead to use reflectance measured at 530 nm and 630 nm to model the absorption coefficient at 488 nm [136].

- Hemodynamic effects removal with PCA. If reflectance data was not acquired, PCA can be used to isolate unwanted physiological noise [140]. When doing PCA it is assumed that the variance in the original data can be expressed as a sum of temporal components. Hemodynamic effects are, however, multiplicative so PCA should be performed on the logarithm of fluorescence data which reduces this problem[135]. Performing PCA on the logarithm of the fluorescence data yields two components that resemble the temporal dynamics of GCaMP signal and hemodynamic confounding factors. This method works best for short recordings in conjunction with noise reduction preprocessing steps such as low-pass filtering and averaging across trials [140].

2.2.2 Applications of wide-field calcium sensor imaging in neuroscience

Owing to its good SNR and high sampling rate, wide-field calcium imaging has been used for the study of information encoding across large cortical regions on a trial-by-trial basis [137,141,142]. Sensory information was found to be represented in distinct spatio-temporal patterns across the cortex [124,141–143]. Having the capacity to image most of the dorsal cortex also proved advantageous in probing the mechanisms underlying learning behavior[143,144]. It was revealed that, during learning, heterogeneous brain activation patterns become more stereotypical as the task is mastered and patterns are refined to essential activation sequences [145,146]. The performance of tasks is dependent on the presence of a brain state that can sustain complex behavior. Several studies have investigated the characteristic features of the functional neural network under anesthesia [147–149] and dissociation [139].

Apart from these studies related to information processing and goal-directed learning, wide-field calcium imaging was also useful in describing the remodeling of resting-state cortical activity patterns after photothrombotic stroke [148], and monitoring wave-like patterns of activation in models of neurodegenerative disease [150,151].

A limitation of this imaging method is represented by its spatial resolution which is confined to 2D representations. Photoabsorbers at different depths contribute to varying degrees to the signal in the final image. If absorbers are located at a fixed depth in the brain tissue, emitted light will diffuse and lead to a 'blurred' image of the sources. The amount of blurring will ultimately depend on the depth of the fluorescent sources. If the sources of fluorescence are situated at multiple depths, the superficial ones will have a larger contribution to the final image to the detriment of the deeper ones.

The absorption of a photon by the fluorescent sensor is isotropic, i.e. photon absorption can occur regardless of the direction it is traveling. Likewise, fluorescence emission is also isotropic, meaning that a photon can be emitted by the fluorophore in any direction. This may lead to an additional blurring of the object that is being imaged although the photons with shorter paths will have a better chance of contributing to the final signal [136].

Both synthetic and genetically encoded calcium sensors are expressed in neuronal bodies as well as in the neuropil. Widefield calcium imaging can be done at cellular resolution, however, cellular bodies will be distinguishable only if they are situated just below the dura and if imaging is done through a glass window that has been installed after skull removal. Deeper neuronal bodies will be blurred by scattering effects, regardless of the preparation strategy [20]. If imaging is done through the skull, the thin layer of bone will scatter these signals and cellular resolution will be lost entirely. Practically this means that in most widefield optical imaging applications, signals coming from the neuropil are summed up with those originating in neuronal bodies to form the final image.

Constraints on this imaging modality are also imposed by the brightness of the calcium sensors as well as their dynamics. Exposure time and illumination intensity have to be adapted to the characteristics of the fluorescent signal sources to produce images with high SNR at acceptable temporal resolution [135]. Calcium sensors mainly report action potential events, thus subthreshold depolarizations, as well as hyperpolarisations, are not accessible to this imaging technique [152,153].

To address some of these challenges, wide-field calcium sensor imaging has been carried out simultaneously with other neurorecording techniques to enrich and also validate observations. Two-photon imaging at cellular resolution can be carried out simultaneously with wide-field imaging to reveal how the temporal activation of single neurons correlates with cortex-wide activation trends [138]. The same goal can be achieved by combining single-cell electrical recordings with wide-field imaging [154,155].

3D imaging of the entire mouse brain can be achieved with fMRI and adding 2D fluorescence imaging to the system was useful in describing the origin of the BOLD effect by correlating it to calcium transients in excitatory neurons [92]. High-frequency activity above 10 Hz is difficult to record with wide-field calcium imaging. Combining imaging with electrophysiology can both aid in covering the entire spectrum of neuronal activity and relate the function of deeper structures to that of the cortex [156,157]. This synergistic approach is opening new avenues of research while also raising interesting questions for data scientists because it is not clear what weight to attribute to these observations which are based mainly on correlations either between deeper brain nuclei or single cells and the wider cortex.

2.3 Manipulating neuronal activity with optogenetics

In 1979 the discoverer of the DNA structure, Francis Crick, stated the biggest factor preventing progress in neuroscience was the lacking ability to control genetically defined cells in the brain while the others remained intact. It is desirable to access entire cell populations at once with high temporal precision and electrophysiological and chemical methods lacked either the spatial or temporal resolution to accomplish this. Francis Crick speculated that making brain cells photosensitive would allow neurons to be controlled with light pulses, enabling cell-type-specific experimentation [158].

The light-sensitive channels and pumps, known as opsins, which enable optogenetics were discovered in microbes [159,160] and later cloned and transfected into neurons [161]. The first opsin used for depolarizing neurons, channelrhodopsin-2 is a cation channel sensitive to blue light around 470nm. Halorhodopsin is a chloride pump that hyperpolarizes neuronal membranes inhibiting the firing of APs and is sensitive to yellow light around 580 nm [162,163]. After these initial breakthroughs, a large variety of opsins were developed which featured faster kinetics that allowed tighter control of neuronal APs [164].

The need for genetic tool multiplexing led to the production of opsins which are sensitive to different wavelengths of light. Light penetration is a decisive factor in optogenetics. Incoming photons are scattered by biological tissue and this phenomenon is more pronounced at shorter wavelengths leading to lower penetration for blue light compared to red [165]. Scattering is also tissue-dependent, skin scatters less than bone and the scattering of the skull is dependent on the level of mineralization [166]. As detailed in the wide-field imaging chapter, another factor limiting blue light penetration in tissue is absorption by hemoglobin. All-in-all red light penetrates deeper into the brain and can enable also non-invasive stimulation experiments through the intact skull.

Tissue damage is reduced in red light compared to blue. Shorter wavelengths are more energetic than long ones and when absorbed are more likely to induce phototoxic effects [167]. Red and infrared light, on the other hand, induce tissue heating which may lead to cell death. Both in the case of red and blue light, adopting pulsed stimulation schemes helps mitigate these issues [168]. Another advantage of using red light is that the mouse retina is dominated by rods and light sensitivity in the red spectrum is two orders of magnitude lower compared to the blue [169].

Several opsins have been put forward for optogenetic applications in the red, ReaChr [170], ChrimsonR [171], C1V1[172] representing some of the more popular variants. ChrimsonR induces strong neuronal responses around 630nm in Drosophila though responses can be elicited at wavelengths as long as 720nm (with higher light intensity). CrimsonR presents intermediate activation kinetics enabling modulation of stimulation pulses at around 20 Hz which makes it suitable for the study of a large spectrum of neuronal subtypes [171]. A strong motivation for using red-shifted optogenetic actuators is the potential of coexpressing another opsin for the stimulation of two neuronal populations, or a calcium indicator for all-optical input/output experiments. In cortical mouse brain slices, ChrimsonR induced spikes only after irradiation with blue light above 0.5 mW, and this enabled two neuronal populations to be driven with blue and red light respectively [171].

Optogenetics can be used for the optical dissection of neuronal circuits in the intact brain in vivo and for establishing the roles of distinct neuronal populations. On the microscopic scale, the application of optogenetics in vivo in rodents has led to an increased understanding of the mechanisms underpinning sensory perception, motor functions, memory formation, and behavior [173]. While the stimulation of neurons can be done with electrodes or magnetic fields, optogenetics is unique in that it also enables the inhibition of entire neuronal populations. Through optogenetic stimulation and inhibition, it is possible to disentangle the identity of cells that are sufficient or necessary for certain behaviors [174].

Whole-brain connectomics also benefited from advances in optogenetics and imaging technology. Optogenetics allows direct brain stimulation without going through the spinal or thalamic relays of natural sensory pathways. Structural brain connectivity describes the hard-wiring of the brain [2] and functional connectivity denotes the temporally correlated neuronal activity of the whole cortex. More recently, a third type of connectivity has been described:

effective connectivity. Effective connectivity lies between structural connectivity and FC and reveals the influence that one region can have on other brain areas [14,175]. Stimulating brain regions directly, enabled effective connectivity to be studied in vivo. Asymmetries in connection strength between two regions might be masked by network-wide synchronization but are revealed with the help of direct brain stimulation using TMS [18] or direct electrical stimulation with miniaturized electrodes [176].

Optogenetics can improve on these stimulation strategies by allowing genetically defined neuronal populations to be targeted. Transgenic mice expressing ChR2 under Thy1 promoter control were investigated with wide-field optical hemodynamic imaging and the responses to optogenetic stimulation were recorded and analyzed to produce maps of effective connectivity [177].

An exciting area of research involves bringing together our knowledge of healthy brain connectivity patterns with the ability to directly manipulate the activity of extended neuronal networks with optogenetics. It was shown that slow waves during sleep are impaired in patients and mouse models of Alzheimer's disease and this cortical rhythm could be restored by enhancing GABAergic inhibition. Furthermore, restoring the healthy activity patterns was shown to lower the amyloid burden in the cortex [150].

Slow waves can also be initiated by optogenetic stimulation of ChR2 and it was shown that this less invasive method applied in mouse models was effective in preventing calcium overload and plaque deposition [178].

Additionally, optogenetics enables fast interventions which are impossible to achieve by chemical methods and neuronal inhibition which cannot be carried out through electrical interventions. In a closed-loop system of optogenetic inhibition, seizures were forecast based on local electrical activity and optogenetic inhibition of these regions was effective in preventing generalized epileptic states [10]. Such examples underline the prospects of forcing transitions from pathological to healthy brain states and offer great promise for the treatment of psychiatric and neurologic diseases.

2.4 Functional brain states

The simplest states available to biological systems are activity and rest. These can be viewed on-off states and can be observed in simple organisms such as algae as a response to sunlight. Mammals have evolved to be able to function in a wide range of environmental conditions. As a consequence, they evolved more complex neuronal networks and a broader range of brain states [179]. Generally, functional brain states refer to distinct and specific characteristics of the spatiotemporal dynamics of both ongoing, spontaneous activity and stimulus-evoked activity. Traditionally brain states were linked to vigilance states like wakefulness, sleep, and anesthesia. These terms have strong functional significance as they indicate the broad range of behavior that can be expected from subjects when their brains are in the configuration that is underlying one of these vigilance states. Because not all brain states result in observable behavioral changes, a clear distinction was made between states of vigilance and functional brain states [4]. A more concrete definition of brain states is needed to make progress in their characterization.

A modern definition of brain states that stems from the field of computational neuroscience, postulates that brain states "consist of continuously evolving dynamics of widespread networks that are characterized by condition-dependent self-organization, going through stable, quasi-stable, high or low activities, and transient arrangements" [11]. This definition will allow us to make progress in describing and categorizing brain states provided that we figure out how to best capture and model their dynamic features [180].

It follows that brain states are characterized by high dimensionality. Functional brain states can be visualized as points in a high-dimensional space where the coordinates represent groups of neurons and their levels of activation. When observed for longer periods, single points in this parameter space form clusters that represent general brain states. [4].

Another feature of brain states refers to their continuous evolution. Brain states are inherently dynamic showing discrete or continuous evolution towards related or different states. Discrete shifts could be represented by transitions from REM to non-REM state while continuous changes in the pupil diameter could indicate a progressive change in the level of alertness [11,181].

Functional states can vary without an obvious external manifestation. An example can be found in the pathological condition known as "locked-in syndrome", where subjects are immobilized but the brain is capable of wake-sleep transitions which are not immediately obvious to the observer. However, substantial changes in observed behavior have their causal roots in evolving brain states [4]. It would be desirable to identify the state of the brain based on measurements of brain activity which are independent of externally observable behavioral changes.

Finally, spontaneous variation in the activity of brain networks can give rise to substates which greatly increases the state space for neuroscientific study. A universally accepted taxonomy of brain states is not available at the moment and this is partly due to the difficulty in defining substates and closely related brain states in a clear and workable manner. Thus, in the next section, the focus will be placed on a limited number of clearly defined brain states.

An interesting point to consider is the necessary spatial and temporal resolution needed to adequately characterize the complex dynamics which give rise to functional states. Recent data from the field of perception encoding suggests that the activation of a single pyramidal neuron in the barrel cortex of rodents can have a significant influence on the behavioral state of the animal [182]. These findings suggest that it would be desirable to record the activity of all neurons in the brain network with millisecond resolution. As discussed in the previous chapters, both molecular sensors of neuronal activity and imaging hardware impose limits on the spatio-temporal resolution of functional brain recordings. Therefore measuring and statistically modeling numerous components of the brain network at multiple spatio-temporal scales is seen as a practical approach to this problem.

In the next sections, I will address broad functional states which have been defined starting from microscale or mesoscale recordings of brain activity and explore the relationship between functional brain states and states of vigilance.

2.4.1 Functional states during wakefulness

Brain activity in awake, behaving animals is heterogeneous and highly context-dependent, yet some overarching functional trends have been characterized. High-amplitude, low-frequency fluctuations are typically observed when animals are quiet and immobile, while faster and smaller amplitude activity is recorded during active periods. Transitions between these types of cortical activity can occur in circumscribed regions or encompass the whole cortex [183]. Furthermore, it was shown that during wakefulness clusters of neurons can transition to slow-wave activity [184]. These transitions in functional activity can occur on time scales of milliseconds to seconds and this heterogeneity is also reflected in the observed effects of cortical stimulation, manifesting through high intrasubjective variability of evoked cortical responses[185].

Cortical activity emerges from the interactions between firing patterns of individual cells and can be described across wide temporal and spatial scales. Consequently, different neurorecording modalities offer different perspectives on the functional organization of cortical activity during the awake state. In the following, these different descriptions will be explored to achieve a multi-level overview of the dynamic phenomena.

Intracellular cortical neuronal recordings suggest that, during wakefulness, neurons are in a predominantly depolarized state [186]. High levels of neuronal excitability lead to sparse firing rates and complex network configurations[6]. When the electrical activity of multiple neurons is recorded during wakefulness their firing patterns tend to be desynchronized. Contrasting with sleep and anesthesia where APs are tightly bundled in periods of high synchrony [187].

The hallmark of awake brain activity in EEG is represented by high-frequency cortical rhythms. Wakefulness is described as a state of global neocortical desynchronization, dominated by low-voltage, high-frequency activity. The gamma oscillation is defined as having a frequency greater than 30 Hz and is closely associated with active information processing. This type of electrical signal can be observed in the sensorimotor cortex during finger movements and the occipital lobe when subjects have their eyes open and process visual stimuli. This cortical rhythm is usually short-lived, present in bursts that can last several seconds, and coexists with lower-frequency oscillations [188].

The coexistence of different frequency components in the same brain region means that higher frequency oscillations ‘ride’ on top of lower frequency ones. Neuronal spikes need to be precisely timed to ensure an efficient exchange of information between distantly located neurons. Neuronal oscillations can be conceptualized as windows for potential neuronal communication because they not only influence spiking events but also neuronal sensitivity to incoming electrical signals [189,190]. Given that transmission delays in the brain are far shorter than the window of opportunity represented by the oscillation cycle length, it is likely that the reception and sending of information happen within one excitability peak. This hypothesis is called “communication through coherence” and there is information to suggest that during the awake periods, the brain can process complex tasks by maximizing the opportunities for information transfer between functionally connected groups of neurons [191].

The brain at rest, i.e. when not engaged in an obvious task shows highly correlated activity between functionally related regions of the left and right hemispheres [13,192]). The presence of this structured activity supports the idea that the mammal brain reverts to default modes of information processing when not actively interacting with the environment. The waxing and waning activity patterns during the awake state exhibit rich temporal dynamics and are organized in well-defined functional networks [193,194]. This observation comes from the field of fMRI and was later confirmed by EEG in the theta and alpha frequency bands (4-12 Hz) [195,196].

These spontaneous functional connectivity patterns are also present during light sedation [197–199]. During sedation, brain activity is chemically modulated but the underlying structural connections (i.e. axons, dendrites, larger nerve tracts) remain unchanged. Consequently, it was suggested that the persistence of complex activity during sedation was a reflection of spontaneous semi-random circulation of neural signals through a network with a fixed correlation structure. In silico modeling of spontaneous activity seemed to support this view as it was found that passing noisy reverberations through a whole-brain model produced activation patterns that matched experimental data acquired in periods when no obvious tasks were performed [181,200].

The most prominent of the spontaneous activity networks in humans [13,201,202] and non-human primates [203–205] is the default mode network (DMN). The DMN consists of brain regions that are more activated during rest periods than while a task is being performed. A correspondent of this network has also been described in rats [198] and mice [206–208].

Abnormal DMN connectivity has been observed in Alzheimer's disease, Parkinson's disease, depression, schizophrenia, epilepsy, and drug addiction[209–214]. The presence of this network in other mammal species allows for a mechanistic investigation of these aberrant findings using all the genetic tools of modern neuroscience. The translational relevance of these findings from rodents is however unclear given the diminished complexity of the DMN in these animals.

The existence of this network across species also suggests that baseline brain activity might have an important physiological role in ensuring the integrity of cortical circuits and in processing streams of information that do not originate in the outside world. There is increasing evidence suggesting compartmentalized spontaneous activity is not an exclusive hallmark of awake brain activity as most animal studies examine the DMN in sedated or even anesthetized conditions [198].

In humans, the DMN has been associated with self-referential neural processes and inward-directed lines of thought. It has been observed that external stimuli were leading to a decrease in the activity of the DMN while inward-oriented activity led to an increase in default activity. This explanation seems less likely in rodents, such that we must consider other possible functions of compartmentalized network activity such as the carrying out of housekeeping tasks or that this type of activity can arise from spontaneous fluctuations in strongly interconnected networks as suggested by computational studies [181].

2.4.2 The persistent brain state during sedation

The term sedation refers to a state of diminished vigilance in which subjects show responses to strong stimulation but are otherwise motionless and appear to be in a sleep-like state [215]. This vigilance state is typically induced by low doses of gamma-Aminobutyric acid (GABAA) receptor agonists (for example isoflurane) [216], and alpha-adrenergic receptor agonists (for example medetomidine) [198].

Medetomidine belongs to the imidazole subgroup of alpha-adrenergic receptor agonists which is used in clinics for the sedation of ventilated patients as well as for sedating pediatric and adult patients in preparation for medical procedures and imaging studies [217]. It induces an $\alpha 2$ receptor-mediated alteration of arousal by mainly targeting neurons in the locus coeruleus [218] causing hyperpolarization through increased K+ efflux, inhibition of voltage-sensitive Ca2+ channels, and a reduction of norepinephrine release in these neurons [219]. During wakefulness, the locus coeruleus inhibits the preoptic area of the hypothalamus which would normally have an inhibitory effect on the ascending arousal centers, thus promoting the awake state. The hyperpolarization of locus coeruleus neurons by medetomidine also causes an activation of the preoptic area, promoting a state which is behaviourally similar to non-REM sleep [216].

During sedation, intracellular recordings show power spectra that closely approximate those of awake animals, with persistently high levels of neuronal excitability [186]. In mesoscale recordings, during sedation, compartmentalized spontaneous network activity is present. In the following, the term ‘persistent brain state’ will be used to denote the presence of compartmentalized mesoscale network activity.

EEG shows brain activity under medetomidine is dominated by sleep spindles. Spindles are short bursts of 11-14 Hz [220,221] and are thought to disrupt sensory information processing in the brain and prevent the return to the state of arousal [221]. These features led researchers to use medetomidine as a means of achieving “pharmacological sleep”, a state useful for mechanistically studying the typical oscillations of stage 2 sleep. Compared to propofol which represents GABA-ergic induced unconsciousness, medetomidine showed less power and coherence in the Alpha band. Similarly, lower amplitude slow oscillations were observed in medetomidine compared to propofol [220].

The medetomidine induced persistent brain state is employed in neuroimaging studies because it preserves patterns of activation that are similar to the awake state [222,223], though less pronounced negative correlations between cortical areas were observed under medetomidine with respect to awake recordings [224]. It was observed in mice that under medetomidine functional connections between the DMN and thalamic networks were preserved while isoflurane activity failed to show these subcortical connections [225]. This suggests that medetomidine may have an advantage over other anesthetics in preserving the activity of subcortical networks.

Recordings in the persistent state under medetomidine have also been used for mapping the cortical and subcortical representation of somatosensory stimuli with fMRI [80,226,227]. The results from these fMRI studies were confirmed using wide-field imaging in transgenic GCaMP6s mice [148]. Responses to stimulation were localized to specific brain networks and this differed when compared to the global responses recorded under anesthesia [91].

Experiments in a sedation are lower in complexity compared with awake experiments where brain reactions are largely dependent on the behavioral context which has to be laboriously monitored and characterized over the entire duration of the imaging session. Furthermore, sedation enables complex imaging experiments to be carried out with as little stress for non-human subjects as possible. Sedation however is not a perfect substitute for awake experiments since the introduction of a pharmacological agent will modulate the interactions between brain networks to some degree. It was demonstrated that awake, spontaneous brain activity differs from the anesthetized in that fewer negative correlations between related brain regions were present [199]. While urethane and propofol are best suited for preserving functional brain connectivity, the necessity for intravenous administration of propofol and terminal experiments in the case of urethane make these two options more difficult to apply in vivo in small rodents [224].

It should also be stressed that medetomidine sedation is also not a substitute for investigating all aspects of natural sleep since no combination of drugs is currently able to recreate the complex brain dynamics of sleeping animals [228]. Additionally, while brain activation patterns in fMRI might look similar in sedation and awake states, fMRI only has access to lower frequency brain activation patterns. For investigative techniques with high sampling rates like EEG, the absence of high-frequency rhythms like the Gamma oscillation represents a major point of difference between the awake and the sedated states [220].

2.4.3 The slow-wave state during anesthesia

Anesthesia is a drug-induced reversible state characterized by unconsciousness, analgesia (lack of pain perception), akinesia (loss of motor functions), and amnesia (loss of memory)[228]. The first drug found to induce these complex effects on the human brain was diethyl ether, $(C_2H_5)_2O$, a highly volatile, sweet-smelling compound. The potential of this substance for enabling complex surgeries was recognized by dentist William T. Morton and chemist Charles Jackson in the middle of the 19th century. The term anesthesia was coined by Oliver Wendel Holmes, a professor at the Harward medical school, and stems from the Greek term anaisthesia which can be translated as lack of sensation [229].

Ether was so successful in rendering patients insensate, that modern variants of this substance like sevoflurane and isoflurane are still used in selected patients. Modern anesthesia protocols include injectable agents like propofol in combination with opioid analgesics and muscle relaxants to achieve unconsciousness, analgesia, akinesia, and amnesia [216]. Inhalation anesthetics like isoflurane exhibit all the effects above without the need for adjuvant medication [230]. Consequently, these inhalant drugs are used in neuroscience to investigate brain dynamics in the anesthetized state [230,231].

Inhalant anesthetics from the ether family, like isoflurane, cause increased neuronal inhibition and decreased synaptic excitability ultimately leading to a state of increased neuronal hyperpolarization [232]. These drugs bind to target receptors in the neuronal membrane to act as allosteric modulators of synaptic transmission. Isoflurane increases GABA-A and Glycine receptor activity [233] and reduces the activity of glutamate NMDA (N-methyl-D-aspartate) receptors [234,235]. Isoflurane also elicits a modulatory effect on ion flow through the membrane inhibiting voltage-gated sodium [236] and potassium [237] channels while augmenting the activity of two-pore potassium channels [238]. Long-term potentiation refers to the 'strengthening' of a synapse due to recent patterns of activity and has been proposed as an essential process underlying memory formation [239]. The amnesic effects of isoflurane could be mediated by a disruption in long-term potentiation and neuronal ability to store information [240].

These complex effects on multiple molecular targets cause up-down transitions in neuronal excitability [230]. Intracellular electrophysiology in cats revealed slow oscillations <1 Hz in pyramidal neurons during non-REM sleep and quiet wakefulness. These oscillations consist of a hyperpolarized down state lasting several hundred ms in which the neuron remains in a quiescent state followed by an up state in which neurons fire multiple action potentials [241]. During up states, the thalamocortical system shows remarkable activation, with neurons firing at higher rates than in the awake state [242]. Slow waves are observed in thalamocortical networks, and it was shown that the cortex alone is capable of sustaining this oscillation if thalamocortical connections are severed [243–245].

In humans, EEG reveals that a "spectral slowing" occurs when inhalant anesthetics are introduced [246]. The fast rhythms associated with the human awake state are replaced by alpha oscillations with a coherence peak at 10 Hz, delta oscillations with maximum coherence at 4.9 Hz, and slow oscillations. Additionally, alpha oscillations seemed to shift from predominantly occipital locations during the awake state to the frontal lobe after sevoflurane-induced loss of responsiveness. This phenomenon which has also been described for propofol is referred to as “anteriorization” [247].

These EEG changes were also confirmed in rats which indicates rodents may be useful model animals for systems-level studies of anesthesia-induced brain oscillations. This rodent model enables the mechanistic investigation of slower cortical rhythms and their possible role in the loss of consciousness. In rats, the observed oscillations were dependent on the anesthetic dose. At 1.6% sevoflurane (during induction), increased beta/low gamma activity in the prefrontal cortex, the parietal cortex, and central thalamus was associated with increased motor activity. At anesthetic gas concentrations between 1.6 and 2.8%, there was a shift of the EEG traces to the slow-delta spectral frequencies, and a motionless state accompanied by a loss of muscle tonus was observed. From 2.2% to 2.8% burst suppression (alternating high-frequency activity with isoelectric periods) was present. These findings seem to suggest that slow cortical rhythms together with a marked decrease in fast oscillatory activity may be the hallmark of EEG activity under anesthesia.

EEG is well suited to investigate electrophysiological events on a systems level. The spatial discrimination of EEG in rodents is, however, relatively low. In humans, a larger number of electrodes can be fitted on the scalp and provide more detail about the spatial characteristics of slow cortical rhythms. In humans, during non-REM sleep, EEG was used to track the systems-level spatio-temporal features of the slow oscillation. It was demonstrated that slow oscillations have a distinct point of origin and spread outward from this source with a speed of 1.2-7 m/sec to eventually encompass the entire cortex [248]. For this reason, the slow oscillation is also known as slow-wave.

Notably, slow waves are also observed during anesthesia [241,249–252] and can be distinguished from sleep slow waves by longer off periods and likely place of origin in the cortex [253].

A mechanistic description of cortical slow waves necessitates cell-type-specific manipulations and a fast readout of brain activity for which the mouse is well suited. Additionally, repeatable slow waves can be initiated in the desired cortical areas by using brief somatosensory stimulation [254,255]. Optogenetic stimulations have also been shown to trigger slow waves under isoflurane anesthesia in mice.

The role of the thalamus in the generation of slow waves is unclear. After stimulation of the dorsolateral geniculate thalamic nucleus, a slow wave was first recorded in the occipital cortex and arrived in the frontal cortex 80 ms and in the thalamus 190 ms later. This would seem to suggest that the origin of slow waves is in the cortex rather than in the thalamus, a finding also supported by electrical recordings [244,252]. It could be shown that slow waves have a refractory period during which optogenetic and somatosensory stimulation failed to trigger any functional cortical responses [252].

The high degree of synchrony between spatially and functionally distinct brain regions may suggest that deeper structures are involved in slow-wave initiation and propagation. Attention has been focused recently on the claustrum, a thin sheet-like island of gray matter located between the insular cortex and the striatum. The claustrum is comprised of large neurons which send fibers to all cortical regions [256,257] and for this reason, it was hypothesized to play a role in the synchronization of global cortical events such as slow waves. Channelrhodopsin2 was expressed in excitatory claustral neurons and after optogenetic stimulation, it was revealed that cortical inhibitory interneurons were primarily activated. As a result, after brief optogenetic stimulation of claustral neurons, a downstate ensued in the cortex [258].

The speed of cortical slow waves was measured in mice at around 40 mm/sec [252]. This may indicate that slow-wave dynamics under anesthesia differ from sleep where, at least in humans, slow waves propagate much faster [248].

Results from mesoscale and macroscale imaging studies appear less clear than those from implanted electrodes and fiber-photometry. Previous research into functional connectivity (FC) of the brain in deep anesthesia using fMRI in humans and non-human primates reported a reduction in functional connectivity [259,260]. Others reported a loss in functional segregation during anesthesia and global synchronized cortical activity [91,197,261]. A study into transitions from light sedation to anesthesia using fMRI in mice reported a reduction in homotopic correlations as well as cortical functional network segregation levels [262]. These findings seem contradictory since the loss of functional segregation would lead to global activity patterns and these would produce an increase in homotopic correlations.

Functional connectivity during the awake and anesthetized states was investigated with wide-field optical data collected in transgenic GCaMP6s mice. After the removal of the first three principal components from imaging data depicting slow waves, the resulting correlation structure resembled that obtained from awake recordings. Of course, structural connectivity does not change with the introduction of anesthesia possibly explaining the presence of activation patterns similar to the awake state [149]. It was also shown that, in awake mice, cortical waves <1Hz, as well as delta waves, travel from back-to-front and from front-to-back at different time scales, and the direction of propagation is reversed during anesthesia as compared with the awake brain. These reversals in propagation trajectory were not observed in higher frequency ranges [147].

Global slow waves were identified in fMRI datasets from rats [91] and mice [263] with the help of ‘ground truth’ fiber-photometry fluorescent calcium indicator recordings. The fluorescence data was used as a regressor in a general linear model for the analysis of fMRI data and revealed pancortical increases in cerebral flow as a delayed response to calcium slow waves.

The prevalence of slower cortical rhythms during anesthesia could be associated with disrupted cortical information flow caused by oscillatory coherence in thalamocortical networks. Furthermore, cortical slow waves contribute to the fragmentation of cortical activation patterns [264]. The high degree of similarity between cortical rhythms observed under propofol and sevoflurane suggests that the modulation of GABA-ergic transmission could be an essential mechanism for explaining the loss of consciousness under sevoflurane [232,265]. Cortical slow waves are present both during non-REM sleep and anesthesia and both of these are states that do not allow conscious experiences to form. Furthermore, as outlined above, slow waves represent stereotypical and global brain responses to heterogeneous somatosensory and optogenetic stimulation. Conscious brain responses to stimuli would be expected to have high degrees of complexity. It is for these reasons that cortical slow waves have been linked to unconscious brain states.

Most of the data on slow waves comes from electrophysiology and fMRI studies. Electrophysiology is limited in the spatial resolution that is attainable while fMRI represents an indirect method for recording neuronal activity. For this reason, data from recent publications on functional connectivity contains contradictory results. It was reasoned that calcium fluorescence neuronal recordings from the entire mouse cortex will allow identifying the precise patterns of neuronal activity responsible for transitions from the persistent to the slow-wave state.

2.4.4 Dissociation-unconsciousness

Dissociation refers to an altered behavioral state in which the unitary nature of experience is disrupted. There is a disconnection between thoughts, feelings, memories, sensory experiences, and the sense of self. Most prominently, stimuli are perceived but the affective responses usually associated with them are absent, nociceptive stimuli, for example, are not associated with the feeling of pain while visual or auditory stimuli can lead to hallucinations. Dissociation can be the result of epileptic seizures, trauma, or the use of dissociative drugs like ketamine [266]. There is mounting evidence that specific neuronal activation patterns underlie the complex behavioral features of dissociation hinting at a dissociated brain state [139]. During this work, spontaneous activity and responses to stimulation under ketamine will be investigated in an effort to strengthen these arguments with quantitative data. The concentration of ketamine used ensured a sedation-like state so the brain activity recorded reflected both dissociation rhythms and ones more common in altered states of vigilance.

Ketamine is an arylcyclohexylamine that has found a wide range of uses in medicine for its analgesic, hypnotic and dissociative properties [267]. In neuroscience, ketamine has been used to study the dissociated state [139,268] and as a drug for the induction of auditory and visual hallucinations in animal models of schizophrenia [269]. Its hallucinogenic and dissociative properties also make it a popular recreational drug [270].

The principal molecular target of ketamine is the NMDA receptor, a major postsynaptic binding site of glutamate. Ketamine blocks this receptor by binding to a subunit that is different than the glutamate binding site. It has been shown that GABAergic interneurons are targeted first and their activity is diminished. Because these interneurons elicit an inhibitory effect on cortical pyramidal cells, the net effect of ketamine is the disinhibition of pyramidal neurons throughout cortical and subcortical areas [268]. It has also been shown that ketamine increases cortical dopamine levels and this could also be reflected in increased gamma activity [271]. This disinhibits tightly controlled spatial and temporal activation patterns that usually govern the awake state and could play a fundamental role in dissociation and the generation of hallucinations [216]. Analgesic effects are most likely generated through the inhibition of NMDA receptors in the spinal cord and the dissociative properties of ketamine [272].

The pharmacological properties of ketamine are directly reflected in the electrical patterns generated by the brain in drug-induced dissociation. Contrary to most other medications used in anesthesia, ketamine causes an activation of the EEG, featuring prominent oscillations in the Gamma range [273]. The increased power in this frequency band is most likely caused by the increased ketamine efficiency in blocking NMDA receptors on fast-spiking interneurons compared to the same receptors on pyramidal cells [274]. Gamma oscillations can occur in bursts or in a stable state accompanied by beta waves. The coherence profile gamma activity may reflect disruptions in neuronal activity which could play a role in generating hallucinations, however, it is not clear whether it plays a role in causing unconsciousness. In humans, an increase in coherent theta oscillations and reduced alpha and gamma oscillations were also present [275]. In rats, gamma activity was increased by 200-400% [276] in the prefrontal cortex compared to the awake state while power in other bands did not change significantly [277]. Slow oscillations were also present in alternation with faster rhythms, and this so-called “saw tooth” pattern was associated with increased doses of ketamine [275].

In mice, it was possible to mechanistically study the molecular underpinnings of brain rhythms under ketamine. With the help of wide-field GCaMP6 imaging, a 1-3 Hz rhythm was observed in the retrosplenial cortex after the administration of 50 mg/kg of ketamine.

Furthermore, this brain rhythm was confined to layer 5 of the cortex and was potentiated rather than inhibited by optogenetic inactivation of thalamic nuclei [139]. This suggests that the cortex rather than the thalamus is responsible for initiating and sustaining this oscillation. It was observed that hyperpolarization-activated cyclic-nucleotide-gated potassium channel 1 (HCN1) was highly expressed in the retrosplenial cortex and its local optogenetic inactivation in mice led to diminished 1-3 Hz retrosplenial rhythm after ketamine administration.

When this activity was present mice showed dissociation-like behavior with preserved paw-lick reflexes and diminished jump-to-escape behavior [139]. This indicates that, in this state, the sensory and motor pathways in these mice were preserved, however, the animals failed to see the toe pinch as a negative stimulation, which is consistent with dissociated states in humans. To test whether the layer five 1-3 Hz oscillation played a causal role in dissociation, both inhibitory and excitatory opsins were expressed in this region and upon optogenetic stimulation, affective paw-licking and escape behavior were reduced [139].

In a patient suffering from epileptic seizures with dissociation-like auras, a 3.4 Hz oscillation was identified in the deep posteromedial cortex just before the onset of ictal activity. The retrosplenial cortex in mice represents the analog of the human posteromedial area. Electrical stimulation of this area in the patient via the implanted electrodes produced a dissociation-like state [139].

These findings offer the exciting prospect of linking a circumscribed brain rhythm to psychiatric and drug-induced dissociative states. However, this finding might be a part of a more complex picture as suggested by the heterogeneity of EEG brain activity recorded in this state. Particularly, symptoms of dissociation seemed to be associated with decreases in alpha-band activity in EEG rather than an increase in delta oscillations [278,279]. The ketamine dose administered by Vesuna and colleagues in mice (50 mg/kg) is equivalent to 2-3 mg in human subjects and it is well documented that dissociation occurs in humans even at doses lower than 1 mg/kg in humans. The higher dose in mice might cause changes in the animal's state of arousal and these need to be taken into account in the translation of these observations to humans. More data needs to be generated, both in human and non-human subjects to strengthen the case for the retrosplenial rhythm as a causal driver for behavioral aspects present in dissociation [279].

Comparative studies between dissociation-unconsciousness and persistent/slow-wave activity will shed light on the significance of the characteristic features of functional cortical activity described above.

2.4.5 Quantifying and modeling functional brain states

In the sections above imaging and electrophysiological findings thought to underpin functional brain states have been presented. Different research communities have their specific way of describing the characteristic features of functional brain activity in a particular state. The difference in metrics is brought about by the physical limitations of the recording system used.

It is also apparent that none of the phenomena described above is unique to a particular functional state i.e. in the awake condition, in which the persistent or desynchronized brain states occur, small clusters of the cortex can transition into a slow-wave brain state [184]. The gamma rhythm is subdued in anesthesia, except under ketamine where it is more prominent even than in the awake state and compartmentalized network dynamics have been observed both in the awake state and in sedation[275]. There is a need for creating theoretical frameworks and empirical strategies that allow for common concepts to emerge that will help to better define brain states.

Furthermore, the brain states described above are textbook examples of brain activity from wakefulness and profound anesthesia. Both in medical practice and in neuroscience experiments, researchers are confronted with a continuum of brain states that often occupy parameter spaces different than those of the classic states described above. The administration of a psychoactive drug can be done in a gradually increasing concentration and it goes to reason that the observed brain activation patterns would change in a dose-dependent manner, in this case, the transitions from the persistent to the slow-waves states have proven very difficult to model. The oldest anesthetic, ether, had been used as a recreational drug inhaled in small concentrations for its pleasure-inducing properties before medical professionals realized that higher doses would render subjects totally insensate. Describing the dose-dependent impact of psychoactive drugs on the brain network is not trivial and will require the quantification of brain states and transitions.

Some of the earliest efforts to differentiate between conscious and non-conscious brain states rely on EEG indices which are based on signal entropy [280] or entail time-domain, frequency-domain, and bispectral analysis [281,282]. Most of these indices lack a theoretical foundation or can be loosely associated with integration theories of brain function.

A solid theoretical foundation is needed in order to accurately account for the heterogeneous brain activation patterns and dynamics observed in experimental neuroimaging data. In this endeavor, one can find useful approaches in computational neuroscience. Information processing over time and space would have to be captured accurately by computational routines in order to reverse engineer the brain and discover how behaviors are generated

[283].

Most in silico brain models include structural and functional information. A feature of evolving brain states is that they represent functional configurations of a network that is structurally invariant on time scales relevant to most neuroscience experiments. Not all possible structural connections are used all the time, so the anatomical data is enriched with functional information to reveal useful parcellations of the brain that will help simplify the computational models [284]. Structural/functional whole-brain models aim to explain the most salient functional features of network activity by optimizing coupling parameters in the structural data. This approach has been successful in modeling spontaneous brain activity recorded with fMRI [285].

Another category of theories seeking to explain brain states is based on the importance of information integration in the brain [282]. Metastability is relevant to modeling brain dynamics and refers to the balance between segregation and integration. On the one hand, specialized brain networks need to carry out their functions irrespective of interference while producing higher-order content is usually achieved by the synchronization and coordination with other functional areas [286].

Metastability can be conceptualized as a state that lies outside of the natural equilibrium of the system but persists over long time periods [287]. If we imagine the cortical network elements as players in an adversarial game, a metastable state refers to an extended period of winnerless competition [288]. Practically, the phase of brain signals coming from network elements can be leveraged to calculate the synchronizations between brain regions and produce "probabilistic metastable substrates". This method called "leading eigenvector dynamics analysis" (LEiDA) has been proposed for characterizing dynamical brain states [289] and is capable of differentiating between sleep [180], awake activity [289], task processing [290], and hallucinatory states [291]. Models based on metastability offer good perspectives for describing and capturing functional features that may indicate transitions between brain states.

Recently, transitions between sleep and wakefulness have been modeled with LEiDA, and interventions were identified which could force the network to transition between sleep and wakefulness. Despite these encouraging results, most current brain models are falling short of predicting such interventions. One limitation of these computational approaches when modeling the human brain is that they have low spatial and temporal resolutions.

Another theoretical framework based on information integration has been put forward as a way of explaining how conscious perception is generated. In this framework, information is defined as "a reduction of uncertainty among a number of alternative outcomes when one of them occurs" [292]. The information integration theory (IIT) claims that the architecture of an information processing system is the decisive factor in its ability to integrate information [293,294].

To illustrate this the authors consider a digital camera sensor that has 1 million individual photodiodes and can differentiate between 21 000 000 states (each pixel can have only one of 2 states: light present vs. absent). However, in this system, the photodiodes are wired in parallel, not integrating any information. The camera sensor could thus function if all diodes were mounted individually on separate chips instead of on the same board.

The neuronal network is highly interconnected and capable of information integration. For this reason, the spectrum of states in a neuronal network cannot be subdivided into the set of states available in individual neurons. According to G. Tononi, any system that has a large repertoire of states (i.e. information) and cannot be subdivided into causally independent subcomponents would be capable of generating experiences. Practically, the amount of integrated information called phi can be calculated by finding the minimal information bipartition. Next, the number of bits of information flowing between the partitions is calculated and this represents the phi index [295]. This brute-force approach requires a search through all possible network bipartitions and allows the calculation of phi for small networks under 200-300 nodes but for larger assemblies, the calculation time rises super-exponentially with network size and is impractical[296].

The information integration theory can be applied for the assessment of any information processing system be it biological or synthetic but the mathematical structure of IIT has been challenged [297,298] and the explanatory power of IIT remains controversial [297,299].

IIT predicts that brain responses to external stimuli should be both widespread and differentiated. This prediction led to the development of the perturbation complexity index (PCI) which involves stimulating the brain directly with transcranial magnetic stimulation and reading out responses with EEG. PCI is a surrogate measure of effective connectivity.

In EEG sources of activation are identified and binarized to form a spatial distribution of activated brain regions. These images of the cortex are then compressed with the help of the Lempel-Ziv algorithm which is then normalized by the source entropy to calculate the PCI. PCI is sensitive to both integration, captured by local versus global responses, and differentiation evident in complex versus stereotypical responses. PCI was able to differentiate between wakefulness, non-REM sleep, and anesthesia. Furthermore, PCI proved useful in pathological brain states showing high values in patients with locked-in syndrome, intermediate values in minimally conscious patients, and low values in individuals in vegetative states [300]. The estimation of brain EEG sources of activation is computationally expensive, thus PCI measurements needed to be carried out offline. Recently faster algorithms were developed which enable PCI to be measured in near-real-time [301].

Topological complexity is increasingly used in brain imaging studies to assess brain connectivity [302]. For topological complexity measurements, time-varying functional brain recordings are converted into time-varying topological representations [303] in an effort to capture the spatial and temporal scales of the observed phenomena. The inputs for this analysis are represented by 2D images acquired over a set of time steps and aligned to a standard brain map [304]. The activation function is maped to a 3D data structure for the purpose of analyzing activation patterns brought about by somatosensory and visual stimulations. The vascular pattern of superficial veins and arteries of the brain is highly variable between subjects. Stimulation experiments in transgenic mice typically involve small cohorts thus a robust approach to topological variability when assessing cortical responses to stimulation is desired. This method was used to assess the complexity of evoked responses to stimulation.

Predicting how perturbations will influence the activity of functional cortical networks is a long-standing goal in computational neuroscience. In physics, researchers study complex dynamical systems by perturbing their components and observing the effects in order to infer underlying mechanisms. Analogously to physics, it would be desirable for computational neuroscience to make theoretical predictions that could be tested to confirm theories regarding brain function.

Network models of the human brain usually rely on structural connectivity information from diffusion MRI measurements which have a relatively high degree of uncertainty [305] and functional data from human neuroimaging studies is usually acquired with EEG or fMRI or a combination of both. These neurorecording methods lack information about the genetic identity of the neurons which are contributing to signal fluctuations and fMRI signals do not distinguish between excitatory and inhibitory activity. The uncertainty inherently present in functional and structural imaging studies could propagate through to the models and affect their accuracy.

More precise characterizations of brain structure and function can be achieved in rodent models. Particularly, more functional data is needed on functional state transitions, for example regarding the level of arousal. These functional datasets would benefit from structural connectivity obtained for example by tissue clearing techniques [306,307] or annotated electron microscopy mouse brain datasets [308]. The entire arsenal of genetic manipulations is available in mice and is already illuminating the neurocircuit origins of behavior [309]. Mouse brain models based on these rich datasets are coming online and their predictions are being explored for the purpose of identifying interventions that will force transitions between brain states in health and disease [310].

3

Materials and methods

3.1 Ethics statement

Animal experimentation: Animal husbandry and experimental manipulation were carried out in accordance with protocols approved by the government of Upper Bavaria.

3.2 Mice

Mice were housed in specific pathogen-free units under a 12-hour light/dark cycle, and food and water were provided ad libitum.

27 adult male B6 mice (>8 weeks old 30-40g) were used in this study. B6;CBA-Tg(Camk2atTA)1Mmay/J mice were bred with B6;DBA-Tg(tetO-GCaMP6s) - 2Niell/J) [124], genotyped for the GCaMP6s gene, and homozygous male mice were selected for experiments. All GCaMP6s positive animals were generously provided by the A. Stroh Lab (Univ. Mainz, Germany). 3 mice were used in fiber-photometry experiments. 6 mice underwent fMRI experiments: 3 were used for hind paw stimulation experiments and 3 for hybrid optogenetic and fMRI experiments. 18 mice were utilized in wide-field optical imaging experiments: 10 mice underwent viral injections for the expression of the optogenetic actuator ChrimsonR (5 in the somatosensory cortex and 5 in the visual cortex) and glass window implantation was carried out 4 weeks after injection. 5 mice underwent glass window implantation only and received somatosensory and visual stimulation. Immunohistochemistry was carried out on 3 animals. Indocyanine green (ICG) angiography was performed on 3 animals.

3.3 Surgical procedures

3.3.1 Intracranial injections

- 0.1 mg/kg buprenorphine was administered intraperitoneally 30 minutes before the start of the surgical procedure.
- Isoflurane was used as an anesthetic agent. 3.5% iso. concentration was used for induction and 1.5-2% for maintenance. Anesthesia depth was checked throughout the procedure with toe pinch reflexes.
- Temperature regulation was achieved with an electrical heating mat. Body temperature was maintained around 36.5°C.
- The cornea was hydrated with eye ointment (Bepanthen, Bayer).
- Mice were positioned in a stereotaxic frame, hair was removed and the skin was cleaned with Betadine (Braun).
- Local skin and periosteum anesthesia was done with a subcutaneous, 50 microL, lidocaine 2% (Braun) injection.
- A 7 mm incision was made with a scalpel, the fascia was pushed aside, and the skull was cleared of tissue and passively dried for 3 minutes.
- A 400 µm in diameter burr hole was made with a dental drill.
- A 33 gauge, stainless steel injection cannula (Plastics One) was fastened to the stereotaxic arm and lowered about 1mm below the dura mater.
- 1 microL AAV solution was injected over a 7 min period using a syringe pump (PHD 22/2000, Harvard Apparatus).
- The cannula was kept in place 10 minutes after the injection to allow for enhanced diffusion in the brain.
- Tissue glue (Vetbond, 3M) was used to seal the incision.
- Lidocaine 2% was applied to the skin for local postoperative pain relief.
- 5mg/kg Meloxicam (Metacam 2 mg/ml, Boehringer Ingelheim) was injected subcutaneously for systemic anti-inflammatory effect and pain relief.
- Mice were kept on a heated mat and monitored until they regained consciousness.
- A once-daily dose of 5mg/kg Meloxicam was administered subcutaneously for two days after the procedure to provide postoperative analgesia.

3.3.2 Optical fiber implantation

After viral injection, the encoded proteins are allowed 4 to 8 weeks to express. The glass fiber implantation procedure was carried out under isoflurane anesthesia.

- 0.1 mg/kg buprenorphine was administered intraperitoneally 30 minutes before the start of the surgical procedure.
- The surgery was conducted under isoflurane anesthesia. 3.5% isoflurane concentration was used for induction and 1.5-2% for maintenance. Anesthesia depth was regularly checked.
- Body temperature was maintained at around 36.5°C with an electrical heating mat and drying out of the cornea was prevented through the use of eye ointment (Bepanthen, Bayer).
- Mice were positioned in a stereotaxic device, after hair removal, the skin was cleaned with Betadine (Braun) and 50 microL lidocaine 2% (Braun) were injected subcutaneously for additional skin and periosteum anesthesia.
- A 7x4 mm in diameter oval incision was made and the fascia and other organic tissue is removed from the skull.
- A 2x2mm cranial window is made with the dental drill above the viral injection site
- A small groove is made with the dental drill caudally to the craniotomy to ensure that the glass fiber can be lowered close to the cortex.
- A 400µm in diameter optical fiber with a 45° mirror tip is positioned above the dura mater and covered with a drop of silicone gel (Kwik-Sil, World Precision Instruments). This represents a transparent medium that covers the cannula tip.
- The cannula and the exposed skull are covered with dental cement and the skin is secured to the edge of the dental cement with tissue adhesive (Vetbond, 3M)
- lidocaine 2% was applied to the skin to prevent postoperative pain.
- 5mg/kg Meloxicam (Metacam 2 mg/ml, Boehringer Ingelheim) were injected subcutaneously and the animals were allowed to recover on heated mats until conscious.
- 5mg/kg Meloxicam was administered subcutaneously once a day for two days to provide postoperative analgesia.

3.3.3 Skull window implantation

Alternatively to the optical fiber implantation, a cranial window has to be implanted for optical imaging. The cranial window implantation is carried out 4-8 weeks after intracranial viral injection.

- 0.1 mg/kg buprenorphine was administered intraperitoneally 30 minutes before the start of the surgical procedure.
- Isoflurane was used as an anesthetic agent. 3.5% iso. concentration was used for induction and 1.5-2% for maintenance. Anesthesia depth was checked throughout the

procedure with toe pinch reflexes.

- Temperature regulation was achieved with an electrical heating mat. Body temperature was maintained around 36.5°C.
- The cornea was hydrated with eye ointment (Bepanthen, Bayer).
- Mice were positioned in a stereotaxic frame, hair was removed and the skin was cleaned with Betadine (Braun).
- Local skin and periosteum anesthesia was done with a subcutaneous 50 microL lidocaine 2% (Braun) injection.
- An 8x4 mm in diameter oval incision was made and the fascia and other organic tissue is removed from the skull.
- The skull was gently rubbed with a brush and tin oxide (Sn_2O) powder.
- To protect the grass window, a narrow stainless steel frame was glued in place.
- A 10 mm glass window (Labmaker) was glued onto the skull with transparent UV-curing glue (Loctite 4305).
- The glue was slowly hardened over 10 min with 350 nm light from an LED.
- The skin is secured to the edge of the dental cement with tissue adhesive (Vetbond, 3M) and lidocaine 2% was applied to the skin to prevent postoperative pain.
- 5mg/kg Meloxicam (Metacam 2 mg/ml, Boehringer Ingelheim) were injected subcutaneously.
- Animals were allowed to recover on heated mats until spontaneous righting.
- Two doses of 5mg/kg Meloxicam were administered subcutaneously once a day for two days to provide postoperative analgesia.

3.4 MRI imaging protocols

Imaging is carried out one week after optical fiber implantation. All MRI imaging was done under isoflurane sedation.

Animal preparation:

- 3.5% iso. concentration was used for induction and 1-2% for maintenance.
- Body temperature was monitored and maintained at around 36.5°C with a heated water system that is integrated into the MRI mouse holders.
- Breathing rate is monitored via an integrated pressure sensor
- Drying of the cornea was prevented through the use of eye ointment (Bepanthen, Bayer).
- Both resting-state and stimulated datasets were acquired. The stimulation was carried out with subcutaneously implanted electrodes (15-sec stimulation blocks at 5Hz frequency / at 1mA intensity) or with optogenetic laser pulses (50 ms pulses every 10

s). The optogenetic stimulation was carried out with a fiber-photometry setup (Doric Lenses).

- The maximum experiment duration including all preparation steps was 3 hours.

All fMRI data have been acquired using a Bruker Biospec 94/20 small animal MR system (Bruker BioSpin MRI, Ettlingen, Germany) operating at 400 MHz (9.4 T) equipped with a two-channel receive-transmit cryogenic phased array coil (Bruker BioSpin AG, Fällanden, Switzerland).

MRI sequences:

Gradient Echo-Planar Imaging(GE-EPI): FOV = 20 × 13 mm2, MD = 96 × 64, yielding a voxel dimension of 200 x 200 x 500 µm, flip angle (FA) = 90°, bandwidth = 350 kHz, TR = 1000 ms, TE = 13 ms, NA = 1, yielding a temporal resolution of 1 s, with interleaved acquisition of slices. The duration of the image time series was 6 min.

T2-TURBO-RARE: FOV = 20 × 16 mm2, MD = 250 × 200, yielding a voxel dimension of 80 x 80 x 500 µm, flip angle (FA) = 90°, rare factor=8, bandwidth = 50 kHz, TR = 2500 ms, TE = 33 ms, NA = 2, with interleaved acquisition of slices.

3.5 Fiber photometry

Fiber photometry data was acquired with a fiber photometry setup consisting of a fiber photometry console (D460-2002, Doric Lenses), a dual-channel LED driver (LED-2, Doric Lenses), a blue fiber-coupled LED (CLED-465, Doric Lenses) for GCAMP excitation, a red fiber-coupled LED (M625M2, Thorlabs) for ChrimsonR activation, a beamsplitter/combiner (FMC5-E1(465-480)-F1(500-540)-E2(555-570) - F2(580-680), Doric Lenses and a Newport visible femtowatt photoreceiver (NPM-2151-FOA-FC). Cannulas with a 45° mirror tip were mounted above the cortex and directed light towards neurons expressing GCaMP and ChrimsonR (MFC-400/430 -0.37 -6mm-ZF1-MA45). Fiber photometry data was recorded at 1000Hz. Data was acquired symultaneously with fMRI, please see above for animal preparation.

3.6 Wide-field optical imaging setup

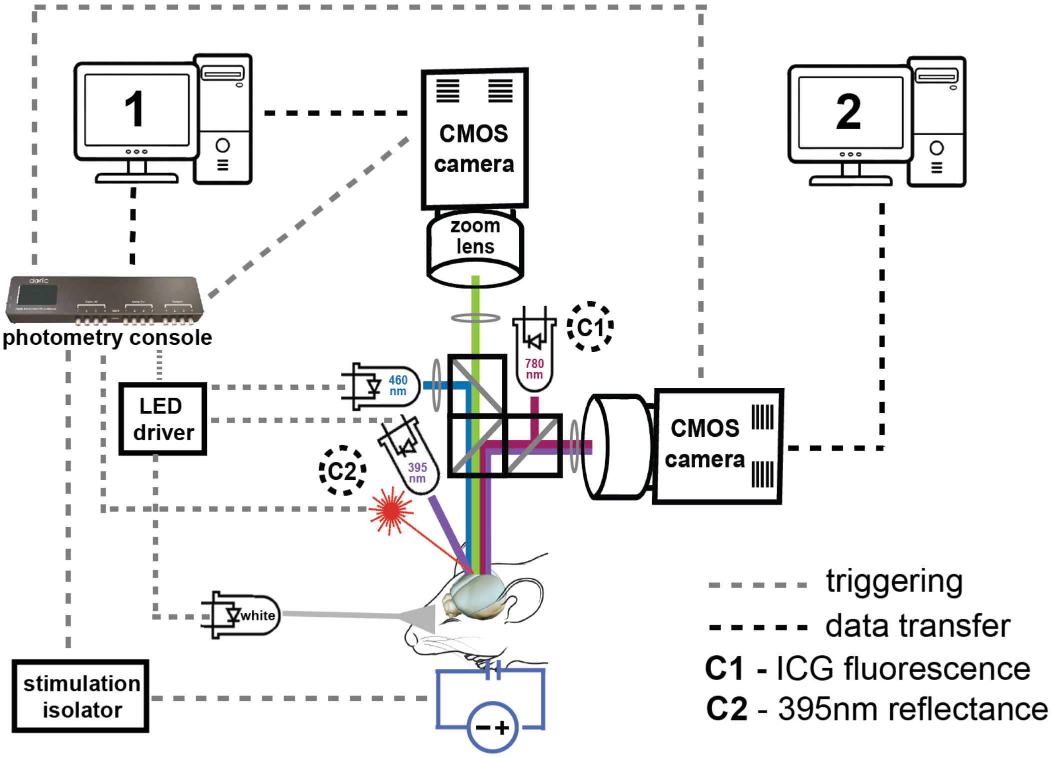

Figure 3.1: Widefield imaging setup and integrated stimulation devices. Schematic representation of the widefield imaging setup. The vertical optical path was used for imaging GCaMP and the horizontal path for hemodynamic imaging. Hemodynamic imaging was done in two configurations: C1 angiography after intravenous injection of indocyanine green (ICG) micelles and illumination at 780 nm and C2 reflectance imaging at 395 nm (isosbestic wavelength for hemoglobin). The two cameras and the stimulation devices were controlled by TTL pulses generated by a fiber-photometry console.

The imaging instrument (Fig. 3.1) supports two light paths: the vertical path optimized for fluorescent GCaMP6s imaging and the horizontal light path for hemodynamic imaging. Both light paths contain identical optical elements and identical scientific CMOS (sCMOS) detectors. Hemodynamic imaging was conducted using two configurations: reflectance imaging at 395 nm (configuration 1) and fluorescence imaging of ICG micelles as blood pool agents (configuration 2).

GCaMP imaging (vertical imaging axis)

Illumination: Light was provided by a 3.3 Watt LED (UHP-T-LED-460, Prizmatix) and was spectrally cleaned with a 480/40 nm bandpass filter (ET 480/40 X, Chroma). The light was reflected toward the brain with a 495 nm long pass dichroic (T495lpxr-UF1, Chroma). **Fluorescence detection:** light emitted by GCaMP6s passed through two emission filters (ET 525/50 M, Chroma). 450nm long-pass filter (FELH0450, Thorlabs) 650 nm short-pass filters

(FESH0650, Thorlabs) excluded light from 395 nm reflectance imaging and fluorescence ICG imaging from reaching the GCaMP detection camera. Fluorescence light passed through a 0.5x objective (PlanAPO 0.5x, Leica 10447177), and a zoom lens (Z16 APO, Leica) before reaching the sCMOS camera (Zyla 5.5, Andor). This configuration enabled exposure times of 10 ms and spatial resolution of 0.03mm/pixel.

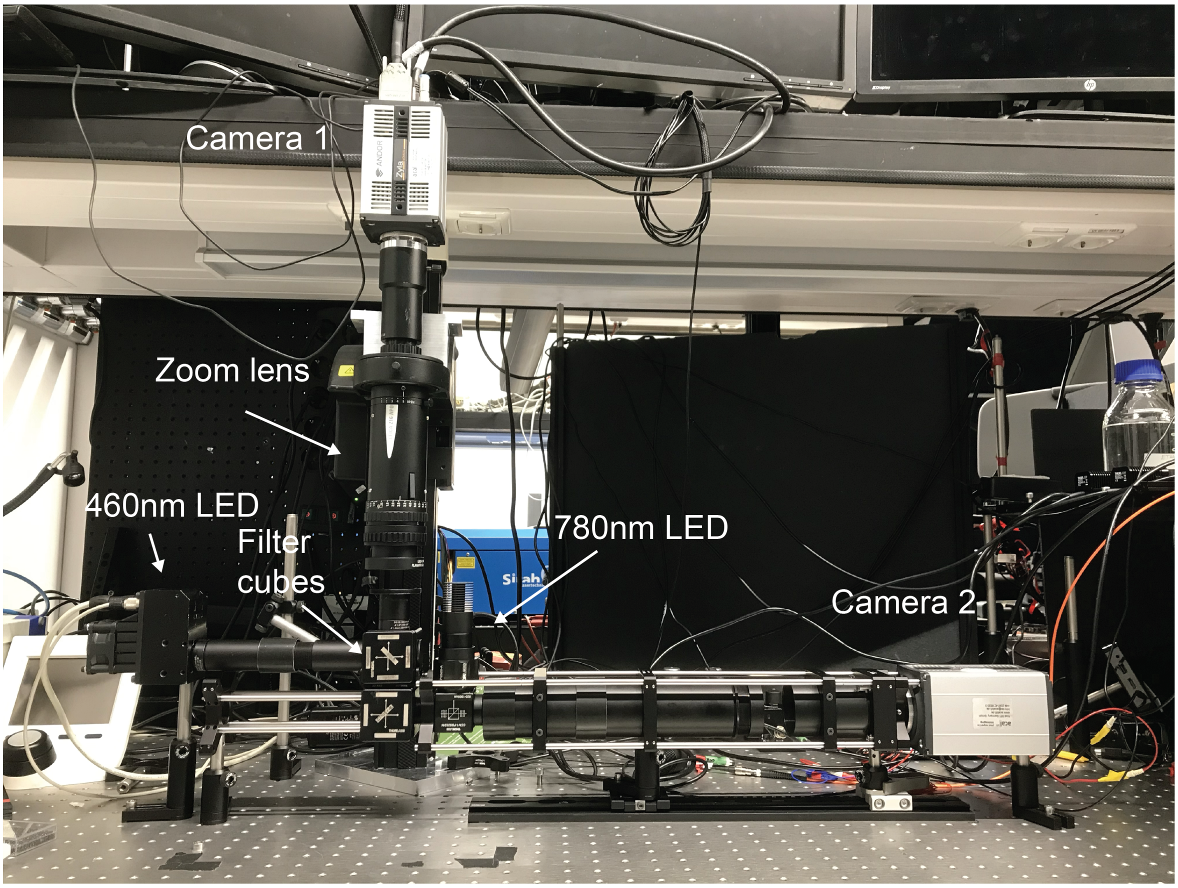

Figure 3.2: Photograph of the wide-field imaging system

Hemodynamic imaging (horizontal imaging axis)

Configuration 1, 395 nm reflectance imaging:

Illumination: 395 nm LED (M395L4, ThorLabs) filtered through a 390 nm filter (FB 390/19, ThorLabs). The cortical surface was illuminated at a 60° angle. Light was reflected towards the camera with a 425 nm dichroic (DMLP425R, Thorlabs) and filtered by a polarizing beamsplitter cube (CCM-PBS251/M, Thorlabs). Reflectance light was further filtered by a 390/10 nm filter (FB 390/10, ThorLabs). **Reflectance detection:** the objective and zoom lens were identical to the vertical light path and images were captured by a sCMOS camera (Zyla 5.5, USB3, Andor).

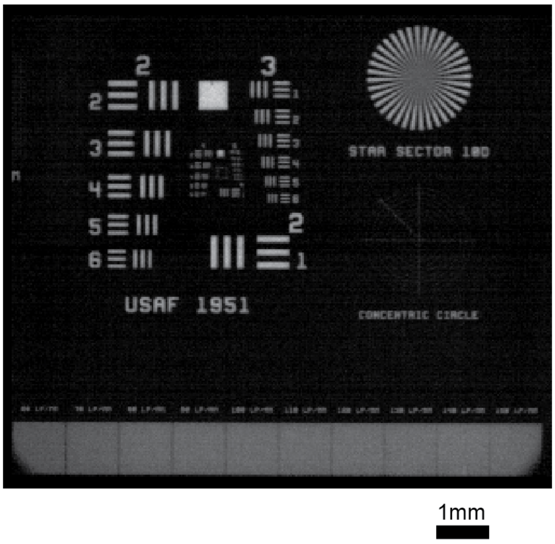

Figure 3.3: Imaging system spatial resolution. Resolution determination- imaging of a 1951 USAF Resolution and Distortion Test Target yielded a spatial resolution of 0.03mm/pixel.

Configuration 2, fluorescence ICG micelle imaging:

Illumination: 780 nm LED (M780L3, ThorLabs), light was filtered by 769/41 nm optical filter (84-105, Edmund Optics). Excitation light was reflected by a 801 nm dichroic (86-336, Edmund Optics). ICG emission light was filtered by an 832/37 nm filter (84-107, Edmund Optics). **Fluorescence detection:** the objective, zoom lens, and sCMOS camera were identical to configuration 1.

Camera and stimulation device synchronization

A fiber photometry console (D460-2002, Doric Lenses) triggered the cameras LEDs and stimulation devices. Current was provided to the LEDs by a dual LED driver (D480-2037, Doric Lenses).

3.7 Stimulation devices

Optogenetics: A Fabry-Perot laser (S4FC637, Thorlabs) coupled to an optical fiber (P1-630Y-FC-2, Thorlabs) and a collimator (F230FC-B-633, Thorlabs) delivered light to the cortex. This setup allowed for an unobstructed field of view and a round 1.5 mm^2 stimulation spot in the desired cortical region. Laser intensity was 11-16 mW/mm^2 and ensured adequate ChrimsonR stimulation through the intact skull.

Visual stimulation: white light flashes for visual stimulation were provided by a fiber-coupled LED (MCWF2, Thorlabs) and were guided through an optical fiber (M98L01, Thorlabs) in front of the eye.

Electrical stimulation: Stimulation current was provided by stimulus isolator (A365R, World Precision Instruments). The hind paw was disinfected with 80% ethanol solution and two thin platinum-iridium electrodes were implanted subcutaneously. Stimulation current was set at 1 mA intensity and pulses had a 50 ms duration. After stimulation, the paw was checked for minor hemorrhage and the skin was again rubbed with 80% ethanol solution.

3.8 Optical imaging protocols

All imaging sessions were conducted after the administration of isoflurane, medetomidine, or ketamine.

Imaging under isoflurane. Anesthesia induction was carried out with 3.5% isoflurane. Once fixed in the stereotactic frame, the isoflurane level was reduced to 1%. Eye ointment (Bepanthen, Bayer) was applied and animals were ventilated with 80% air and 20% O_2. Body temperature was kept to 36.5°C with a heating mat. In each anesthetic level, 5-minute runs of spontaneous activity and 5-minute runs of stimulated activity were acquired. Subsequently, the anesthesia level was increased by 0.2% and 5 minutes were allowed to pass for the higher isoflurane concentration to take effect. These steps were repeated for 5 isoflurane concentrations: 1%, 1.2%, 1.4%, 1.6% and 1.8%. The total imaging time was 50 minutes. After imaging, mice were kept on a heated mat until spontaneous righting.

Imaging under medetomidine. Induction with isoflurane was conducted as previously described. 0.08 mg/kg Medetomidine was diluted in 100 microL saline solution and injected intraperitoneally while isoflurane was turned off. The first 5-minute recording represents the transition to medetomidine. Next, one 5-minute spontaneous activity and two 5-minute sessions of optogenetically initiated brain activity were recorded. Imaging was conducted for a total duration of 20 minutes. After imaging mice were kept on a heated mat until conscious.

Imaging under ketamine. Induction was performed with isoflurane as described above. 1 minute of spontaneous brain activity under isoflurane was recorded before the ketamine injection. 100 mg/kg ketamine diluted in 100 microL saline solution was administered i.p. The imaging experiments lasted 20 minutes. The end of the experiment, animals were euthanized with ketamine (120 mg/kg) and xylazine (8 mg/kg).

3.9 Image processing

3.9.1 Wavelet-based Event Separation (WBES) and Brain Pattern Dimensionality (BPD)

The WBES processing pipeline was developed together with Helmholtz AI and is the result of work conducted by Dr. Dominik Thalmeyer, Dr. Marie Piraud, Dr. Dominik Jüstel and myself. The review of the literature, coding, and conceptual development were done by Dr. Dominik Thalmeyer under the supervision of Dr. Marie Piraud and Dr. Dominik Jüstel. During the development phase of the analytical method, I held weekly meetings with the Helmholtz AI team, guiding their efforts so as to reach the scientific goals of this study. In the latter stages of development, I tested the code on multiple datasets and was involved in debugging and final adjustments. The development of the BPD metric was based on my observation that slow wave activity could be characterized by fewer PCA components than persistent activity. Dr. Dominik Thalmeyer implemented this finding and gave it a rigorous mathematical formulation. After the method was finalized, I analyzed all datasets included in this study.

To analyze complex non-linear brain dynamics characteristic of brain states like sedation, anesthesia, and dissociation we have taken inspiration from the field of fluid dynamics. When analyzing turbulent flow, proper orthogonal decomposition (POD) is used to decompose a time series of spatial fields (in a 2D setting this is a video) into a set of static spatial modes and their temporal variation [311]. Since it is based on PCA (principal components analysis) the POD can explain most of the variance of the data with only a few modes. However, this compression into very few distinct modes can lead to different brain activation phenomena being represented together in the same modes.

Dynamic mode decomposition (DMD) is a spectral decomposition where the data is represented over many modes since each mode cannot represent a phenomenon that exhibits frequency modulation or is localized in time [312]. Multi-resolution DMD (mrDMD) is a method that is based on DMD and was developed to improve the ability to localize patterns in time [313]. However, this comes with the disadvantage that the data is represented by an even larger number of modes, which makes it difficult to interpret.

To solve these challenges we propose an image processing pipeline, Wavelet-based Event Separation processing (WBES) consisting of spectral decomposition with continuous wavelets. This allows the separation of raw brain signals in their time and frequency components. Next, the wavelet modes are embedded into a low-dimensional space using Uniform Manifold Approximation and Projection (UMAP). The wavelet decomposition results in high numbers of redundant modes, thus we clustered the different modes according to visual similarity [313] in order to obtain interpretable results.

Apart from reducing dimensionality, UMAP embedding, can simplifiy the geometry of the data and thus, facilitates correct clustering [313]. The clusters are reconstructed into videos which can be used for connectivity or evoked responses analysis. These sub-videos, capture different ranges in time and frequency to separate categories of neuronal activity.

PCA is used to further analyze the videos and calculate the brain pattern dimensionality (BPD) which is a measure of cortical network compartmentalization.

Notations

With $x_{t,i,j}$ we denote the signal at time index t and pixel with coordinates i, j of a single channel (GCaMP or 395 nm). Where t ∈ [1,6000]. If we refer to one of these channels specifically we denote them as $g_{t,i,j}$ for the GCaMP channel and as $h_{t,i,j}$ for the 395 nm channel. $x_{t:,i,j}$ refers to the entire time-series signal of a pixel, $x_{t,i:,j:}$, refers to a 2D image at time point t and by $x_{t:,i:,j:}$ we mean an entire video record of a single channel.

Preprocessing: Raw brain images were registered to a 2D top-projection image of the mouse cortex generated from the Allen Brain Atlas [304]. The mean image of the first imaging run was affine-transformed in MATLAB (MathWorks), to match the atlas reference using manually selected control points corresponding to the bregma as well as the edges of the olfactory bulbs and the cerebellum. The calculated transformation parameters were used to register all images of all runs in the experiment. The 395nm reflectance images and the 780nm stimulated angiography images were registered in the same way using blood vessels and the edges of the glass window as landmarks.

Each image was processed to represent the percentage change (Δf/f) to the mean of each 5-minute imaging run.

$$x_{t:,i,j} = \frac{x^{raw}_{t:,i,j} - \mu_{i,j}}{\mu_{i,j}} \cdot 100$$

where

$$\mu_{i,j} = Mean\left(x^{raw}_{t:,i,j}\right)$$

Continuous wavelet transformation

A continuous wavelet transformation of each pixel's time series is done first:

$$\tilde{x}_{f:,t:,i,j} = WaveletTransformation(x_{t:,i,j})$$

the continuous wavelet transformed signal $\widetilde{x}_{f:,t:,i,j}$ of pixel (i, j) depends on frequency

f and time t. For the continuous wavelet analysis, we use Morlet wavelets [310] which are the established waveforms used in other neuroscience applications such as EEG [311,312]. To perform the wavelet transform we used the python package pycwt (https://github.com/regeirk/pycwt). Data acquired at 20 Hz was processed with the settings: time step for the analysis (dt) of 0.05, the fastest time scale (s0) was 0.05 sec., a frequency step (dj) of 0.5 resulting in 2 sub-octaves per octave and 20 frequency levels (J). These parameters are listed in Table 3.1. The chosen parameters result in a logarithmically spaced frequency spectrum with frequencies ranging between 0.02Hz and 16.23Hz.

Parameter	Value	Comment
dt	0.05[s]	time step
dj	0.5	frequency step (logarithmic scale)
s0	0.05[s]	fastest time scale
J	20	number of frequency levels
Motherwavelet	Morlet(5)	wavelet used for the analysis

Table 3.1: Parameters used for the wavelet analysis

Cluster modes

Next we cluster the continuous wavelet transformed data which shows high redundancy. The clustering algorithm we apply consists of three substeps: normalization of the modes, dimensionality reduction, and hierarchical clustering.

Normalization of the modes:

The goal of this substep is to make certain that modes with similar spatial patterns are assigned to the same cluster in spite of variations in their absolute intensities and contrast.

$$\tilde{x}^{norm}_{t,f,i,j} = \frac{\tilde{x}_{i,j,t,f} \cdot mask_{i,j} - Mean\left(\tilde{x}_{f,t,i:,j:} \cdot mask_{i:,j:}\right)}{Std\left(\tilde{x}_{f,t,i:,j:} \cdot mask_{i:,j:}\right)}$$

A 2D binary mask ($mask_{i:,j:}$). is applied to the movie to exclude contributions to the mean and standard deviation from pixels located outside the brain.

Dimensionality reduction: wavelet modes are embedded into a low-dimensional space with UMAP [313].

$$x^{embedded}_{t:,f:,k:} = UMAP\left(\tilde{x}^{norm}_{t:,f:,i:,j:}\right)$$

Parameters:

- $n\_neighbors$ represents the size of the local neighborhood, determining how UMAP balances the local versus global data structure and was set at 30.

- *min_dist* refers to the minimum distance between points on the manifold and was set at 0 allowing for thigh packing of data in clusters. This distance was computed with a *'euclidean'* metric.
- *n_components clustering:* wavelet modes were embedded on a 5-dimensional manifold.
- *n_components plotting:* 2-dimensional embedding for plotting.

An overview of the parameters used for UMAP embedding can be found in Table 3.2:

Parameter	**Value**
n-neighbors	30
min-dist	0.0
n-components	5 (for clustering, 2 for plotting)
metric	'euclidean'

Table 3.2: Parameters used for the wavelet analysis

Hierarchical clustering

Apart from reducing dimensionality, UMAP topological data representations simplify the geometry of the underlying data and thus make it easier for a clustering algorithm to determine the correct clustering solution. Embedding as a preprocessing for clustering has the advantage that the distances in a UMAP embedding correspond to the natural distances of the data along curved data manifolds which is also conducive to clustering.

We apply hierarchical ward-clustering to UMAP-processed wavelet modes using the *scipy* package:

$$cluster_{f:,t:,l:} = HierarchicalClustering\left(x^{embedded}_{t:,f:,k:}\right)$$

The algorithm calculates a hierarchy of clusters. To obtain a concrete clustering from this hierarchy, there are two possibilities:

- either a target number of clusters is specified, in which case the clusters can be computed automatically by recursively splitting the hierarchy of clusters until the target number is reached. In each recursion, the cluster to be divided is chosen such that the distance between the newly created child clusters is maximized.
- alternatively, during the analysis, it can be manually decided how to extract a clustering from the cluster hierarchy by defining which clusters to split and which to merge.

The result of clustering is a cluster assignment $cluster_{f:,t:,l:}$ that maps each wavelet mode, specified by the frequency f and time t, to a cluster l:

$$cluster_{f,t,l} = \begin{cases} 1 \; if \; mode \; f,t \; is \; in \; cluster \; l \\ 0, \; otherwise \end{cases}$$

Recomposition

After we have assigned the wavelet modes into clusters, we obtain the wavelet transform of a cluster l by point-wise multiplication of the original wavelet-transformed video with the cluster assignment array:

$$\tilde{x}^{l}_{f,t,i,j} = cluster_{f,t,l} \cdot \tilde{x}_{f,t,i,j}$$

Using a pixel-wise inverse wavelet transformation:

$$x^{l}_{t:,i,j} = InverseWaveletTransform(\tilde{x}^{l}_{f:,t:,i,j})$$

we can (re-)construct a video $x^{l}_{t:,i,j}$ from each cluster l.

Due to the linearity of the wavelet transformation, this approach divides the original video into a set of subvideos:

$$x_{t:,i:,j:} = \sum_{l} x^{l}_{t:,i:,j:}$$

Estimation of data complexity - Brain Pattern Dimensionality (BPD)

Brain states may be characterized by the complexity of their spatio-temporal dynamics [293]. A strategy for quantifying the complexity of brain activity is to measure the effective dimensionality of the functional imaging data reflecting cortical activation patterns. The effective dimensionality of a set of variables represents the number of orthogonal dimensions that produce the same overall pattern of covariation as the original dataset [318].

From a neuroscience perspective, effective dimensionality can be viewed as a measure of cortical network segregation since the dimensions correspond to well-characterized functional brain networks. Practically, the higher the effective dimensionality of our imaging datasets the higher the number of physiological cortical networks which are active in that particular recording. We have termed the effective dimensionality of our imaging data Brain Pattern Dimensionality (BPD) to highlight the physiological significance of this index. In the following, the terms BPD and effective dimensionality can be used interchangeably.

PCA allows to decompose a video into modes:

$$x_{t:,i:,j:} = \sum_{p} \Psi^{p}_{t:} \cdot \Phi^{p}_{i,j}$$

where $\Psi^p_{t:}$ denotes the spatial modes and $\Phi^p_{:i,j}$ are their temporal dynamics. The total variance of the video averaged over time and space can be written as:

$$Var\left(x_{t:,i,j}\right) = \sum_p \lambda^p$$

PCA component eigenvectors are orthogonal to each other and can be used for the calculation of effective dimensionality.

The eigenvalues λ^p specify the contribution of the respective PCA component to the total variance. The distribution of power along these eigenvalues determines how many PCA components are actually needed to describe the data.

To illustrate this, let us consider two concrete examples:

- first, consider that one of the eigenvalues λ^p is equal to 1, and the rest have the value zero. In this case, the data can be accounted for using a single PCA component, i.e. the data is effectively one-dimensional.
- second, let us suppose that all eigenvalues are equal. In this case, we need all PCA components to properly describe the data, since none can be disregarded without losing data. In this case, the effective dimensionality of the data is equal to the full dimensionality of the videos (i.e., the number of pixels).

In the field of importance sampling, one has weighted samples and wants to know how many effective unweighted samples these correspond to. Several ways have been developed that allow in a self-consistent manner to compute an effective sampling size from a set of weights [319,320]. We use this concept to compute an effective number of dimensions from a set of weighted dimensions.

BPD is defined as the entropy-based effective PCA dimensionality:

$$BPD = -\frac{N-1}{logN} \times \sum_p \frac{\lambda^p}{\sum_p \lambda^p} \times log\frac{\lambda^p}{\sum_p \lambda^p} + 1$$

BPD estimations depend on removing unwanted physiological noise which artificially increases imaging data dimensionality so this step should be performed on the neuronal cluster only.

3.9.2 Network measures of brain connectivity

Functional brain network features were calculated with the Functional Brain Connectivity toolbox for Matlab [16]. A custom Matlab script was used for extracting the averaged time series from 40 functional brain regions as defined in the Allan Mouse Brain Atlas [304]. Pearson's correlation coefficients were calculated to form correlation arrays. Correlation arrays were thresholded to 0.7 correlation values for all pharmacological conditions to obtain adjacency matrices. The network type setting chosen for modeling was "weighted undirected networks".

The path length and global efficiency were used to assess functional integration while functional segregation was characterized by modularity, local efficiency, and clustering coefficient.

The shortest path length between all pairs of nodes is known as the characteristic path length. It is the most widely employed measure of functional integration and is mostly influenced by long paths. The average inverse shortest path length is known as the global efficiency and is primarily influenced by short paths. Local efficiency is a measure that ranges from 0 to 1, with high values indicating maximum local efficiency in the network. Modularity refers to the strength of the compartmentalization of a network into modules (also called groups or communities). Modular networks have numerous connections linking nodes within modules but few connections between nodes belonging to other modules. The clustering coefficient describes the tendency of nodes in a graph to cluster together. The degrees of the network graph represents the average number of edges that are associated with a network node. Essentially we are calculating the number of above-threshold correlations per network node.

3.9.3 Topological complexity of responses to visual and paw stimulations

The aim of topological data analysis is to exploit the complex geometric structures underlying data that can be represented as point clouds in high-dimensional Euclidean spaces. The topological complexity (based on cubical persistence measurements) is a non-parametric framework used for transforming time-varying functional brain imaging recordings into time-dependent topological features [303]. Imaging data was first processed with our custom WBES routine to remove physiological artefacts from the images and registered to the Allen Mouse Brain Atlas [304]. Mouse brains show little macroscopic variance within the same strain. In spite of this, the distribution, caliber and pattern of superficial blood vessels is highly variable between mice. Typically, stimulation experiments in transgenic mice entail small cohorts, consequently a robust approach for extracting relevant topological features while disregarding the anatomical blood vessel configuration is desired.

The aim was to analyze activation patterns caused by somatosensory, optogenetic, and visual stimulations. The processing pipeline includes three steps:

- cubical complex conversion: cubical complexes are advantageous for image processing because they are equivalent to analyzing functional data directly, representing it in terms of cubes, squares, edges, and points. Compared to methods that use triangulations, no additional interpolations are required.

- filtration calculation (to account for individual scales in the data) allows us to calculate topological features in the form of diagrams, taking into account a wide range of spatial scales in the data [303]. For each voxel activation values are matched to higher-order elements (cubes, squares, . . .) and sorted in ascending order to these values.
- calculation topological descriptors - all values are evaluated for statistical significance.

3.9.4 Perturbation Complexity Index-State Transitions (PCI-ST)

PCI-ST assesses the complexity of brain responses to direct stimulations [301]. The aim is to quantify the direct impact that activation of one brain region has on other brain areas by directly stimulating the cortex and analyzing the activation patterns that are generated. Signals from peripheral receptors pass through multiple relays on their way to the brain and these modulate signals that reach the cortex. Direct stimulation of the cortex bypasses the reticulate substance and thalamic nuclei as well as peripheral relays. Local responses to direct brain stimulation suggest a loss of integration whereas global and stereotypical cortical activations signify a lack of segregation. PCI can assess both the integration and segregation in cortical networks.

The perturbational strategy for recording effective connectivity patterns included optogenetic stimulation of ChrimsonR [171] and GCaMP6s readout of brain activation [124]. The resulting functional patterns were then assessed with PCI-ST. Since PCI-ST is a data-driven computation it is generalizable in principle to any type of evoked brain response [301].

29 responses to stimulation were recorded in each imaging run. These were averaged and the mean activation movies were reshaped into a 2D arrays (Npixel x Time). The baseline window included one second before stimulation and the response window lasted three seconds after optogenetic stimulation. 100 baseline optimization steps were carried out.

Computational steps include:

- Dimensionality reduction with singular value decomposition to account for 99% of the response amplitude
- Fluorescence-amplitude distance matrix calculations for the baseline window and the response window
- Generation of contour plots by thresholding the distance matrices. Contours are considered to signify transitions between states of the cortex.
- An iterative search (100 iterations) was done to find the threshold that maximizes the

number of transitions in the response window compared to the baseline window.

- PCI-ST is determined by multiplying the number of components after singular vector decomposition and the average number of state transitions.

3.9.5 Leading Eigenvector Dynamic Analysis (LEiDA) and Probabilistic Metastable Substates

LEiDA was proposed for the analysis of brain substate switching behavior in time-resolved functional connectivity data. The LEiDA toolbox for Matlab was used for this analysis [180,289]. The imaging data were preprocessed as described in the WBES section.

The pipeline for LEiDA computation includes:

- Extraction of averaged time series from 40 functional brain regions as defined in the Allan Mouse Brain Atlas
- Bandpass-filtering of time-resolved activations between 0.02 and 6 Hz, with a 2nd order Butterworth filter.
- The exposure time was set to 0.05 sec.
- The phase of fluorescence signals is estimated using the Hilbert transform in Matlab.
- Phase coherence matrices are computed for each time point and leading eigenvectors are calculated for each phase coherence matrix.
- K-means clustering is used for finding 12 metastable substates. The clustering routine is repeated 20 times and all k-clustering solutions are analyzed with Dunn's score.
- FC motif lifetime is defined as the number of consecutive epochs during which the pattern dominates
- The probability of occurrence is computed.
- The identification of statistically significant differences between experimental conditions is done using statistical analysis: One-way ANOVA followed by Tukey's multiple comparisons test.
- Custom-written Matlab scripts were developed for rendering the spatial FC patterns onto the mouse cortex.

3.9.6 Slow-wave speed determination

Slow waves propagate across the cortex from a distinct point of origin. To be able to compare the propagation characteristics of slow waves, these have to be triggered in the same cortical region. The occipital cortex is the best triggering site since slow waves initiated here will spread toward frontal regions over a distance of 1 cm. Optical imaging data was acquired at 100 frames/second in 3 animals. A total of 44 visually and 30 optogenetically initiated slow waves were imaged. A custom brain mask was used to extract signals from 10 ROI locations along a line from the occipital to the prefrontal cortex. The ROIs were positioned 0.8 mm apart. To find the time point when slow waves occurred at the location of the ROI, signals were thresholded at 20% of the maximum fluorescence of each ROI recording. The propagation speed was determined by linear regression of the time-to-threshold vs. distance traveled. The estimated speed is indicated by the slope of the regression line.

3.9.7 MRI data analysis

fMRI image processing

Preprocessing was carried out with the SPM12 toolbox for Matlab. All data were aligned to images coming from the first subject in an experiment, smoothed with a 0.5 x 0.5 x 0.5 mm Gaussian filter, and motion-corrected. General linear model analysis was carried out either with a block design or with regressors derived from the calcium fluorescence recordings. The identification of slow waves for this purpose was done with the use of previously published routines in Matlab [321]. Group ICA was calculated with the GIFT Toolbox for Matlab and the infomax algorithm.

Relaxation rate determination for novel contrast agents

Relaxation rates were calculated by fitting a monoexponential function to the measured sample intensity values using the Image Sequence Analysis Tool, ParaVision 6.0.1 (Bruker BioSpin MRI GmbH, Ettlingen, Germany).

3.10 Immunohistochemistry

Brains were perfused with 40 ml PBS and afterwards with 30 ml 4% PFA solution. Subsequently, brains were incubated at a temperature of 4°C for a period of 24 hours in 4% PFA (diluted in MiliQ water). After this fixation step, the brain was incubated for 48 hours in 30% sucrose diluted in water until it sank to the bottom of the falcon. After this, tissues were placed in 3 ml falcons and frozen at -80°C. 70 µm thick coronal slices were cut on a cryotome. For permeabilization/blocking brain slices were incubated for 1 hour at room temperature in a solution of 1% BSA and 0.2% Triton X-100 in PBS. For staining, tissue samples were incubated at 4°C for 12 hours in an anti-FLAG Cy3 (A9594, Sigma Aldrich) monoclonal antibody (the ChrimsonR construct was marked with Flag-Tag). The antibody solution was diluted to a 1:500 ratio in 1% BSA and 0.2% TritonX-100 in PBS. 3 washing steps followed: for 5 min in PBS and incubated with DAPI solution, 10 mM diluted 1:1000 in 1% BSA and 0.2% Triton X-100 in PBS. After 3 washing steps of 5 minutes with PBS, the brain slices were mounted on glass slides with Aqua Poly Mount (Polysciences, Warrington, PA). Images with specific excitation for Cy5, DAPI, and GCaMP (eGFP) were acquired on an Axio Scan.Z1 (Zeiss) fluorescence microscope at 20x magnification.

3.11 Statistical analysis

The sizes of the experimental cohorts were determined using standards common in the field of preclinical neuroscience for in-vivo experiments. Statistics are reported using the mean ± standard deviation. Statistical tests were used as indicated in the respective figure legends. Tukey-Kramer tests (α=0.05) were calculated to characterize multiple comparisons as follow-up tests after One-way and Two-way ANOVA. Statistical tests were performed in either GraphpadPrism 9.3.1 or Matlab2020.

4

Results

4.1 Intergating cell-type-specific information with MRI imaging

4.1.1 Inferring systems-wide cortical activation patterns from local calcium fluorescence recordings.

The study of functional brain states benefits from imaging modalities that can record the entire brain. MRI offers well-tested empirical and computational platforms for characterizing brain activation responses to external stimuli. To infer how stimulus representations change as a function of the brain state, stimulation experiments were conducted under two concentrations of isoflurane, 1.4% isoflurane was used to induce a rather compartmentalized functional state while 1.8% isoflurane induced slow waves Small animal fMRI imaging systems take advantage of the small bore size which enables strong and homogeneous magnetic fields like 9.4T to be maintained. Still, mouse brains have a volume of 440 mm3 which practically means that despite the stronger 9.4 T magnetic field, fMRI in small animals has a 5-fold lower SNR when compared to human brain imaging at 3 T [322]. To compensate for this, data acquisition was done using a 9.4T MRI system equipped with a cryogenic coil for signal acquisition (Fig. 4.1 b). This setup enables anatomical scans in brain phantoms at 20 µm isotropic resolution (Fig. 4.1 a). Compared to room-temperature coils, the cryogenic coils produce 2.5 times more signal which significantly increases image quality. For in vivo fMRI the spatial resolution is much lower, each voxel measuring 0.25x0.25x0.55 mm and depicting a 0.03 mm^3 brain volume.

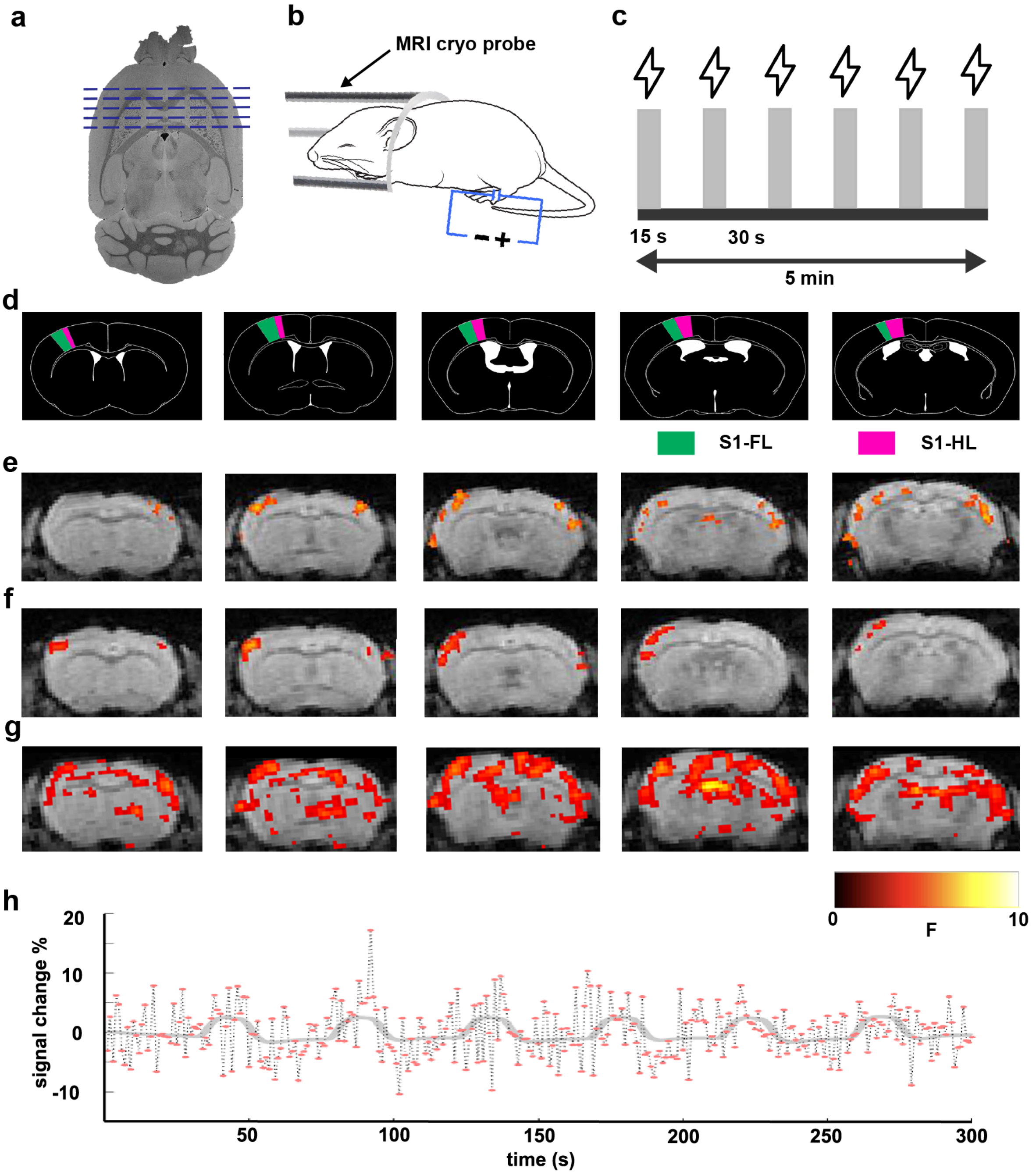

Figure 4.1: Brain activation patterns after hind paw somatosensory stimulation. a, T2* weighted volumetric imaging of a mouse brain phantom, axial view, dashed lines indicate the positions of the coronal slices in panels d-g. **b,** Experimental setup, for recording brain responses to hind paw stimulation, data acquisition was carried out with a cryogenic MRI coil. **c,** Hind paw stimulation strategy, six 15 second periods of stimulation were interleaved with 30 seconds of resting-state recording in a so-called "block design" scheme. Stimulation pulses of 50 ms and 1 mA were delivered at 5 Hz. **d,** Allen Mouse Brain Atlas images showing the somatosensory flont limb (S1-FL) and hind limb (S1-HL) areas where responses to stimulation were expected. **e-g,** Activation maps overlaid on coronal fMRI brain slices, from left to right from rostral to caudal. **h,** Measured (dotted line) vs. fitted responses to somatosensory stimulation (gray).

The whole mouse forebrain was imaged with a temporal resolution of 1 imaging volume/sec. Hind paw stipulation was carried out with 50 ms pulses, with a current intensity of 1mA and a frequency of 5 Hz. Stimulation was carried out for 15 sec. and these stimulation periods were alternated with 30-seconds of baseline data acquisition (Fig. 4.1 c). The long stimulation times are meant to ensure a strong hemodynamic response is generated in the targeted brain regions. During the experiment, animals were sedated with 1.4% isoflurane and their heart rate and temperature were monitored remotely.

3 mice were imaged and the analysis was done with a general linear model implemented in Statistical Parametric Mapping (SPM12). The measured activation patterns are displayed in Fig. 4.1 e-g. The level of statistical significance was set at a T-score of the first mouse was set at T=4.72 and the p threshold was set at 0.05 which was corrected for family-wise error (FWE). Cortical activation patterns, largely confined to the somatosensory cortices of both hemispheres were observed in the first mouse. All activation clusters, in this case, had $p<0.0001$. In the second mouse, the level for statistical significance was set at T=4.7 and activation patterns were mostly limited to the contralateral somatosensory cortex to the right paw which was stimulated ($p<0.0001$). In the last mouse, the significance threshold was T=4.6 and responses were predominantly cortical but also in the basal ganglia ($p<0.0001$).

To independently confirm the results of the GLM analysis and further investigate the heterogeneous nature of the responses to stimulation, Group ICA analysis (GIFT toolbox for MATLAB) was used on the same datasets as in the previous figure . ICA revealed 3 components that show activation in the somatosensory cortex (Fig. 4.2, b,d,f). The temporal activation of the first ICA component (Fig. 4.2 b and c) shows the most similarity to the predicted responses from the GLM analysis (Fig.4.1 h) the calculated correlation between these two time courses was, however only 0.26. The distribution of activated areas is bilateral and mostly confined to the somatosensory S1 region. The second component (Fig. 4.2 d and e) has a low negative correlation value to the predicted responses from the GLM r=-0.11 and activation patterns are distributed in the somatosensory cortex on the left side and also more rostrally in the motor regions of the left hemisphere. The third ICA component (Fig. 4.2, f and g) also shows activation in the somatosensory cortex on the left side which is the contralateral side to the stimulated hind paw. Also in this case there was a weak negative correlation of -0.12 with the expected activations from the GLM.

Additionally to these components which capture aspects of somatosensory information processing, there was a further pancortical activation pattern (Fig. 4.2, h and i) which had a -0.22 correlation strength to the Temporal GLM component. Such a pancortical activation during isoflurane anesthesia has been associated with the presence of slow cortical waves which have a distinct point of origin and spread out over the entire cortex [91].

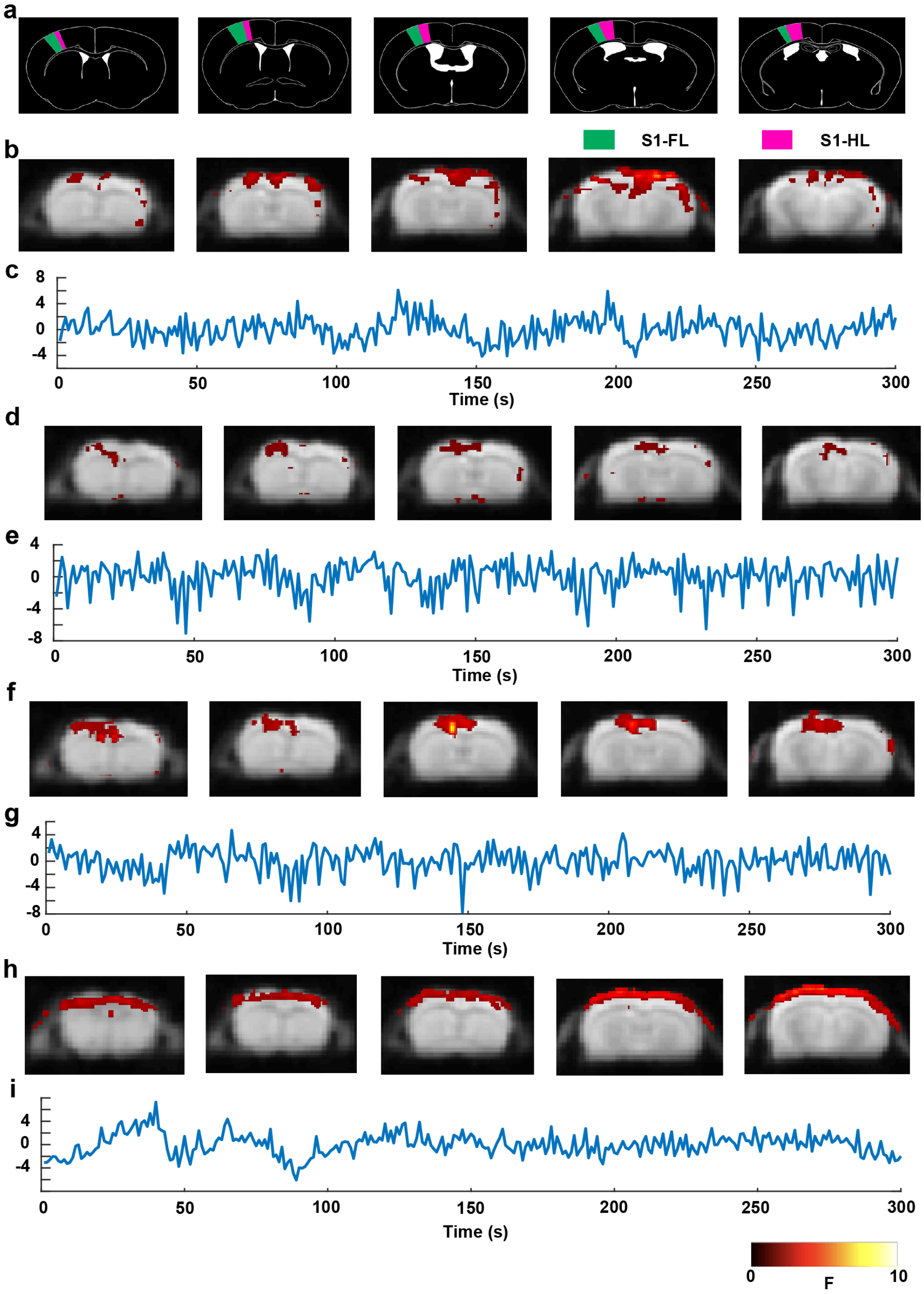

Figure 4.2: ICA identifies paw stimulation patterns and global activation component. **a,** Allen Mouse Brain Atlas images showing the somatosensory region 1 where responses to stimulation were expected. Independent components **b, d, f,** and **h,** and corresponding time series **c, e, g,** and **i**.

The source of the signal variations described above is difficult to ascertain with certainty from fMRI data alone. For this reason, in human experiments, EEG is employed to provide independent validation of the activation events which are responsible for the fMRI activation patterns. Such empirical setups are difficult to implement in small animal fMRI since the strong magnetic field is very sensitive to disturbances.

For this reason, fMRI findings were validated using simultaneously acquired calcium fluorescence transients recorded with a fiber photometry setup (Fig. 4.3 a). The fiber photometry console was utilized for the acquisition of fluorescence data and for generating stimulation pulses as well as triggering the fMRI acquisition start. The system also included 2 LEDs, one for stimulation of GCaMP6f and the second one for optogenetic stimulation of ChrimsonR, a red-shifted optogenetic tool. Light from these two LEDs is combined in one fiber optic guide with a beam splitter/combiner.

Fluorescent light generated by GCaMP6f is diverted to a femtowatt meter and finally digitized in the fiber photometry console. This setup enables the optogenetic stimulation and the recording of neuronal responses from the same cortical region (Fig. 4.3 f). AAV viral particles coding for GCaMP6f and ChrimsonR were injected into the Somatosensory cortex of the left hemisphere (Fig. 4.3 b and f) and IHC later confirmed a strong expression of both constructs (Fig. 4.3 c and d) and an optical fiber with a mirror tip was placed over the injection site.

The average traces from 30 slow-wave events in 3 mice are shown in Fig. 4.3 e. The slow-wave activity was triggered under 1.8% isoflurane anesthesia. Responses to hind paw (black) and optogenetic stimulation (orange) were recorded from the S1 cortex. Both hind paw (Fig. 4.3 g) and optogenetic stimulation (Fig. 4.3 i) reliably triggered slow-wave events. Average responses revealed similar amplitudes but slightly different temporal activation for optogenetic slow waves as opposed to slow waves initiated by hind paw stimulation. The optogenetic traces contained 2 peaks, the first was immediately after stimulation, and the second was around 1 second later. The first peak could correspond to local activation which later causes slow waves to propagate [252].

Optogenetically triggered slow waves averaged a latency of 0.07±0.007 seconds while hind paw elicited slow waves had latencies of 0.16±0.05 seconds. These measurements were significantly different with a $p<0.0001$ (Fig. 4.3 h). The duration of optogenetically initiated slow waves was 1±0.35 s while the mean duration for hind paw slow waves was 0.86±0.37 s and the difference was not statistically significant (Fig. 4.3 j).

Next, fMRI data were acquired simultaneously with GCaMP6f fluorescence and repeatable slow wave events were elicited by optogenetic stimulation (Fig. 4.4 a). The calcium traces were processed and slow wave events were isolated [321](Fig. 4.4 d). A total of 330 stimulations in 3 animals were included in the analysis.

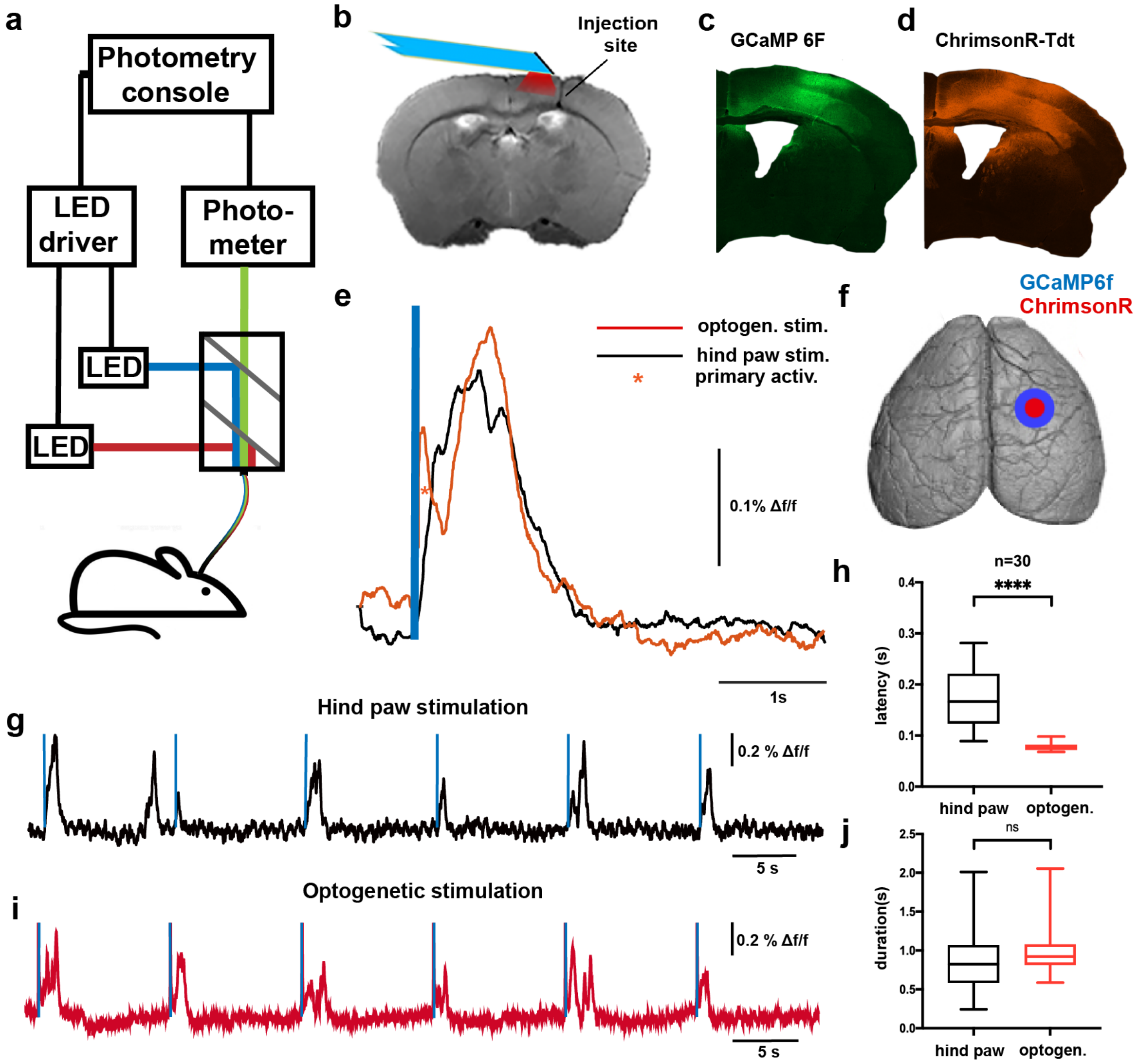

Figure 4.3: Hind paw and optogenetic stimulation trigger slow waves in the anesthetized mice. a, Fiberphotometry setup for the registration of GCaMP6f fluorescence from cortical neurons and red light optogenetic stimulation of ChrimsonR. A Fiberphotometry console was employed to control two LEDs for 460 nm GCamp6f illumination and 625 nm stimulation of ChrimsonR. Fluorescence signals in the 500-550 nm range from GCaMP6f were recorded by a photoreceiver and digitized by the fiber photometry console. Light integration and separation were enabled by an optical filter cube. **b,** Transversal T2-weighted MRI sectional imaging, light was delivered to the brain by a mirror-tipped fiber optic waveguide which was positioned above the viral injection site. **c,** Coronal microscopy showing GCaMP6f expression in the right brain hemisphere. **d,** ChrimsonR-tdT was expressed in the same region as GCaMP. **e,** Average signal intensity from 30 stimulations recorded in the S1 region after somatosensory (black) and optogenetic (red) stimulation. An initial peak in the optogenetic trace denotes primary neuron activation before a larger amplitude slow wave was initiated. **f,** Top-down view of the brain hemispheres showing the viral injection site in the left hemisphere. **g,** Time trace recorded after hind paw stimulation (blue vertical lines). **h,** Slow-wave latency after hind paw and optogenetic stimulation, 30 stimulations in 3 mice, Mann Whitney test, p<0.0001. **i,** Time trace recorded after optogenetic stimulation of ChrimsonR. **j,** Slow-wave duration after hind paw and optogenetic stimulation, 30 stimulations in 3 mice Mann Whitney test, p>0.05.

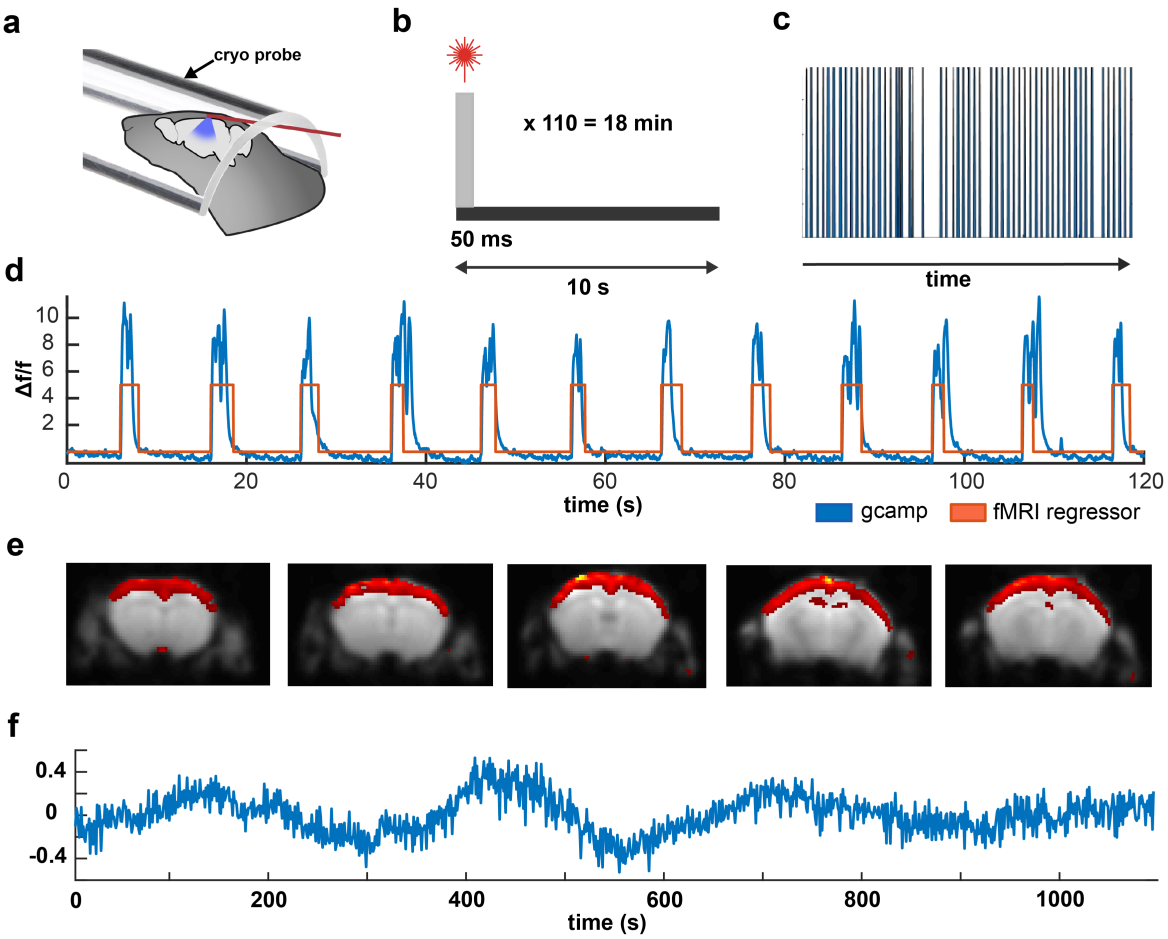

Figure 4.4: Brain activation patterns elicited by optogenetic stimulation during surgical-level anesthesia. **a,** fMRI data were acquired simultaneously with fiber photometry fluorescence. **b,** 50 ms, 625 nm, 5 mW stimulation pulses were delivered every 10 sec for the whole duration of the 18 min of recording. **c,** Binarized slow-wave vector. **d,** GCaMP6s trace showing slow-wave activity (blue) and slow-wave identification (orange). **e,** Statistically significant activations derived by ICA. **f,** Activation vector associated with the ICA component in g.

A pancortical activation pattern was expected because slow-wave events during surgical-level anesthesia usually cover the entire cortex [241,248] in rats [91] and mice [263]. Group ICA revealed a pancortical activation pattern and this represents strong evidence that this activation corresponds to symultaneously recorded slow cortical waves (Fig. 4.4 e and f).

It was demonstrated that in low anesthesia conditions, local activations (revealed with GLM) coexist with global activation patterns (revealed by group ICA). In low isoflurane conditions, significant BOLD signal increases were found in the projection areas for the respective stimulations. During surgical-level anesthesia with isoflurane, hind paw and optogenetic stimulations elicited similar responses in the form of slow waves. These experiments were useful in validating GCaMP6 and Chrimson, molecular tools which would be used throughout this study. fMRI however relies on statistical analysis to differentiate between averaged experimental conditions. Single-trial analysis of stimulation effects are not possible using this technique so optical imaging was chosen for this application

4.1.2 Exploring genetic contrast mechanisms for MRI

This drawback can be partially overcome by combining MRI measurements with local optical recordings as shown above. This strategy necessitates an extra step that involves inferring the relationship between local calcium signals (from fiber photometry) and global brain hemodynamic readout (from MRI). It would be desirable to have genetically encoded contrast agents capable of generating signals which could be detected by MRI. The work presented in this section has been carried out in collaboration with Dr. Mariia Efremova and Dr. Felix Sigmund.

Ferritin is an intracellular protein that stores iron and releases it in a controlled fashion. It is produced by almost all living organisms, including bacteria, algae, plants, and animals and represents the primary intracellular iron-storage protein keeping iron in a soluble and non-toxic form. Ferritin can be overexpressed in cells in order to generate MRI contrast using the paramagnetic properties of iron atoms [323]. However, ferritin exhibits weak magnetic properties and a structure that is not conducive to their improvement.

An alternative route to generating MRI contrast by way of iron accumulation is to build iron nanoparticles inside bacterial protein nanocompartments called encapsulins [324,325]. Encapsulin nanocompartments, or encapsulin protein cages, are spherical bacterial compartments approximately 25-30 nm in diameter and their function depends on the proteins loaded into the nanocompartment [326]. A number of different types of proteins have been loaded into encapsulin nanocompartments, peroxidases and ferritins are the two most common types of cargo proteins.

In this way, contrast can be obtained after the transfection of cells with the encapsulin construct and the passive accumulation of an iron nanoparticle inside the protein shell owing to ferroxidase activity enhanced by coexpression of the iron transporter Zip14. Encapsulins have been shown to hold as many as 30000 iron atoms which is about 10 times the capacity of ferritin. This approach has the advantage that the iron nanoparticle is sequestered inside the encapsulin shell which reduces cellular toxicity [327].

Encapsulin reporter genes from Quasibacillus thermotolerans were expressed in human hepatocellular carcinoma cell line HepG2, as a two-component system representing a nanoshell (QtEncFLAG) and a cargo protein that can induce iron oxide biomineralization (QtIMEF). Cell pellets were scanned in MRI for the determination of T2 and T2* relaxation

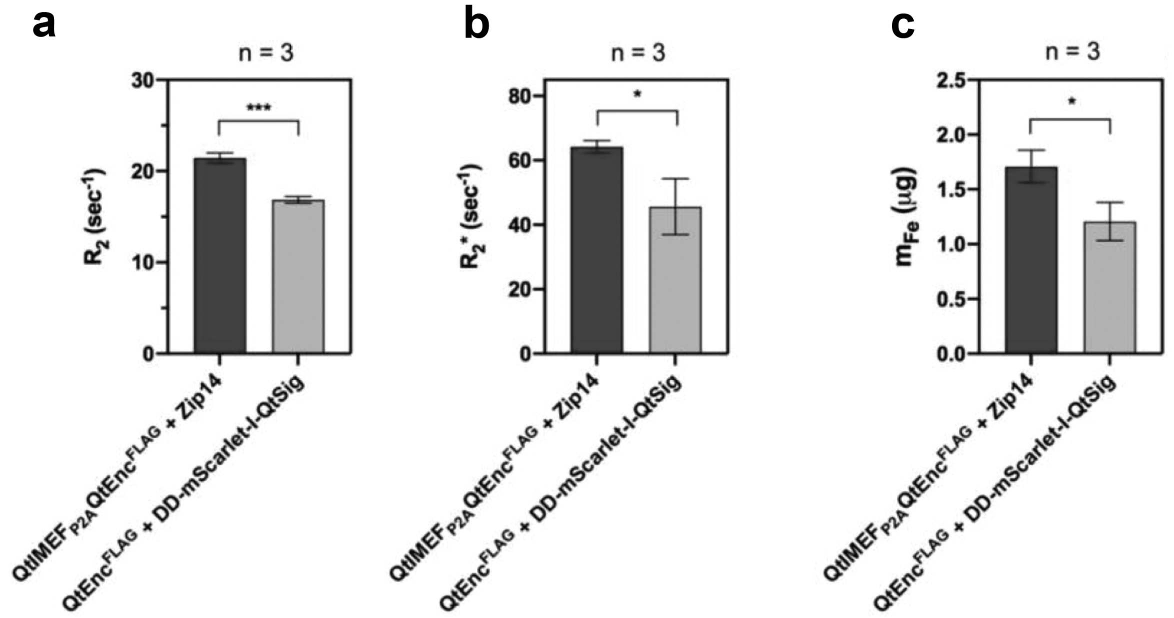

Figure 4.5: MRI relaxometry of HepG2 cells a, R2 and **b,** R2* values were computed from cell pellets comprising 8×10^6 cells. **c,** Iron masses in the same cell pellets determined by inductively coupled plasma mass spectrometry (ICP-MS). All values represent means ± SD (n = 3) analyzed with an unpaired t-test (*** corresponds to p-value < 0.001, * corresponds to p-value < 0.05). Figure adapted from *Efremova et al. 2021*.

times and iron masses in the pellets were determined by inductively coupled plasma mass spectrometry (ICP-MS).

R2 and R2* values of the test sample containing QtIMEF cargo were significantly higher than the control sample with DD-mScarlet-I-QtSig cargo (R2 = 21.4 ± 0.6 vs. 16.8 ± 0.4 s^{-1}) and R2* = 64.2 ± 2.0 vs. 45.6 ± 8.6 s^{-1}). This finding was corroborated by the difference in iron mass between the QtIMEF cargo and the DD-mScarlet-I-QtSig cargo samples tested by ICP-MS. (Fig. 4.5).

Since T2 relaxation is less susceptible to magnetic field inhomogeneity, T2 values were measured with a T2-weighted multi-slice-multi-echo (MSME) sequence with a TR of 6000 ms. At 9.4T, T2* relaxation is accelerated by even the slightest magnetic field disturbance which makes T2* determinations especially difficult at this field strength. That is why measurements were done with an ultra-short echo time (UTE) sequence with a TR of 100 ms, measuring signal from 16 echoes between 0.3 and 50 ms. The ability to acquire data at just 0.3ms after radiofrequency stimulation is essential for the accurate calculation of the exponentially decaying MRI signal which is caused by magnetic field inhomogeneity due to the Fe nanoparticles present in the encapsulin particles that were located in the cell cytoplasm.

Both R2 and R2* were significantly higher in cells expressing encapsulins compared to control cells indicating that iron biomineralization inside encapsulin nanocompartments represents is feasible for the generation of genetic contrast in MRI.

The accumulation of Fe in encapsulin nanocompartments represents a promising mechanism for generating MRI contrast through the expression of gene reporters but delivering an adequate amount of iron to the cytoplasm remains a challenge. This drawback can be partially overcome in cellular cultures by coexpressing the iron transporter Zip14 and the supplementation of the growth medium with Fe.

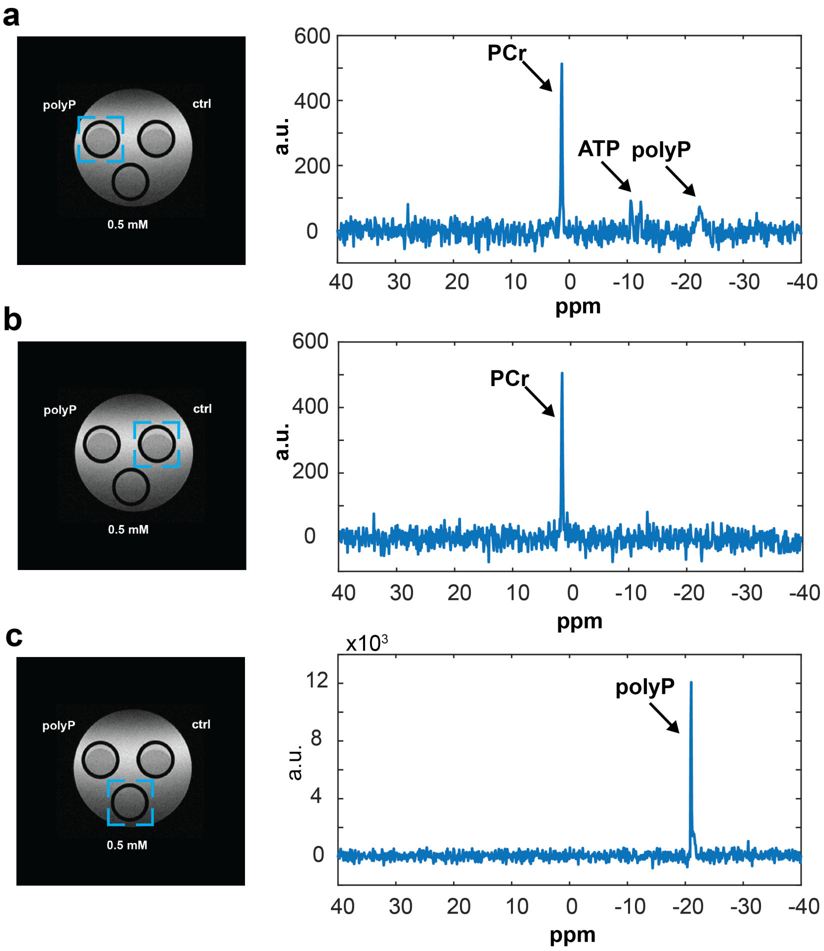

Figure 4.6: MRI spectroscopy of cells shows polyphosphate peak. a, 31P MRI spectroscopy in cells expressing encapsulins and polyphosphate kinase and accumulating polyP. **b,** 31P MRI spectroscopy in cells expressing encapsulins without polyphosphate kinase. **c,** 31P MRI spectroscopy of a standard solution of 0.5 mM polyP.

An alternative strategy for generating genetically encoded MRI contrast involves the production of polyphosphates (polyP) with the enzyme polyphosphate kinase from Escherichia coli. The polyphosphate kinase catalyzes the synthesis of inorganic polyphosphate (polyP) from ATP. Because mammalian cells do not contain detectable levels of polyP, it can be identified by MRI phosphorus MRI spectroscopy after transfection in human cells [328].

For these experiments, polyphosphate kinase was expressed as a cargo protein in the encapsulin nanocompartments which were expressed in human embryonic kidney cells. For this experiment, PolyP is sequestered from the rest of the cytoplasm, and mammalian cells are protected from the potentially toxic effects of polyP which is not normally found in these cells.

For initial experiments (not shown here), cell pellets were washed three times with isotonic NaCl solution removing all growth medium and resuspended in an isotonic NaCl solution before being pelleted by centrifugation. Subsequently, phosphorus spectroscopy MRI measurements were carried out and showed a peak at -20 ppm which corresponded to the chemical shift of the polyP. To prove that this peak was indeed measuring the concentration of polyphosphates, constructed an MRI phantom with 3 compartments for holding cells which were encased in a tube filled with distilled water. This setup was necessary to minimize magnetic susceptibility artifacts. The tubes were loaded with cells expressing encapsulins that were agglomerating polyP (Fig 4.6 a), control cells expressing encapsulins without the polyphosphate kinase (Fig 4.6 b), and a standard solution of 0.5 mM polyP (Fig.4.6 c). The data acquisition was done with a single voxel 31P, ISIS spectroscopy pulse sequence for each of the samples. The cells expressing polyphosphate kinase inside encapsulins showed a clear polyP peak at -20 ppm alongside the most prominent phosphocreatine (PCr) around 0 ppm and the beta-ATP peaks around -10 ppm. Control cells only showed the PCr peak because the ATP had likely been used up by the time of the measurement (which followed the encapsulin polyP cell spectroscopy acquisition). Finally, the 0.5 mM polyP solution showed a clear peak at -20 ppm without PCr or ATP peaks. Localized PolyP signal was measured without any cross-talk between the samples.

Both iron and polyP work by accumulation and the MRI signal is dependent on the level of expression of the genetically encoded proteins. This type of contrast is appropriate for applications concerning tumor cell tracking [327] however, for neuroscience applications it would be desirable to have dynamic contrast agents which change their properties as a function of neuronal activation. Such contrast agents are not available at the moment.

This shortcoming can be partially mitigated by integrating calcium sensor imaging with fMRI. However individual stimulation trials cannot be investigated with fMRI because of low SNR. For this reason, optical imaging in transgenic mouse models expressing GCaMP6s in cortical excitatory neurons was used for the main part of the experimental work.

4.2 Wide-field imaging system captures neuronal activity and brain hemodynamics

Wide-field optical imaging of transgenic mouse reporter models represents an emerging preclinical imaging modality that combines fast temporal sampling with high-resolution imaging to enable access to both high-frequency activation events and highly detailed spatial brain activation patterns.

As described in the section on hemodynamic imaging, physiological noise contaminates optical imaging data. Most imaging setups for wide-field optical imaging of the cortex include one scientific camera and 2 light sources. In this case, imaging the fluorescent sensor is interleaved with frames that aim to record differences in cerebral blood volume. Practically this means that the light sources which provide illumination for these two imaging channels have to be switched on and off for each frame. This limits the maximum temporal resolution which can be achieved and may also impede experiments where visual responses of the brain are of interest.

For this reason, a dual-camera wide-field microscope was designed and assembled in the course of this work. The system includes 2 cameras and three light sources which enable imaging of GCaMP6s and hemodynamic effects in parallel (Fig. 4.7). The vertical optical axis is used for imaging GCaMP6s under illumination with a 460 nm blue LED. This imaging axis is used for all experiments as it delivered information on the calcium transients occurring in cortical pyramidal neurons at a spatial resolution of 0.03 mm/pixel and a temporal resolution ranging between 20 and 100 frames/sec (Fig. 4.7 c). Upon inspection of an imaging dataset, activation in well-characterized neuronal networks is visible, as illustrated in Fig. 4.7 f.

The horizontal imaging axis can be configured to image the cerebral blood volume using hemoglobin (configuration C1) as well as intravenously injected contrast agents (configuration C2). These operating modes do not run in parallel as they require different dichroic mirrors and optical filters, but a change between these configurations is possible within minutes. Configuration C1 takes advantage of the properties of hemoglobin for hemodynamic imaging. Illumination is carried out with a 395 nm LED, an isosbestic wavelength at which oxygenated and deoxygenated hemoglobin absorb light equally. Like this, changes in blood volume can be mapped independently of the oxygenation state of hemoglobin (Fig. 4.7 d). Configuration C2 necessitates the intravenous injection of a fluorescent ‘blood pool agent’. For these experiments, a contrast agent consisting of micelles filled with indocyanine green (ICG) was injected i.v. A 780 nm LED is used for illumination and this strategy produces highly detailed images of the venous and arterial cerebral vasculature which is contrasted by the ICG.

Although the contrast agent is slowly removed from the bloodstream by the reticuloendothelial system which is mostly represented by the liver an injection of 100 µL of contrast agent enables 30-minute optical recordings.

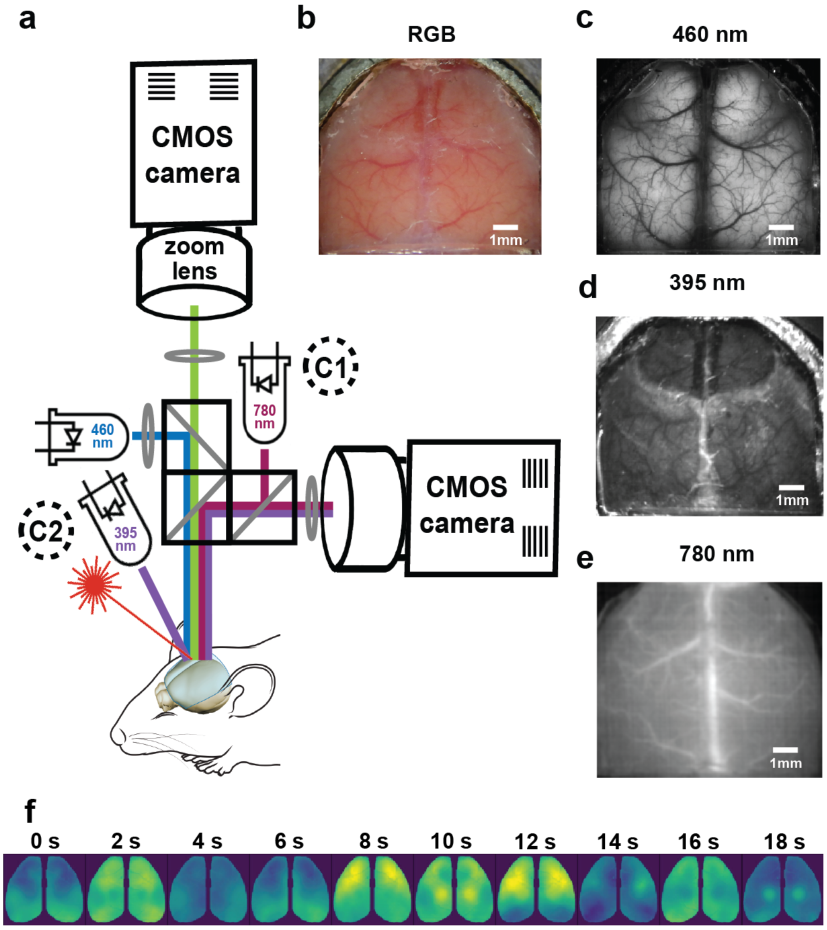

Figure 4.7: Wide-field optical imaging captures brain neuronal brain activity and hemodynamics a, Schematic representation of the widefield imaging setup. The vertical light path was used for imaging GCaMP6s and the horizontal path for hemodynamic imaging. Hemodynamic imaging was done in two configurations: C1 angiography after intravenous injection of indocyanine green (ICG) micelles and illumination at 780 nm and C2 reflectance imaging at 395 nm (isosbestic wavelength for hemoglobin).**b,** RGB image of the skull window preparation. **c,** 460 nm stimulated image showing GCaMP fluorescence from B6;CBA-Tg(Camk2atTA)1Mmay/J x B6;DBA-Tg(tetO-GCaMP6s)2Niell/J) mice. **d,** 395 nm reflectance image acquired by the horizontal optical axis (configuration 2). **e,** 780 nm stimulated fluorescence image acquired after intravenous injection of ICG micelles (configuration 1) producing a brain angiography. In a dynamic imaging series acquired at 780 nm, time-dependent variations are due to changes in cerebral blood volume. **f,** Dynamic GCaMP6s imaging sequence reveals activation of visual somatosensory and motor networks across the dorsal cortex in B6;CBA-Tg(Camk2atTA)1Mmay/J x B6;DBA-Tg(tetO-GCaMP6s)2Niell/J) mice.

4.3 Removal of physiological imaging noise with the Wavelet-based Event Separation processing pipeline

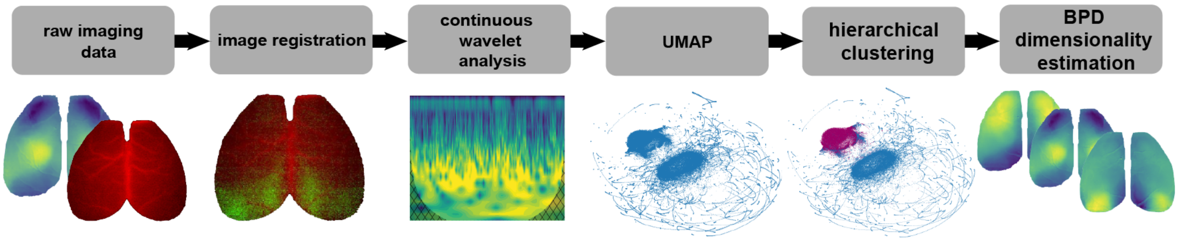

Figure 4.8: Image processing pipeline for the data-driven removal of physiological noise and effective dimensionality estimation. Imaging data processing pipeline. Raw images from the two cameras were registered to each other and subsequently to a functional cortical map from the Allen Mouse Brain Atlas. This step was followed by continuous wavelet analysis and UMAP dimensionality reduction. UMAP clustering was employed to identify functional activity classes and PCA allowed us to extract the activity of functional networks from the previously isolated clusters. The final step consists of calculating the Brain Pattern Dimensionality (BPD) which is equivalent to the effective dimensionality of the imaging data.

A bespoke image processing pipeline, was developed in collaboration with Helmholtz AI, to characterize populational-level neuronal activation events. The first step was to register all imaging datasets to a common coordinate framework for the mouse cortex which was published by the Allen Institute [23]. A total of 40 brain regions, 20 per hemisphere were included in the brain map. Additionally, the brain map contained information on all regions displayed in Fig. 4.8 a, so average time traces from these regions were extracted. Correct registration was checked by visual and hind paw stimulations. The patterns of activation occurred as expected in the primary visual (V1) (Fig. 4.8 b) and somatosensory 1 hind limb areas (S1-HL) (Fig. 4.9 c). Both visual and hind paw stimulation produced bilateral responses and this is in line with previously published results. Notably, in the case of visual stimulation, the V1 responses are accentuated in the right hemisphere which is contralateral to the stimulated retina while in the left hemisphere responses are strongest in the visual association areas bordering V1(Fig. 4.8 b).

Imaging data contains rich temporal, spectral and spatial information, for this reason, our processing pipeline includes computational steps tailored to extracting information from these different dimensions. After image registration, followed the continuous wavelet analysis a data decomposition step that captures both spectral and temporal components. This produces a large increase in the dimensionality of the dataset such that a dimensionality reduction step is needed and this was carried out with UMAP. UMAP is a fast algorithm that is designed to handle large datasets such as those that are routinely used in machine learning applications. In the resulting UMAP 2D projections (Fig. 4.8 second row, fourth from the left) every point represents an imaging frame in frequency and time. Next, clustering is required to isolate related neuronal events and remove physiological noise.

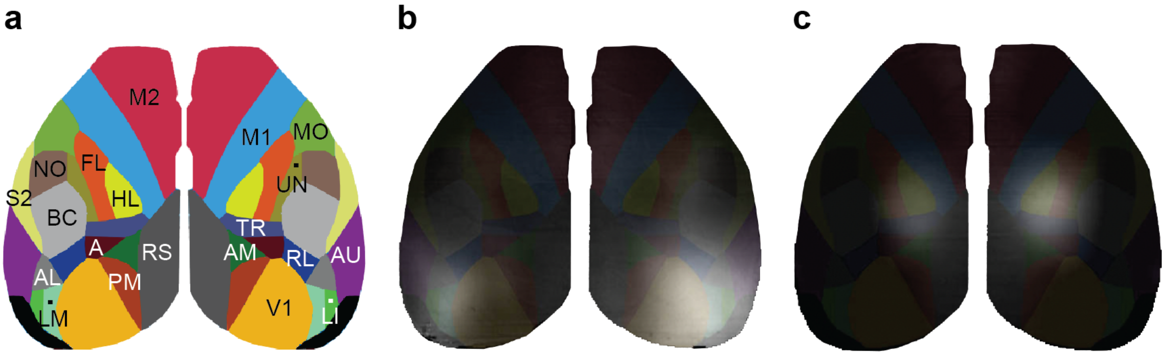

Figure 4.9: Coregistration of functional imaging data to a cortical mask based on the Allen Mouse Brain Atlas. a, Brain parcellation mask based on the Allen Institute Atlas, 20 brain regions were taken into account per hemisphere. M1 - primary motor area, M2 - secondary motor area, HL - hind limb, FL - front limb, S2 - secondary somatosensory area, MO - mouth, NO - nose, TR - trunk, A - anterior association area, AL - anterolateral, AM - anteromedial, LM - lateromedial, LI - laterointermediate, PM - posteromedial, RL - rostrolateral regions of the extrastriate visual areas, AU - auditory, RS - retrosplenial, BC - barrel cortex, V1 - visual area, UN - somatosensory area unassigned.**b,** Validation of correct registration by visual stimulation: after stimulation of the left retina, an increase in signal was observed in the primary visual region (V1) of the contralateral hemisphere. Ipsilateral activation was also observed in visual association areas (LM, AL, and RL). **c,** Validation of correct registration by left hind paw stimulation. An increase in signal was observed in the contralateral hemisphere in the hind limb area (HL) while a weaker response is present also in the HL area of the ipsilateral hemisphere.

Apart from reducing dimensionality, UMAP, as a preprocessing for clustering has the advantage that the distances in a UMAP embedding correspond to the natural distances of the data along curved data manifolds. This can simplify the geometry of the underlying clusters, and thus, makes it easier for a clustering algorithm to find the correct clustering solution [313]. The resulting clusters are eventually reconstructed back into videos and a PCA is conducted in order to calculate BPD, our index for cortical network segregation (Fig. 4.8).

The spatio-temporal components of the GCaMP6s fluorescent signals were investigated and it was observed that most power was concentrated in frequencies between 0 and 4Hz. A prominent 8-12Hz component was also observed that was fairly stable during the entire recording. Previous theoretical work suggests that calcium fluorescence imaging data is contaminated by signal fluctuations caused by changing cerebral blood volume. Since the 8-12Hz frequency component corresponds well to the mouse heart rate (400-800 beats/min), the origin of the prominent 8-12Hz signal fluctuations was investigated next (Fig. 4.10 a and b).

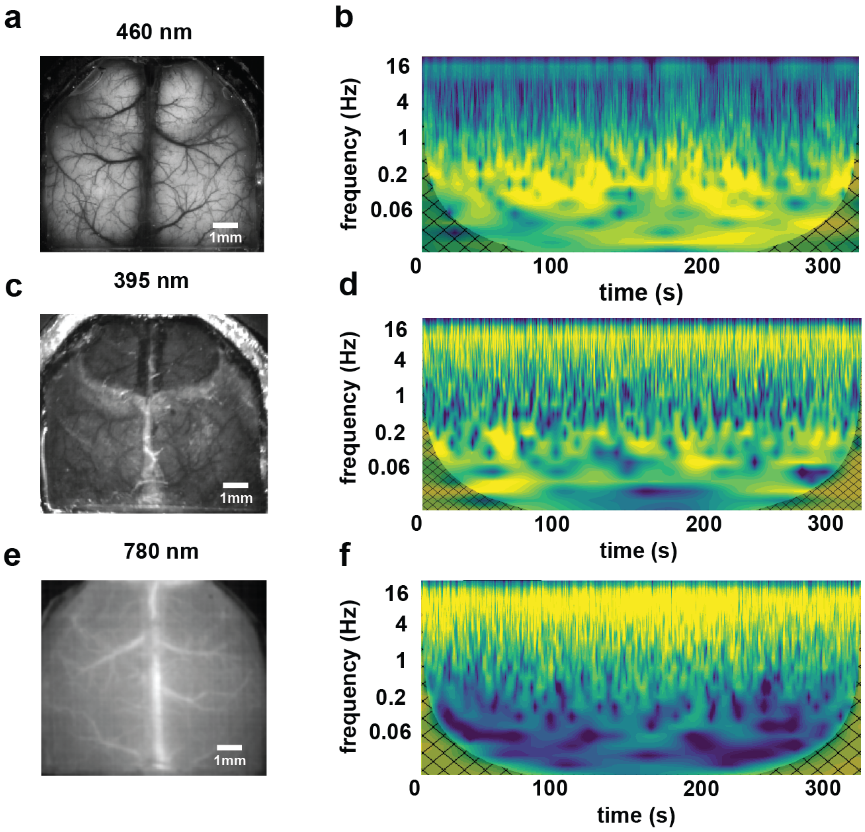

Figure 4.10: Continuous wavelet analysis reveals a putative 8-12 Hz physiological noise component. **a,** 460 nm stimulated GCaMP6s fluorescence image. **b,** Continuous wavelet analysis of a 5 min GCaMP imaging sequence reveals complex time-frequency components up to the theta band as well as strong 8-12 Hz noise. **c,** 395 nm reflectance imaging. **d,** Continuous wavelet analysis of a 5 min 395 nm stimulated imaging sequence shows prominent time-frequency components in the 8-12 Hz band. **e,** 780 nm fluorescence imaging of intravenously injected ICG micelles characterizing cerebral blood flow. **f,** Continuous wavelet analysis of a 5 min 780 nm stimulated imaging sequence shows strong variations in the 8-12 Hz band.

The dual-channel imaging capabilities of the custom-built dual-camera instrument allowed for reflectance imaging at 395 nm wavelengths. 395nm represents an isosbestic point where oxygenated and deoxygenated hemoglobin have the same absorption rates. In the 395nm imaging dataset, a strong 8-12Hz frequency component was found and this matched well with the similar frequency band which was described above in the GCaMP dataset (Fig. 4.10 c and d).

Additionally, ground truth data on cerebral blood volume fluctuations was acquired by imaging a blood pool agent. 100µL of ICG micelle solution was injected intravenously and imaging was done under 780 nm illumination. ICG fluorescence was recorded at 810nm. The presence of a strong 8-12Hz component was established and this seemed to correspond to the findings in the GCaMP channel (Fig. 4.10 e and f).

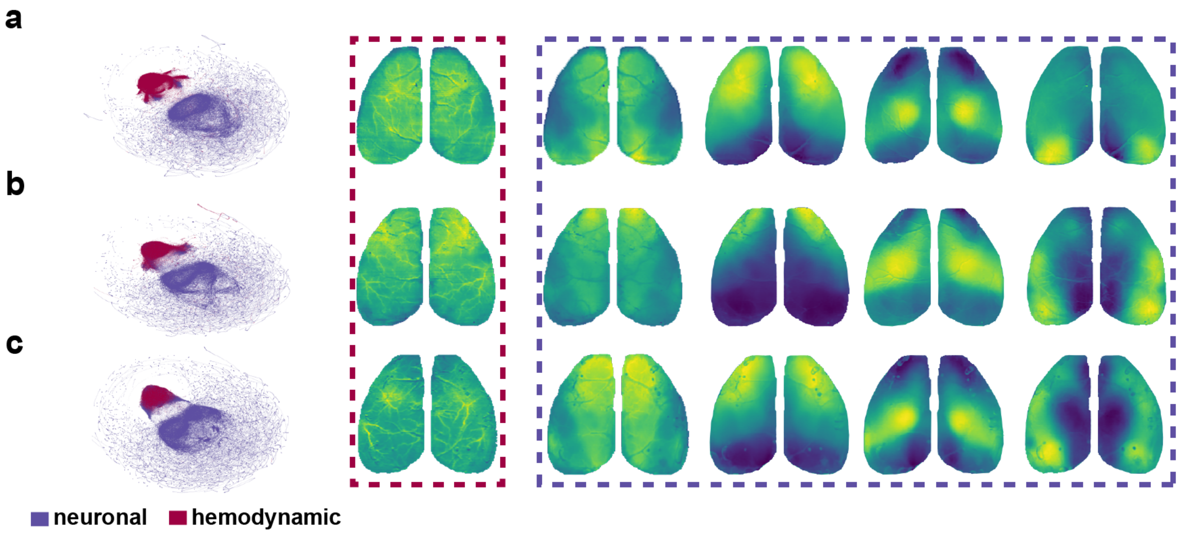

Figure 4.11: UMAP-derived clustering isolates physiological noise from neuronal activity. a-c Clustering results from three representative subjects, from left to right: UMAP 2D projection, showing the hemodynamic cluster (red), and the neuronal activity cluster (blue); the first PCA component of the hemodynamic cluster containing signal arising from the brain vasculature; first four PCA components of the neuronal cluster showing a global component followed by patterns corresponding to frontal, somatosensory and occipital brain networks.

Having a data-driven approach to remove the unwanted physiological noise caused by CBV changes from calcium fluorescence data is highly desirable since it would improve the accuracy of downstream quantitative measurements and this can be done with UMAP-derived clustering. In all mice, the UMAPS contained two very distinctly separated regions, a more compact region (Fig. 4.11 a-c first panel from the left in red) and a more spread out region in blue (Fig. 4.11 a-c first panel from the left in red). These data structures were easily and cleanly separated by hierarchical clustering. The clusters were reconstructed into 3D imaging datasets (2D images over a series of time steps) and PCA was used to investigate the spatial and temporal patterns contained herein.

The red and more compact cluster contained very detailed spatial patterns corresponding to the brain vasculature and this finding was reproducible across animals as illustrated in 3 representative cases in Fig. 4.11 a-c 2nd panel from the left. Apart from this most prominent pattern, the other PCA components were showing only readout noise which can be amplified after the expression of the data in percentage change relative to the baseline (Δf/f). In contrast, the bigger cluster in blue contained a richer spectrum of interpretable PCA components.

Next, time-frequency components of the clusters were investigated with continuous wavelet analysis. It was observed that the red cluster (Fig. 4.12 a) mainly contains high-frequency activity in the 8-12Hz range (Fig. 4.12 b) while the bigger blue cluster features most activity below 4Hz (Fig. 4.12 c). Evidence from Fig. 4.11 and Fig. 4.12 suggests that it is possible to identify a red cluster containing a spatial pattern that depicts the brain vasculature and the temporal and spectral features of this activity fall within the range which is characteristic of the mouse heart rate of 400-800 beats/min.

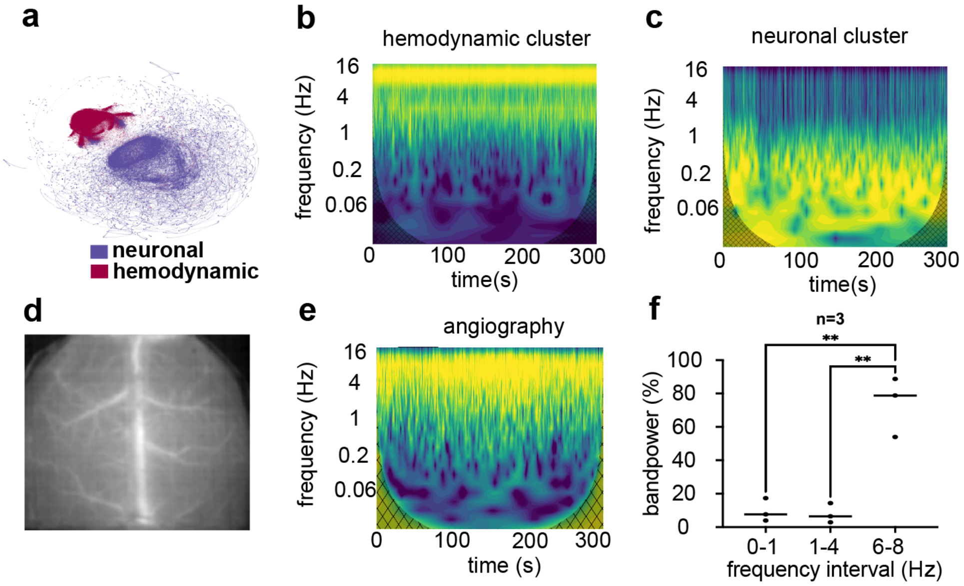

Figure 4.12: The hemodynamic cluster contains physiological noise. a, 2D UMAP embedding showing two distinct clusters from a GCaMP dataset. **b,** Typical wavelet power spectrum from a GCaMP dataset, the hemodynamic cluster showing greatest power in the 6-8 Hz band corresponding to the mouse heart rate. **c,** Corresponding wavelet power spectrum from a GCaMP dataset from the neuronal cluster with most power concentrated in the frequency band below 4 Hz. **d,** Image showing the angiography data acquired under 780 nm illumination after ICG micelle injection. **e,** Typical wavelet power spectrum, of ICG angiography image series showing greatest power in the 6-8 Hz band corresponding to the mouse heart rate **f,** Bandpower measurements for 3 ICG angiography datasets: around 80% of bandpower concentrated in the 6-8 Hz frequency range. One way ANOVA (n=3), 6-8 Hz band vs. 1-4 Hz band p=0.0011; 6-8 Hz band vs 0-1 Hz band p=0.0012. ** corresponds to p-value < 0.01.

Angiography recordings served as a positive control as they contained the most direct data available to us regarding brain hemodynamics (Fig. 4.12 e). The wavelet decomposition revealed that most hemodynamic activity was concentrated in the 6-8Hz range matching the characteristics of the hemodynamic cluster (red) (Fig. 4.12 b).

The bandpower in the 8-12 Hz frequency range was calculated in three mice and it accounted for 73.82±17.9% of total bandpower in the angiography datasets. In comparison, the 0-1 and 1-4 Hz intervals contained 9.6±6.9 and 7.9±5.8% of total bandpower respectively. The 8-12Hz frequency band corresponds to the heart rate of the mouse which ranges from 500 to 800 beats/minute (8.33-11.6 Hz) [329].

For these reasons, the red cluster is referred to as the as the “hemodynamic cluster” and the blue cluster as the “neuronal cluster”.

Linear regression represents the most frequent method used for physiological noise removal [137]. To compare the results of linear regression (Fig. 4.13) with our data-driven method for hemodynamic noise removal (Fig. 4.14), both processing strategies were applied to the same imaging dataset.

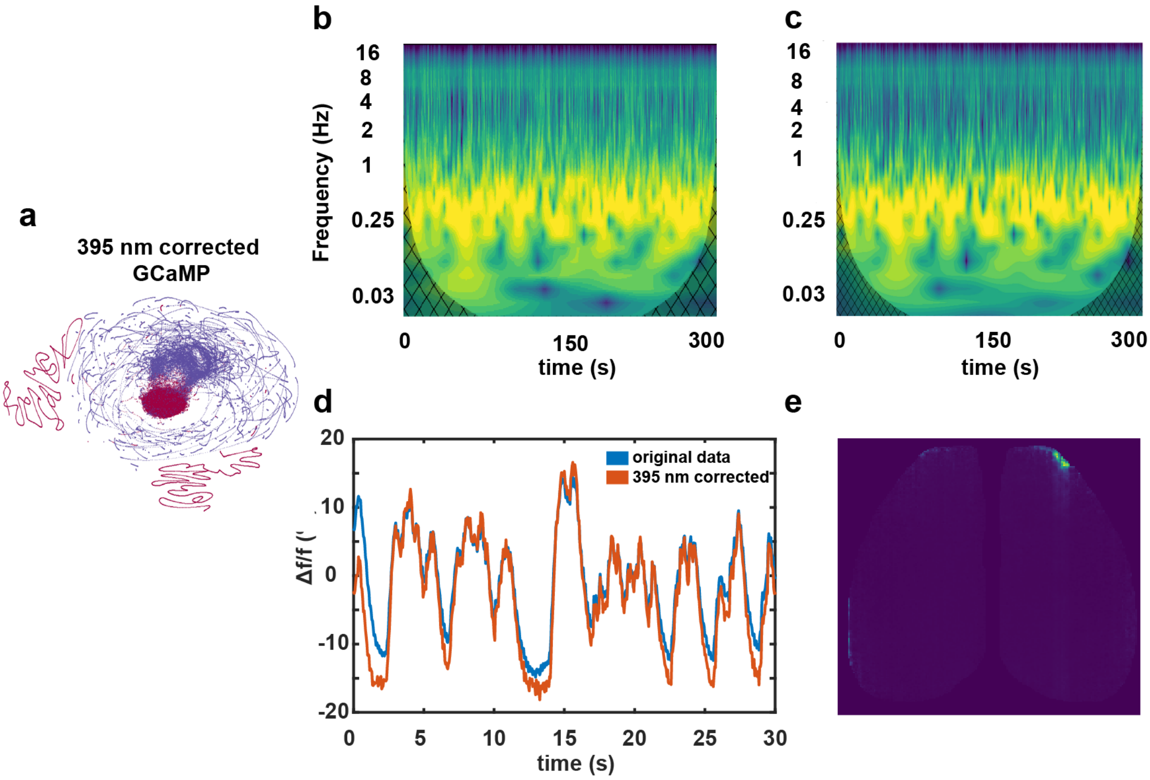

Figure 4.13: Removal of physiological noise with linear regression. **a,** UMAP of a functional imaging dataset after regression of 395nm imaging data out of the original GCaMP images showing the hemodynamic cluster (red) and neuronal cluster (blue). The morphology of the neuronal cluster (blue) seems disrupted after regression of 395 nm reflection data **b,** Continuous wavelet analysis of the entire dataset before clustering. **c,** Continuous wavelet analysis of the GCAMP dataset after regression of the 395nm dataset showing the 8-12Hz frequency component was not entirely removed by the regression method. **d,** Average of entire cortex before (blue) and after (orange) regression of 395 nm dataset showing good agreement in temporal trajectories. **e,** PCA of the high-frequency cluster after regression showing that the hemodynamic PCA pattern was removed by linear regression.

Reflectance images at 395 nm, an isosbestic hemoglobin wavelength, were co-recorded and regressed from the GCaMP6s signals. Figure 4.13 shows that while regression is also effective in removing the hemodynamic noise from the fluorescence data (Fig. 4.13 b-e), it is not as effective in removing the 8-12 Hz noise component (Fig. 4.13 c). Inspection of the data post-regression revealed that noise had been introduced by the procedure and the shape of the neuronal cluster has also been affected (Fig. 4.13, a). Temporal and spatial smoothing of both the raw GCaMP6s and 395 nm datasets before regression might solve this issue at the cost of compromising spectral resolution in the delta and theta bands. Our UMAP-derived clustering method is efficient in removing the 8-12 Hz frequency component from the imaging data (Fig. 4.14 b-e) while preserving higher frequency events that are associated with neuronal activity (Fig. 4.14 c).

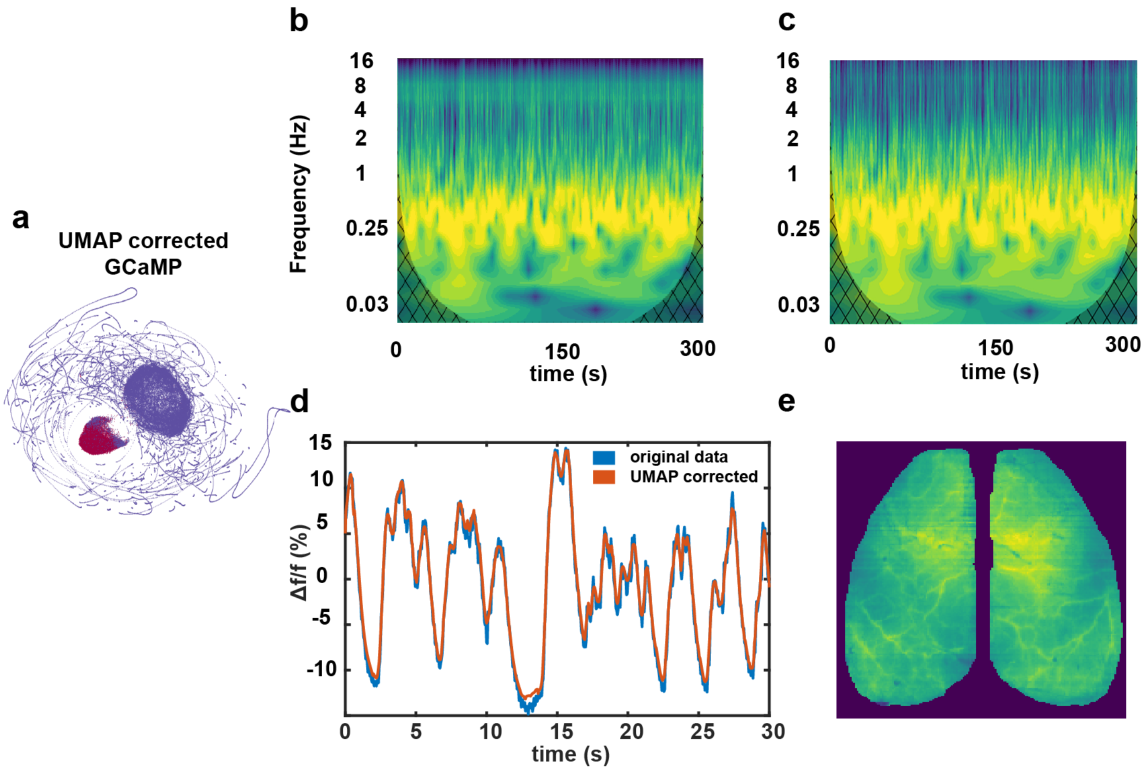

Figure 4.14: UMAP clustering efficiently removes physiological noise from the raw GCaMP imaging data. a, UMAP of a GCaMP functional imaging dataset acquired under 1% isoflurane sedation showing the hemodynamic cluster (red) and neuronal cluster (blue). **b,** Continuous wavelet analysis of the entire dataset before clustering. **c,** Continuous wavelet analysis of the neuronal cluster showing the 8-12Hz frequency component associated with physiological noise was efficiently removed. **d,** Average of entire cortex before (blue) and after (orange) removal of hemodynamic noise components. **e,** PCA of the hemodynamic cluster which was removed showing a clear vascular pattern.

4.4 Functional network dynamics of spontaneous cortical activity

4.4.1 Continuous wavelet analysis and UMAP-derived clustering reveal spatiotemporal and spectral features of spontaneous activity

To assess the characteristics of spontaneous functional network dynamics and the features of stimulus processing, spontaneous activity recordings (6000 frames at 20 Hz) were interleaved with stimulated recordings (6000 frames at 20 Hz). Three experiments were carried out per animal, after the administration of isoflurane, medetomidine, and ketamine (Fig. 4.15 a). For isoflurane experiments, 5 anesthetic concentrations were investigated: 1%, 1.2%, 1.4%, and 1.6% isoflurane. For each concentration, 5 min. of spontaneous activity was acquired first and followed by five minutes of recordings where either visual, hind paw, or optogenetic stimulations were applied. Before starting the recording with a new concentration of isoflurane, 3 minutes were allowed to pass for the animal to stabilize in this new condition. This strategy allowed us to study the relationship between spontaneous cortical activity and different anesthetics as well as the dose-dependent effects of isoflurane on brain states. The same mice were also imaged under medetomidine and ketamine, but these imaging sessions only included one concentration of the pharmacologic agent. Like this, the amount of data acquired was maximized while the number of animals used was kept to a minimum. Between the isoflurane, medetomidine, and ketamine experiments, mice were allowed 1 week to recover.

After data acquisition, images were registered to a common brain template from the Allen Mouse Brain Atlas [23]. The continuous wavelet analysis and UMAP dimensionality reduction followed and after the UMAP calculation data were clustered in 2 clusters. As detailed in the Materials and Methods section, the compact cluster (Fig. 4.15 b) in red corresponds to high-frequency noise as well as physiological noise and was not included in the analysis. Reconstructions of the ‘neuronal’ cluster shown in blue in Fig. 4.15 b were used for all subsequent computations.

Inspection revealed that regardless of the pharmacological agent used, the depth of anesthesia, and the stimulation status of the experiment, 2 clusters were always present and clearly differentiated. Changes in the shape of the ‘neuronal’ cluster were observed as a function of brain state (Fig. 4.15 b). During sedation with isoflurane or medetomidine, the neuronal cluster takes a compact ellipsoid shape. Likewise, under ketamine, the neuronal cluster has a compact structure. The transition from sedation to anesthesia under isoflurane leads to a progressive breakup of the neuronal cluster which becomes less dense and poorly defined.

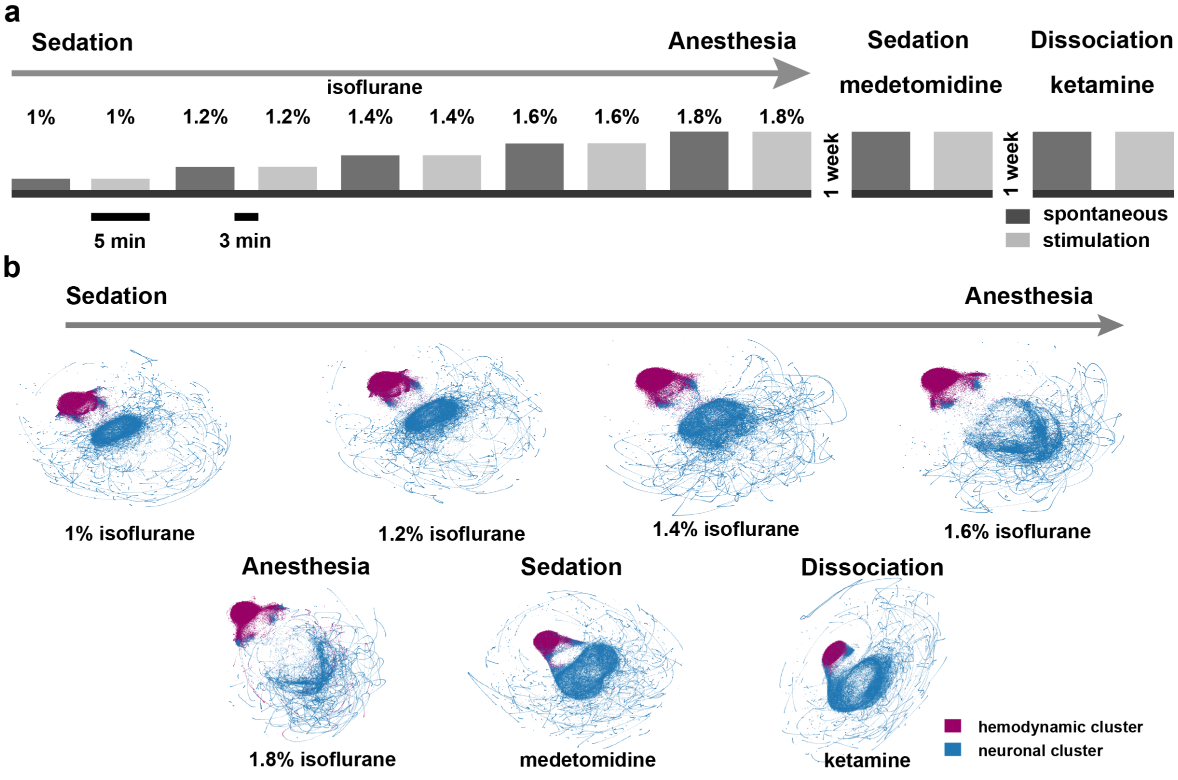

Figure 4.15: Cluster morphology reflects the functional properties of resting-state brain networks. a, Schematic of the experimental design, Isoflurane: 5-minute spontaneous recordings were followed by a 2-minute break and a 5-minute stimulated recording. This sequence was repeated for isoflurane concentrations from 1% to 1.8%, increasing in 0.2% increments. Imaging under medetomidine and ketamine was performed in the same animals in separate sessions. **b,** Representative UMAPs of spontaneous activity from isoflurane, medetomidine, and ketamine: hemodynamic cluster in red, neuronal cluster in blue.

After wavelet decomposition, the UMAP contains a representation of all frames in the imaging dataset in frequency and time. Therefore the transition from broadband activity during sedation to slow-wave activity in anesthesia significantly impacts the spectral features of the data and this change is reflected in the appearance of the neuronal cluster.

The shape and 'density' of the hemodynamic cluster were very similar under all investigated conditions. Anesthesia with isoflurane does not significantly impact the heart rate of the mice, consequently the hemodynamic cluster remains constant. This seems to indicate that physiological noise can always be differentiated from neuronal activity with our data-driven method.

To check the reproducibility of the clustering method, all UMAPS from 10 animals under isoflurane were plotted and it was confirmed that the change from the sedated to the anesthetized arousal state induced a breakup of the neuronal cluster in all animals, see Fig. 4.16.

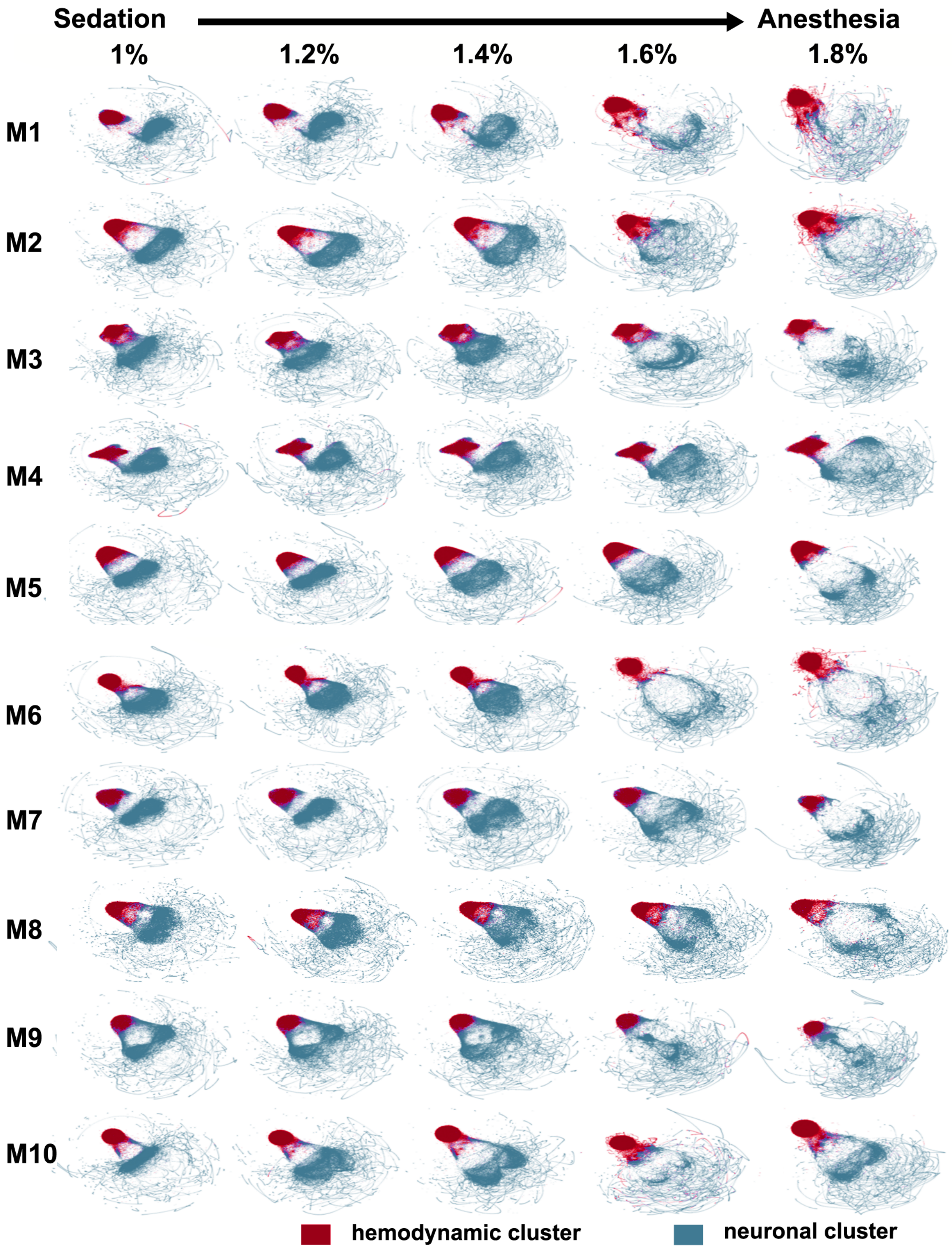

Figure 4.16: The neuronal cluster changes morphology reflecting the transition from sedation to anesthesia under isoflurane. UMAPs were calculated for animals M1-M10 (rows) over increasing concentrations of iso. from 1% to 1.8% (columns). The transition between brain states induced the degradation of the neuronal cluster from a dense structure during sedation (iso. 1%) to a more spread out and less dense configuration under anesthesia (iso. 1.8%)

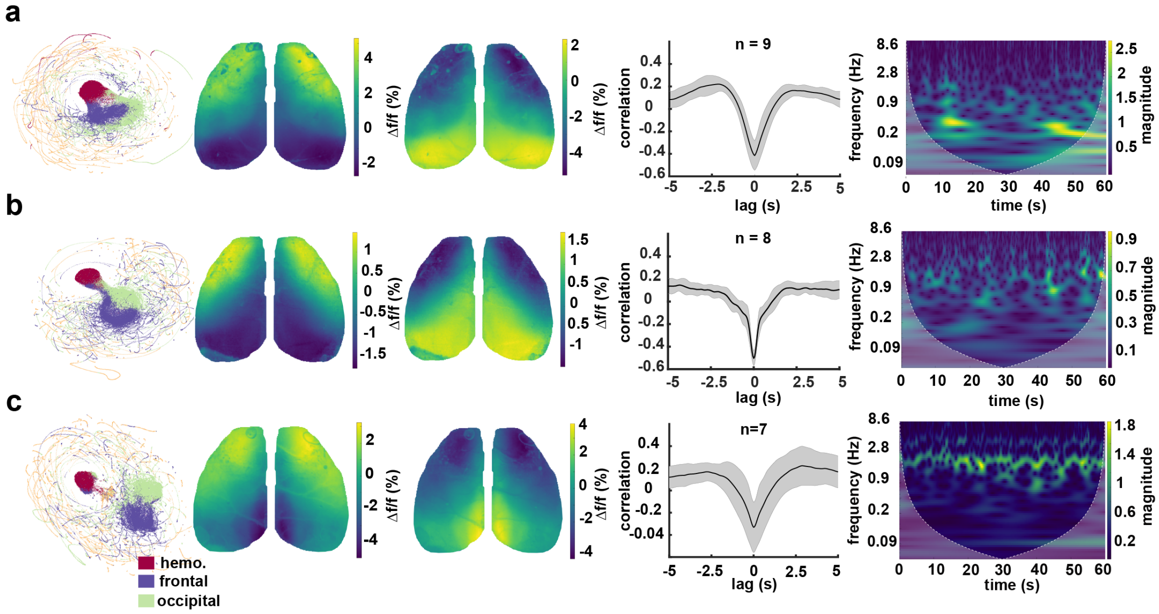

Figure 4.17: Subclustering reveals brain state-specific spatial and spectral features. a-c, spontaneous activity under 1% isoflurane (c), medetomidine (d), and ketamine (e); from left to right: UMAP, hemodynamic cluster (red), frontal cluster (blue), and occipital cluster (green); average of the frontal cluster; average of the occipital cluster; lagged correlations from the standard deviation of images in the occipital and frontal clusters, mean correlation at 0 lag for isoflurane -0.41, medetomidine -0.5, and ketamine -0.33; typical wavelet power spectrum (Morlet) from averaged retrosplenial cortex signal.

Neuronal clusters from mice under 1% isoflurane (Fig. 4.17, a), medetomidine (Fig. 4.17, b), and ketamine (Fig. 4.17, c) were divided into 2 subclusters, and their spatial and spectral features were investigated for brain-state-specific activity. A mean of the subclusters reveals that under isoflurane and medetomidine most activity is concentrated in the frontal and occipital regions respectively (Fig. 4.17, a, b, 2nd and 3rd from left). Ketamine exhibits a different spatial pattern of activation with occipital activity concentrated in the retrosplenial cortex (RSP) of both hemispheres (Fig. 4.17 c 2nd and 3rd from left).

Next, the temporal relationship between these clusters was investigated. The standard deviation of each image over the entire imaging period was calculated and we cross-correlated the standard deviation vectors for the frontal and occipital clusters. Minimum correlations were observed at zero lag for isoflurane (mean correlation -0.41±0.13), medetomidine (-0.50±0.06), and ketamine (-0.34±0.22). Introducing lag resulted in a symmetric increase in the correlation between the frontal and occipital clusters, suggesting that frontally-weighted and occipitally-weighted networks exhibit fluctuating activity and are offset in time by up to 2 seconds (Fig. 4.17 a-c 4th from left). We found a strong 1-3 Hz oscillation in the RSP in ketamine (Fig. 4.17 e, 5th from left) but not isoflurane (Fig. Fig. 4.17 a, 5th from left) or medetomidine (Fig. Fig. 4.17 b, 5th from left).

4.4.2 Brain Pattern Dimensionality

We used pharmacological agents to induce distinct functional brain states. To illustrate, Fig. 4.18 shows averaged activity traces measured from the entire cortex under isoflurane (five concentrations), medetomidine, and ketamine. During 1% iso. average traces of cortical activity show high-frequency oscillations coexisting with lower frequency trends (Fig. 4.18, top row), as isoflurane concentration increases more wave-like patterns start to appear (Fig. 4.18, 1.4% iso.). During surgical-level anesthesia (Fig. 4.18, 1.8% iso.) stereotypical up-down transitions called slow waves dominate brain activity. Under med. and ket. we observed higher frequency fluctuations as well as prominent low-frequency components.

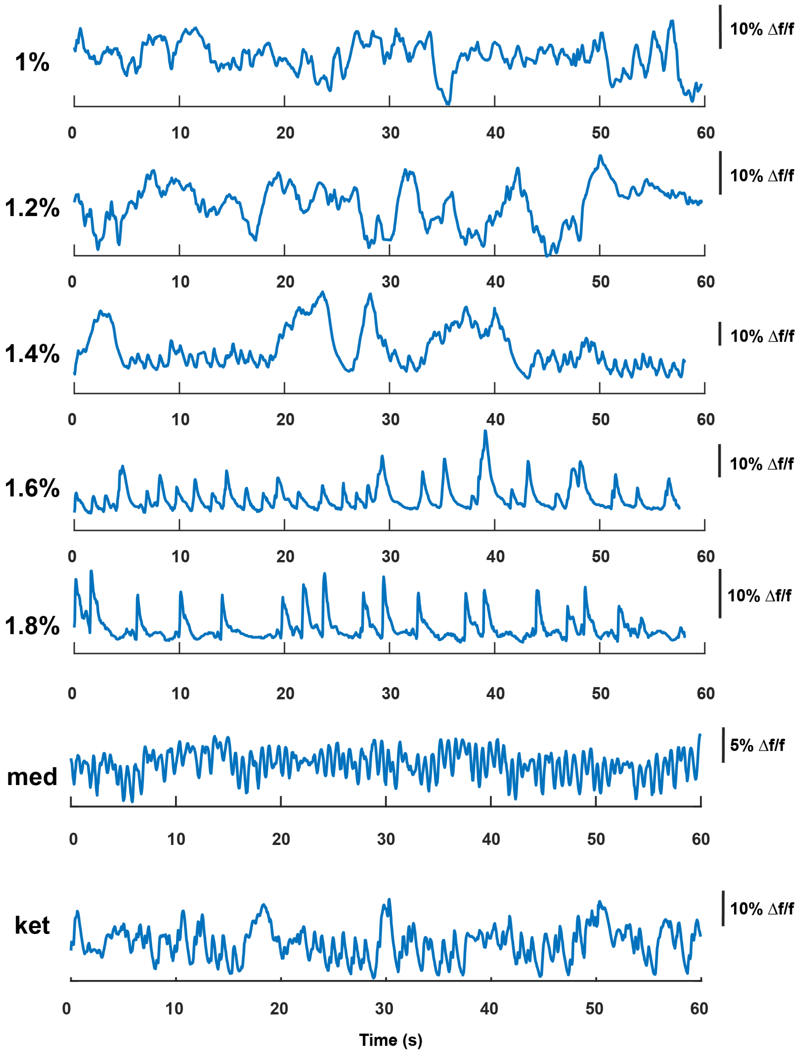

Figure 4.18: Exemplary average activity traces for the pharmacologically induced experimental conditions. Averaged activity (right) from the entire cortex under (from top to bottom) 1% iso.,1.2% iso., 1.4% iso., 1.6% iso., and 1.8% iso. Complex activation patterns in 1% iso., change gradually to slow waves in 1.6 and 1.8% iso. No slow waves were observed in med. and ket.

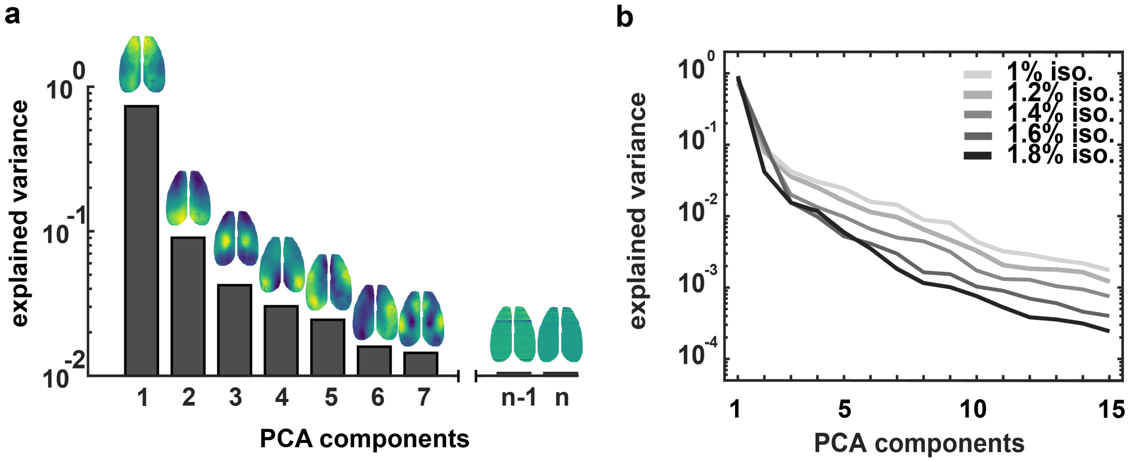

Figure 4.19: BPD index is based on physiological brain networks. **a,** Physiological brain patterns are extracted with principal component analysis (PCA). **b,** Explained variance ratio per PCA component computed from one subject acquired from 1-1.8% isoflurane concentrations (0.2% increments). In high isoflurane anesthesia conditions, fewer components are needed to explain most of the variance in the dataset.

A global index, BPD was developed to quantify the changes described above. This project was carried out in collaboration with the Helmholtz AI department, especially Dr. Marie Piraud and Dr. Dominik Thalmeyer. We conducted principal component analysis (PCA) (Fig. 4.19 a) of the imaging data and observed that during deep anesthesia, fewer principal components were required to characterize the overall covariance in the imaging data. To illustrate this, in Fig. 4.19 b a we plot the explained variance relative to the number of PCA components. Steeper descent of the logarithmic curve results in lower BPD values for this dataset. The steeper the descent of this curve, the fewer PCA components are necessary to characterize the data.

Calculating the effective dimensionality i.e. the minimum number of dimensions needed to recreate the covariance of the imaging data, provides a metric for quantifying the complexity of the spatiotemporal activity patterns. The normalized Shannon entropy of the eigenvalue distribution was computed to assess its information content. If the normalized entropy is equal to 1 we would need all PCA components to adequately characterize the imaging data, conversely, if the entropy is zero only one PCA component would be enough to characterize the dataset [318]. By rescaling the normalized entropy by the total number of PCA components, we arrive at the quantitative measure BPD.

The principal components correspond to spontaneously occurring physiological brain networks (Fig. 4.19 b). BPD estimates the level of functional segregation in cortical networks because the higher the BPD of our imaging datasets the higher the number of physiological cortical networks which are active in that particular recording and the more complex the brain state. BPD can be used to reduce the set of weighted PCA components (the weighting is the explained variance of PCA components) to a set of unweighted elements, an effective number of dimensions required to reproduce the overall pattern of covariation in our original dataset.

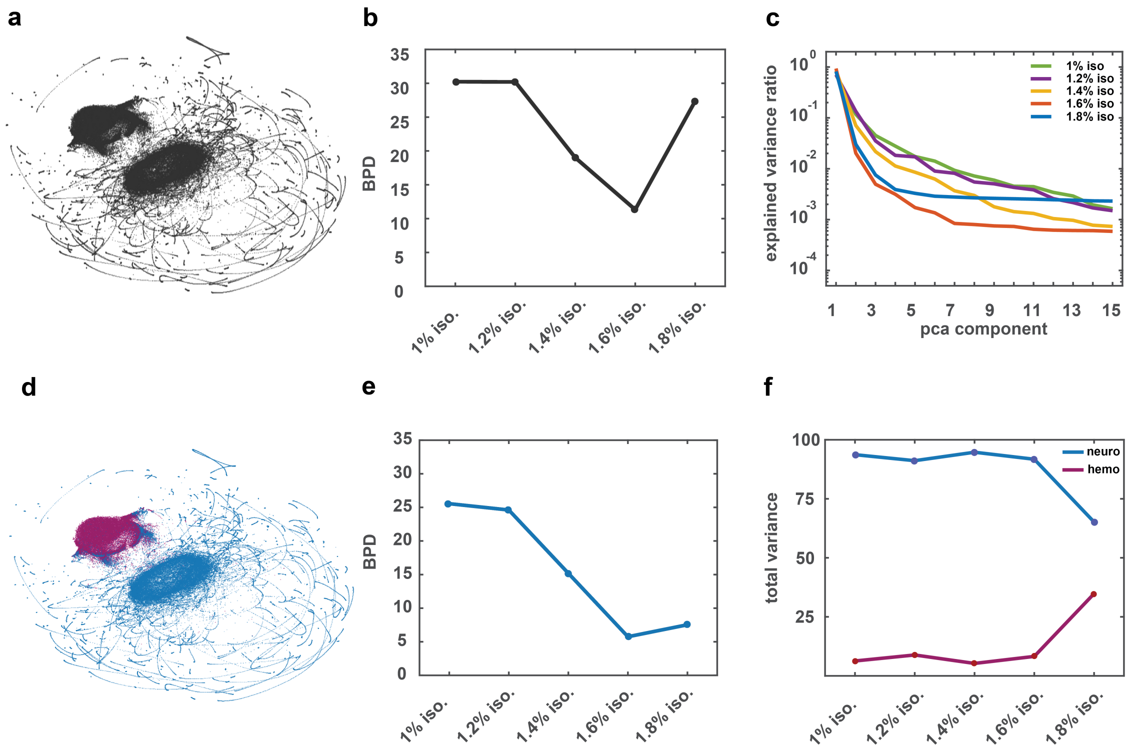

Figure 4.20: Accurate BPD measurements depend on the removal of physiological noise. a, UMAP of a functional imaging dataset acquired in mouse M1 during 1% iso. sedation, no clustering was performed. **b,** The evolution of brain BPD over the iso. concentration shows a marked increase during 1.8% vs. 1.6% iso. despite both conditions featuring slow waves. **c,** Explained variance ratio over PCA components shows the 1.8% iso. curve flattening after the 5th PCA component (green line) suggests that noise is heavily featured in this dataset. **d,** UMAP of the same dataset as in a, with isolation of the hemodynamic noise cluster (red) and neuronal cluster (blue). **e,** When only the dimensionality of the neuronal cluster is calculated, BPD values in 1.6% and 1.8% iso. are very similar.**f,** We calculated the total contribution of the neuronal (blue) and hemodynamic (red) clusters to the variance observed in our imaging data over iso. level. The explained variance for the neuronal cluster decreases while there is an increase in the variance of the hemodynamic cluster in iso 1.8%, suggesting that without clustering, physiological noise artificially increases BPD estimations.

The accurate calculation of BPD depends on the suppression of physiological noise, as noise will artificially increase the dimensionality of brain imaging data so we calculate BPD after UMAP clustering and physiological noise removal, i.e. we estimate the dimensionality of the neuronal cluster only (Fig. 4.20).

Without physiological noise removal, the evolution of brain BPD over the iso. level shows a marked increase during 1.8% vs. 1.6% iso. in spite of both conditions featuring slow waves (Fig. 4.20 b). The explained variance ratio over PCA components in 1.8% isoflurane shows a flattening curve after the 5th PCA component (green line) suggesting that noise is heavily featured in this dataset (Fig. 4.20 c). In 1.8% isoflurane, the explained variance for the neuronal cluster decreases while there is an increase in the explained variance of the hemodynamic cluster (Fig. 4.20 f) suggesting that without clustering, physiological noise artificially increases BPD estimations. When only the dimensionality of the neuronal cluster is calculated, BPD values in 1.6% and 1.8% are similar (Fig. 4.20 e).

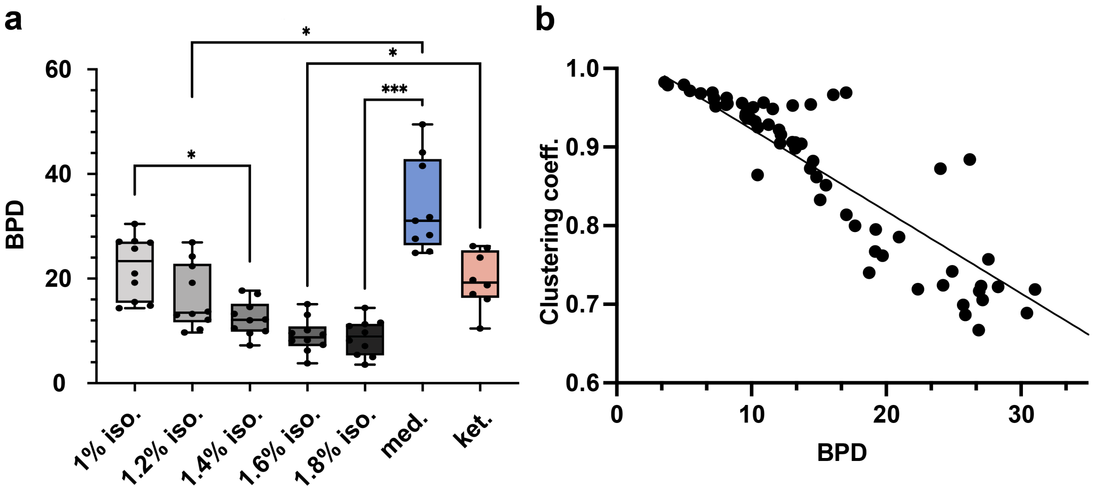

Figure 4.21: Brain Pattern Dimensionality index measures the functional segration level of cortical networks. a, Brain pattern dimensionality of spontaneous activity recordings. One-way ANOVA repeated measurements / Tukey's multiple comparisons test (n=10 iso., n=9 med., n=8 ket.): 1% isoflurane vs. 1.4% isoflurane p=0.013; medetomidine vs. 1.2% isoflurane p=0.011; medetomidine vs. 1.8% isoflurane p=0.0006; ketamine vs. 1.8% isoflurane p=0.012. **b,** Linear regression BAPD vs. clustering coefficient calculated with graph theory, R-squared=0.68, slope -0.01, F=142.3, p<0.0001. * corresponds to p-value < 0.05, *** corresponds to p-value < 0.001.

Spontaneous activity was recorded in 10 mice under isoflurane, 9 mice under medetomidine and 8 mice under ketamine. The transition from sedation to anesthesia (1% isoflurane to 1.8% isoflurane) is accompanied by a gradual decrease in BPD (Fig. 4.19, c): 1% isoflurane, 22.2±5.9; 1.2% isoflurane, 16.47±6.1; 1.4% isoflurane, 12.4±3.3; anesthesia with 1.6% isoflurane, 9±3.2; anesthesia with 1.8% isoflurane, 8.7±3.4. Statistically significant differences were found between 1% isoflurane and 1.4% isoflurane (p=0.013), 1.6% isoflurane (p=0.001) and 1.8% isoflurane (p=0.0006). We do not observe a 'phase change' when analyzing BPD values over isoflurane concentrations. Rather, the level of segregation of spontaneous activity networks decreases from isoflurane 1% to isoflurane 1.4% and stabilizes at low values during surgical-level anesthesia with 1.6% and 1.8% isoflurane (Fig. 4.21 a).

Sedation with medetomidine showed the highest BPD average value of 33.77 but also the highest SD of 8.9, so when compared to sedation with 1% isoflurane, the means were not significantly different (p=0.14). Dissociation under ketamine was also indistinguishable from 1% isoflurane (19.77±5.4 vs. 22.21±5.9, p=0.95) but was significantly different from anesthesia with 1.6% isoflurane (19.77±5.4 vs. 9.04±3.2, p=0.02) and showed a clear trend towards significance when compared to sedation with medetomidine (19.77±5.4 vs. 33.7±8.9, p=0.065).

These results show that the level of resting-state network segregation is similar in isoflurane 1%, ketamine 100 mg/kg, and medetomidine 0.055 mg/kg. Making the differentiation between these conditions, therefore, requires analyzing the nature of the FC patterns generated by these drugs which all have different molecular targets.

BPD measures functional segregation levels, to show this, we carried out linear regression between BPD and a network measure of functional segregation, the clustering coefficient. There is a moderately strong correlation between these two variables. The clustering coefficient has its highest values in fully connected networks such as can be found in the slow-wave state, hence the negative slope between BPD and the clustering coefficient (Fig. 4.21 b).

4.4.3 Complex network connectivity measures

Functional segregation and integration during spontaneous activity can also be characterized using graph theory. For this, functional imaging data has to be represented in the form of a network graph. The nodes of the graph are represented by brain regions and the vertices by the strength of the correlation between time-varying signals from these areas. All data has been registered to a common coordinate framework [304] and time-varying signals were extracted from the anatomically distinct areas. This step was followed by the calculation of Pearson's correlation coefficient between brain regions to form correlation matrices. Because the columns and rows of these matrices represent the same cortical areas in identical order the correlation matrices are symmetrical along the main diagonal (Fig. 4.22).

Correlation matrices were calculated for all subjects and all pharmacological conditions and representative matrices are shown in Fig. 4.22. In isoflurane 1%, medetomidine, and ketamine, functional units are revealed by the higher levels of correlation between their subunits. It was observed that somatomotor brain areas have higher correlations amongst their subcomponents than with visual areas and vice-versa. This pattern is present within the left and right hemispheres but also in the case of interhemispheric correlations. This is expected because there is a high degree of coordination between the activity of ipsi- and contralateral brain regions. In the case of isoflurane 1.8%, the level of correlation between brain areas is very high, approaching 0.95. Notwithstanding, some remnants of the modular correlation patterns from low isoflurane anesthesia are still present.

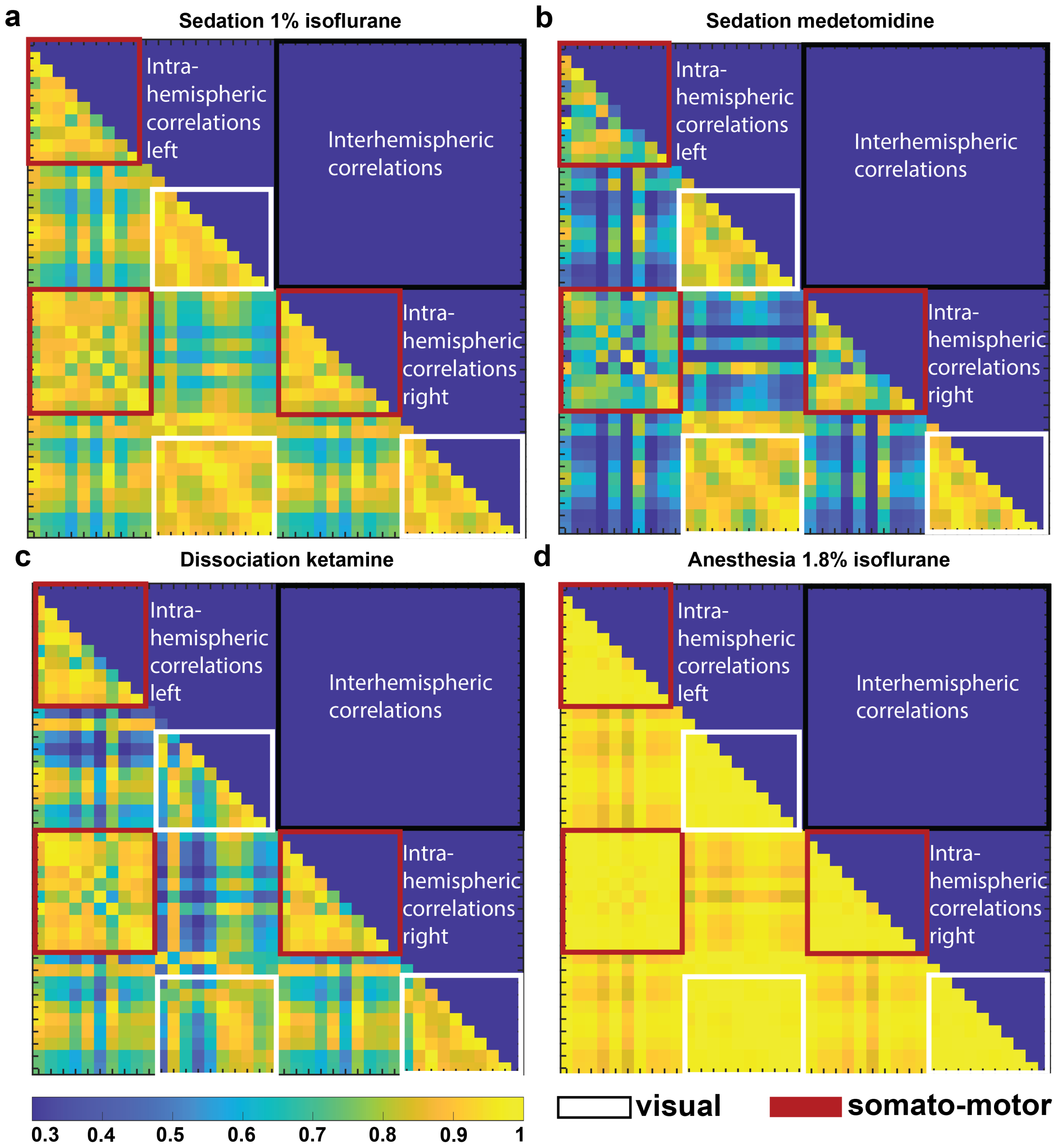

Figure 4.22: Brain connectivity analysis reveals functional cortical units. Cortical connectivity matrices for **a,** sedation with 1% isoflurane **b,** sedation with medetomidine **c,** dissociation with ketamine, and **d,** surgical-level anesthesia under 1.8% isoflurane. The x and y axes represent functional brain regions as extracted based on the Allen Mouse Brain Atlas. Brain regions were sorted in left and right hemispheres so as to enable comparisons between interhemispheric, right-intrahemispheric, and left-intrahemispheric correlations. Brain connectivity matrices are symmetrical, so only values under the main diagonal are shown. Red and white borders indicate somatomotor brain areas and visual brain areas respectively.

Mean correlation values between all regions of interest were investigated in all pharmacological conditions and it was found that all conditions had an average correlation above 0.5.

Under isoflurane, overall correlations increased progressively from concentrations of 1% to 1.8%. Statistically significant differences were found between isoflurane 1% vs. isoflurane 1.4% (0.77±0.06 vs. 0.88±0.04, p=0.01), isoflurane 1.4% vs. isoflurane 1.6% (0.88±0.04, vs. 0.92±0.03, p=0.0005), medetomidine vs. isoflurane 1.4% (0.63±0.13, vs. 0.88±0.04, p=0.01). Medetomidine was not significantly different from isoflurane 1% (p=0.15) and interestingly, ketamine average correlation values were not significantly different from any of the other conditions (Fig. 4.23).

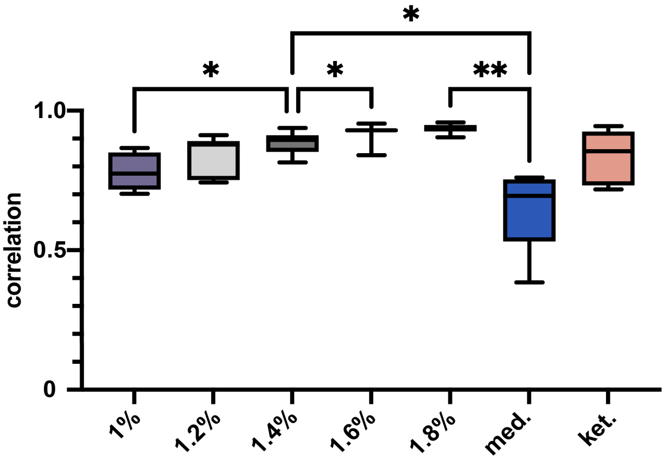

Figure 4.23: The average correlation strength between brain regions is dependent on the brain state. Comparison between average correlation levels in 1% iso., 1.2% iso, 1.4% iso., 1.6% iso., med. and ket. One-way ANOVA repeated measurements / Tukey's multiple comparisons test (n=10 iso., n=9 med., n=8 ket.): 1% iso. vs. 1.4% iso. p=0.019; 1.4% iso. vs. 1.6% iso. p=0.03; med. vs. 1.4% iso. p=0.01; med. vs. 1.8% iso. p=0.002. * corresponds to p-value < 0.05, ** corresponds to p-value < 0.01.

Network measures of integration were calculated next (Fig. 4.24). The degrees of the network graph represent the average number of edges that are associated with a network node i.e. the number of above-threshold correlations per network node. The maximum number of degrees is equal to the maximum number of network nodes, i.e. 40. Using this metric, it was possible to distinguish between isoflurane 1% and isoflurane 1.4% (30.28±5.6 vs. 38.34±1.3, p=0.01) and medetomidine and isoflurane 1.4% (20.45±8.7 vs. 38.34±1.3 p=0.003). Medetomidine, ketamine, and isoflurane 1% network degrees were not significantly different (Fig. 4.24 a).

The average inverse shortest path length is known as the global efficiency and is primarily influenced by short paths. This is a point of difference respective to the path length which is more heavily affected by long paths. Significant differences were found between iso. 1% vs. iso 1.4% (0.76± 0.08 vs. 0.90±0.044, p=0.01) and med. vs. iso. 1.4 (0.61±0.13 vs. 0.90±0.044, p=0.004). Again there were no significant differences between, medetomidine, isoflurane 1%, and ketamine (Fig. 4.24 b).

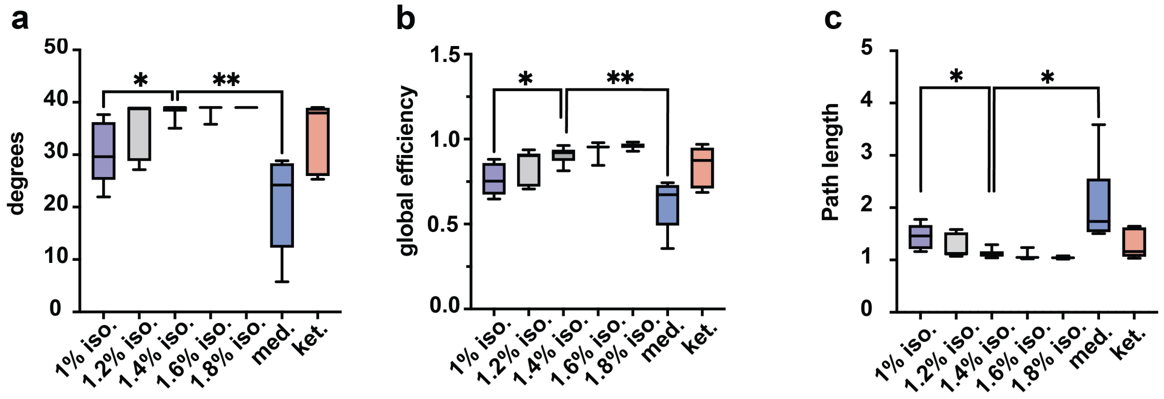

Figure 4.24: Complex network measures of functional integration. a, Node degrees across anesthesia conditions i.e. the average number of connections per network node. One-way ANOVA / Tukey's multiple comparisons test (n=10 iso., n=9 med., n=8 ket.); 1% iso. vs 1.4% iso. p=0.016; medetomidine vs. 1.2% iso. p=0.003.**b,** global efficiency One-way ANOVA / Tukey's multiple comparisons test (n=10 iso., n=9 med., n=8 ket.); 1% iso. vs. 1.4% iso. p=0.016; 1.4% iso. vs. 1.6% iso. p=0.043; medetomidine vs. 1.4% iso. p=0.004. **c,** Path length One-way ANOVA / Tukey's multiple comparisons test (n=10 iso., n=9 med., n=8 ket.); 1% iso. vs. 1.4% iso. p=0.019; medetomidine vs. 1.4% iso. p=0.04. * corresponds to p-value < 0.05, ** corresponds to p-value < 0.01.

The shortest path length between all pairs of nodes is known as the characteristic path length and is the most widely employed measure of functional integration. Based on the path length estimation, it was possible to distinguish between isoflurane 1% vs. isoflurane 1.4% (1.45± 0.22 vs. 1.12±0.08, p=0.01) and medetomidine vs. isoflurane 1.4% (2.08±0.7 vs. 1.12±0.08, p=0.04). It was not possible to statistically distinguish between isoflurane 1% and medetomidine, furthermore, ketamine was not significantly different with respect to any of the other conditions investigated (Fig. 4.24 c).

Next, network measures of functional segregation were investigated: modularity (Fig. 4.25 a), clustering coefficient (Fig. 4.25 b), and local efficiency (Fig. 4.25 c). Modularity refers to the strength of segregation of a network into modules. Networks with high modularity have high numbers of connections inside modules but few connections between nodes located in different modules. Modularity was significantly different between isoflurane 1% vs. isoflurane 1.4% (0.12±0.07 vs. 0.13±0.02, p=0.02) and medetomidine vs. isoflurane 1.4% (0.28±0.15 vs. 0.13±0.02, p=0.009)(Fig. 4.25 a).

The clustering coefficient measures the degree to which nodes in a graph tend to cluster together. This measure was significantly different between isoflurane 1% vs. isoflurane 1.4% (0.76±0.07 vs. 0.90±0.05, p=0.01) and medetomidine vs. isoflurane 1.4% (0.66±0.11 vs. 0.90±0.05, p=0.007) (Fig. 4.25 b). Local efficiency is a measure that ranges from 0 to 1, with high values indicating maximum local efficiency in the network. In functional cortical brain networks, high local efficiency indicates a topological organization indicative of segregated neural processing. Local efficiency was significantly different between isoflurane 1% vs. isoflurane 1.4% (0.81±0.05 vs. 0.9±0.04, p=0.01) and medetomidine vs. isoflurane 1.4% (0.07±0.08 vs. 0.9±0.04, p=0.01)(Fig. 4.25 c).

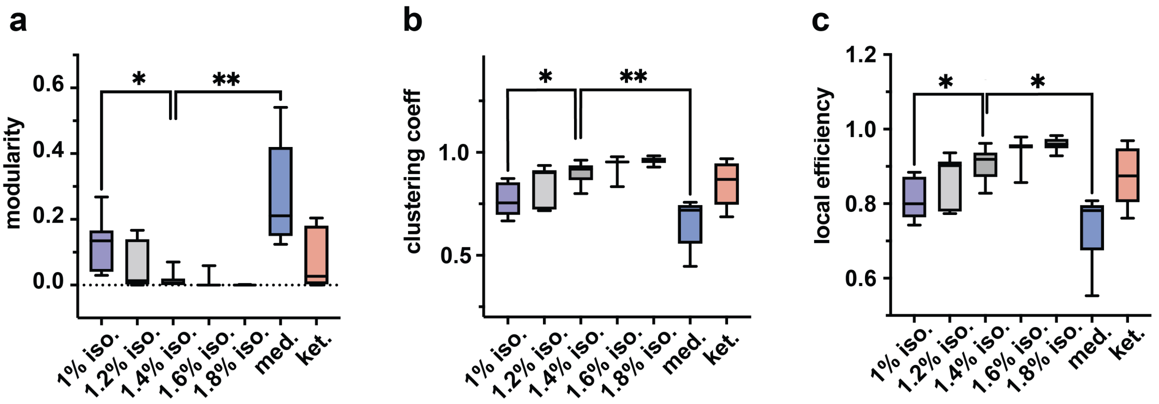

Figure 4.25: Complex network measures of functional segregation. **a,** Modularity, One-way ANOVA / Tukey's multiple comparisons test (n=10 iso., n=9 med., n=8 ket.); 1% iso. vs. 1.4% iso. p=0.021; medetomidine vs. 1.4% iso. p=0.009. **b,** Clustering coefficient One-way ANOVA / Tukey's multiple comparisons test (n=10 iso., n=9 med., n=8 ket.); 1% iso. vs. 1.4% iso. p=0.012; 1.2% iso. vs. 1.6% iso. p=0.03; 1.4% iso. vs. 1.8% iso. p=0.03; medetomidine vs. 1.4% iso. p=0.007. **c,** Local efficiency, One-way ANOVA / Tukey's multiple comparisons test (n=10 iso., n=9 med., n=8 ket.); 1% iso. vs. 1.4% iso. p=0.016; 1.2% iso. vs. 1.6% iso. p=0.015; 1.4% iso. vs. 1.6% iso. p=0.039; medetomidine vs. 1.4% iso. p=0.013. * corresponds to p-value < 0.05, ** corresponds to p-value < 0.01.

4.4.4 Functional connectivity motifs responsible for brain state transitions

Metastability in a dynamical system refers to an intermediate energy state which is stable to small perturbations but unstable when larger changes appear in the physical system. Specialized neuronal networks have to be able to work separately from their neighbors while also sharing their outputs with connected regions to integrate their activity. For this reason, in neuroscience, metastability refers to a combination of integration and segregation of functional neuronal activity which is meant to increase the number of states that are available to the network at any one time.

First a global metastability measure was calculated for the entire duration of the dataset (Fig. 4.26). Subsequently, spatio-temporal metastable patterns were computed for the purpose of determining the functional connectivity patterns with explanatory power for brain states and transitions (Fig. 4.26 and 4.28). One strategy for studying metastability involves characterizing the ability of a region to propagate its feed-forward and recurrent neuronal activity to other regions in the absence of extrinsic influences [330]. For this analysis brain region activation was extracted from spontaneous activity recordings.

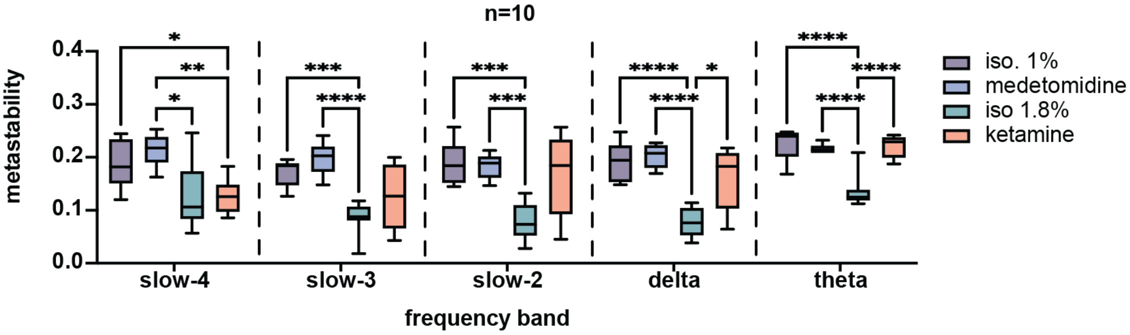

Figure 4.26: Metastability is dependent on the functional brain state. Metastability over canonic frequency bands for iso. 1%, med., iso. 1.8%, and ket. One-way ANOVA / Tukey's multiple comparisons test (n=10 iso., n=9 med., n=8 ket.). Slow-4: iso. 1% vs. ket, p=0.002; med. Vs. iso. 1.8%, p=0.04; med. vs. ket, p=0.002; Slow 3: iso. 1% vs. iso. 1.8%, p=0.0003; med. vs. iso. 1.8%, p<0.0001. Slow-2: iso. 1% vs. iso. 1.8%, p=0.0009; med. vs. iso. 1.8%, p=0.0006. Delta: iso. 1% vs. iso. 1.8%, p<0.0001; med. vs. iso. 1.8%, p<0.0001; iso. 1.8% vs. ket, p=0.017; Theta: iso. 1% vs. iso. 1.8%, p<0.0001; med. vs. iso. 1.8%, p<0.0001; iso. 1.8% vs. ket, p<0.0001. * corresponds to p-value < 0.05, ** corresponds to p-value < 0.01, *** corresponds to p-value < 0.001, **** corresponds to p-value < 0.0001.

Metastability was calculated for datasets acquired under sedation with isoflurane 1% and medetomidine, anesthesia under isoflurane 1.8%, and dissociation under ketamine across canonical frequency bands slow-4, slow-3, slow-2, delta, and theta (Fig. 4.26). In the slow-4 band, it was possible to differentiate between isoflurane 1% vs. ketamine (0.187±0.04 vs. 0.127±0.032, p=0.03), medetomidine vs. 1.8% isoflurane (0.19±0.03 vs. 0.12±0.05 p=0.045) and medetomidine vs. ketamine (0.19±0.03 vs. 0.12±0.03, p=0.002). In the slow-3 band isoflurane 1% vs. isoflurane 1.8% (0.17±0.02 vs. 0.08±0.02, p=0.0003) and medetomidine vs. isoflurane 1.8% (0.19±0.03 vs. 0.08±0.02, p<0.0001) were found to be statistically significant. Slow-2 band metastability was useful in differentiating isoflurane 1% vs. isoflurane 1.8% (0.19±0.03 vs. 0.07±0.03, p=0.0009) and medetomidine vs. isoflurane 1.8% (0.18±0.02 vs. 0.08±0.03, p<0.0006). Metastability in the delta band was significantly different between isoflurane 1% vs. isoflurane 1.8% (0.19±0.03 vs. 0.07±0.027, p<0.0001), medetomidine vs. isoflurane 1.8% (0.2±0.02 vs. 0.07±0.027, p<0.0001) and isoflurane 1.8% vs. ketamine (0.07±0.027 vs. 0.16±0.05, p=0.01). In the theta frequency band, isoflurane

1% vs. isoflurane 1.8% (0.22±0.03 vs. 0.13±0.03, p<0.0001), medetomidine vs. isoflurane 1.8% (0.2±0.008 vs. 0.13±0.03, p<0.0001) and isoflurane 1.8% vs. ketamine (0.07±0.027 vs. 0.16±0.05, p<0.0001) were found to be significantly different. These results show that under ketamine, metastability in slow frequency domains closely resembles isoflurane anesthesia while in higher-frequency bands values approach those of medetomidine sedation. The distinction between 1% isoflurane and 1.8% isoflurane can be made across frequency bands but it is difficult to differentiate between isoflurane 1% and medetomidine despite these drugs acting on different molecular targets.

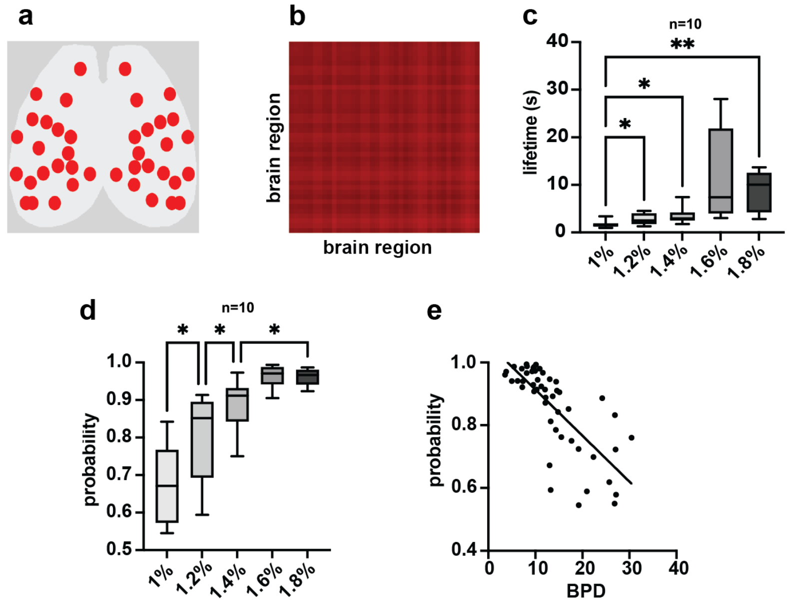

Figure 4.27: LEiDA - fully connected functional motif under isoflurane. a, Spatial representation of the functional connectivity pattern overlaid on the mouse cortex. Red indicates positive correlations between brain regions and circle size denotes the strength of the correlation. **b,** Functional connectivity matrix corresponding to the fully connected motif. **c,** Lifetime of the FC pattern in seconds. One-way ANOVA / Tukey's multiple comparisons test (n=10). 1% iso. vs. 1.2% iso. p=0.02; 1% iso vs. 1.4% iso, p=0.03; 1% iso vs. anesthesia 1.8% iso, p=0.006; **d,** Probability of occurrence of the FC pattern in seconds. One-way ANOVA / Tukey's multiple comparisons test (n=10). 1% iso. vs. 1.2% iso., p=0.02; 1.2% iso. vs. 1.4% iso., p=0.04; 1.4% iso vs. anesthesia 1.8% iso, p=0.02; **e,** Linear regression BPD vs. probability of fully connected motif, slope=-0.01, R squared = 0.54, F=58.17, p<0.0001. * corresponds to p-value < 0.05, ** corresponds to p-value < 0.01.

Next, leading eigenvector dynamic analysis (LEiDA) was used to investigate the metastable functional connectivity (FC) motifs responsible for the transition between brain states. For this analysis, the averaged signal from 40 brain regions was extracted from spontaneous activity recordings under isoflurane to characterize the changes in FC motifs induced by a brain state transition. LEiDA [289] was followed by the determination of probabilistic metastable substates [180], and the determination of the lifetime and probability of 12 FC motifs that had a likelihood of occurrence greater than 1%.

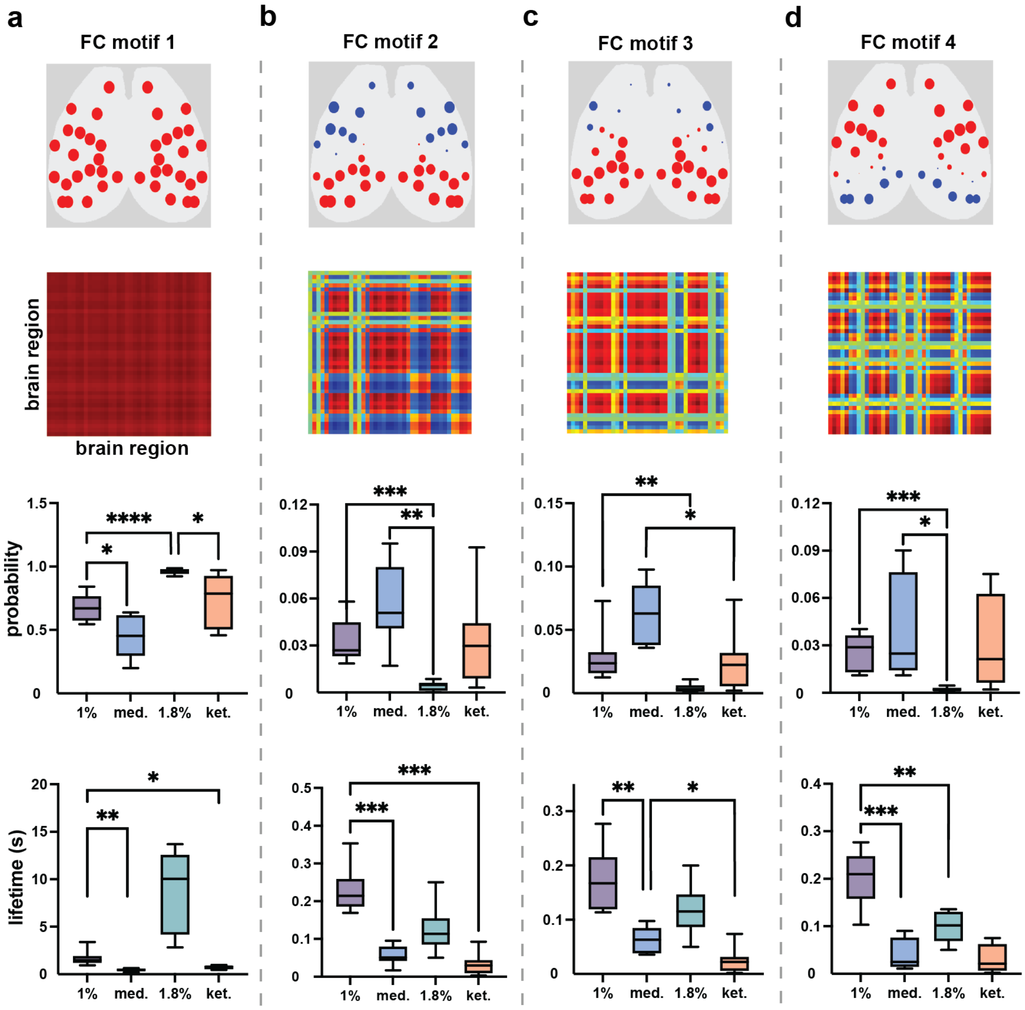

Figure 4.28: Differentiation between brain states with similar levels of functional segregation with LEiDA. Analysis conducted on n=10 iso., n=9 med., n=8 ket. **a,** FC motif 1 from upper to lower: FC patterns, first two panels; Probability of FC motif 1: iso. vs. med. p=0.01; iso. 1% vs. iso. 1.8% p<0.0001; iso. 1.8% vs. med. p<0.0001; iso. 1.8% vs. ket. p=0.04; Lifetime of FC motif 1: iso. 1% vs med. p=0.22; med. vs. iso. 1.8% p<0.0015; iso. 1% vs. ket. p=0.01; iso. 1.8% vs. ket p=0.003.**b,** FC motif 2 from upper to lower: FC patterns, first two panels; Probability of FC motif 2: iso. 1% vs. iso. 1.8% p=0.0006; iso. 1.8% vs. med. p=0.001; Lifetime of FC motif 2: iso. 1% vs. med. p=0.0003; iso. 1% vs. iso. 1.8% p=0.001; iso. 1.8% vs. ket. p=0.02.**c,** FC motif 3 from upper to lower: FC patterns, first two panels; Probability of FC motif 3: iso. 1% vs. iso. 1.8% p=0.004; iso. 1.8% vs. med. p=0.0005; med. vs. ket. p=0.02; Lifetime of FC motif 3: iso. 1% vs. med. p=0.008; med. vs iso. 1.8% p=0.02; iso. 1.8% vs. ket. p=0.003; med. vs. ket. p=0.02; **d,** FC motif 4 from upper to lower: FC patterns, first two panels; Probability of FC motif 4: iso. 1% vs. iso. 1.8% p=0.0002; iso. 1.8% vs. med. p=0.02; Lifetime of FC motif 4: iso. 1% vs. med. p=0.0003; med. vs. iso. 1.8%, p=0.03; iso. 1.8% vs. ket p=0.0003; iso. 1% vs. iso. 1.8%, p=0.001. * corresponds to p-value < 0.05, ** corresponds to p-value < 0.01. *** corresponds to p-value < 0.001, **** corresponds to p-value < 0.0001.

Amongst these motifs, the one with the longest lifetime and highest probability exhibited high correlation values between all functional brain regions (Fig. 4.27, a and b). The lifetime of this motif increased from 1.68±0.7 s during 1% isoflurane to 8.7±4.4 s during 1.8% isoflurane anesthesia (Fig. 4.27, c) and its probability of occurrence increased from 0.67±0.11 during 1% isoflurane to 0.96±0.02 during 1.8% isoflurane anesthesia (Fig. 4.27, d).

The relationship between BPD and the likelihood of occurrence of the fully connected network motif was investigated by linear regression and it was found that BPD values had a moderate explanatory power for the probability of occurrence of this FC pattern, R-squared= 0.54, F=58.17, p<0.0001 (Fig. 4.27 e).

Similar to isoflurane, the most prevalent functional motif featured high connectivity between all brain regions (Fig. 4.28 a). Based on the probability of occurrence of the FC motif 1 it was possible to distinguish between isoflurane 1% and medetomidine (0.67±0.11 vs. 0.44±0.16, p=0.01). The lifetime of FC motif 1 also allowed for the differentiation of isoflurane 1% from medetomidine (1.6±0.71 sec. vs. 0.44±0.16 sec. p=0.002) and isoflurane 1% from ketamine (1.6±0.71 sec. vs. 0.72±0.20 sec. p=0.01)(Fig. 4.28 a). The lifetime FC motif 2 enabled the differentiation between isoflurane 1% vs. medetomidine (0.23±0.06 vs. 0.05±0.02, p=0.003) and isoflurane 1% vs. ketamine (0.23±0.06 vs. 0.03±0.02, p=0.02) (Fig. 4.28 b). The lifetime of FC motif 3 was useful in differentiating iso 1% from medetomidine (0.17±0.05 vs. 0.06±0.02, p=0.008) and medetomidine from ketamine (0.06±0.02 sec. vs. 0.02±0.02 sec., p=0.02) (Fig. 4.28 c). The lifetime of FC motif 4 was significantly different for isoflurane 1% and medetomidine (0.2±0.05 sec. vs. 0.04 sec. vs. 0.03 sec. p=0.0003) (Fig. 4.28 d).

The determination of metastable substates with LEiDA can help in the differentiation between experimental conditions that have similar levels of resting-state network segregation and this is accomplished by investigating the spatial nature of FC connectivity patterns.

4.5 Cortical responses to sensory stimulation are dependent on the functional brain state

Stimulus processing is a key step in the intricate chain of neuronal events that motivates behavior. Under anesthesia, mammals become insensate to outside influences. The processes that underlie this phenomenon are not completely understood. In this section, the cortical representation of sensory stimuli was investigated as a function of the brain state. Brain state transitions from the persistent state to the slow-waves state were induced with progressively increasing levels of isoflurane gas. Hind paw stimulation was used to activate somatosensory networks and visual networks were accessed with light pulses to the retina. Experiments were done on 5 animals for hind paw and 5 animals for visual stimulation.

4.5.1 Hind paw stimulation

As highlighted in Fig. 4.15, five different concentrations of isoflurane were used to induce transitions from complex spontaneous activity to slow waves. For each isoflurane concentration, five-minute baseline recordings were followed by five-minute recordings of stimulated brain activity. 50 ms electrical pulses with an amplitude of 1mA were delivered every 10 seconds resulting in 30 stimulations per five-minute recording. 30, 10-second intervals after stimulation were averaged and the data were reconstructed into movies showing the cortical representations of stimuli. During 1% isoflurane, left hind paw stimulation produced primary activation in the S1 hind limb (S1-HL) area with a peak activation between 0.3-1 second after stimulation Fig. 4.29 c). Less pronounced activation in this first phase was observed in board parasagittal regions as well as the visual areas. After left hind paw stimulation, activation was strongest in the contralateral hemisphere although strong increases in GCaMP6s fluorescence were also observed in the ipsilateral S1-HL cortex. Beyond one second, activity in the S1-HL subdued and gave way to more prominent activity in the associative areas bordering the V1 region. This could indicate the first second after stimulation is primarily dedicated to the local processing of the stimulus in specialized cortical regions and later activity aims to integrate information in associative areas.

In contrast to the elaborate patterns of activation described above, during surgical-level anesthesia with isoflurane, activation levels exceed 10% $\Delta f/f$ in large parts of the cortex (Fig. 4.29 d). At 0.3 seconds after stimulation, the strongest activation extends from the S1-HL to the retrosplenial cortex. After this, high levels of global activation take over most of the cortex at 0.6 seconds. This temporal pattern suggests that activation events are propagating across the cortex from a point of origin situated in the somatosensory projection areas to eventually involve the whole cortex.

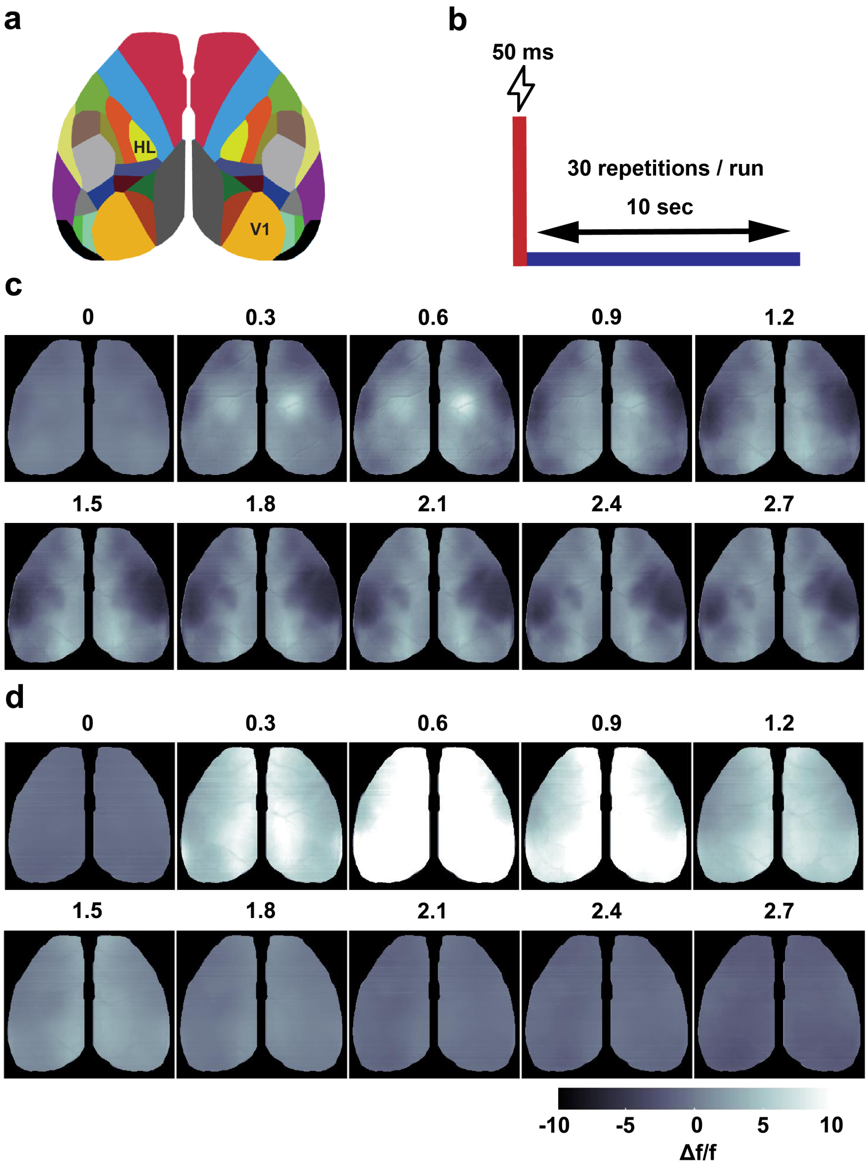

Figure 4.29: Spatio-temporal responses to hind paw stimulation under 1% and 1.8% isoflurane. a, Brain region map HL denotes the hind limb projection areas, and the primary visual areas are marked with V1. **b,** 30 stimulations with a duration of 50 ms each were averaged and assessed for cortical activation patterns. **c,** Imaging time-series form an average of 30 hind paw stimulations during 1% iso. **d,** Imaging time-series form an average of 29 hind paw stimulations during 1.8% iso. The time index in sec. is indicated above the brain activity maps.

Left hind paw stimulation during low isoflurane resulted in activation of the right S1 hind limb area (Fig. 4.30 d upper row, first 2 panels from left), with activation intensity of 6.3±2.81% (Fig. 4.30 d lower row, first 2 panels from left) and during 1.8% isoflurane recordings, responses were global (Fig. 4.30 d upper row, 4th and 5th panels from left) with

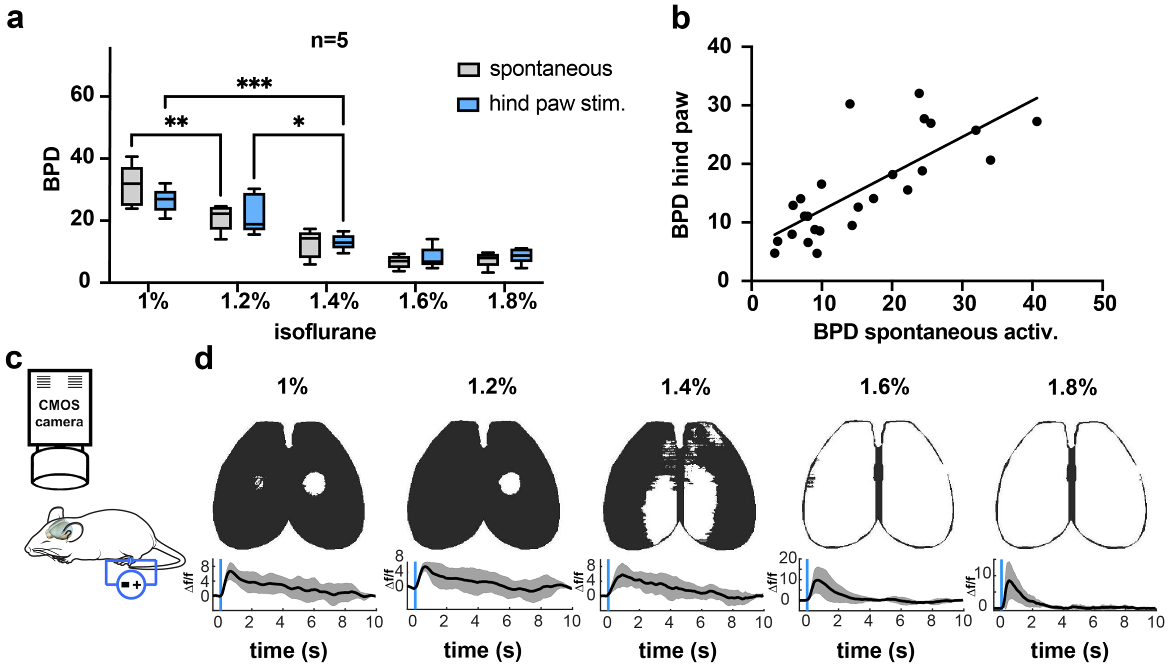

Figure 4.30: Cortical responses to stimulation of the left hind paw decrease in complexity with increasing anesthesia.
a, Changes in brain pattern dimensionality (BPD) as a response to anesthesia and hind paw stimulation n=5. Two-way ANOVA repeated measurements: 1% iso. vs 1.2% iso. p=0.006; 1.2% iso. hind paw vs. 1.4% iso. hind paw p=0.02; 1% iso. hind paw vs. 1.4% iso. hind paw p=0,0004.**b,** Linear regression BPD spontaneous activity vs. BPD hind paw stimulation, slope=0.62, R squared = 0.58, F=31.85, p<0.0001. **c,** Hind paw stimulation: 1 mA, 50 ms long pulses were delivered every 10 sc. resulting in 30 stimulations per imaging run. **d,** Upper: binarized response 0.6 sec. after hind paw stimulation for isoflurane 1%, 1.2%, 1.4%, 1.6% and 1.8%. The binarization threshold was set at 50% of maximum activation in the S1 region under 1% isoflurane and was retained for the subsequent anesthesia levels. Lower: df/f mean normalized fluorescence shaded error bar traces from the V1 region (n=5). * corresponds to p-value < 0.05, ** corresponds to p-value < 0.01, *** corresponds to p-value < 0.001.

maximum activation of 6.2±4.3% (Fig. 4.30 d, 4th and 5th panels from left).

The quantitative assessment of the functional state was done with BPD during spontaneous activity and hind paw stimulation recordings. Left hind paw stimulation during low isoflurane resulted in activation of the right S1 hind limb area (Fig. 4.30 d upper row, first 2 panels from left), with activation intensity of 6.3±2.81% Δf/f (Fig. 4.30 d lower row, first 2 panels from left) and during 1.8% isoflurane recordings, responses were global Δf/f (Fig. 4.30 d upper row, 4th and 5th panels from left) with maximum activation of 6.2±4.3% (Fig. 4.30 d lower row, 4th and 5th panels from left). Stimulations in high anesthesia result in the initiation of slow cortical waves which have a stereotypical character and usually encompass the whole cortex.

Using BPD it was possible to differentiate between spontaneous activity isoflurane 1% vs. spontaneous activity isoflurane 1.2% (31.2±6.7 vs 21, p=0.0015), hind paw stimulation 1%

isoflurane vs. hind paw stimulation 1.4% isoflurane (26.5±4 vs. 13.3±2.5, p=0.0002), 1.2% isoflurane hind paw vs. 1.4% isoflurane hind paw (22.1±6.4 vs. 13.13±2.5, p=0.02). There were no statistically significant differences in BPD values between spontaneous activity and hind paw stimulation recordings at the same isoflurane level.

BPD seems to represent a robust measure of functional network segregation regardless of brain stimulation. To prove this, linear regression analysis was carried out between BPD values for spontaneous activity and hind paw recordings (spontaneous activity was always acquired before stimulated activity for every concentration of isoflurane). BPD values for spontaneous activity had a moderate explanatory power relative to BPD hind paw stimulation values with a slope=0.62, R squared = 0.58, F=31.85, and p<0.0001(Fig. 4.30 b).

4.5.2 Visual stimulation

Five-minute spontaneous activity recordings were followed by five-minute recordings of stimulated brain activity in each isoflurane concentration. 50 ms white light pulses with an amplitude of 0.5 mW were delivered every 10 seconds resulting in 30 stimulations per five-minute recording.

Thirty, 10-second intervals after stimulation were averaged and the resulting movies show the cortical representations of visual stimuli. During 1% isoflurane, left visual stimulation produced primary activation in the primary visual area (V1) with a peak activation between 0.6-1.5 seconds after stimulation (Fig. 4.31 c). Less pronounced activation in this first phase was observed in both parasagittal regions as well as the somatosensory cortices. After left visual stimulation, activation was strongest in the contralateral hemisphere although strong increases in GCaMP6s fluorescence were also observed in the ipsilateral V1 cortex. After 1.8 seconds, activity in the V1 subdued and gave way to more prominent activity in the associative areas bordering the V1 region in the somatosensory cortices. In comparison to hind paw stimulation, visual stimulation showed significant activation of the bordering associative areas early on indicating different dynamics of information integration.

In contrast to the elaborate patterns of activation described during 1% isoflurane, during surgical-level anesthesia with isoflurane, activation levels exceed 10% $\Delta f/f$ in large parts of the cortex (Fig. 4.31 d). At 0.3 seconds after stimulation, the strongest activation encompassed the visual cortices. After this, high levels of global activation take over most of the cortex at 0.6 seconds and last till about 1.5 seconds after stimulation. This temporal pattern suggests that activation events are propagating across the cortex from a point of origin situated in the somatosensory projection areas to eventually involve the whole cortex. Different from hind paw stimulation, between 2.1 and 2.7 seconds, strong activation persisted in the V1 area contralateral to the stimulation.

Left retina stimulation during 1% iso. resulted in activation of right visual areas (Fig. 4.32 d upper row, first 2 panels from left) with a magnitude of activation of 7.2±2.36% (Fig. 4.32 d lower row, first 2 panels from left) while in 1.8% anesthesia, cortical responses were global (Fig. 4.32 d upper row, 4th and 5th panels from left) with maximum activation of 18.1±8.9% (Fig. 4.32 d lower row, first 2 panels from left).

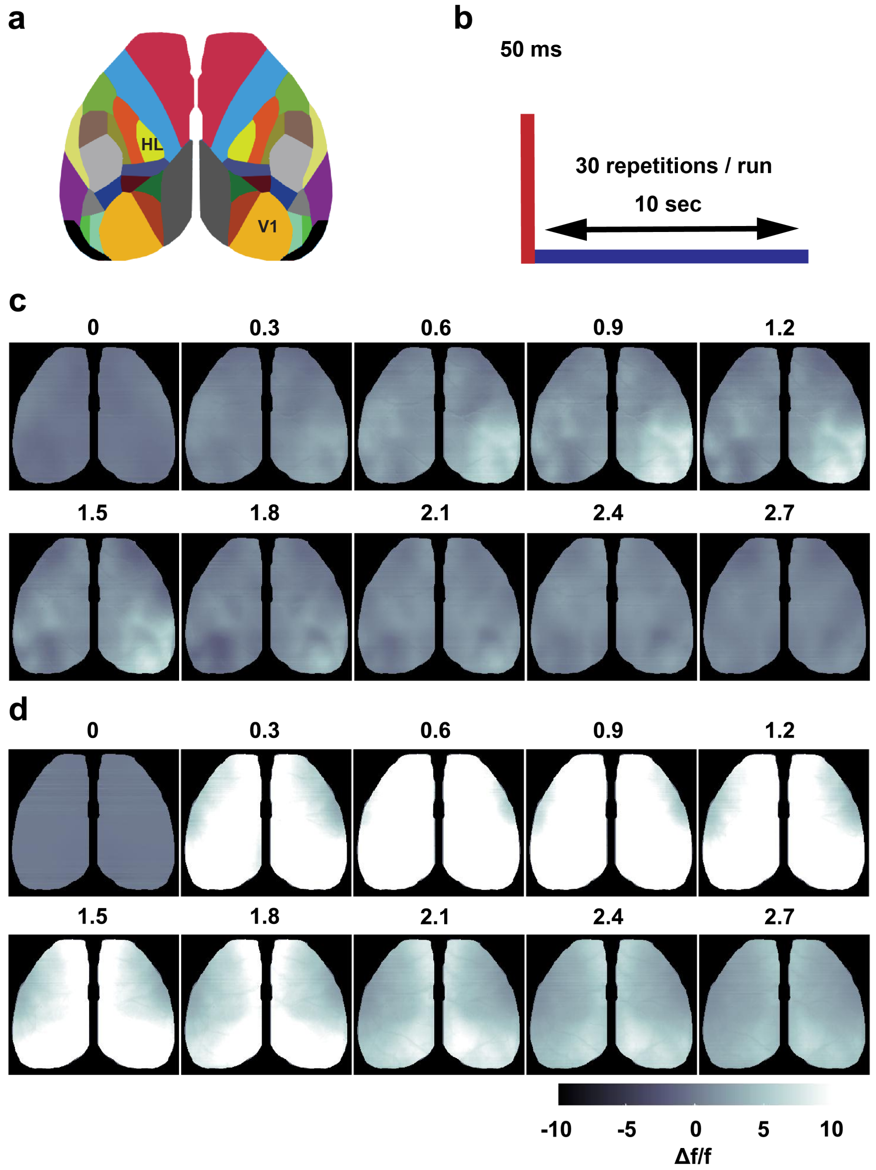

Figure 4.31: Spatio-temporal responses to visual stimulation under 1% and 1,8% isoflurane. a, Brain region map HL denotes the hind limb projection areas, and the primary visual areas are marked with V1. **b,** 30 stimulations with a duration of 50 ms each were averaged and assessed for cortical activation patterns. **c,** Imaging time-series form an average of 29 visual stimulations during 1% iso. **d,** Imaging time-series form an average of 29 visual stimulations during 1.8% iso. The time index in sec. is indicated above the brain activity maps.

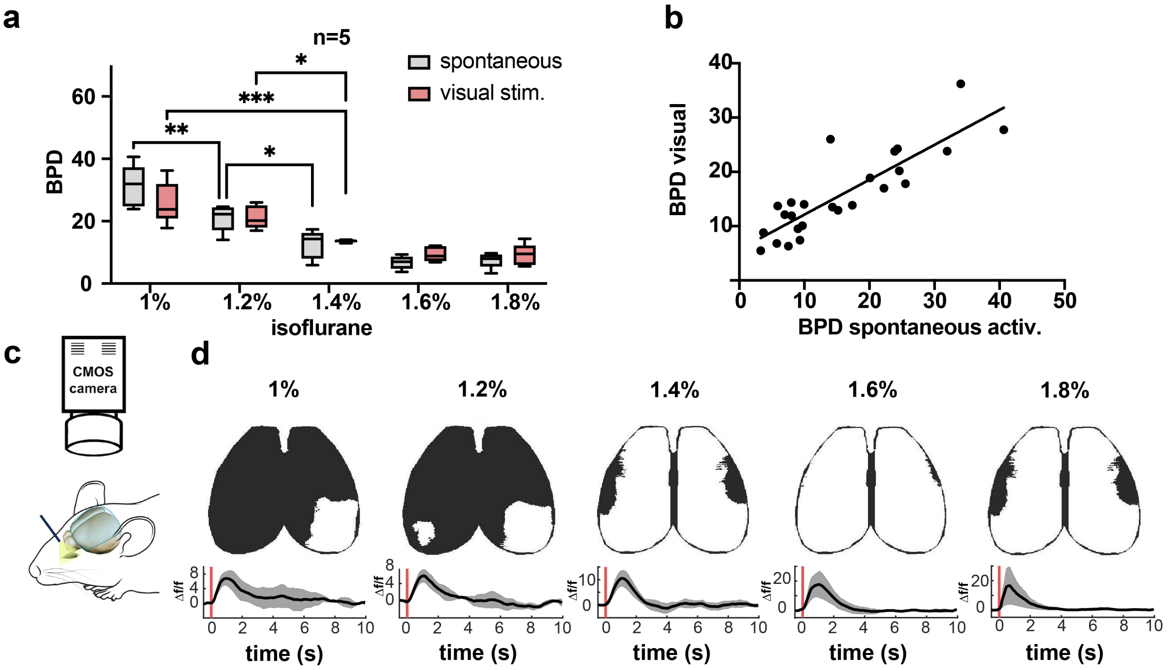

Figure 4.32: Cortical responses to stimulation of the left retina decrease in complexity with increasing anesthesia. **a,** Changes in brain pattern dimensionality (BPD) as a response to iso. concentration and left visual stimulation n=5. Two-way ANOVA repeated measurements: 1% iso. resting-state vs. 1.2% iso. resting-state p=0.0025; 1.2% iso. resting-state vs. 1.4% iso. resting-state p=0.01; 1% iso. visual vs 1.4% iso. visual p=0.0003; 1.2% iso. visual vs. 1.4% iso. visual p=<0.02. **b,** Linear regression BPD resting-state vs. BPD hind paw stimulation, slope=0.62, R squared = 0.73, F=62.38, p<0.0001. **c,** Visual stimulation: white light was delivered in 50 ms long pulses every 10 sec. resulting in 30 stimulations per imaging run. **d,** Upper: binarized response 1 s. after visual stimulation for isoflurane 1%, 1.2%, 1.4%, 1.6% and 1.8%. The binarization threshold was set at 50% of maximum activation in the V1 region under 1% isoflurane and was retained for the subsequent anesthesia levels. Lower: df/f mean normalized fluorescence shaded error bar traces from the V1 region (n=5). * corresponds to p-value < 0.05, ** corresponds to p-value < 0.01, *** corresponds to p-value < 0.001.

Similar to the hind paw experiment, BPD did not change significantly as a function of brain stimulation but, the effective dimensionality of imaging data was significantly different between anesthesia levels. It was not possible to differentiate between spontaneous activity activity isoflurane 1% vs. isoflurane 1.2% (31.2±6.7 vs 21, p=0.0015) and isoflurane 1.2% vs. isoflurane 1.4% (21±4.3 vs 12.5±4.5, p=0.01). BPD for visual stimulations was significantly different between isoflurane 1% vs. stimulation isoflurane 1.4% (25.8±6.7 vs. 13.6±0.4 p<0.0001) and isoflurane 1.2% vs. stimulation isoflurane 1.4% (21.25±3.7 vs. 13.6±0.4 p<0.0001)(Fig. 4.32 a).

Linear regression analysis was carried out to establish the relationship between BPD values for spontaneous activity and hind paw recordings. BPD spontaneous activity values have a moderate explanatory power relative to BPD hind paw stimulation values(slope=0.62, R squared = 0.58, F=31.85, p<0.0001)(Fig. 4.32 b).

4.5.3 Topological features of brain responses to stimulation

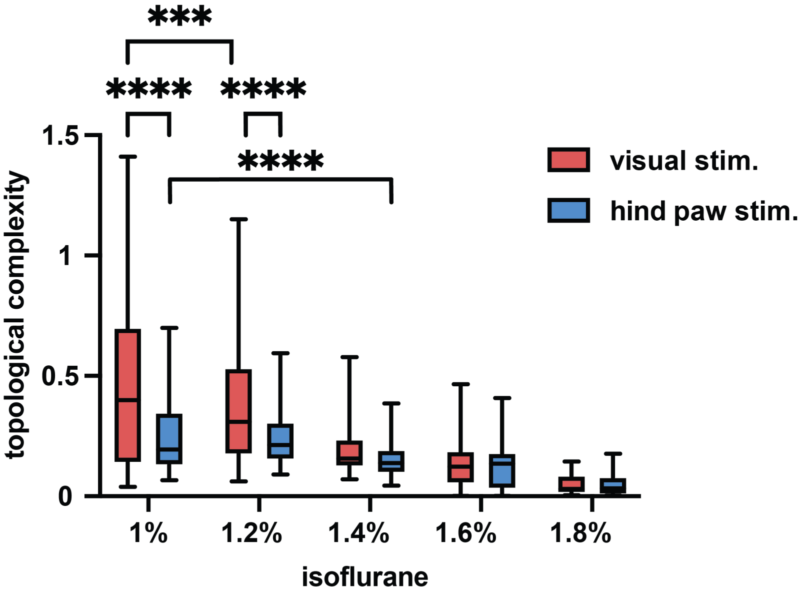

Figure 4.33: Topological features of visual and somatosensory stimulation depend on the functional state of brain networks. topological complexity was computed as explained in the material and methods section for experimental runs with somatosensory or visual stimulation for increasing concentrations of isoflurane. Two-way ANOVA repeated measurements (n=145 stimulations visual, n=145 stimulations hind paw): visual stim. 1% iso. vs. hind paw stim. 1.2% iso. p<0.0001; 1.2% visual stim. iso. vs. hind paw stim. 1.2% iso. p=<0.0001; visual stim. 1% iso. visual stim. vs. 1.2% iso. hind paw p=0,0004; hind paw stim. 1% iso. hind paw stim. vs. 1.4% iso. hind paw p<0,0001. *** corresponds to p-value < 0.001, **** corresponds to p-value < 0.0001.

As described above, inspection revealed that visual and hind paw stimulations under low concentrations of isoflurane produced more localized responses while the same stimuli under high concentrations of isoflurane gave rise to stereotypical waves of brain activation.

Topological features, i.e., features assessing the extrema of the response function, from hind paw and visually stimulated recordings can be used to quantify these effects. Imaging data were represented as cubical complexes to capture topological features, measuring the prominence, of all obtained features to infer which datasets contained patterns of activation that are expressed over the largest range of spatial scales [303].

Topological complexity was calculated for the first three seconds after stimulation, a total of 30 stimulations for every subject and every isoflurane concentration were included in the analysis. The total persistence, a summary statistic quantifying the overall topological activity of recordings, was found to be inversely proportional to the concentration of iso. During brain state transitions from the persistent state to the slow-wave state, no sharp changes in the topological features of the cortical responses to stimulation were observed, but rather gradual transitions.

Topological complexity was found to be inversely proportional to the concentration of iso. While the visually elicited activation patterns show significantly higher topological complexity for low iso. concentrations of 1% and 1.2% , no stimulus-selective difference were detected for higher iso. concentrations, for which the measure showed a gradual decrease (Two-way ANOVA with main effect of iso. conc. (F=154.7, p<0.0001), stimulation type (F=58.6, p<0.0001) and a significant interaction term (F=11.8, p<0.0001) (Fig. 4.33).

For visually stimulated recordings, total persistence was significantly different between iso. 1% and iso. 1.2% (p=0.0004) and for hind paw stimulation, total persistence was significantly different between iso. 1% and iso. 1.4% (p<0.0001) (Fig. 4.33).

4.5.4 Data-driven differentiation between recordings with visual and hind paw stimulation

Next, LEiDA was used to differentiate between recordings with hind paw and visual stimulations. The analysis was done using only recordings under 1% isoflurane since this condition contained rich and spatially distinct activation patterns after hind paw and visual stimulations. The first 3 functional connectivity motifs did not differ significantly between the datasets. These motifs were very useful for differentiating between spontaneous activity under the different pharmacological conditions which would suggest that these motifs are sensitive to global changes in neuronal network functional parameters.

Statistically significant differences were found in two FC motifs that exhibited anticorrelations between the somatosensory and visual cortices (Fig. 4.33 c, 6th panel from the left and Fig. 4.33 d, panels 5 and 6 from the left). The probability of FC motif number 6 allowed the differentiation between hind paw stimulation, 0.04±0.01, and visual stimulation, 0.01±0.01, p=0.02. The lifetime of FC motif 5 enables the differentiation between hind paw stimulation, 0.04±0.01, and visual stimulation, 0.01±0.01, p=0.02, Likewise, for motif 6 means for paw stimulation of 0.25±0.07 and visual stimulation 0.16±0.06 were significantly different with a p-value of 0.0035.

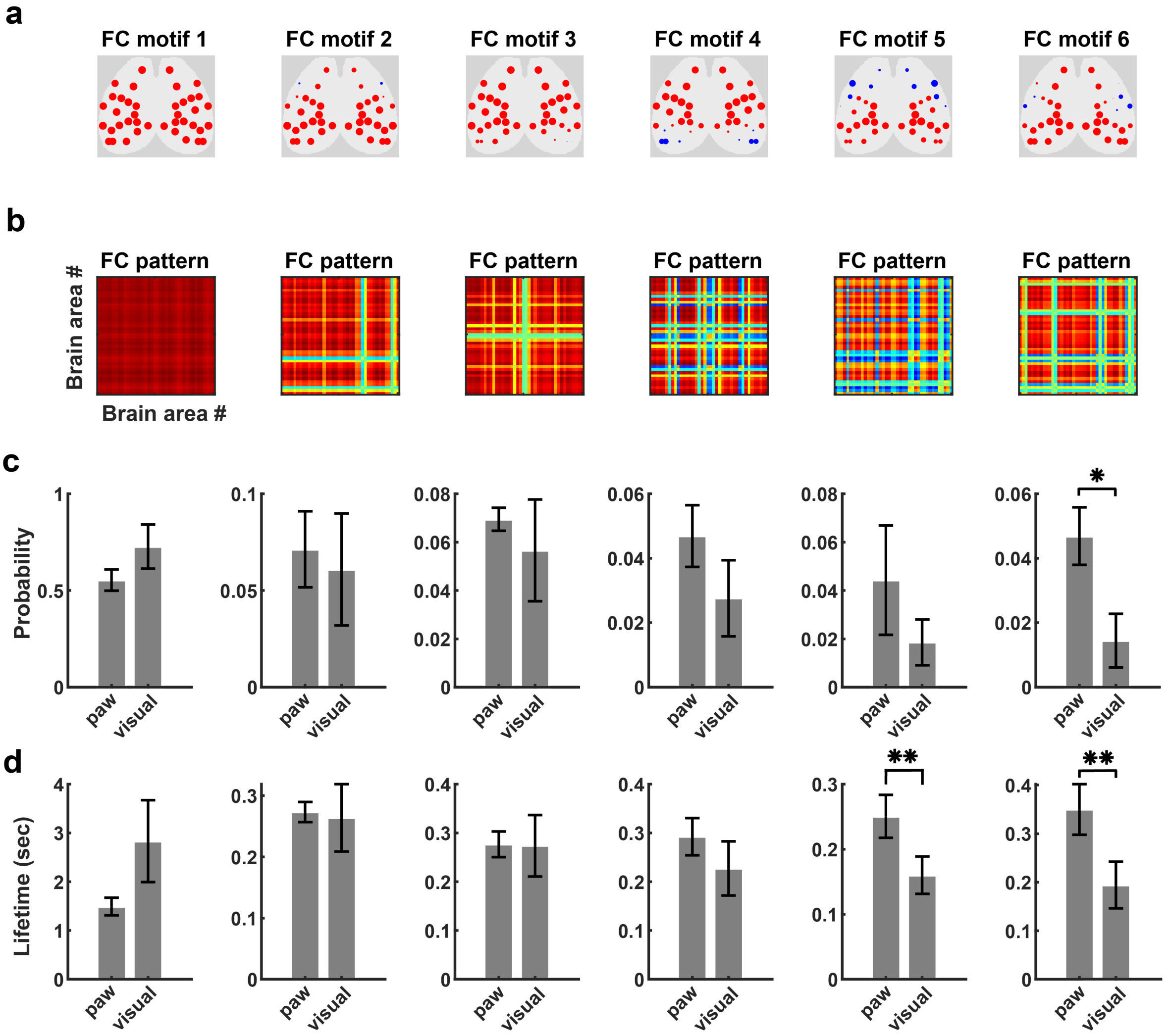

Figure 4.34: Differentiation of hind paw from visual stimulation with LEiDA N=5 visual, n=5 hind paw subjects under 1% iso. were included in the analysis. **a,** Spatial distribution of functional connectivity motifs 1 to 6. **b,** Functional connectivity (FC) matrices corresponding to the FC motifs in a. **c,** Probability of occurrence of the functional connectivity motifs. Motif 6, permutation htest, paw vs. visual p=0.02. **d,** Lifetime of the functional connectivity motifs. Motif 5, permutation htest, paw vs. visual p=0.0034. Motif 6, permutation htest, paw vs. visual p=0.0035. * corresponds to p-value < 0.05 , ** corresponds to p-value < 0.01.

4.6 Optogenetic probing of effective connectivity in the cortex

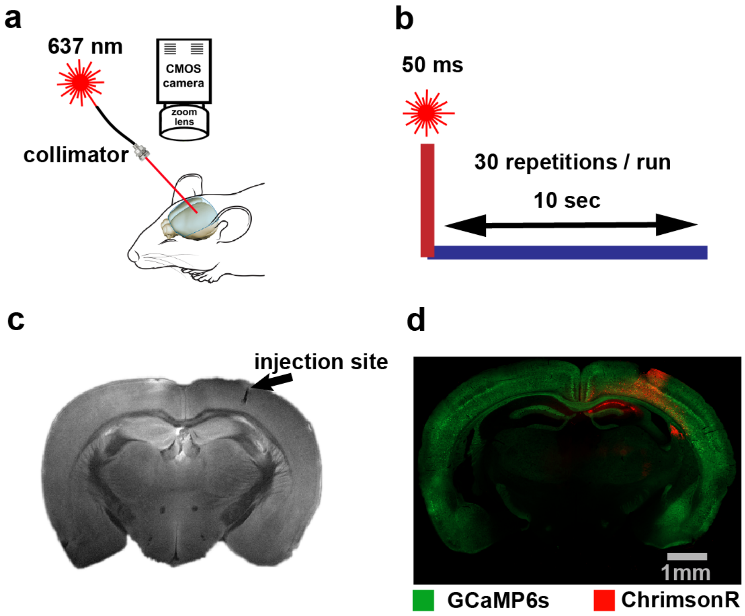

Figure 4.35: Experimental setup for measuring effective connectivity with optogenetic stimulations and GCaMP6s readout of neuronal activity. **a,** Schematic of the optogenetic stimulation setup: light from a fiber-coupled 637 nm laser was collimated to achieve optogenetic stimulation and artifact-free, unobstructed GCaMP6s recordings upon 460 nm illumination. **b,** 10-15 mW/mm^2 laser stimulation was delivered for 50 ms every 10 sec. resulting in 30 stimulations per imaging run. **c,** T2 weighted coronal MRI indicating the viral injection site in the S1 cortex. **d,** A coronal mouse brain section was immunostained with an anti-Flag-Cy5 antibody to reveal ChrimsonR positive neurons in red while GCaMP6s positive neurons were imaged using 488 nm illumination and are shown in green.

When assessing functional connectivity, correlations between brain regions may arise as a consequence of stimulus-locked activity that is driven by a common input or could be elicited by deeper structures that promote high levels of synchronization. Brain responses to stimulation may be influenced by the sensitivity of receptors that are outside of the cortical network and synaptic relays which could modulate cortical responses.

For these reasons, integration in distributed cortical networks is better characterized by effective connectivity. Effective connectivity denotes the capacity of a set of neuronal groups to causally affect the activity of other neuronal groups within the wider network [14,17] consequently one way of studying effective connectivity is to directly stimulate key areas of the cortical network and quantify the responses to this direct stimulation.

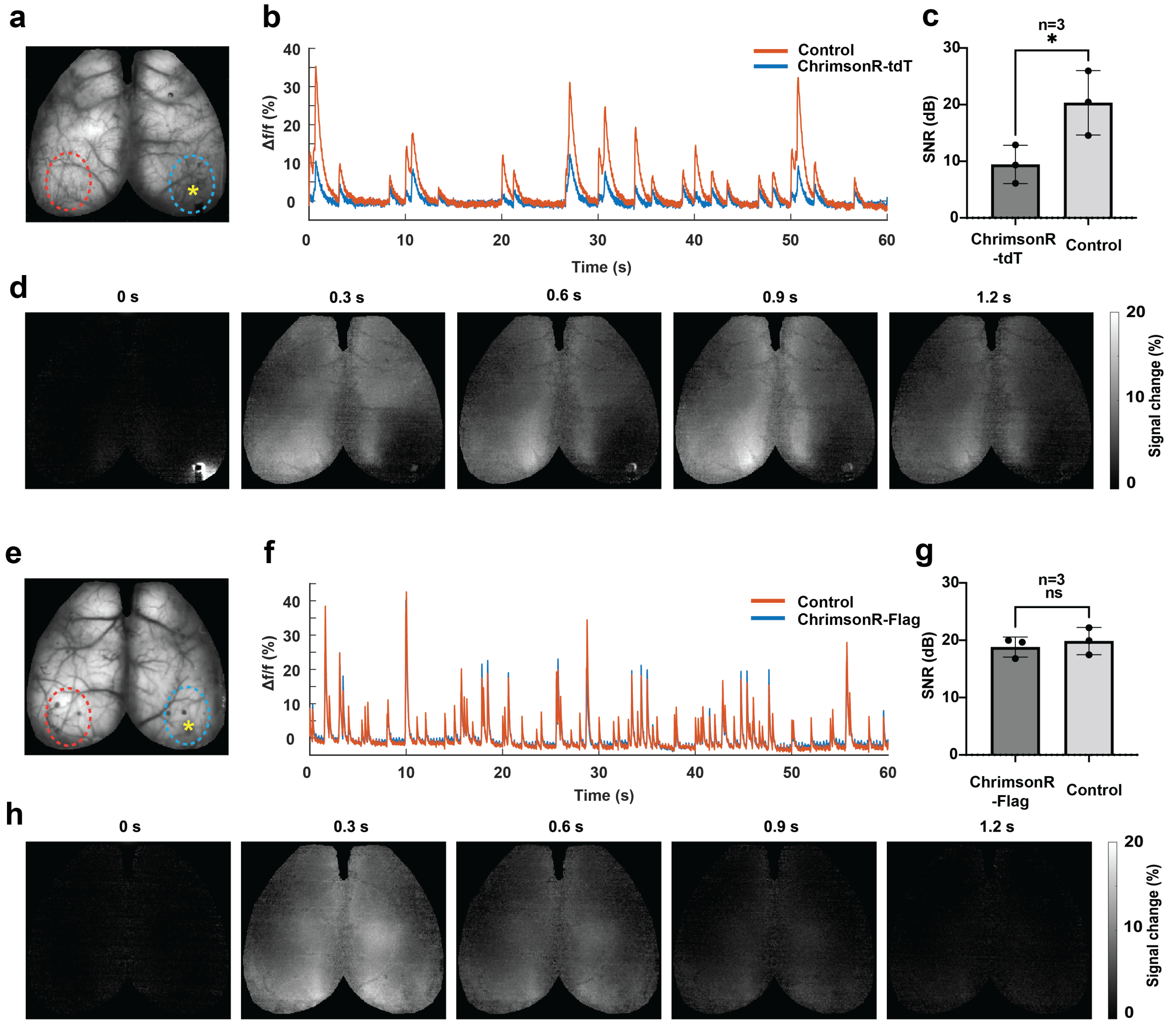

Figure 4.36: Optimization of ChrimsonR expression for wide-field fluorescence imaging of GCaMP6s in transgenic mice. **a,** Wide-field image in a mouse injected with AAV5-hSyn-ChrimsonR-tdT in the right V1 region (blue dashed oval) yellow star indicates the injection spot. The contralateral V1 region is marked with a red dashed oval. **b,** Time trace extracted from the ChrimsonR-tdT V1 area in blue (integration of blue ROI in panel a) and the control area in red (integration of red ROI in panel a). **c,** Signal-to-noise ratio (decibel - dB) between ChrimsonR-tdT injection and control side comparison in 3 animals T-test, p=0.046 (* corresponds to p-value < 0.05) . **d,** Montage of 30 averaged slow waves showing signal dropout in the right V1 region after injection with AAV5-hSyn-ChrimsonR-tdT. **e,** Wide-field image in a mouse injected with AAV5-hSyn-ChrimsonR-Flag in the right V1 region (blue dashed oval) yellow star indicates the injection spot. The contralateral V1 region is marked with a red dashed oval. **f,** Time trace extracted from the ChrimsonR-Flag V1 area in blue (integration of blue ROI in panel e) and the control area in red (integration of red ROI in panel e). **g,** Signal-to-noise ratio (decibel - dB) between ChrimsonR-Flag injection and control side comparison in 3 animals T-test, p>0.05. **h,** Montage of 30 averaged slow waves showing no signal dropout in the right V1 region after injection with AAV5-hSyn-ChrimsonR-Flag.

For the effective connectivity experiments, the optogenetic actuator ChrimsonR was expressed either in S1 (5 animals) or V1 (5 animals) regions in transgenic mice expressing GCaMP6s in cortical pyramidal neurons. ChrimsonR is a transmembrane ion channel that is responsive to red light thus, stimulation was carried out with light from a fiber-coupled 637 nm laser. Laser light was collimated in order to maintain the geometric properties of the laser beam over a distance of at least 15 cm. In this way, optogenetic stimulation was done without obstructing the field of view of the camera (Fig. 4.35 a). For optogenetic stimulation, 10 mW laser pulses lasting 50 ms were delivered every 10 seconds resulting in 30 stimulations per five-minute recording (Fig. 4.35 b).

Somatosensory (S1) and visual areas (V1) were stimulated with the laser to match our natural stimulation experiments. To stimulate cortical neurons with a red laser, ChrimsonR has to be virally expressed. For this purpose, an adeno-associated virus (AAV) was injected into the cortex and imaging experiments were carried out 4 weeks after injection (Fig. 4.35 c and d). The commercially available AAV5-hSyn-ChrimsonR-tdT construct was initially used for ChrimsonR expression. Upon inspection of the recorded cortical responses, a GCaMP6s fluorescence signal dropout was observed in the cortical areas where ChrimsonR-tdT was coexpressed (Fig. 4.36 d).

4.6.1 Optimization of ChrimsonR expression for wide-field imaging

To investigate the cause for the lower fluorescence signals, the signal-to-noise ratio (SNR) was measured in 3 mice that were injected with AAV5-hSyn-ChrimsonR-tdT in the visual cortex. SNR values on the side expressing ChrimsonR-tdT were 50% lower in comparison to SNR values on the contralateral side. The ChrimsonR-tdT ROIs had a mean SNR of 9.4±3.3 while the contralateral side had a mean SNR value of 20.33±5.6 and this difference was statistically significant with a p=0.04. Inspection of the brain ex vivo revealed that tdTomato was strongly expressed around the injection site. Lower SNR values could be caused by the expression of tdTomato interfering with GCaMP6s expression or green GCaMP6s emission light being absorbed by the red tdTomato fluorophore.

To test this hypothesis, a bespoke AAV that encoded ChrimsonR together with a colorless Flag tag was designed (AAV5-hSyn-ChrimsonR-Flag). The Flag-Tag is colorless and is attached to the ChrimsonR channel facing the exterior of the cell. Like this, it was possible to detect ChrimsonR expression without the need to express an additional fluorophore.

3 mice were injected with AAV5-hSyn-ChrimsonR-Flag and SNR was measured from an ROI around the injection site (V1 right) and also on the contralateral side (V1 left). SNR measurements in 3 mice, yielded values of 18.8±1.7 on the ChrimsonR-Flag side (V1 right) and 19.8 in the contralateral visual cortex (V1 left), the difference between the two means was not statistically significant. Furthermore, visual inspection did not reveal a significant signal dropout in the right V1 area in an average movie from 30 slow waves (Fig. 4.36 h).

4.6.2 Optogenetic stimulation of the somatosensory 1 region (S1)

Effective connectivity was investigated under five concentrations of isoflurane, medetomidine, and ketamine. Qualitative inspection of optogenetic stimulation results under 1% isoflurane (Fig. 4.37 a) and 1.8% isoflurane revealed that similar to natural stimulation, brain responses under low concentrations of isoflurane produced more localized patterns while in high anesthesia conditions, activations tended to be global and stereotypical.

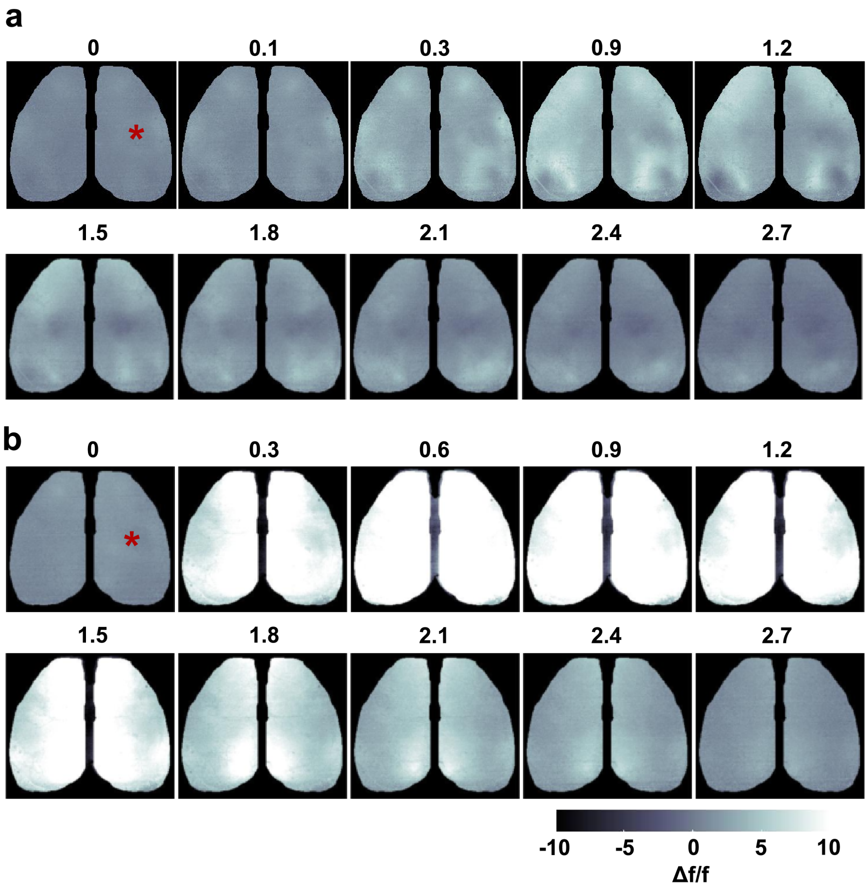

Figure 4.37: Responses to optogenetic stimulation of the right S1 area under 1% and 1.8% isoflurane. a, Imaging time-series form an average of 29 optogenetic stimulations of the S1 region during 1% iso. **b,** Imaging time-series form an average of 29 optogenetic stimulations of the S1 region during 1.8% iso. The time index in sec. is indicated above the brain activity maps.

During 1% isoflurane, stimulations produce rapid increases in fluorescence in the S1-HP region, and marked increases in activation were also observed bilaterally in the frontal motor regions, barrel cortex, and also in association areas bordering the V1 cortex. The V1 region itself did not show large fluorescence increases initially but there was later activation here beginning 1.8 sec. after stimulation. (Fig. 4.37 a).

Activation under 1.8% isoflurane led to fast parasagittal increases in fluorescence with strong activity in the retrosplenial cortex. The responses to stimulation were relatively short-lived, returning to baseline 1.5 sec after stimulation (Fig. 4.37 a).

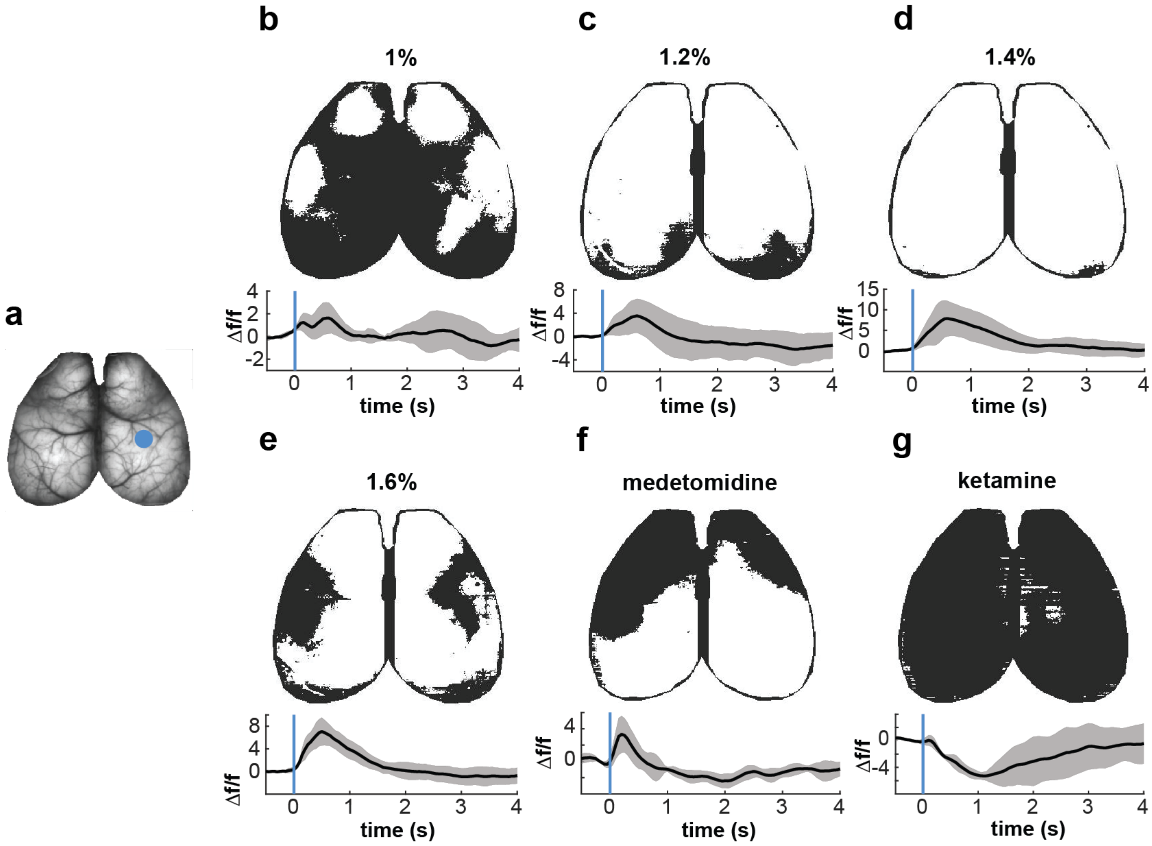

Figure 4.38: Cortical responses to S1 optogenetic stimulation a, Brain image with the stimulation site located in the right somatosensory cortex marked with a blue disc. **b-g upper,** binarized early response to S1 optogenetic stimulation for isoflurane (1%, 1.2%, 1.4%, 1.6%), medetomidine, and ketamine. **b-g lower,** df/f mean normalized fluorescence shaded error bar traces from the S1 region (n=5) The binarization threshold was set at 50% of maximum activation in the S1 region under 1% isoflurane activation and was retained for the subsequent anesthesia levels.

After optogenetic stimulation in the S1 area, GCaMP6s fluorescence increased by 2.3±0.9% under isoflurane 1% (Fig. 4.38 b), 7.27±2.3% under isoflurane 1.6% (Fig. 4.38 e) and 2.7±2.4% under medetomidine (Fig. 4.38 f). Ketamine exhibited paradoxical reactions to optogenetic stimulation, immediately after the laser pulse, GCaMP6s fluorescence decreased by 4.9±1.9% after S1 optogenetic stimulation (Fig. 4.38 g).

The level of segregation of functional brain networks was assessed using BPD for spontaneous activity and S1 optogenetically stimulated recordings. Optogenetic stimulations in the S1 region were recorded under medetomidine, ketamine, and 5 levels of isoflurane. Statistically-significant differences were found between 1% isoflurane spontaneous activity vs. 1.4% isoflurane spontaneous activity (22.4±6.4 vs. 11.3±2.9, p=0.009), 1% isoflurane spontaneous activity vs. medetomidine spontaneous activity (22.4±6.4 vs. 32.3±3, p=0.02), medetomidine spontaneous activity and ketamine spontaneous activity (32.3±3 vs. 19.7±6.9, p=0.008), 1% isoflurane optogenetic stimulation vs. 1.4% isoflurane optogenetic stimulation (23±6 vs. 11.5±3.7, p=0.007). It was not possible to statistically differentiate between stimulated and spontaneous activity based on BPD within the same pharmacological condition (Fig. 4.39 a).

BPD represents a global measure of functional network segregation and is not directly assessing the responses to optogenetic activation. PCI-ST (Perturbation Complexity Index - State Transitions) has been specifically designed to measure the complexity of evoked cortical responses. For these measurements, data from 30 stimulations within a recording under each pharmacological condition were averaged and the resulting average stimulation was used to calculate PCI-ST. The complexity of effective connectivity patterns after S1 optogenetic stimulation allowed the differentiation of isoflurane 1% vs. isoflurane 1.6% (15.11±7.1 vs. 4.83±1.8, p=0.0018), isoflurane 1.2% vs. medetomidine (8.2±4.6 vs. 19.3±5.3, p=0.015) and medetomidine vs. ketamine (19.3±5.3 vs. 7.9±1.9, p=0.018) (Fig. 4.39 b).

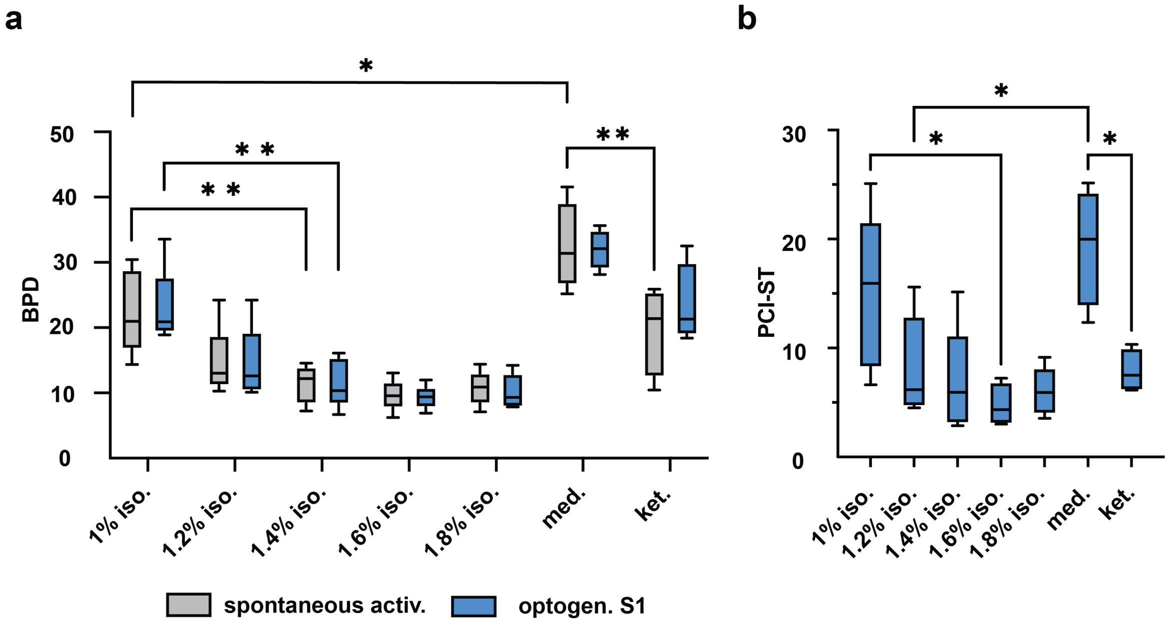

Figure 4.39: Quantitative assessment of cortical responses to S1 optogenetic stimulation **a,** Changes in brain pattern dimensionality (BPD) as a response to anesthesia and S1 optogenetic stimulation. Two-way ANOVA repeated measurements / Tukey's multiple comparisons test (n=5 iso., n=4med., n=4 ket): 1% iso. no stim vs 1.4% iso. no stim p= 0.009; 1% iso. optogen. S1 vs 1.4% iso. optogen. S1 p= 0.007; medetomidine no stim. vs 1.2% iso. no stim p=<0,0001; medetomidine no stim. vs ketamine no stim p= 0.008. **b,** Complexity of brain responses to S1 optogenetic stimulation (PCI-ST), ordinary one-way ANOVA repeated measurements / Tukey's multiple comparisons test (n=5 iso., n=4 med., n=4 ket.): 1% iso. vs. 1.6% iso. p=0.0018; 1.2% iso. vs medetomidine p=0.0015; medetomidine vs. ketamine p=0.018. * - p-value < 0.05, ** - p-value < 0.01.

BPD and PCI measurements did not reveal phase transitions in functional network properties as a response to changes in isoflurane concentration. The values of these indices gradually decreased from 1% isoflurane to 1.6% isoflurane and plateaued at low values during 1.6% and 1.8% anesthesia.

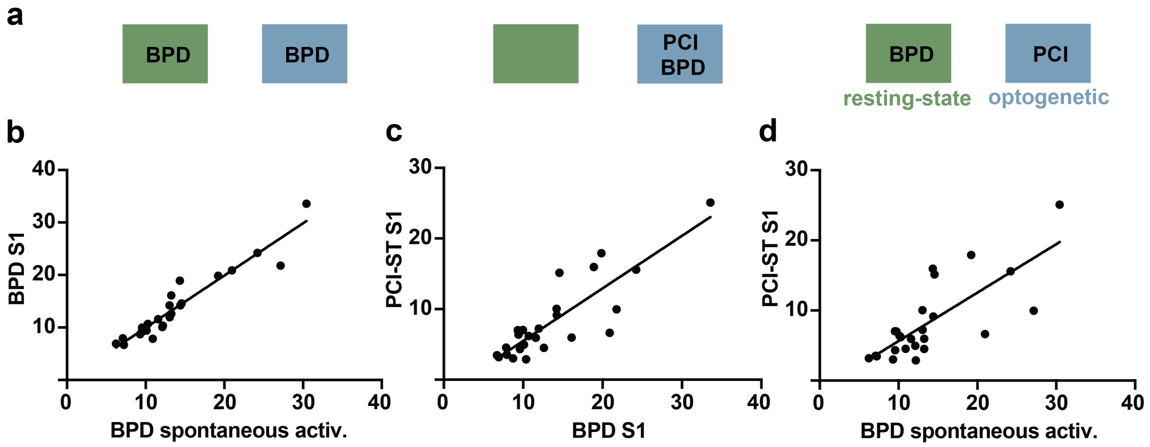

Figure 4.40: S1 effective connectivity depends on the functional segregation of spontaneous activity networks a, We calculated BPD for spontaneous activity and optogenetic runs and PCI for optogenetic runs (n=5 subj. x 5 iso. levels). b, we performed linear regression to investigate the relationship between BPD spontaneous activity and BPD optogenetic stimulation (panel **b,**); BPD optogenetic stimulation and PCI optogenetic stimulation (panel **c,**); BPD spontaneous activity and PCI optogenetic stimulation (panel **d,**);

PCI-ST describes the complexity of brain responses to optogenetic stimulation and BPD measures the functional segregation level. The relationship between the level of segregation from spontaneous activity recordings, measured by BPD, and the complexity of effective connectivity patterns, measured by PCI-ST was investigated next. For this, only isoflurane data acquired under the five different concentrations were considered.

First, it was assessed whether the optogenetic stimulation had an impact on the level of segregation of functional networks. Linear regression analysis of the spontaneous activity BPD and optogenetic stimulation BPD revealed a very strong linear relationship between these two variables, R squared = 0.90, F=229.3, $p<0.0001$ (Fig. 4.40 a, first from left). These results suggest that BPD can be used to accurately assess the functional state of cortical networks from spontaneous activity as well as task processing imaging datasets (Fig. 4.40 b).

Next, the relationship between the level of segregation of functional networks (BPD) and the complexity of effective connectivity responses within the same run (PCI-ST) was studied (Fig. 4.40 a, second from left). Moderate levels of dependence were found between these two variables for the S1 cohort, R squared = 0.73, F=63.4, $p<0.0001$ (Fig. 4.40 c).

Spontaneous recordings were always acquired before optogenetically stimulated runs.

Finally, it was tested whether functional segregation levels of spontaneous activity measured by BPD are predictive of the complexity of effective connectivity responses measured by PCI-ST in the imaging run which immediately followed the spontaneous activity acquisition (Fig. 4.40 a, third from left). Also, in this case, spontaneous activity BPD had moderate explanatory power for PCI-ST values calculated after optogenetic stimulation for the S1, R squared = 0.57, F=31.6, p<0.0001 (Fig. 4.40 d).

4.6.3 Optogenetic stimulation of the primary visual area (V1)

The effective connectivity of the primary visual cortex (V1) was investigated under five concentrations of isoflurane, medetomidine, and ketamine. Qualitative inspection of optogenetic stimulation results under 1% isoflurane and 1.8% isoflurane showed that brain responses to V1 stimulation under low concentrations of isoflurane produced more localized patterns while in high anesthesia conditions, activations tended to be global and stereotypical(Fig. 4.41).

In 1% isoflurane stimulation produced rapid increases in fluorescence in the V1 region bilaterally but also in parasagittal areas, the S1, and the barrel cortex. Compared to S1 optogenetic stimulation, initial responses after V1 stimulation seemed to be less widespread. Activation was also observed in the associative areas bordering the V1 area (Fig. 4.41 a).

Under 1.8% isoflurane, very fast parasagittal increases in fluorescence with strong activity in the retrosplenial cortex were observed. The responses to stimulation were relatively short-lived, returning to baseline 1.5 sec after stimulation (Fig. 4.41 b).

The amplitude of responses after optogenetic stimulation was lower than for visual stimulations. Under 1% isoflurane, V1 responses after optogenetic stimulation amounted to 3.17±0.6 (Fig. 4.42 b), during 1.6% isoflurane signals increased by 8.72±5.3% (Fig. 4.42 e), and an increase of 7.2±3.9% was observed under medetomidine (Fig. 4.42 f). Ketamine exhibited a paradoxical reaction to optogenetic stimulation in the V1 region with an immediate decrease in GCaMP6s fluorescence of 5.01±3.8%.

The level of segregation of functional brain networks was assessed by BPD for spontaneous activity and V1 optogenetically stimulated imaging runs. For the V1 cohort, BPD allowed the differentiation of 1% isoflurane resting state from 1.6% isoflurane resting state (21.99±6.2 vs. 8.5±4.1, p=0.04), medetomidine spontaneous activity vs. 1.2% isoflurane spontaneous activity (34.87±11.1 vs. 18.3±6.8, p=0.006), medetomidine resting state and ketamine resting state (34.87±11.1 vs. 19.7±4.5, p=0.02), 1% isoflurane optogenetic stimulation from 1.4% isoflurane optogenetic stimulation (26.09±8.8 vs. 11.5±2.2, p=0.02), and medetomidine optogenetic vs. ketamine optogenetic (31.17±6.9 vs. 17.1±2, p=0.04)(Fig.

4.43, a).

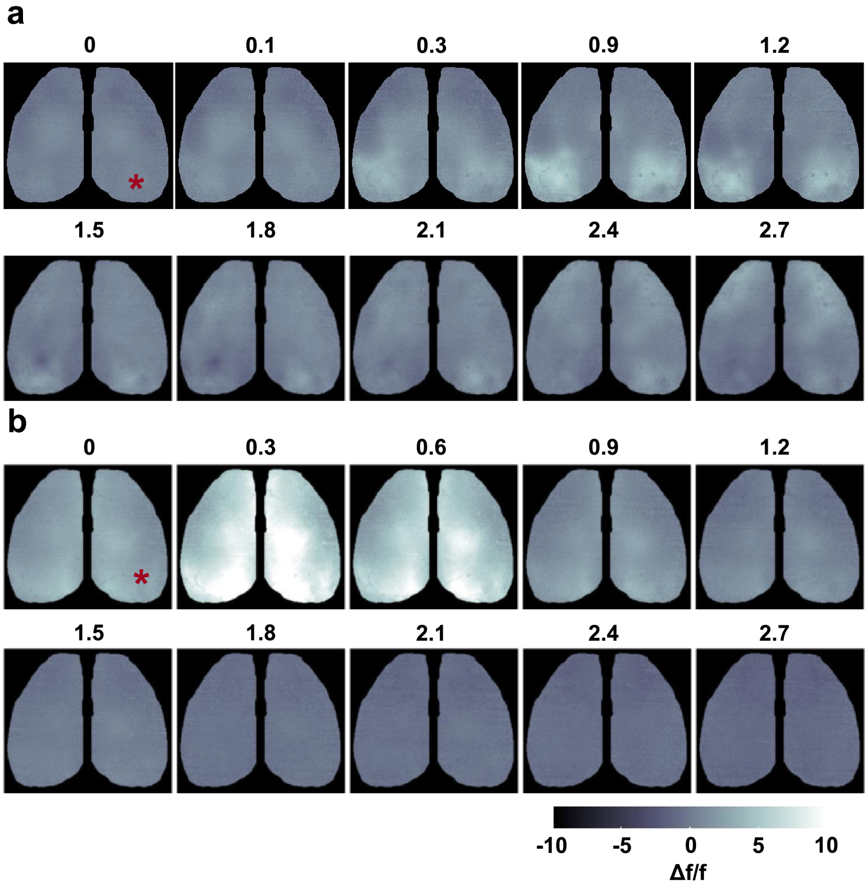

Figure 4.41: Responses to optogenetic stimulation of the right V1 area are under 1% and 1.8% isoflurane. **a,** Imaging time-series form an average of 29 optogenetic stimulations of the V1 region during 1% iso. **b,** Imaging time-series form an average of 29 optogenetic stimulations of the V1 region during 1.8% iso. The time index in sec. is indicated above the brain activity maps

It was not possible to differentiate between stimulated and spontaneous activity based on BPD within the same pharmacological condition.

The complexity of effective connectivity activation patterns was quantified next, by calculating the PCI-ST for the V1 cohort. PCI-ST can only be calculated for patterns that arise after direct brain stimulation, thus spontaneous brain activity cannot be evaluated in this way. After optogenetic stimulation, PCI-ST values followed a similar trend to BPD for the respective conditions. After V1 stimulation, statistically significant differences were found between isoflurane 1% vs. isoflurane 1.6% (19.29±5.3 vs. 4.83±1.7, p=0.0014), isoflurane 1.2% vs. isoflurane 1.6% (14.83±5 vs. 4.83±1.7, p=0.04) and medetomidine vs. isoflurane 1.6% (15.71±5 vs. 4.83±1.7, p=0.02) (Fig. 4.43 b).

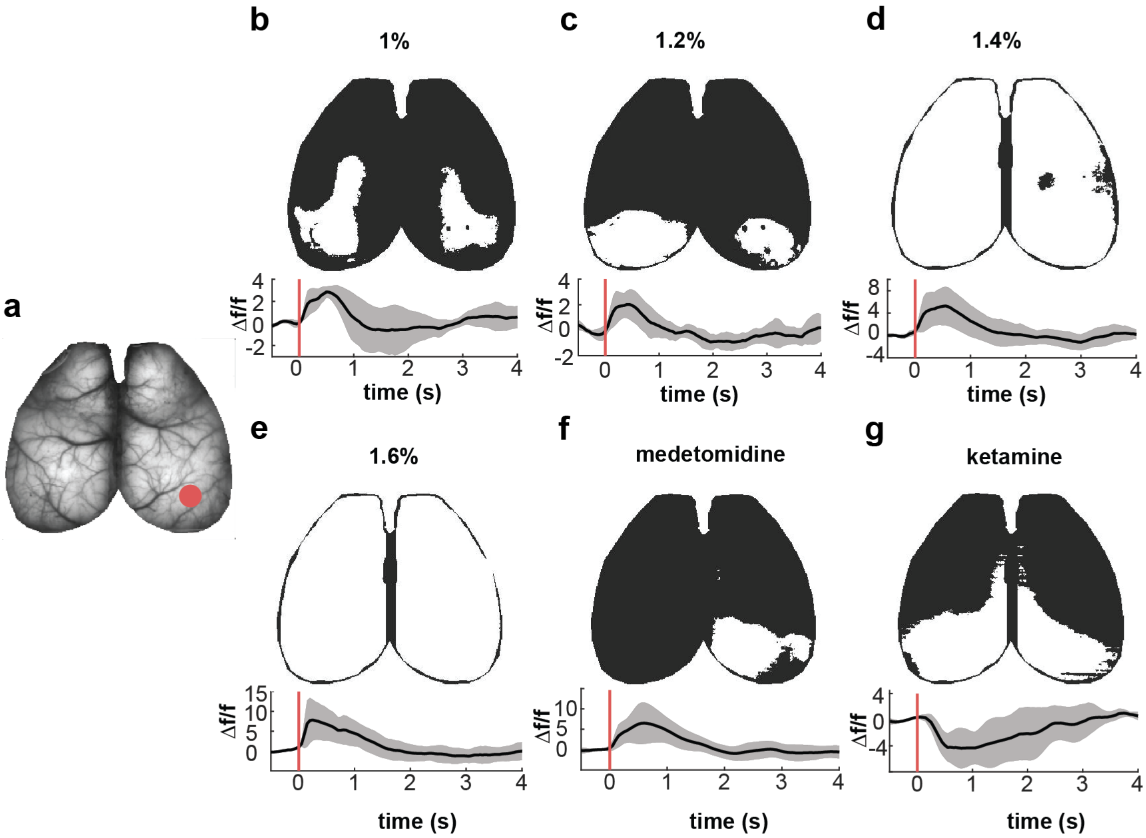

Figure 4.42: Cortical responses to V1 optogenetic stimulation. a, Brain image with the stimulation site located in the right visual cortex marked with a red disc. **b-g upper,** binarized early response to V1 optogenetic stimulation for isoflurane (1%, 1.2%, 1.4%, 1.6%), medetomidine, and ketamine. **b-g lower,** df/f mean normalized fluorescence shaded error bar traces from the V1 region (n=5) The binarization threshold was set at 50% of maximum activation in the V1 region under 1% isoflurane activation and was retained for the subsequent anesthesia levels.

BPD and PCI measurements did not reveal sudden changes in functional network properties as a response to changes in isoflurane concentration. The values of these indices followed a gradual descending trend from 1% isoflurane to 1.6% isoflurane and leveled off at low values during 1.6 and 1.8% anesthesia.

The relationship between the level of segregation of spontaneous activity networks (measured by BPD), and the complexity of effective connectivity patterns, (measured by PCI-ST) was studied next. Only isoflurane data was used for this analysis, to avid confounds.

It was tested whether V1 optogenetic stimulation had an impact on the level segregation of functional networks. For this, a linear regression analysis was performed between the BPD for spontaneous activity and the corresponding BPD of the optogenetic stimulation data (Fig. 4.44 a, first from left). Spontaneous activity A strong linear relationship was observed between these two variables, R squared = 0.85, F=136.3, p<0.0001 (Fig. 4.44 b).

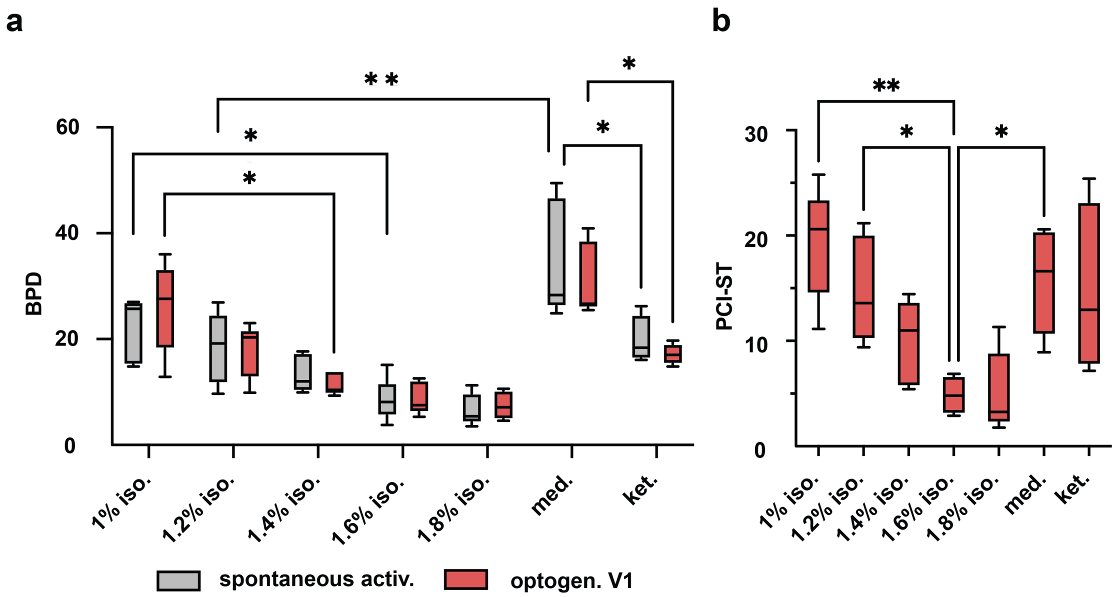

Figure 4.43: Quantitative assessment of cortical responses to V1 optogenetic stimulation. a, Changes in brain pattern dimensionality (BPD) as a response to anesthesia and V1 optogenetic stimulation. Two-way ANOVA repeated measurements / Tukey's multiple comparisons test (n=5 iso., n=4 med., n=4 ket.). 1% iso. no stim. vs. 1.6% iso. no stim. p=0.04; medetomidine no stim. vs 1.2% iso. no stim, p=0.006; 1% iso. optogenetic V1 vs 1.4% optogenetic V1 p=0.02; medetomidine no stim. vs. ketamine, no stim p=0.02; medetomidine optogenetic V1 vs ketamine optogenetic V1 p=0.02; **b,** Complexity of brain responses to V1 optogenetic stimulation (PCI-ST), ordinary one-way ANOVA repeated measurements / Tukey's multiple comparisons test (n=5 iso., n=4 med., n=4 ket.): 1% iso. vs. 1.6% iso. p=0.001; 1.2% iso. vs 1.6% iso. p=0.04; medetomidine vs. 1.6% iso. p=0.02. * corresponds to p-value < 0.05, ** corresponds to p-value < 0.01.

The relationship between the level of segregation of functional networks (BPD) and the complexity of effective connectivity responses within the same run was evaluated (Fig. 4.44 a, second from left). Moderatel strong linear dependence was found between these two variables for V1 stimulation: R squared = 0.65, F=43.6, p<0.0001 (Fig 4.44 c).

Because spontaneous activity was always acquired before stimulation runs, it was checked whether the level of segregation of spontaneous activity measured by BPD was predictive of the complexity of effective connectivity responses measured by PCI-ST (Fig. 4.44 a, third from left). It was determined that spontaneous activity BPD had moderate explanatory power for PCI-ST values calculated after optogenetic stimulation for the V1 cohort, R squared = 0.58, F=31.9, p<0.0001 (Fig. 4.44 d).

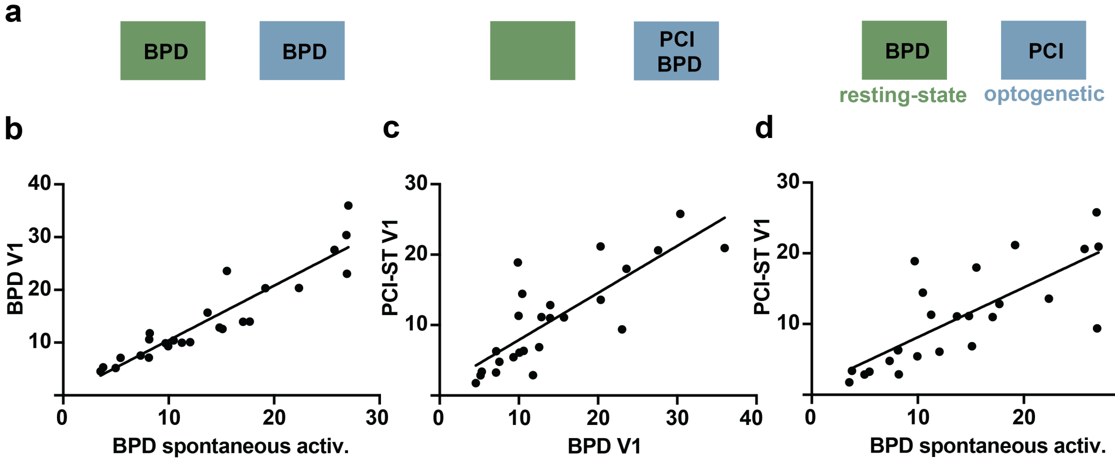

Figure 4.44: V1 effective connectivity depends on the functional segregation of spontaneous activity networks. **a,** We calculated BPD for resting-state and optogenetic runs and PCI (n=5 subj. x 5 iso. levels) for optogenetic runs, next we performed linear regression to investigate the relationship between BPD spontaneous activity and BPD optogenetic stimulation (panel **b**); BPD optogenetic stimulation and PCI optogenetic stimulation (panel **c**); BPD resting-state and PCI optogenetic stimulation (panel **d**).

4.6.4 Data-driven differentiation between recordings with V1 and S1 optogenetic stimulation

Data-driven computational techniques were applied to differentiate between optogenetic stimulations of the S1 and V1 cortices. Only recordings under 1% isoflurane were included in this analysis since in this condition different activation patterns were observed after S1 paw and V1 stimulations. For this, LEiDA and probabilistic metastable motifs were calculated and plotted in Fig. 4.45.

The first 3 functional connectivity motifs did not differ significantly between the datasets. These motifs proved most powerful when differentiating between spontaneous activity under the different pharmacological conditions(Fig. 4.28). Statistically significant differences were found in two FC motifs that exhibited bilateral anticorrelations between the somatosensory and visual cortices. The probability of FC motif number 5 allowed the differentiation between S1 stimulation (0.04±0.006) and V1 stimulation (0.02±0.01) p=0.036 (Fig.4.45 c, 5th panel from the left). The lifetime of FC motif 4 enables the differentiation between S1 stimulation (0.28±0.04) and V1 stimulation (0.19±0.04), p=0.014, likewise, for motif 5 means for S1 of 0.30±0.05 and V1 stimulation 0.17±0.06 were significantly different with a p-value of 0.0029 (Fig. 4.45 d, panels 4 and 5 from the left).

In addition to this, the 6th FC motif featured anticorrelations between the S1-HL right, S1-FL right, and S1-TR right while less pronounced anticorrelations were observed also in the S1-HL and on the left. The lifetime of this FC motif amounted to 0.28±0.08s for S1 stimulation and 0.17±0.03s for V1 stimulations, p=0.021 (Fig. 4.45 c, 6th panel from the left). This result was intriguing because the laser stimulation occurred in the S1 region of the right hemisphere and at this location, anticorrelations were observed.

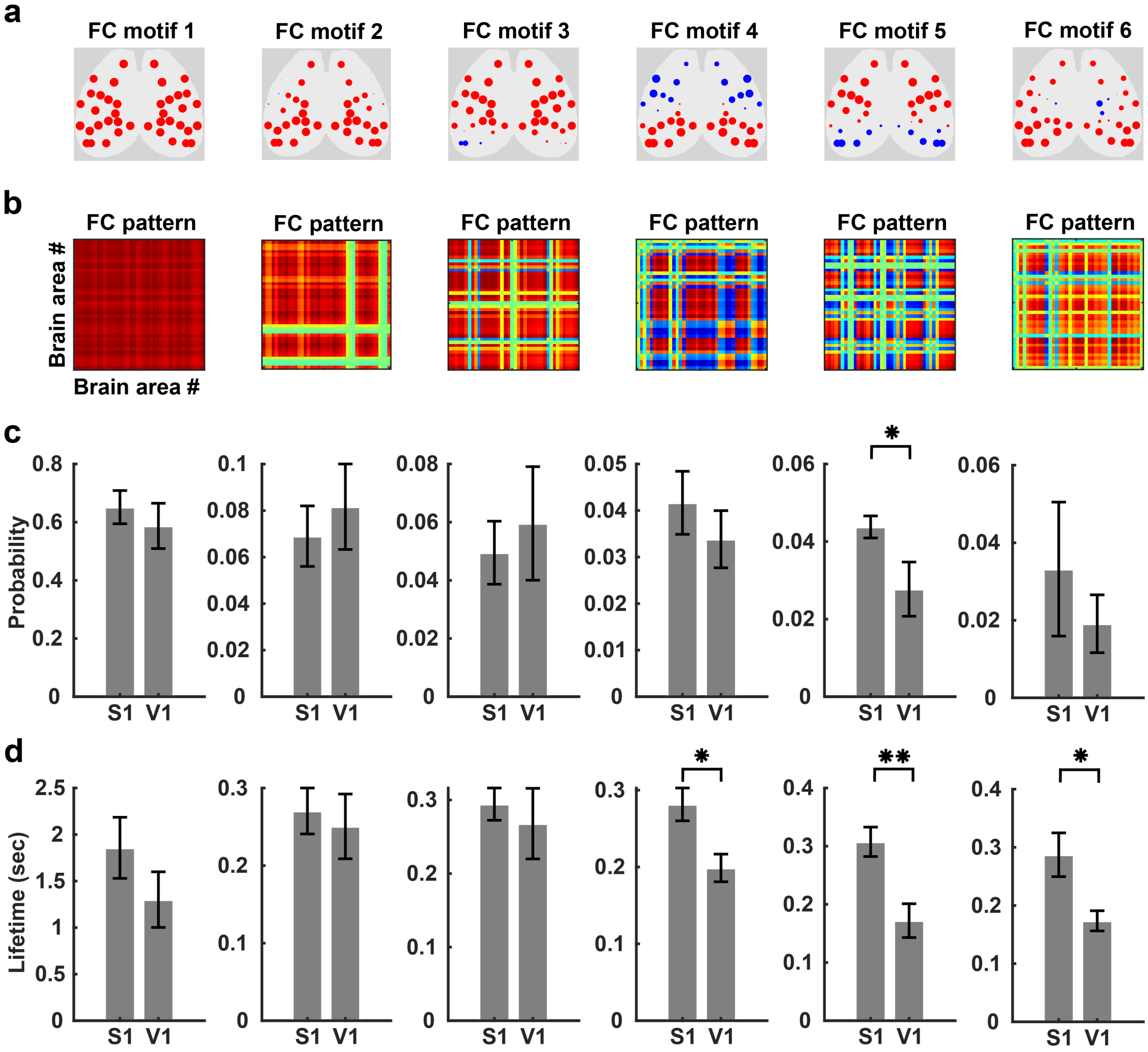

Figure 4.45: LEiDA followed by probabilistic metastable motif determination can differentiate between optogenetic stimulations in the S1 and V1 regions under 1% isoflurane (n=5 V1, n=5 S1). a, Spatial distribution of functional connectivity motifs 1 to 6. **b,** Functional connectivity (FC) matrices corresponding to the FC motifs in a. **c,** Probability of occurrence of the functional connectivity motifs. Motif 5, permutation htest, paw vs. visual p=0.036. **d,** Lifetime of the functional connectivity motifs. Motif 4, permutation htest, paw vs. visual p=0.014. Motif 5, permutation htest, paw vs. visual p=0.0029. Motif 6, permutation htest, paw vs. visual p=0.021. * corresponds to p-value < 0.05, ** corresponds to p-value < 0.01.

4.6.5 Optogenetic stimulation under ketamine produces paradoxical cortical responses

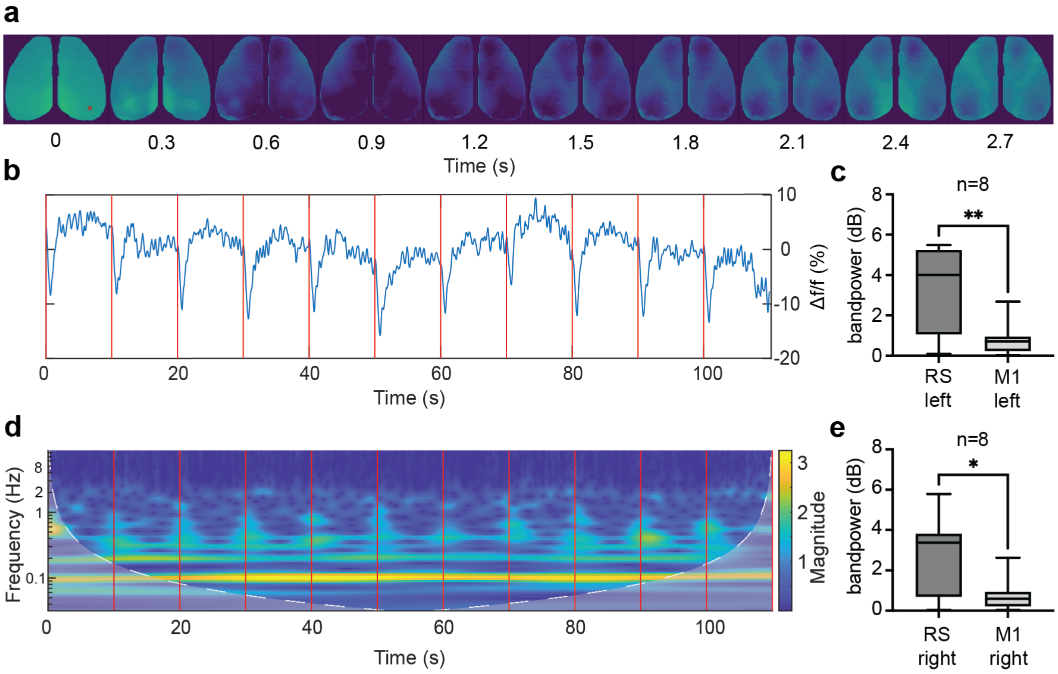

Figure 4.46: Paradoxical responses to optogenetic stimulation under ketamine in the presence of increased delta band activity. a, Dynamic imaging sequence acquired after optogenetic stimulation of the right visual cortex at time point 0. **b,** Time-varying activity levels recorded in the RS cortex showing decreases in GCaMP fluorescence after optogenetic stimulation (vertical red lines). **c,** Comparison of delta-band activity in the left RS and the left M1 region, T-test: RS left 3.5±2.1 dB, M1 left 0.8±0.8 dB, p=0.0063. **d,** Magnitude scalogram of RS wavelet decomposition showing a prominent 1-3 Hz oscillation interrupted by low-frequency components after each optogenetic stimulation (vertical red lines). **e,** Comparison of delta-band activity in the right RS and the right M1 region, T-test (n=8): RS right 2.8±1.9 dB, M1 right 0.8±0.8 dB, p=0.009.

An unexpected finding was represented by the brain responses to optogenetic stimulation under ketamine. In this pharmacological condition, optogenetic stimulation caused a small increase in activation of the region targeted by the laser pulse followed by a sharp decrease in GCaMP6s fluorescence across the cortex (Fig. 4.46 a). This low activity state lasted around 3 seconds before fluorescent signals returned to baseline. This activity pattern was highly reproducible as shown in Fig. 4.46 b from one stimulation to another but also with respect to the stimulation site. Both S1 (Fig. 4.38 g) and V1 (Fig. 4.42 g) stimulations resulted in this stereotypical cortical activation.

During spontaneous activity recordings, a characteristic 1-3Hz oscillation was observed in the retrosplenial cortex (Fig. 4.17) which was present under ketamine but not under isoflurane or medetomidine. A strong 1-3Hz rhythm was also found during optogenetic recordings in the retrosplenial cortex. Upon optogenetic stimulation, calcium fluorescence signals from the cortex decreased in intensity and additionally, the 1-3Hz rhythm was paused and replaced by lower frequency oscillations. A visual representation of this phenomenon can be seen in the wavelet decomposition of the time-varying signal extracted from the retrosplenial cortex during an optogenetically stimulated recording (Fig 4.46 d).

This phenomenon was associated with increased bandpower in the 1-3Hz interval during recordings with optogenetic stimulation. Time-varying activity from the retrosplenial and primary motor (M1) cortices was extracted and the bandpower in the 1-3Hz range was compared. The bandpower in the left retrosplenial cortex was significantly higher vs. the left M1 cortex, 3.4±2.1dB vs. 0.83±0.82dB, p=0.006 (Fig. 4.46 c). The bandpower difference between the right retrosplenial cortex vs. the right M1 cortex was also statistically significant, 2.8±1.9dB vs. 0.7±0.8dB, p=0.01 (Fig. 4.46 e).

These differences in spectral features of RSP activity were in spite of every stimulation causing a pausation of the 1-3Hz oscillation.

4.6.6 Optogenetic stimulation causes cortical activations which recapitulate the features of sensory stimulation during surgical-level anesthesia

A manifest goal of systems neuroscience is to achieve millisecond control over the activity of the extended cortical network in order to influence behavior and treat systems-wide neurological conditions. In previous chapters, we showed how brain activations during 1% isoflurane conditions differed when S1 and V1 networks were accessed by hind paw/visual versus optogenetic stimulations.

Brain activations during 1% isoflurane conditions differed when S1 and V1 networks were accessed by hind paw/visual versus optogenetic stimulations. It was also demonstrated that under surgical-level anesthesia brain responses were much simpler than during sedation. During anesthesia, stimulations were causing transitions from on to off states. These off/on transitions represent the simplest type of state change that one can induce in a dynamic system. Additionally, this brain activation has the features of a propagating wave [248,252].

For these reasons, it was important to test whether optogenetic stimulations exhibited the characteristics of traveling cortical waves. The first prerequisite to achieving this goal was to acquire cortical activity recordings at a high temporal resolution so, in 3 mice, brain activity during stimulation was recorded at 100 frames per second. Secondly, a way of generating reproducible slow waves with a known point of origin is needed. Triggering is essential because slow cortical waves can be initiated in any region of the cortex [248,252]. Slow waves were triggered in the visual cortex by stimulation of the retina and by V1 optogenetic stimulation (Fig. 4.47 a). Like this, slow-wave propagation can be observed over almost 1 cm across the entire posterior to anterior cortical length.

Visual stimulation reliably triggered slow waves (Fig. 4.47 c) and this activity was initiated in the visual cortex, only to propagate later to the frontal areas (Fig. 4.47 b). Likewise, optogenetic stimulation was reliably initiating propagating waves (Fig. 4.47 e) with a starting point in the stimulated V1 region on the right. Activation waves propagated towards the frontal cortex over a shorter period with respect to visually triggered waves (Fig. 4.47 d).

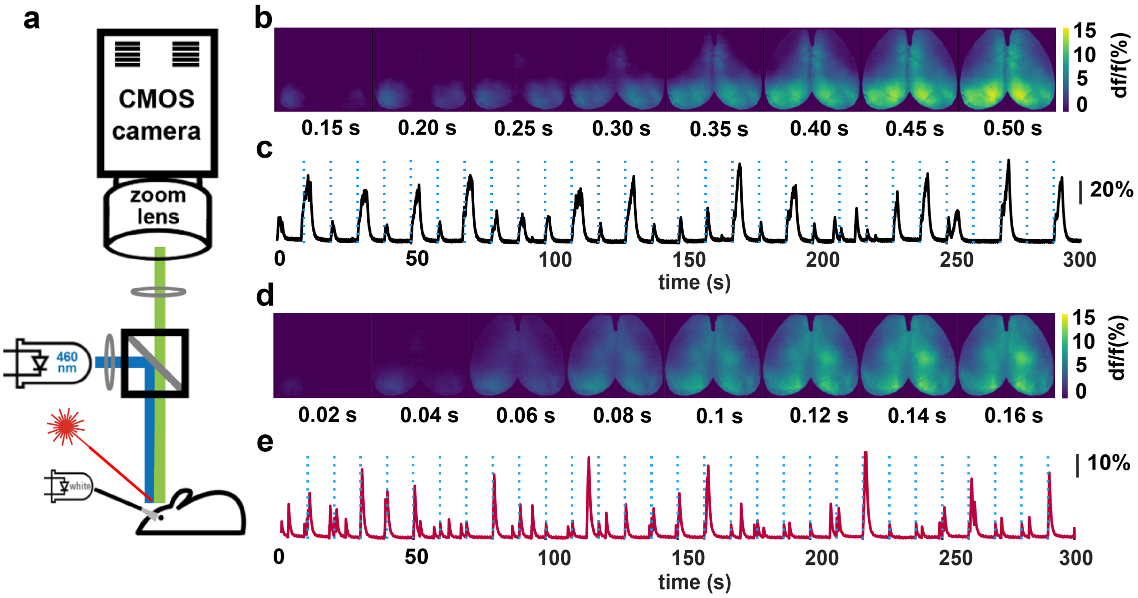

Figure 4.47: V1 optogenetic and visual stimulations trigger slow waves during isoflurane anesthesia. a, Wide-field fluorescence imaging setup, GCaMP6s excitation was done with a 460 nm high-powered LED, and visual stimulation was achieved with a cool white light that was directed through a fiber guide. Optogenetic light was delivered by a 637 nm laser which was collimated and targeted at the V1 region on the right side. **b,** Montage showing slow-wave propagation pattern after visual stimulation, image intensity denotes signal changes to baseline in percent. **c,** Fluorescence time trace from the whole cortex after white light stimulation of the retina, stimulation times are marked in blue dotted vertical lines. **d,** Montage showing slow-wave propagation pattern after Optogenetic V1 stimulation, image intensity denotes signal changes to baseline in percent. **e,** Fluorescence time trace from the whole cortex after optogenetic V1 stimulation, stimulation times are marked in blue dotted vertical lines.

Signals from ten equally spaced regions situated between the occipital to the frontal cortex were extracted (Fig.4.48 a) and the time of arrival of the waves was inferred by calculating the time index when the signal had reached a 50% of the max intensity for the respective wave. Next, the time of arrival versus distance traveled was plotted and linear regression was performed to estimate the speed of the recorded slow waves (Fig. 4.48 d). Visual stimulations triggered slow waves with an average speed of 4.9±3.7 cm/s and optogenetically triggered waves had a speed of 18.77±10.2 cm/s. The difference in speed was found to be statistically significant, p<0.0001 (Fig. 4.48 e).

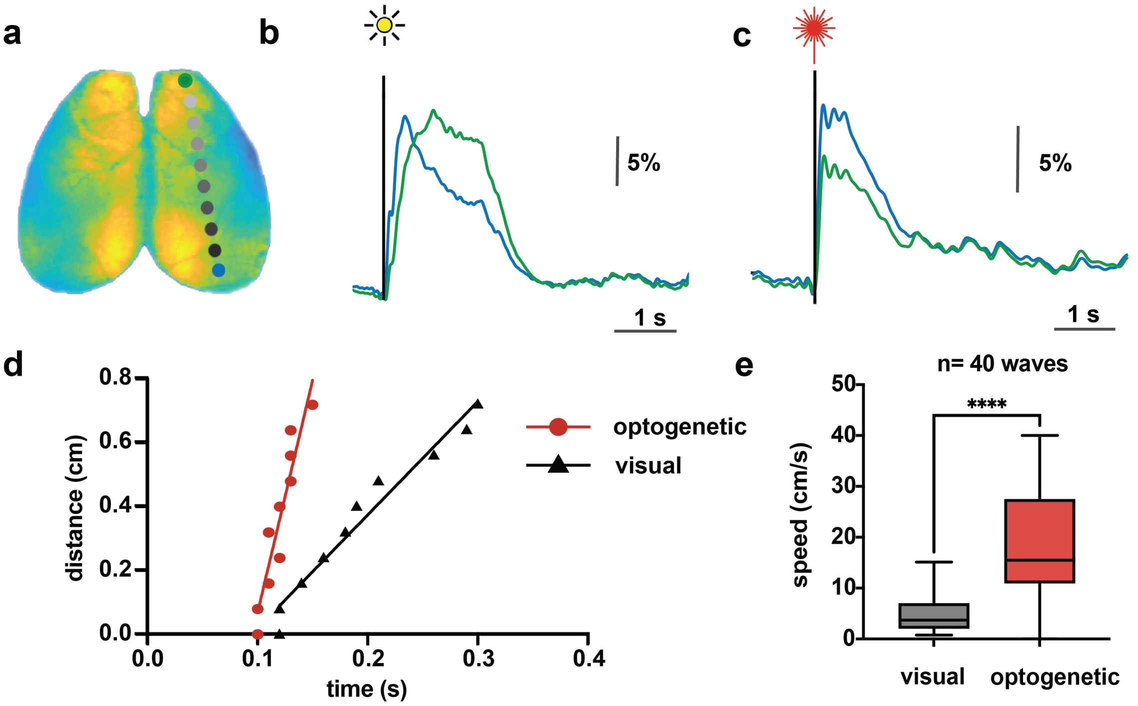

Figure 4.48: Slow-wave propagation speed after V1 optogenetic and visual stimulations. a, ROI signal from occipital to frontal was extracted and used for Wave speed determinations. **b,** Average time traces over 40 visual stimulations from an occipital ROI (blue) and a frontal ROI (green). **c,** Average time traces over 40 optogenetic V1 stimulations from an occipital ROI (blue) and a frontal ROI (green). **d,** Slow-wave speed by linear fitting time vs. distance traveled, across the 10 ROI from panel f, optogenetic slope 14.55, R squared=0.88, F=59.53; visual slope 3.55, R squared=0.96, F=194.4. **e,** Visual vs. optogenetic slow-wave speed comparison, T-test, n=40, p<0.00001.

4.7 Functional brain state characterization by aggregate quantitative measurements

It was tested whether quantitative measurements concerning functional brain network segregation (BPD) and the complexity of effective connectivity (PCI) could be used to identify brain states from functional imaging data (Fig. 4.49).

Data acquired under 1% isoflurane, 1.8% isoflurane, medetomidine, and ketamine were used for this analysis. For medetomidine and 1% iso. (persistent iso.), high levels of functional segregation were observed together with complex effective connectivity patterns.

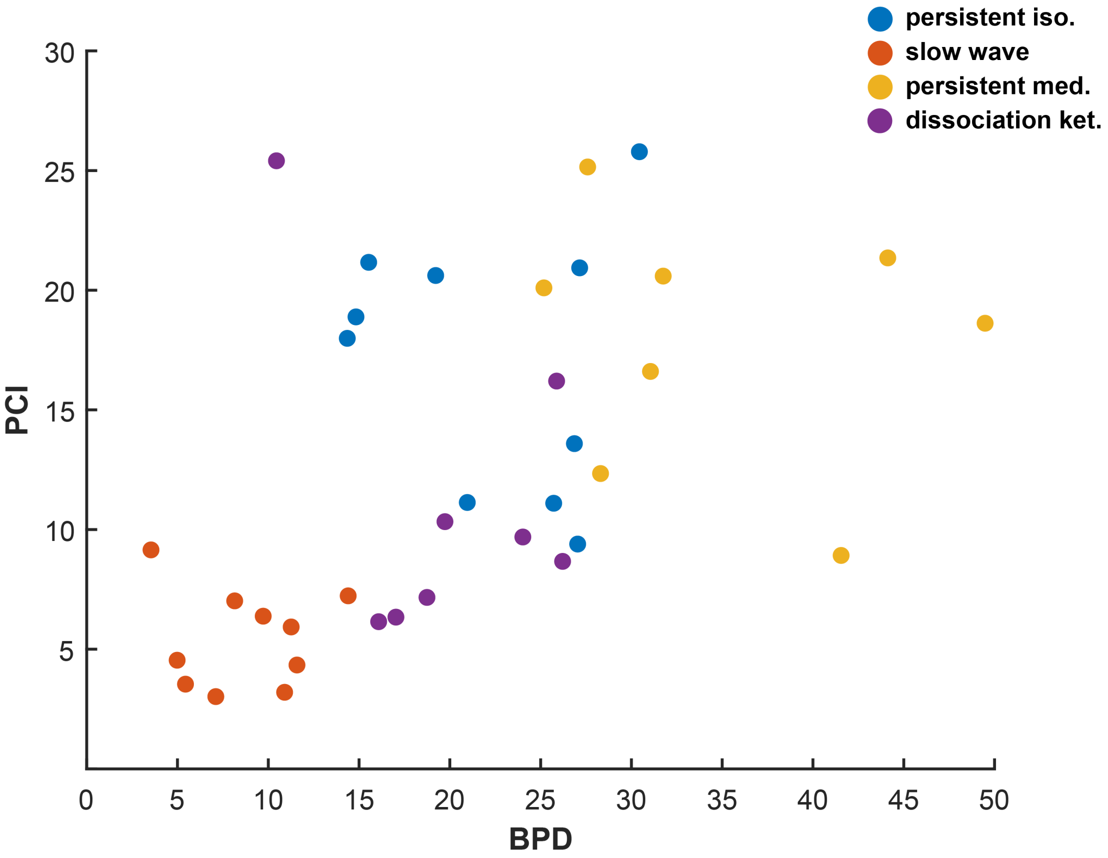

Figure 4.49: Functional brain state determination using network segregation (BPD) and the complexity of effective connectivity responses (PCI). Values in the scatter plot represent BPD measurements for entire 5-minute imaging runs versus the complexity of optogenetically-evoked cortical responses (PCI) in the same functional states.

During 1.8% isoflurane, low levels of functional network segregation (BPD) were registered and in this state, effective connectivity responses with low complexity were observed. Qualitative inspection of these recordings revealed that during this condition, slow waves of propagating neuronal activity dominated. This would suggest that the slow-waves state is characterized by decreased complexity of both spontaneous activity and responses to optogenetic stimulation.

During ketamine-induced dissociation-unconsciousness, network segregation levels (BPD) were comparable to isoflurane 1%, and responses to optogenetic stimulation were characterized by low complexity (PCI). Two outlying PCI measurements during dissociation were recorded and these might be due to the difficulty of analyzing responses to optogenetic stimulation consisting of a general decrease in fluorescence signal (Fig. 4.46). These data suggest that dissociation unconsciousness could be considered a functional state distinct from the persistent and slow-wave states.

5

Discussion

5.1 Inferring systems-wide cortical activation patterns from local recordings.

fMRI represents a widely used imaging modality for the structural and functional characterization of the brain [76,84,87,331]. Assessing the functional state of brain networks benefits from macroscale recordings which can cover the entire cerebrum. EPI fMRI acquisition techniques can image the entire mouse brain with a temporal resolution of one brain volume per second, leveraging the neurovascular coupling to generate BOLD contrast [84].

fMRI data acquisition for preclinical studies has to be carried out under anesthesia because awake recordings would cause discomfort to the animal subjects due to the restraint and loud noise caused by fMRI gradient switching. In our experiments, 1.4% inhaled isoflurane anesthesia was used to induce an unconscious state. In this vigilance state, complex spontaneous oscillations should be present as a feature of the persistent state.

fMRI was used to characterize brain responses to somatosensory hind paw stimulation. Cortical activation patterns were concentrated in the somatosensory cortices in two mice while more widespread cortical and subcortical activation was observed in a third animal (Fig. 4.1). These results matched previous reports of mouse brain fMRI activation patterns after hind paw stimulation [80]. ICA, a data-driven feature extraction method was used to verify these findings. GLM findings of activation in the somatosensory cortex were confirmed and this was in line with previously published work [80]. ICA also revealed a further pattern of activation which encompassed the entire cortex (Fig. 4.2).

Other groups observed global activation patterns during isoflurane anesthesia which were shown to be caused by propagating slow waves of cortical activity [6,91,263]. Consequently, cortical slow waves were imaged during 1.8% isoflurane, surgical-level anesthesia. GCaMP6f was expressed in the S1 cortex and local fluorescence calcium recordings (fiber photometry) were simultaneously acquired with the EPI. The local fluorescence measurements were used as a positive control for ensuring that the brain was producing slow waves.

Additionally, the study of slow waves requires a way of triggering reproducible events. It has been shown that slow waves can be triggered by sensory stimulation as well as optogenetics [252]. Cortical waves of activation were triggered in the S1 area by hind paw stimulation as well as by optogenetic stimulation of the red-shifted opsin ChrimsonR. ChrimsonR stimulation and GCaMP6f readout were done through the same fiber-optic. Slow-wave latencies for hind paw-generated slow waves were higher than for optogenetically induced ones. Latencies for both visually and optogenetically triggered slow waves were previously reported to be around 80 ms [252]. This is in line with my findings upon optogenetic S1 stimulation, latencies for hind paw stimulation were around 170 ms (Fig. 4.3). The reason for this higher latency could have to do with higher nerve signal transmission times from the limb to the brain, processing in relays such as the thalamus, and local processing in the somatosensory cortex.

These experiments proved that the genetically encoded calcium sensor GCAMP6f and the transmembrane cation channel ChrimsonR can be used in tandem to provide a readout of neuronal activity (GCaMP6f) and direct stimulation of those same neurons (ChrimsonR). This strategy allowed locally acquired calcium fluorescence to be recorded symultaneously with fMRI and to validate findings of a pancortical BOLD activation component (Fig. 4.4). ICA can capture non-linear features of functional imaging data and this likely helped reveal the pancortical activation pattern corresponding to locally recorded slow waves[91].

Two clases of genetically encoded contrast agents were validated during this work,. The effectiveness of iron accumulating contrast agents was demonstrated in cell experiments using MRI relaxometry. PolyP accumulating contrast agents were evidentiated with MRI spectroscopy. The contrast agents were confined inside protein nanoshells thus protecting the cells from the potentially harmful effects of contrast agent accumulation. The MRI contrast of these substances is dependent on the amount of iron or polyP which can be produced by the cells a mechanism that will prove valuable for oncologic applications [327].

For neuroimaging studies, it would be desirable to have dynamic contrast agents which change their properties depending on the level of neuronal activation. Dynamic contrast agents are currently not available for MRI but are already established for optical imaging applications. For this reason, most of the experimental work was done using wide-field calcium fluorescence recordings.

5.2 Wide-field optical imaging - a versatile platform for recording and manipulating mouse brain activity

A custom wide-field fluorescence microscope was developed in the course of this work. This instrument can record both GCaMP6s fluorescence and brain hemodynamics with a spatial resolution of 0.03mm per pixel and a temporal resolution of up to 100 frames per second. The system is fully accessible to modification and can be converted within minutes between two modes of hemodynamic imaging, recording either 395nm reflectance or fluorescence imaging after ICG micelle injection (Fig. 4.7).

This flexibility proved valuable because functional calcium imaging datasets contain physiological noise which is mainly caused by time-varying changes in hemodynamic parameters. Using vascular and neuronal contrast, it was possible to identify physiological noise and computationally remove it using a bespoke image processing pipeline(Fig. 4.14).

A prominent goal of neuroscience is to elucidate how genetically defined neuronal populations work together in order to process information and give rise to behavior [124,332]. To achieve this goal genetically defined neuronal populations have to be recorded and their activity needs to be accessible to manipulation.

Both goals can be achieved with the use of wide-field fluorescence imaging in combination with optogenetic manipulation of neuronal activity. Progress in mouse reporter lines has led to the development of several classes of transgenic animals expressing different molecular sensors which capture various aspects of neuronal activity. In the course of this work, functional imaging was carried out in transgenic mice expressing GCaMP6s [40], a fluorescent calcium reporter, in cortical pyramidal neurons [124].

Manipulating the activity of extended cortical networks involves expressing optogenetic tools in the membranes of the genetically targeted populations of neurons. It is important that these tools be spectrally separated from the calcium sensors. Thus, the red-shifted excitatory opsin ChrimsonR was used. This enables us to carry out GCaMP6s imaging with blue light excitation in parallel with optogenetic stimulation in the red channel(Fig. 4.35).

Cortical information integration can be captured by effective connectivity. Effective connectivity denotes the capacity of a set of neuronal groups to causally affect the activity of other neuronal groups within the wider network [14,17]. EC has successfully been measured in humans by observing the effects of TMS stimulation on EEG activity [18]. This represents the perturb-and-measure approach and in this study, the cortex was perturbed with optogenetics, and brain activity was recorded with calcium imaging(Fig. 4.39 and 4.43). This represents a novel implementation since, previously, optogenetic stimulation was done with blue wavelengths (using Channelrhodopsin2) while brain activity readout was done with optical hemodynamic imaging [177].

Existing AAV vectors for ChrimsonR expression were not perfectly suited for concomitant expression in GCaMP positive neurons and this was due to the coexpressed fluorescent tag TdTomato. TdTomato absorbs both blue GCaMP6s excitation light and green GCaMP6s emission light leading to a loss in GCaMP6s fluorescence. For this reason, TdTomato was replaced with a colorless Flag-Tag, and this enabled concomitant and artifact-free GCaMP imaging and optogenetic stimulation (Fig. 4.36). An additional advantage of wide-field calcium imaging is represented by the high signal-to-noise ratio of this imaging method, some activation events had a magnitude of up to 30% over baseline. This made subsequent data processing steps easier.

Furthermore, wide-field fluorescence microscopy is situated between fMRI and EEG in terms of temporal resolution. As a result, it was possible to use data-driven processing routines developed for both fMRI [333] and EEG [301] in order to generate relevant insights from functional data. We have also developed a custom processing pipeline based on wavelet decomposition, UMAP dimensionality reduction, and hierarchical clustering which allows us to calculate the level of segregation of functional cortical networks with BPD(Fig. 4.21).

Wide-field optical imaging with genetically encoded calcium sensors is straightforward in its interpretation and in its implementation. The signals recorded come from action potential-induced calcium transients in pyramidal neurons and the same population can be optogenetically stimulated. For this reason, most of the experimental work was done using wide-field optical imaging with integrated optogenetic stimulation capability.

5.3 Functional integration and segregation during spontaneous cortical activity

The notion that specific brain functions can be attributed to precisely defined brain regions has been a central concept driving neuroscience research since the 19th century [334]. This theory pertaining to cortical organization known as localizationism seemed to be strengthened by clinical work from Broca and Wernicke that linked impairments in patients to lesions in anatomically defined brain regions.

Connectionism holds that the activity of a specialized brain region is dependent on its anatomical connections to other brain areas [335]. In contrast to localization, segregation postulates that brain areas are specialized in some aspects of sensory or motor processing and that these areas are segregated within the cortex. The computational processes underlying a particular function involve many specialized areas that integrate their outputs to produce sensations and behaviors [17].

Segregation and integration in resting-state cortical networks were investigated using data from wide-field optical imaging in transgenic mice expressing GCaMP6s in cortical pyramidal neurons under CaMKII control. The global variables used for the modulation of the brain states were anesthesia type and anesthesia depth. States of arousal like sedation were induced with medetomidine and isoflurane 1%, 1.8% isoflurane was employed for anesthesia and the injection of ketamine caused dissociation-unconsciousness. Functional transitions from the persistent to the slow-wave brain state were induced by the increase of inhaled isoflurane from 1 to 1.8% in 0.2% increments.

Computationally, segregation and integration were assessed using 3 strategies: 1) BPD - a data-driven computation for estimating the degree of segregation in functional networks, 2) complex network measures of functional connectivity and 3) measures of metastability and spatial FC motives.

5.3.1 Assessment of functional network segregation levels with BPD

BPD is a data-driven computation that uses well-characterized functional networks in order to infer the effective dimensionality of the imaging data. The functional networks are identified with PCA and represent spatial features corresponding to physiological brain networks (Fig. 4.19). The Shannon entropy of the PCA components' variance is calculated and rescaled by the total number of PCA components to arrive at the quantitative measure BPD (Fig. 4.19).

Essentially BPD measures the level of functional segregation in cortical brain networks. By measuring BPD, we compute the number of dimensions needed in order to reproduce the overall variance in our original dataset. BPD has a very precise physiological interpretation, it measures the level of functional segregation in cortical brain networks because the higher the BPD of our imaging datasets the higher the number of physiological cortical networks which are active in that particular recording and the more complex the functional brain state.

Low levels of isoflurane and medetomidine exhibit segregated FC networks [6,91,198], and this activity corresponds to prior descriptions of the persistent cortical state [6], while surgical-level anesthesia features slow waves, the slow-wave state [6,91,252,253]. It was shown that the persistent state exhibits high levels of BPD whereas the slow-wave state has lower levels of functional segregation (Fig. 4.21).

Transitional states spanning from the persistent to the slow-wave state were induced by progressively increasing concentrations of inhaled isoflurane. The expectation was to find clear "phase transitions" in brain activity metrics between these two extremes. Instead, for isoflurane concentrations from 1% to 1.6%, a gradual decrease in functional networks' segregation levels was observed. BPD measurements settled at low levels during 1.6% isoflurane and 1.8% isoflurane. In these later concentrations, slow-wave oscillations were observed(Fig. 4.19 and Fig. 4.18).

Previously, progressively increasing levels of isoflurane were reported to reduce homotopic correlations as well as cortical segregation levels in fMRI mouse recordings. [262]. These findings seem to contradict each other since the loss of functional segregation would lead to global activity patterns and these would produce an increase in homotopic correlations. It was demonstrated using direct neuronal recordings that increasing doses of isoflurane lead to brain state transitions from complex spontaneous activity to slow-wave activity. Slow waves are global propagating patterns of activation and these lead to a loss of brain network segregation. As will be detailed in the section below slow waves also induce an increase in homotopic correlations because they often encompass the entire cortex (Fig. 4.22). The divergence between our findings and those of Bukhari et al. could be explained by the superior temporal resolution which can be achieved in optical imaging vs. MRI (20Hz vs. 1Hz), which allowed us to capture dynamic cortical phenomena in greater detail.

Another factor that might have contributed to this discrepancy, could be represented by the complicated data processing pipelines used by Bukhari et al. which include tunable parameters [262]. Functional connectivity analysis for fMRI [6,80] and optical imaging [149] often involves global signal removal. This removes an important driver of functional connectivity and may artificially cause lower homotopic correlations. Such interventions are not necessary when using BAPD for brain state characterization.

In a previous study, the awake versus slow-wave brain states were investigated using optical imaging and PCA analysis [149]. In this study, the authors showed that after removing the first three principal components from datasets with slow-wave activity, the remaining principal components were similar to those found in the awake state. From a methodological, point of view, the removal of the first three principal components can be seen as an arbitrary intervention. Furthermore, these principal components were attributed to slow oscillations after data inspection and this represents a qualitative assessment rather than one based on mathematically defined criteria. The more conservative approach is to find measurements that have explanatory value for the observed phenomena, i.e for transitions from the persistent to the slow-wave state. BPD offers a quantitative description of functional brain states and does not rely on tunable parameters or subjective interpretations.

Yet another approach to measuring and estimating the state of vigilance for wide-field optical imaging recordings relies on calculating the entropy of spontaneous brain signals [148]. This method stems from empirical experience and the physiological significance of such a measurement is unclear. This approach is based on practices from anesthesiology where practical considerations favor simple measures for the assessment of patients' EEG activity which can be implemented online during surgery to infer the vigilance state [282].

While the brain state induced by medetomidine tended to have higher BPD values than 1% isoflurane, it was not possible to statistically distinguish between the two. Likewise, sedation with isoflurane 1% was not significantly different from dissociation unconsciousness under ketamine but there was a clear trend toward statistical significance between sedation with medetomidine and dissociation- unconsciousness with ketamine.

It was demonstrated that transitions from the persistent state (complex connectivity patterns) to slow-wave activity are accompanied by a reduction of brain activation pattern complexity as measured by BPD. This seems to support the view that anesthetics induce the loss of consciousness by replacing complex cortical activity with more stereotypical patterns of global activation [19].

5.3.2 The Functional network architecture is influenced by the brain state

Complex network measures of functional connectivity assess functional segregation and integration by using brain network modeling tools from graph theory [16]. The degrees of the network together with the global efficiency and path length were used in order to estimate cortical integration in the brain states investigated (Fig. 4.24). The modularity, clustering coefficient, and local efficiency are considered (Fig. 4.25).

The segregation and integration metrics did not reveal a clear-cut inflection point during transitions from the persistent state (compartmentalized spontaneous activity) to the slow-wave state under isoflurane (Fig. 4.24 and 4.25). This computation served as an independent validation of the BPD metric. Network measures of FC are computed starting from assumptions about the parcellation of the brain in functional regions. Free parameters of the analysis include a threshold for correlations that are taken into consideration for network modeling such that weak correlations and negative correlations between brain regions are discarded [16]. In contrast, BPD assesses brain networks' segregation directly from imaging datasets by measuring the effective dimensionality of imaging data and does not include tunable parameters. Similar levels of functional network segregation were observed in isoflurane 1%, medetomidine, and ketamine in spite of spatio-temporal and spectral differences between these conditions.

Network measures of functional connectivity during medetomidine and low levels of isoflurane and ketamine, matched well to a small-world network architecture indicating the tendency of the cortical network in this state to form partitions, as indicated by high values of the clustering coefficient, modularity, and local efficiency. Also, integration metrics such as global efficiency, path length, and degrees were high in these three states. In contrast, in surgical-level anesthesia with slow waves, the brain network exhibits minimal clustering tendencies and very high values of both global efficiency and local efficiency matching a non-differentiated fully connected network.

Our results from graph theory under isoflurane are compatible with previous work involving 3D fMRI functional imaging and fiber photometry in rats. In this work, during sedation with low concentrations of isoflurane and medetomidine, compartmentalized functional network dynamics were observed, this is the persistent brain state [6]. A modular small-world network was described in this state [5,6]. In the high isoflurane condition, a fully connected (non-differentiated) network model best matches our data. This result is also compatible with our qualitative assessment of the activity during high anesthesia where mainly slow waves were observed. Previous reports describe slow waves as periods of high synchrony between all brain regions i.e. periods of very high connectivity between all brain areas [91,150,248,252].

During high concentrations of isoflurane high global efficiency and lower local efficiency were reported [6]. In contrast, during high levels of anesthesia, we found both high global and local efficiency. Furthermore, evidence is presented that definitively disproves previous results in mice of progressively decreasing homotopic correlations with increasing isoflurane levels [262]. Increasing the anesthetic concentration leads to slow-wave activity and increased correlations between all brain regions. The diverging results in our study compared to the studies cited above could be due to the differences in temporal sampling rate and the frequency range available to optical imaging vs. fMRI. Also, fMRI recordings represent an indirect report of neuronal activity mediated by the neurovascular coupling and it was shown that hemodynamic responses could be affected by high isoflurane concentrations due to induced vasodilation [336] leading to inaccurate results.

These findings underscore the importance of having direct measurements of neuronal activity in mice as a control for fMRI studies in more complex mammals.

5.3.3 Spatio-temporal FC patterns relevant for brain states and transitions

Metastability is a feature of dynamic systems and refers to a state which falls outside the natural equilibrium of the system but is present over an extended period of time. The persistence of states over time is a key feature that distinguishes this type of analysis from bulk measurements which refer to the entire duration of an experiment. Topological network communities can give an indication of integration and segregation but do not provide any information about data processing over time [12].

Following this model, ignition events can be defined as the capacity of a brain area to propagate its activity to other regions over time. This measurement is suited only for spontaneous brain activity recordings, as ignition events are intrinsic in nature and do not have any relation to outside stimuli. This metastability index is calculated by averaging the level of integration for each intrinsic ignition event in each brain region over all events [330].

This measure of metastability was analized for medetomidine, ketamine, isoflurane 1%, and isoflurane 1.8% over canonical frequency bands from slow-4 to theta. Medetomidine and isoflurane 1% showed high metastability levels across frequency bands. Ketamine resembled iso. 1.8% in low-frequency bands and med./iso. 1% in the delta and theta bands (Fig. 4.26). These results could be brought about by alternating gamma/theta bursts with slow-delta frequencies during dissociation-unconsciousness under ketamine as described by EEG [275].

This method has been previously tested on fMRI recordings from human subjects acquired during wakefulness and deep sleep [330]. This quantitative approach is useful in elucidating frequency band-specific segregation and integration during spontaneous brain activity under different anesthetics and also in different anesthetic doses (isoflurane 1% and 1.8%). Furthermore, this method can be applied to neuronal data directly rather than recordings using the neurovascular coupling.

The quantitative approach presented above produces bulk measurements where spatial aspects of brain activation are averaged to produce concise summaries of cortical segregation and integration. Leading Eigenvector Dynamic Analysis (LEiDA) has been developed for the purpose of calculating spontaneous network switching from functional brain recordings. We extract time-varying signals from cortical brain areas and calculate the instant phase of brain signals which are grouped in time-varying phase-coherence matrices. Next, eigenvectors are calculated for each time point for every subject and every experimental condition. As a subsequent step, these eigenvectors can be clustered to produce probabilistic metastable substates which represent spatial functional connectivity patterns that have metastable characteristics.

By performing LEiDA followed by probabilistic metastable substate determination

[180,289] it was possible to identify a functional connectivity motif that has high explanatory power for the functional state of brain networks. This metastable motif is characterized by high levels of connectivity between all anatomically-defined brain areas. It underlies transitions from the persistent state (present in sedation) to the slow-wave state (present in anesthesia) under isoflurane. In low isoflurane concentrations, this motif has shorter lifetimes and a lower probability while in high isoflurane conditions, its likelihood of occurrence increases to 95% (Fig. 4.27).

This metastable pattern is attributable to periods of time when activity in all brain areas are highly correlated, i.e. periods of high cortical excitability. There is broad consensus that fluctuations in whole-brain network excitability underlie slow-wave activity [6,241,252]. In this state, periods of baseline cortical activity which are called off states alternate with intervals of increased neuronal excitability, on states, when action potentials are highly synchronized across widespread regions of the cortex [244,248,252,337]. During slow-wave activity, the fully connected metastable motif lasts up to 10 seconds and has a very high probability of occurrence.

Fluctuations in excitability can be viewed in a more general sense as important constituents of cortical dynamics during other brain states apart from the slow-wave state. The fully connected FC motif was found also during the persistent brain state which was induced with low isoflurane concentrations. The features which make the difference are the lifetime (around 1 second) and the probability of occurrence (around 67%) in the persistent state. Having such descriptors allows us to analyze brain activity across different functional states in a coherent, and mathematically precise way (Fig. 4.27).

Consistent with our BPD measurements in isoflurane conditions, LEiDA did not reveal sharp transitions between brain states but rather a gradual increase in the probability of the fully connected FC pattern from isoflurane 1% to isoflurane 1.6% followed by a leveling-off in 1.6% isoflurane and 1.8% isoflurane. The same trend was observed in our BPD measurements.

Evidence is presented that global fluctuations of cortical excitability exist more generally in different states of arousal like medetomidine-induced sedation and ketamine-elicited dissociation-unconsciousness. This suggests that this FC motif can be seen as a descriptor that is generalizable also to pharmacological conditions different than isoflurane. Using this single functional connectivity pattern, it is possible to differentiate between isoflurane 1%, isoflurane 1.8%, medetomidine, and ketamine (Fig. 4.28). Notably, BPD measurements indicate that brain activity was most complex under medetomidine and during this condition, the fully connected motif had the lowest probability of occurrence and the shortest lifetime.

Apart from the fully connected metastable motif, most of the other functional connectivity patterns from LEiDA feature anticorrelations between frontal and occipital regions. In Fig. 4.17 it is shown that network activity under isoflurane 1% and medetomidine fluctuates between frontal and occipital areas on timescales of up to 2 sec. The spatial distribution of correlated and anti-correlated regions shows remarkable similarity to the functional activity observed in the frontal and occipital subclusters.

5.4 The role of the functional states for processing sensory information in the cortex

In order to understand how animals function in their environment, we must understand the chain of events that leads to behavioral changes. To approach this problem the sequence of neuronal events that ultimately lead to behavior has to be broken down into its constituent elements. The first stage in this process is usually motivated by a change in the environment which is picked up by sensory receptors. After local processing in the peripheral nervous system and subcortical nuclei, an “edited” version of the captured sensory information is transmitted to the cortex. Next, the information is processed in the cortex and this step is influenced by motivation, drive, memories, projections of the future, and the state of arousal. A decision-making process follows which may or may not be followed by goal-directed motor activity [338].

This model emphasizes the importance of the arousal state in modulating behavior and for this reason, it was decided to investigate cortical sensory information processing as a function of the vigilance state. As shown in section 5.3, heterogeneous functional brain states underlie states of vigilance. Isoflurane was used to induce transitions from the persistent state to the slow waves state and the cortical representation of stimuli was observed in order to infer the features of cortical information processing in these states. This transition was achieved by gradually increasing the inhaled concentration of isoflurane gas. Simple visual and hind paw simulations were carried out and brain activations were observed with our optical imaging system. V1 and S1 cortical areas were accessed, and these regions were also later targeted with optogenetic stimuli.

Qualitative assessment of the cortical responses to sensory stimulation revealed that under low isoflurane concentrations, responses were mostly local while under anesthesia stimulation produced global responses (Fig. 4.29 and 4.31). Under low isoflurane conditions, our findings of local activations are in line with previous results from the field of fMRI imaging [80]. fMRI reports of localized activity after hind paw stimulation in isoflurane may be dependent on the arbitrary step of thresholding statistical scores leading to heterogeneous results.

During surgical-level anesthesia with isoflurane, in the slow waves state, stimulations give rise to stereotypical brain activation patterns. These types of responses have been observed with fiber-photometry [252] as well as a combination of fiber-photometry and fMRI [6,91,263]. In these studies, local calcium transients which are recorded with fiber-photometry are related to global activation patterns recorded with fMRI.

In wide-field optical imaging, sensory information was mapped over the corresponding cortical areas responsible for primary processing [135] and sensory-motor integration was characterized [124,141–143]. However, these studies mainly focused on the processing of sensory information before the generation of goal-directed behavior and did not include an assessment of the functional brain state. Studies using wide-field optical imaging for the investigation of brain states mainly focus on spontaneous cortical dynamics [147,149].

The direct dependence of stimulus processing on the brain state is insufficiently explored. Brain responses under low [80] and high [91] isoflurane concentrations had been described by fMRI but the transition between these two extremes remains unexplored.

BPD was used to confirm the link between the functional brain state and the responses to stimulation. BPD is a generalizable computational tool that can be applied to functional imaging data in the presence or absence of stimulation. BPD measurements from stimulated imaging runs revealed a similar trend to the one found in spontaneous recordings. Low isoflurane concentrations have high BPD values while high concentrations of anesthetic gas are characterized by low BPD values. BPD values decreased gradually from 1% isoflurane to 1.6% isoflurane before leveling off at 1.6 and 1.8%. It was also shown that BPD values for spontaneous activity are useful in predicting the BPD of stimulated datasets (Fig. 4.30 and 4.32). BPD in the resting state had moderate to high explanatory power over BPD in stimulated runs and the difference between spontaneous activity BPD and BPD during visual and somatosensory stimulation was not statistically significant within the same concentration of isoflurane.

This seems to strengthen the view that sensory information processing is superimposed on a dynamic background representing internally generated computational streams, execution of housekeeping tasks, and oscillations that reflect brain network architecture [4,181]. Because stimulation does not significantly increase the dimensionality of imaging datasets, we would be inclined to think that the cortical activity that is associated with stimulus processing only represents a small part of the total cortical network fluctuations that occur at any one time in the extended cortical network.

Our stimulation strategy involved delivering 50ms stimuli every 10 seconds and this represents a very sparse stimulation protocol compared to fMRI stimulation procedures which are usually organized in blocks spanning tens of seconds [80]. It should be tested whether the more intensive stimulation regime impacts segregation levels in functional brain networks. Such intense stimulations in fMRI are mainly carried out to ensure that large hemodynamic responses can be recorded in spite of very high noise levels. Fluorescence calcium imaging has a much better SNR and this allowed us to record brain responses to stimulation with a sparser stimulation protocol that matches better natural environmental stimuli.

BPD is a general computation that does not assess the results of stimulation directly, and for this reason, the topological features of stimulated imaging recordings were analyzed. The topological complexity metric refers to the prominence, of stimulation-induced functional features in order to infer which datasets contained patterns of activation that are expressed over the largest range of spatial scales (Fig. 4.33) [303]. In our case determining topological activation features after stimulation is not trivial. The mouse brain images were accurately aligned and their shape is relatively uniform (owing to their identical genotype), however, the vascular pattern of superficial veins and arteries is highly variable between subjects. Stimulation experiments in transgenic mice typically involve small cohorts, thus a robust approach to topological variability when assessing cortical responses to stimulation is desired.

Visual stimuli had significantly greater topological complexity in 1% ans 1.2% isoflurane but were not distinguishable during surgical-level anesthesia (Fig. 4.33). Visual and somatosensory cortical representations have higher levels of topological complexity at low isoflurane concentrations compared to surgical-level anesthesia. In more complex brain states, identified by BPD, cortical activations span a larger number of topological scales. Under anesthesia, in the slow-wave brain state, responses were simpler, manifesting over a lower number of spatial scales. This metric quantifies topological features of cortical responses to stimulation confirming our qualitative assessment that cortical responses during anesthesia were found to be global and stereotypical.

Topological complexity measurements have previously been used on fMRI data for the classification of brain activity as a function of the subject's age and in this case, the stimulation was represented by participants watching a five-minute video during fMRI measurements [303]. The use of this computation to reveal the topological features of simpler stimuli in calcium imaging rather than hemodynamic recordings suggests this data-driven metric could be used for clarifying features of cortical activity in a wider range of experiments studying perception and information processing.

It was shown that cortical sensory processing is strongly influenced by the functional state of brain networks. Transitions from the persistent brain state to the slow-wave state lead to a decrease of the complexity of sensory afferent representations in pyramidal neuron networks. For these reasons, an estimation of the functional brain state should be carried out as a preprocessing step before other computational routines tailored to the analysis of cortical activation patterns. Such an analysis could be carried out with BPD as it delivers reliable measurements of functional network segregation even in the presence of sensory stimulation.

5.5 Effective connectivity is dependent on the functional state of brain networks

Effective connectivity refers to the capacity of a set of neuronal groups to causally affect the activity of other neuronal groups within the wider network [14,17]. Attempts at quantifying information integration mostly rely on functional connectivity. Functional connectivity is defined as a statistical dependency between spatially remote neuronal activation events and is established by calculating correlations between the functional activity of neurons or brain regions over time [17]. Correlations between two brain areas can also occur because of a third structure that may act as a driver for the initially observed brain areas. This would artificially increase the apparent information integration.

Sensory/somatosensory stimulation could be used in order to infer the causal relationships between remote cortical regions, however sensory processing is modulated in peripheral as well as subcortical structures of the central nervous system before reaching the cortex. These relays may act as constraints disrupting efforts to assess the impact of one region on other hubs in the network. For this reason, direct brain stimulation has been proposed as a way of assessing effective connectivity, defined as the maximum impact that the activation of a brain area can have on all connected areas of the cortex [18,19]. These experiments are carried out in human subjects with TMS for brain stimulation and EEG as a readout modality.

Effective connectivity has been measured before in mice using all-optical methods [177]. Optogenetic stimulation was done in transgenic mice expressing channelrhodopsin, an optogenetic construct that can be stimulated with blue light. The readout was done with intrinsic optical imaging making use of the neurovascular coupling for functional readout [177]. This approach has the disadvantage that optogenetic control is only guaranteed for the neuronal population being stimulated and not for the brain activation readout. Additionally, our understanding of the neurovascular coupling remains incomplete and brain responses recorded like this represent a lowpass filtered version of the actual neuronal activation events. It is much more desirable to use fast GCaMP imaging in order to record neuronal activity directly and avoid any data losses caused by the transduction of neuronal activations to hemodynamic signals.

In this work, an all-optical experimental setup for measuring effective connectivity was introduced. Direct brain stimulation is done using laser activation of the red-shifted optogenetic tool ChrimsonR [171] and readout is provided by the widefield optical imaging system which records fluorescence information from transgenic mice that express GCaMP6s in cortical pyramidal neurons [124]. This enables us to record effective connectivity patterns while having complete genetic control over the populations of neurons being stimulated and recorded. Because GCaMP excitation is done with blue light and ChrimsonR stimulation necessitates red laser pulses, the functional readout can be done in parallel with optogenetic stimulation without crosstalk between the channels (Fig. 4.35). Stimulation with red laser light has the added benefit of deeper penetration in tissue, so stimulation can also be carried out through the skull without the need for invasive fiber optic guide placement.

The effective connectivity of the S1 and V1 cortices was recorded using optogenetic stimulation. Visual inspection of the results indicates that under low concentrations of isoflurane and medetomidine (corresponding to the persistent brain state), the patterns produced are more heterogeneous and less widespread, while during isoflurane anesthesia (the slow-wave state), wave-like activations were generated (Fig. 4.37 and 4.41).

These observations seem compatible with previously published results after TMS stimulations, during slow-wave sleep in human subjects. In this context, TMS stimulation generated either slow waves or activation patterns that did not spread beyond the point of stimulation [18,339]. In our case, optogenetic stimulation produced activations that always spread beyond the stimulated area in spite of showing variable intensities of activation.

Previous studies in isoflurane-anesthetized mice using calcium fluorescence fiber-photometry and optogenetic stimulation also reported slow-wave events being triggered after optogenetic stimulation [252]. Optogenetic stimulation in rats during low isoflurane anesthesia produced local BOLD responses in the S1 albeit after stimulation blocks that lasted tens of seconds [340]. A stimulation scheme involving 50 ms laser pulses was used and this is suitable for both generating slow-wave events in general anesthesia [252] and measuring the complexity of effective connectivity [300].

Optogenetic stimulations under medetomidine produced similar response complexity to low isoflurane levels. Both these drugs induce a persistent brain state with rich patterns of activation in segregated brain networks. Under Ketamine, a reduction in calcium fluorescence was recorded immediately after stimulation. This represents a reproducible result present in all mice from the S1 and V1 optogenetic stimulation cohorts (8 animals). Furthermore, these paradoxical responses were present concomitantly with increased spectral activity in the retrosplenial cortex in the 1-3 Hz spectral band (Fig. 4.46). The 1-3 Hz RSP rhythm had been previously described during spontaneous activity recordings [139] but this is the first report describing paradoxical response to optogenetic stimulation of pyramidal neurons during dissociation-unconsciousness. This so-called "saw tooth" appearance of the time-varying fluorescence signals resembles previously reported EEG findings where the authors report a periodic interruption of the gamma rhythm which is replaced by slower frequencies[275].

After this initial assessment, the segregation of functional cortical networks was quantified with BPD. In the case of isoflurane, the trend in BPD values from optogenetic imaging sessions was similar to spontaneous activity and the natural stimulation recordings with high values when complex network activity was present (1% iso. and med.) and low levels in the slow waves state (Fig. 4.39 and 4.43). Again there were no sudden decreases in BPD but rather gradual loss of cortical network segregation during the transition from low to high iso. concentrations. Spontaneous activity was always acquired first before S1 or V1 optogenetic recordings and it was impossible to statistically distinguish between segregation levels (measured by BPD) from spontaneous activity and optogenetically stimulated runs.

Next, the complexity of effective connectivity patterns was investigated using PCI-ST, a computational routine first developed for effective connectivity data acquired with EEG after TMS stimulation [301]. Because this measurement is based on a linear data reduction method (singular vector decomposition) it is applicable, in principle, to any type of functional data which contains responses to direct cortical stimulation[301].

The complexity of effective connectivity patterns, measured by PCI-ST, decreases progressively from 1% isoflurane to 1.6% isoflurane, and in 1.6% and 1.8%, PCI-ST reaches the lowest values. Again no phase transitions in cortical activity were present during the transition from the persistent state to the slow waves state.

During sedation with medetomidine, the complexity of effective connectivity patterns is indistinguishable from the isoflurane 1% condition, both conditions feature the persistent cortical state. Ketamine had lower levels of complexity than isoflurane 1%, though heterogeneous values did not allow us to find statistically significant differences (Fig. 4.39 and 4.43).

Previous studies in human subjects showed that with PCI it was possible to distinguish vigilance states like wakefulness, deep sleep, coma, and anesthesia. Less clear-cut conditions like minimally conscious states were also identified in this way [300,301]. To our knowledge, our study represents the first example of a controlled experiment where the arousal state was gradually manipulated and the progressive breakdown of effective connectivity was quantified using neuronal activation data. BPD measures the segregation of cortical networks while PCI quantifies the complexity of brain responses to optogenetic stimulation.

There seems to be a functional connection between complex functional connectivity patterns being replaced by propagating waves during spontaneous activity and complex effective connectivity responses breaking down to form stereotypical cortical responses after optogenetic stimulation. BPD values measured during the spontaneous recording that preceded the optogenetically stimulated data acquisition have a moderate explanatory power for PCI measurements (Fig. 4.40 and 4.44). This suggests a common network mechanism could mediate the observed effects.

5.6 Effects of psychoactive drugs and their relationship to functional cortical states

Psychoactive drugs were used to reproducibly induce brain states in order to study spontaneous activity, stimulus processing, and effective connectivity and find quantitative descriptors which enable us to develop data-driven computational tools to classify brain states and infer causal mechanisms responsible for the functional patterns observed. It was reasoned that both the type of pharmacological agent and the dosage would produce distinctive functional features.

Isoflurane potentiates GABA-A and Glycine receptor activity [233] and reduces the activity of glutamate receptors such as NMDA [234,235]. Because of these complex molecular interactions, isoflurane has sedative, anesthetic, and hypnotic properties. In low concentrations, isoflurane causes sedation as a result of GABA-ergic potentiation while high concentrations induce surgical-level anesthesia [216]. Previous research has focused on these two states and found during sedation spontaneous functional network dynamics were preserved and this is referred to as the “persistent” state. In surgical-level anesthesia propagating waves were observed and this has been termed the “slow wave” state [6,91].

In order to understand how persistent network activity is replaced by slow waves, brain activity under five different concentrations of isoflurane was studied. Functional compartmentalization was progressively lost between isoflurane 1% and isoflurane 1.6%. This transition was also accompanied by a change in functional network cortical features which gradually changed from a modular to a fully connected architecture. Additionally, global changes in cortical excitability are responsible for the transition from “persistent” to “slow-wave” brain state under isoflurane. Stimuli during the persistent state cause topologically complex cortical representations while the slow-wave state features stereotypical traveling activations. Furthermore, effective connectivity responses decrease in complexity in a similar way only to be replaced by traveling waves during surgical-level anesthesia.

The functional brain state transition under isoflurane results in propagating waves in the resting state, natural stimulation, and optogenetic stimulation. This could imply a common network mechanism is responsible for the observed changes. During the slow-wave state, traveling waves represent the loss of the cortex's ability to contain activation events to anatomically specialized areas such that all activity becomes global and stereotypical.

A possible mechanism underlying these changes could be represented by the loss of lateral inhibition. This refers to the neighboring neurons being inhibited by the strong activation of a particular neuronal cluster, this helps limit the spread of neuronal activity which could otherwise lead to positive feedback effects and epileptic activity [341,342]. Alternatively, feedback disruptions between the cortex and deeper structures like the thalamus and claustrum could lead to inadequate timing of action potentials and potentially to global activation phenomena. A recent study found evidence that a subpopulation of claustral neurons was controlling cortical interneuron activity to induce down states during slow-wave activity[258]. The precise mechanism responsible for these effects was not experimentally addressed in this work and will have to be the subject of future research.

Slow waves, are observed during sleep [243,248] quiet wakefulness [242], and anesthesia [6,91,252,253]. Although the general features of slow waves during sleep and anesthesia appear similar [343], during anesthesia longer silent periods are observed and slow waves are more synchronous [150,253]. Slow waves during anesthesia do not help group spindle activity which is relevant to memory consolidation during sleep [344]. In spite of these differences, cortical slow waves recruit the thalamus and hippocampus indicating that they could play a synchronizing role in wide brain regions during states of unconsciousness [91].

Medetomidine induces an $\alpha 2$ adrenergic receptor-mediated alteration of arousal by mainly targetting neurons in the locus coeruleus [218] causing a reduction of norepinephrine release in this area [219]. The hyperpolarization of the locus coeruleus by medetomidine also causes an activation of the preoptic area, inducing a state which is behaviourally similar to non-REM sleep, and for this reason, medetomidine is used as a sedative in human medicine. [216]. Medetomidine sedation is used in neuroimaging studies because it preserves the patterns of activation that make up the DMN [222,223].

Sedation with medetomidine tended to have higher levels of functional network segregation compared to sedation with isoflurane, though the difference was not statistically significant. The same trend was observed when assessing the functional network measures which indicate a more pronounced tendency towards functional network clustering under medetomidine. Metastability values for medetomidine were also comparable with isoflurane 1% across all frequency bands. Sedation with medetomidine had similar values of response complexity to optogenetic stimulation compared to isoflurane 1%. These results suggest that medetomidine tends to produce a more complex brain state than isoflurane 1%. Medetomidine seems to preserve compartmentalized functional activity which others have found to be similar to the awake state [222,223].

Studying the persistent state present under medetomidine is not a substitute for awake experiments since med. modulates the interactions between brain networks. Fewer negative correlations between related brain regions were present during medetomidine sedation as opposed to the awake state [199]. Additionally, the absence of high-frequency rhythms like the Gamma oscillation represents a major point of difference between the awake and the sedated states [220]. Notwithstanding, medetomidine sedation is employed in neuroimaging studies because it preserves lower frequency patterns of activation that are similar to the awake state [222,223].

Ketamine binds to a subunit of the NMDA receptor that is different from the glutamate binding site and causes a conformational change that inactivates the receptor. Early after injection, ketamine blocks interneurons causing disinhibition of the pyramidal neuron network, subsequently, ketamine also inhibits pyramidal neurons leading to a general decrease in cortical activity [139,275,345]. Ketamine induces dissociative states in mammals and has for this reason been used in models of psychiatric conditions [139,268,279] as well as a potential treatment for depressive disorders [345].

Based on BPD, it was not possible to distinguish between sedation with isoflurane 1% and ketamine, whereas there was a clear trend towards statistical significance when compared to medetomidine. Network characteristics extracted from spontaneous brain activity under ketamine were indistinguishable from medetomidine and isoflurane across all computed metrics. Intriguingly, metastability measurements show that ketamine resembles medetomidine in the higher frequency range and 1.8% isoflurane in the lower frequencies.

A prominent 1-3Hz rhythm in the retrosplenial cortex was observed during spontaneous activity, confirming previously published results [139]. A general decrease in cortical activity was observed after optogenetic stimulation, a finding that was unique to ketamine. This result was observed concomitantly with the prominent 1-3Hz retrosplenial rhythm. Upon optogenetic stimulation, this oscillation was paused and slower frequencies became more prominent. This type of alternation between low and high amplitude oscillations has been previously observed with EEG in spontaneous activity recordings [247]. The most plausible mechanism that could underlie this intriguing finding is the activation of interneurons which would have a global effect on the whole network. It is not clear how such activation would occur but the complex and unequal effects of ketamine on interneurons and pyramidal neurons described above could potentially play an important role in explaining this finding.

It is clear that ketamine acts on the neural network in a way that is distinctive from medetomidine and isoflurane leading us to believe that the functional brain state induced by medetomidine is distinct from both the persistent and slow-wave states. Further study of the dissociated state will bring new insights into brain physiology and potentially also illuminate new avenues for the treatment of neuropsychiatric diseases.

From the data presented above, it can be concluded that the pharmacologically induced brain states studied in this work are highly relevant to our understanding of spontaneously occurring brain states. However, they recapitulate only some functional features of the spontaneously occurring brain states and this should be factored into the design of future experimental work.

5.7 Computational tools for functional cortical state modeling

The discussion above indicates that no single computational metric can deliver satisfactory insights into spontaneous brain activity, stimulus processing, and effective connectivity features as a function of brain state. In the following, the usefulness of the computational tools that were employed in this study will be assessed.

Brain pattern dimensionality (BPD) is a novel metric developed in the course of this work for the assessment of functional network segregation. This tool is accurate in classifying functional cortical states and transitions from the persistent to the slow waves state. This is to our knowledge the first metric of its kind that is adapted to wide-field fluorescence imaging.

BPD is a data-driven computation that does not include free, tunable parameters and is thus robust and potentially generalizable to other neurorecording modalities. BPD could be adapted to 3D functional imaging methods such as fMRI and high-density electrophysiological applications. Effective dimensionality can be artificially increased by noise, for this reason, a strategy for isolating neuronal signals from raw imaging data was also proposed.

BPD was accurate in identifying functional states from spontaneous activity, natural stimulation, and optogenetic stimulation recordings indicating that it could be used to standardize brain stimulation experiments for the purpose of obtaining more consistent insights into cortical information processing. This step can be done in postprocessing and does not require additional experimental procedures or the modification of existing imaging and stimulation protocols. Brain responses to stimulation depend on the functional state so, a functional state estimation should be included in processing pipelines for brain imaging experiments.

BPD offers a very concise and easy to interpret summary of the state of segregation of functional neuronal networks, however, it does not offer specific insights into brain stimulation responses as it analyzes global cortical activity. It also cannot differentiate between brain states that have a similar level of complexity, for example between isoflurane sedation and dissociation-unconsciousness (Fig. 4.21). Another drawback is that BPD is not designed to assess cortical information integration. It could be argued that the principal components used to assess effective dimensionality already contain some evidence of information integration. Each principal component contains a value for every pixel in the brain and for every time step in the imaging sequence and often, multiple anatomically-defined brain regions are present in the same principal component i.e. integrating information. Also, BPD relies on the extraction of linear features with PCA and it should be explored if including non-linear features would add to its accuracy.

Network measures of functional connectivity can assess both integration and segregation and the computational procedure is generalizable to any functional imaging modality. The metrics estimated have a clear mathematical description and a physiological interpretation [16].

However, the procedure relies on prior assumptions and tunable parameters. The first assumption refers to the choice of nodes, i.e the cortical parcellation in brain regions from which time-varying signals are extracted. Secondly, Pearson's correlation between nodes is calculated and as explained in the effective connectivity section correlations can be artificially increased in certain conditions. Thirdly, network modeling involves setting a correlation threshold for the network connections considered meaningful and included in the analysis. This represents a tunable parameter that is left up to the researcher. Furthermore, negative correlations are not considered in the analysis and this seems to be due to current limitations in the theoretical understanding of information theory [16].

Complex network measures of functional connectivity have been developed for spontaneous recordings and should not be used on data from stimulated imaging sessions. This approach is useful as validation for BPD in the characterization of the transitions from sedation to anesthesia under isoflurane. Based on these metrics we could not distinguish between 1% isoflurane, medetomidine, and ketamine(Fig. 4.24 and 4.25).

LEiDA and probabilistic metastable substates assess integration and segregation in a more detailed way. Functional connectivity motifs are identified and the probability, lifetime, and switching characteristics are assessed. One important advantage of LEiDA over BPD is that it has a temporal dimension because metastable features are defined as persisting over time [333]. Free parameters included in the computation concern the bandpass filter options and the number of substates that will be statistically compared. Also, LEiDA, like the network measures relies on signals extracted from predefined cortical regions.

This analytical tool can be used to evaluate any type of functional brain imaging data, with or without stimulation and experimental conditions are statistically compared against each other. It was successful in differentiating between different brain states as well as between different pharmacological conditions using LEIDA.

Furthermore, it is possible to differentiate between hind paw and visual stimulations and between V1 and S1 optogenetic stimulations using this computational routine. A drawback is represented by the high number of substates generated which can make interpretation by the researcher difficult. In this respect, the spatial renderings of the metastable substates are very helpful for extracting physiologically meaningful interpretations (Fig. 4.27 and 4.28).

PCI was developed as a metric for assessing the state of consciousness in human subjects using data on effective connectivity acquired with EEG after direct cortical stimulation with TMS. In its initial formulation, PCI involved the computation of the EEG sources of activation after TMS stimulation, the binarization of those sources, and the assessment of nonredundant information in these images by Lempel-Ziv compression [300]. More recently, a new computational strategy was put forward and this involves feature extraction with singular vector decomposition, the calculation of distance matrices, and the iterative thresholding of these matrices in order to find the maximal difference in “transitions” between baseline activity and stimulation responses. This latter technique is called PCI-ST and is the one that was used in this work [301]. Essentially, both methods measure the complexity of effective connectivity responses and are based on the assumption that, during the conscious state, cortical responses to stimulation should be more complex compared to the unconsciousness state.

Effective connectivity contains information on both segregation and integration. Local responses to stimulation suggest a loss of integration while global but stereotypical activations point to a loss of segregation [300]. For these measurements, a laborious experimental procedure has to be carried out. The brain has to be stimulated directly either with TMS or implanted electrodes and responses have to be recorded with either EEG or LFP. Spontaneous activity cannot be used for these determinations. Also, PCI was calculated for datasets with hind paw and visual stimulations and PCI-ST values were not useful for inferring brain state characteristics.

Methodologically TMS potentials are processed with SVD which is a linear feature extraction method, and potentially, non-linear data characteristics could be lost in this process. A single threshold is used in order to determine the number of transitions between the preand poststimulus periods and the strategy for choosing this threshold is precisely defined. The stability of this approach especially for small sample sizes is questionable, moreover, a threshold that could be generalized to other datasets would be more desirable.

Like BPD, PCI-ST is easily interpretable, the higher the value, the more complex the effective connectivity responses. PCI-ST can successfully differentiate between brain states during the isoflurane-mediated transition from sedation to anesthesia. States like sedation with medetomidine and dissociation with ketamine could not always be distinguished from isoflurane 1% (Fig. 4.39 and 4.43).

In our experience, when assessing the features of a functional brain state, data-driven computational methods should always be preferred over ones that include tunable parameters. Next, the choice of method is dictated by the type of data to be analized and the type of information that needs to be obtained. The conciseness of the metric represents another consideration to be taken into account.

This work demonstrated how a thorough characterization of spontaneous activity, stimulus responses, and effective connectivity can be achieved using BPD, network metrics, LEiDA, and PCI-ST. No single method is successful in capturing all the aspects included in the data but this is not surprising given the complexity of our experiments. Strong evidence presented here suggests that an assessment of the functional brain state should be included in the analysis of functional brain imaging data. BPD could represent a viable alternative for this task due to its versatility with respect to the types of data that can be assessed.

6

Conclusion and outlook

6.1 Conclusive summary

The work presented in this thesis concerned the study and quantitative assessment of functional cortical states in mice in an effort to understand their influence on spontaneous brain activity and information processing. First, I reviewed the state of the art on reporters of neuronal activity, brain imaging technologies, and functional states of the brain. Next, the thesis details the material and computational resources used in this work with an emphasis on the development of the custom wide-field imaging microscope which was used in most of the experiments presented here. Next, the results were presented and discussed in the context of current theories of cortical network organization and information processing. Finally, concrete ways were presented in which this work could be expanded for the purpose of implementing closed-loop optogenetic stimulation capability.

To summarize we will briefly refer to the objectives formulated in Section 1.4.

Design and assemble an optical instrument suited for acquiring fluorescence imaging data from the whole mouse cortex. A dual-camera wide-field fluorescence microscope was designed for imaging neuronal activation events in transgenic mice expressing the fluorescent calcium sensor GCaMP6s in cortical pyramidal neurons. The imaging system has a spatial resolution of 0.03mm/pixel and a maximum temporal resolution of 100 frames/sec. The integrated feature of hemodynamic imaging with 395nm reflectance and ICG fluorescent blood pool agents allowed us to identify and efficiently remove physiological noise using a bespoke postprocessing pipeline. Integrated into the setup is a red laser for optogenetic stimulation, so GCaMP6s imaging can be done simultaneously with optogenetic stimulation of the red-shifted opsin ChrimsonR.

Develop a computational method to quantify functional brain states based only on imaging data. The novel metric Brain Pattern Dimensionality was designed for assessing the level of functional network segregation based solely on brain imaging datasets. This computational technique accurately predicts the brain state from spontaneous activity recordings as well as datasets where sensory or optogenetic stimulation was carried out. Because cortical data processing is strongly dependent on the brain state, this computational tool could be used in the future for standardizing functional brain imaging experiments and ensuring more consistent brain stimulation results.

Investigate how spontaneous brain activity is influenced by sedation-unconsciousness, dissociation-unconsciousness, and anesthesia. Information integration and segregation were assessed with BPD, complex network measures of FC, and metastability measures. No “phase transitions” in functional state metrics were observed during transitions from the persistent state to the slow-wave state but rather gradual trends towards simpler brain activation patterns.

There are two hypotheses that seek to explain the effects of anesthesia on the brain. The first claims anesthesia disrupts cortical networks leading to functional brain regions becoming less coordinated in their activity. The second holds that anesthesia synchronizes activity across large brain regions leading to a loss of spatial confinement of brain activity. This impedes complex information processing and causes a loss of awareness. By studying the activation of cortical pyramidal neurons we have found evidence supporting the second hypothesis.

Develop a strategy for the coexpression of a fluorescent calcium indicator and an optogenetic actuator in excitatory cortical neurons. ChrimsonR which is activated by red laser light and GCaMP6s which can be stimulated by blue wavelengths were coexpressed in excitatory cortical neurons. This spectral separation allows to carry out symultaneous optogenetic stimulations and image calcium transients in pyramidal neurons. This is the first such implementation for wide-field optical imaging and it enabled the detailed study of brain responses to optogenetic stimulation as a function of the brain state. The experimental setup for simultaneous imaging and optogenetic stimulation could be expanded to include closed-loop spatio-temporal control of activated cortical neural networks.

Investigate how somatosensory, visual and optogenetic cortical responses to stimulation are influenced by the functional state of cortical networks. The somatosensory and visual cortices were targeted with hind paw, visual and optogenetic stimulations, and computational strategies were presented for distinguishing between the elicited patterns of activation. In functional states induced by medetomidine and isoflurane, the level of functional network segregation was directly proportional to the complexity of brain responses to optogenetic stimulation. Surprisingly, in ketamine-induced dissociation-unconsciousness, a general decrease in brain activity after optogenetic stimulation was observed. This finding was associated with increased 1-3Hz activity in the retrosplenial cortex. In this state, high levels of functional network segregation and stereotypical responses to stimulation are present. These findings suggest that ketamine-induced dissociation unconsciousness represents a functional state distinctive from the persistent and slow-wave states.

The findings resulting from this work were presented in the context of existing descriptions of functional brain states which are usually regarded by the research community as discrete categories. We here show that brain states that underlie states of vigilance form a continuum and pure states such as the persistent or slow waves state are difficult to define precisely. The central finding of this research is that functional brain states can be characterized by a set of continuous measurements and the aggregate of these metrics will provide a superior description of the brain state than qualitative assignment to predefined categories.

More broadly, this thesis presents empirical and computational strategies for all-optical dissection of mesoscale brain networks that will help expose cell-type-specific mechanisms relevant to healthy brain function and brain pathologies. The mechanistic understanding gained from studying the interactions of genetically labeled neuronal populations could form the basis of theoretical brain models capable of predicting interventions that restore healthy brain function in cases of neuropsychiatric illness.

6.2 Outlook and future perspectives

6.2.1 Explaining brain stimulation response variability using functional brain states

The results presented in this work demonstrate that brain responses to stimulation are heterogeneous and strongly depend on the functional state of cortical networks. Experimentation was conducted under tightly controlled conditions and functional states like the persistent state, slow-wave state, and dissociation were induced in a reproducible manner with the use of psychoactive drugs. In this way, brain stimulations could be carried out under conditions that are not as dynamic as those present during the awake state.

During wakefulness, brain states change on time scales of milliseconds to seconds as neurons are heavily modulated by the spatiotemporal dynamics of spontaneous network activity [185]. It was shown in rodents that rapid changes in spontaneous cortical activity from high-amplitude to low-frequency fluctuations occur when animals shift from quiet wakefulness to active behavior [183]. Reports in rats indicate that brain state changes can be global or localized to circumscribed areas of the cortex [184].

These changes in the state of cortical networks are likely to have an impact on cortical information processing. Intersubjective variability has long been recognized as a challenge for the replicability of stimulation results after TMS. Intra-individual variability across experimental sessions and trials is thought to arise from changes in the brain state during stimulation experiments.

A possible way to overcome these challenges would be to implement closed-loop stimulation systems. These monitor the functional parameters of the brain and adjust the characteristics of brain stimulations to achieve the desired outcome, for example, a brain state. Such systems have been implemented for TMS and EEG [346] but are challenging to use in imaging studies because of the high data load. Alternatively, surrogate measurements for the determination of the arousal state have been proposed. The pupil diameter can serve as a proxy for the brain state as demonstrated using hybrid fMRI and optical fiber calcium recordings[347].

A better way to account for brain-state-related effects on stimulation experiments is to use brain activity to infer the brain state offline for better standardization of brain stimulation outcomes. BPD was introduced in this work as a computation that can be carried out post-hoc on spontaneous brain recordings as well as stimulated imaging sessions. It would be interesting to test whether this strategy for brain state estimation can be carried out using data from fMRI or electrophysiology recordings.

6.2.2 Using functional and effective connectivity to illuminate the mechanisms of brain disease

Functional connectivity has been used to assess cortical information integration and segregation. Alterations in brain FC have the potential to provide useful biomarkers of systems-level brain disease. Large fMRI datasets from patient and control groups have been used for the development of analytical tools for FC assessment.

A variety of measurement strategies have been proposed for the purpose of assessing static FC, for example calculating correlations between regions of interest and modeling the features of functional brain networks [16]. For the evaluation of dynamic functional connectivity, sliding window techniques and intrinsic connectivity states are obtained using decomposition methods.

Challenges persist in finding FC measures with high diagnostic accuracy and ones that offer insights into the mechanisms of neuropsychiatric disease. One of the difficulties is represented by lacking gold standards for diagnostic procedures which are often based on interviews and symptomatology. The data acquired in patient cohorts often comes from heterogeneous neurorecording protocols and data analysis relies on feature extraction routines that produce functional features which can be redundant and may lead to inaccurate results [348]. For these reasons, FC metrics do not currently constitute major evaluation criteria for neuropsychiatric disease.

Notwithstanding, abnormal spontaneous functional network dynamics have been observed in Alzheimer's disease, Parkinson's disease, depression, schizophrenia, epilepsy, and drug addiction[209–214].

Specific oscillations can offer insights into disease progression and underlying mechanisms. Sleep slow waves are disrupted in Alzheimer's disease and may play a role in impaired memory formation [150]. Slow waves are also impaired in children with attention-deficit/hyperactivity disorder where they may play a role in synaptic plasticity [349].

Slow-wave activity is associated with the reduction of functional network segregation levels measured by BPD. Measuring BPD might prove useful in quantifying the disruption of these rhythms in preclinical trials because BPD can be used to assess functional network properties across a wide spectrum of brain activity states.

Effective connectivity gives a superior readout of cortical information integration compared to FC [14,18]. Effective connectivity can help diminish some of the bias inherent in using correlations-based methods for brain function assessment [14,350]. Effective connectivity can provide information about the directionality of signaling pathways and this feature has been used for the purpose of studying DMN activity in Alzheimer's disease [351] and multiple sclerosis [352].

The calculation of effective connectivity remains challenging and often depends on complex computational routines [14,350]. Measurements of effective connectivity in humans using perturbational approaches have proved useful in identifying the vigilance state in patients [300,301] and elucidating brain responses to stimulation during sleep [18].

A more direct strategy for measuring effective connectivity could provide insight into the mechanisms behind neuropsychiatric diseases. An approach to measuring effective connectivity with an all-optical method, using optogenetics was presented in this thesis. This method allows control over the genetic identity of the neuronal populations stimulated (with the use of ChrimsonR) and recorded (with the use of GCaMP6s). This level of control could prove useful in elucidating cell-type-specific mechanisms responsible for brain disease.

For our method to be applied in mouse models of brain disease, it would be necessary to express a fluorescent calcium indicator in cortical neurons. This could be feasibly achieved with intravenous AAV injections [110] provided that the modification does not alter the disease phenotype. Using GCaMP reporter mice, it has been shown that stroke affects functional connectivity patterns over the long term [148]. Studies could be done using our method for measuring effective connectivity in stroke models, potentially providing useful insights into information integration poststroke and cortical remodeling.

6.2.3 Perspectives for neuroengineering

"Neural engineering leverages neuroscience and engineering methods to analyze neurological function as well as to design solutions to problems associated with neurological limitations and dysfunction" [353]. Acquiring information about brain activation and being able to modulate the activity of neuronal systems are essential to neuroengineering.

In the course of this project, I have developed a microscope for monitoring calcium transients across the mouse cortex with the integrated capability of optogenetic brain stimulation. In its current form, this device has the primary function of revealing the features of effective connectivity. This system could form the basis of a closed-loop stimulation setup through the addition of a computer that would analyze stimulation outcomes and compare them against the desired activation pattern via a loss function. Hardware modifications would be needed in order to implement this concept. So far, we have used a continuous laser for optogenetic stimulation which is limited in its maximum output power. This setup is sufficient for point stimulation but expanding the stimulation to broader areas of the cortex would be desirable in a closed-loop system. Using a pulsed laser would allow us to achieve higher energies for stimulation such that sufficient power could be distributed across the whole mouse brain. It would be desirable to stimulate multiple brain regions simultaneously and for this micromirror devices could be used to generate spatial patterns of activation with arbitrarily complex shapes.

Current closed-loop stimulation systems like those implemented in deep brain stimulation have to deal with a relatively low amount of incoming data from a small number of electrodes. This data can be analyzed online with existing signal processing tools. In the case of our microscope, the same speed of processing would have to be ensured but with a much higher data load consisting of imaging datasets. Potentially this could be achieved with fast neural-network-based feature extraction that would have to be trained on large volumes of sample data.

Apart from these hardware changes, a mouse model expressing both ChrimsonR and GCaMP6s in neurons across the cortex would have to be developed, ensuring the consistent expression of both proteins across multiple animals and across the whole cortex. Alternatively, strong pan-cortical expression can be achieved by injecting AAV9 constructs intravenously [110,112].

Following experimental strategies inspired by research in dynamical physical systems, the activity of the cortex was perturbed with global (psychoactive chemicals) and local (sensory, and optogenetic) interventions in order to infer underlying network mechanisms. In this work, it was shown that it is possible to elicit simple transitions i.e. from off to on states, with optogenetics during anesthesia and the resulting activations travel like slow waves across the cortex. Slow waves are disrupted in Alzheimer's disease [150,178,354] and autism [355]. Even simple interventions like restoring slow waves could prove beneficial for the treatment of systems-level brain disease as demonstrated in mouse models of Alzheimer's disease [178,337].

Predicting interventions that force transitions from pathological to healthy brain states is a long-term goal that will enable and accelerate the discovery of efficient treatment strategies [11,356]. Achieving this goal will require interdisciplinary research by engineers, chemists, materials scientists, synthetic biologists, data scientists, neuroscientists, and clinicians.

List of Publications

Bodea S-V, Thalmeyer D, Sigmund F, Piraud M, Wohlschläger A, Jüstel D, Jacob SN, Stroh A, Westmeyer GG. Functional brain states modulate spontaneous activity and stimulus processing in excitatory cortical networks. Submitted

Efremova MV, **Bodea S-V**, Sigmund F, Semkina A, Westmeyer GG, Abakumov MA. Genetically Encoded Self-Assembling Iron Oxide Nanoparticles as a Possible Platform for Cancer-Cell Tracking. Pharmaceutics. 2021;13. doi:10.3390/pharmaceutics13030397

Bodea S-V, Westmeyer GG. Photoacoustic Neuroimaging - Perspectives on a Maturing Imaging Technique and its Applications in Neuroscience. Front Neurosci. 2021 Jun 10;15:655247. doi: 10.3389/fnins.2021.655247 - Review

Conference proceedings

Bodea S-V, Aedo-Jury F, Lingg J, Stroh A, Westmeyer GG. Mesoscopic imaging and optogenetic initiation of slow waves in mice, European Molecular Imaging Meeting (EMIM) 2020

Aedo-Jury F, **Bodea S-V**, Westmeyer GG, Stroh A. Spatio-temporal dynamics of cortical slow waves evoked by optogenetic stimulation and unveiled by fast line fMRI scanning fMRI. European Molecular Imaging Meeting (EMIM) 2020

Publications

Published material and reprint permissions

Figure 4.5 was previously published in: Efremova MV, **Bodea S-V**, Sigmund F, Semkina A, Westmeyer GG, Abakumov MA. Genetically Encoded Self-Assembling Iron Oxide Nanoparticles as a Possible Platform for Cancer-Cell Tracking. Pharmaceutics. 2021;13. doi:10.3390/pharmaceutics13030397

Permissions to reproduce both text and images are granted through the author rights in copyright transfer agreements for the above mentioned publications and have been obtained in written electronic form by the editorial boards.

Acknowledgments

First and foremost, I would like to express my gratitude to my supervisor Prof. Dr. Gil Westmeyer, who guided my quest to understand the brain. He inspired me with his enthusiasm, his wealth of ideas and his determination to address the questions at the cutting edge of neuroscience. His outstanding knowledge and forthcoming attitude attitude shaped an excellent working environment.

I would like to thank the members of my thesis committee Dr. Albrecht Stroh and Prof. Dr. Simon Jacob for their guidance throughout this project. I am especially grateful to Prof. Stroh for welcoming me on multiple occasions to his laboratory and teaching me advanced imaging techniques. His help and the help of his team, especially Dr. Miriam Schwalm and Dr. Felipe Aedo-Jury, allowed me to get a head start in my brain imaging project. I am also grateful to Prof. Dr. Simon Jacob who's sharp insights motivated me to find new angles to look at my work. Also I was fortunate to benefit from the experience and advice of Prof. Afra Wohlschläger who brought her insights to my project.

I also valued working in the dynamic environment of our institute which never ceased to provide fertile ground for new ideas to flourish. I would like to acknowledge the help of Dr. Panagiotis Symvoulidis who advised me on building the imaging setup I used for data acquisition. My gratitude also goes to Dr. Felix Sigmund and Dr. Mariia Efremova for their active involvement in my research project and their joyful friendship. Our technical assistants, Hannes Rolbieski, and Anja Amer and IBMI staff Sarah Glasl, Uwe Klemm, Pia Anzenhofer always had a solution on hand for challenges large and small and i am thankful for their support.

I was fortunate to have the support of the Helmholtz AI team led by Dr. Marie Piraud and I am grateful for the collaboration with Dr. Dominik Thalmeyer and Dr. Dominik Jüstel who had a decisive contribution the development of the bespoke computational tools used in my project.

My gratitude also goes out to Dr. Oliver Bruns and his colleagues Dr. Andriy Chmyrov and Jakob Lingg for sharing their wealth of experience in optical engineering and also often sharing their hardware.

Further, I would like to thank Desislava Zlatanova, Dr. Katrin Offe, Bettina Kratzer, and Raphaela Blum for helping me navigate the 'Medical Life Science and Technology' Ph.D. program.

I am also filled with joy thinking of all my friends in München for accompanying me climbing, hiking, dancing dining, protesting and travelling. It was great fun and you were

always an inspiration.

Finally, I would like to express the deepest gratitude to my parents and my brother who supported me and helped me at every step along the way. I am very fortunate you were at my side.

Bibliography

1. Bennett MR, Dennett D, Dennett DC, Hacker P. Neuroscience and philosophy: Brain, mind, and language. 2007.

2. Sporns O, Tononi G, Kötter R. The Human Connectome: A Structural Description of the Human Brain. PLoS Comput Biol. 2005;1: e42.

3. Lynn CW, Bassett DS. The physics of brain network structure, function and control. Nature Reviews Physics. 2019;1: 318–332.

4. McCormick DA, Nestvogel DB, He BJ. Neuromodulation of Brain State and Behavior. Annu Rev Neurosci. 2020;43: 391–415.

5. D'Souza DV, Jonckers E, Bruns A, Künnecke B, von Kienlin M, Van der Linden A, et al. Preserved modular network organization in the sedated rat brain. PLoS One. 2014;9: e106156.

6. Aedo-Jury F, Schwalm M, Hamzehpour L, Stroh A. Brain states govern the spatio-temporal dynamics of resting-state functional connectivity. Elife. 2020;9. doi:10.7554/eLife.53186

7. Grinenko O, Li J, Mosher JC, Wang IZ, Bulacio JC, Gonzalez-Martinez J, et al. A fingerprint of the epileptogenic zone in human epilepsies. Brain. 2018;141: 117–131.

8. Woodward ND, Cascio CJ. Resting-State Functional Connectivity in Psychiatric Disorders. JAMA psychiatry . 2015. pp. 743–744.

9. Lozano AM, Lipsman N, Bergman H, Brown P, Chabardes S, Chang JW, et al. Deep brain stimulation: current challenges and future directions. Nat Rev Neurol. 2019;15: 148–160.

10. Krook-Magnuson E, Armstrong C, Oijala M, Soltesz I. On-demand optogenetic control of spontaneous seizures in temporal lobe epilepsy. Nat Commun. 2013;4: 1376.

11. Kringelbach ML, Deco G. Brain States and Transitions: Insights from Computational Neuroscience. Cell Rep. 2020;32: 108128.

12. Deco G, Tononi G, Boly M, Kringelbach ML. Rethinking segregation and integration: contributions of whole-brain modelling. Nat Rev Neurosci. 2015;16: 430–439.

13. Damoiseaux JS, Rombouts SARB, Barkhof F, Scheltens P, Stam CJ, Smith SM, et al. Consistent resting-state networks across healthy subjects. Proc Natl Acad Sci U S A.

2006;103: 13848–13853.

14. Friston KJ. Functional and effective connectivity in neuroimaging: A synthesis. Hum Brain Mapp. 1994;2: 56–78.

15. Sporns O. The human connectome: origins and challenges. Neuroimage. 2013;80: 53–61.

16. Rubinov M, Sporns O. Complex network measures of brain connectivity: uses and interpretations. Neuroimage. 2010;52: 1059–1069.

17. Friston KJ. Functional and effective connectivity: a review. Brain Connect. 2011;1: 13–36.

18. Massimini M, Ferrarelli F, Huber R, Esser SK, Singh H, Tononi G. Breakdown of cortical effective connectivity during sleep. Science. 2005;309: 2228–2232.

19. Sarasso S, Casali AG, Casarotto S, Rosanova M, Sinigaglia C, Massimini M. Consciousness and complexity: a consilience of evidence. Neurosci Conscious. 2021 [cited 4 Feb 2022]. doi:10.1093/nc/niab023

20. Kim TH, Zhang Y, Lecoq J, Jung JC, Li J, Zeng H, et al. Long-Term Optical Access to an Estimated One Million Neurons in the Live Mouse Cortex. Cell Rep. 2016;17: 3385–3394.

21. McGraw CM, Ward CS, Samaco RC. Genetic rodent models of brain disorders: Perspectives on experimental approaches and therapeutic strategies. Am J Med Genet C Semin Med Genet. 2017;175: 368–379.

22. Larame M-E, Boire D. Visual cortical areas of the mouse: comparison of parcellation and network structure with primates. Front Neural Circuits. 2015;8: 62.

23. Sunkin SM, Ng L, Lau C, Dolbeare T, Gilbert TL, Thompson CL, et al. Allen Brain Atlas: an integrated spatio-temporal portal for exploring the central nervous system. Nucleic Acids Res. 2013;41: D996–D1008.

24. Panzera LC, Hoppa MB. Genetically Encoded Voltage Indicators Are Illuminating Subcellular Physiology of the Axon. Front Cell Neurosci. 2019;13: 52.

25. Hodgkin AL, Huxley AF, Katz B. Measurement of current-voltage relations in the membrane of the giant axon of Loligo. J Physiol. 1952;116: 424–448.

26. Kole MHP, Stuart GJ. Signal processing in the axon initial segment. Neuron. 2012;73: 235–247.

27. Grienberger C, Konnerth A. Imaging calcium in neurons. Neuron. 2012;73: 862–885.

28. Schiller J, Helmchen F, Sakmann B. Spatial profile of dendritic calcium transients evoked by action potentials in rat neocortical pyramidal neurones. J Physiol. 1995;487 (Pt

3): 583–600.

29. Jones HC, Keep RF. The control of potassium concentration in the cerebrospinal fluid and brain interstitial fluid of developing rats. J Physiol. 1987;383: 441–453.

30. Egelman DM, Montague PR. Calcium dynamics in the extracellular space of mammalian neural tissue. Biophys J. 1999;76: 1856–1867.

31. Berridge MJ. Neuronal calcium signaling. Neuron. 1998;21: 13–26.

32. Berridge MJ, Lipp P, Bootman MD. The versatility and universality of calcium signalling. Nat Rev Mol Cell Biol. 2000;1: 11–21.

33. Baker PF, Hodgkin AL, Ridgway EB. Depolarization and calcium entry in squid giant axons. J Physiol. 1971;218: 709–755.

34. Tank DW, Sugimori M, Connor JA, Llinás RR. Spatially resolved calcium dynamics of mammalian Purkinje cells in cerebellar slice. Science. 1988;242: 773–777.

35. Sabatini BL, Oertner TG, Svoboda K. The life cycle of Ca(2+) ions in dendritic spines. Neuron. 2002;33: 439–452.

36. Ali F, Kwan AC. Interpreting in vivo calcium signals from neuronal cell bodies, axons, and dendrites: a review. NPh. 2019;7: 011402.

37. Kerr JND, Greenberg D, Helmchen F. Imaging input and output of neocortical networks in vivo. Proc Natl Acad Sci U S A. 2005;102: 14063–14068.

38. Tian L, Hires SA, Mao T, Huber D, Chiappe ME, Chalasani SH, et al. Imaging neural activity in worms, flies and mice with improved GCaMP calcium indicators. Nat Methods. 2009;6: 875–881.

39. Kwan AC, Dan Y. Dissection of cortical microcircuits by single-neuron stimulation in vivo. Curr Biol. 2012;22: 1459–1467.

40. Chen T-W, Wardill TJ, Sun Y, Pulver SR, Renninger SL, Baohan A, et al. Ultrasensitive fluorescent proteins for imaging neuronal activity. Nature. 2013;499: 295–300.

41. Fiala T, Wang J, Dunn M, Šebej P, Choi SJ, Nwadibia EC, et al. Chemical Targeting of Voltage Sensitive Dyes to Specific Cells and Molecules in the Brain. J Am Chem Soc. 2020;142: 9285–9301.

42. Knöpfel T, Song C. Optical voltage imaging in neurons: moving from technology development to practical tool. Nat Rev Neurosci. 2019;20: 719–727.

43. Shimomura O. Membrane permeability of coelenterazine analogues measured with fish eggs. Biochem J. 1997;326 (Pt 2): 297–298.

44. Chiesa A, Rapizzi E, Tosello V, Pinton P, de Virgilio M, Fogarty KE, et al. Recombinant aequorin and green fluorescent protein as valuable tools in the study of cell signalling. Biochem J. 2001;355: 1–12.

45. Tsien RY. A non-disruptive technique for loading calcium buffers and indicators into cells. Nature. 1981;290: 527–528.

46. Tsien RY. New calcium indicators and buffers with high selectivity against magnesium and protons: design, synthesis, and properties of prototype structures. Biochemistry. 1980;19: 2396–2404.

47. Tsien RY, Rink TJ, Poenie M. Measurement of cytosolic free Ca2+ in individual small cells using fluorescence microscopy with dual excitation wavelengths. Cell Calcium. 1985;6: 145–157.

48. Shemetov AA, Monakhov MV, Zhang Q, Canton-Josh JE, Kumar M, Chen M, et al. A near-infrared genetically encoded calcium indicator for in vivo imaging. Nat Biotechnol. 2020. doi:10.1038/s41587-020-0710-1

49. Stepanenko OV, Stepanenko OV, Kuznetsova IM, Verkhusha VV, Turoverov KK. Beta-barrel scaffold of fluorescent proteins: folding, stability and role in chromophore formation. Int Rev Cell Mol Biol. 2013;302: 221–278.

50. Nakai J, Ohkura M, Imoto K. A high signal-to-noise Ca2+ probe composed of a single green fluorescent protein. Nat Biotechnol. 2001;19: 137–141.

51. Zhang Y, Rózsa M, Bushey D, Zheng J, Reep D, Broussard GJ, et al. jGCaMP8 Fast Genetically Encoded Calcium Indicators. 2020. doi:10.25378/janelia.13148243.v1

52. Sun XR, Badura A, Pacheco DA, Lynch LA, Schneider ER, Taylor MP, et al. Fast GCaMPs for improved tracking of neuronal activity. Nat Commun. 2013;4: 1–10.

53. Dana H, Sun Y, Mohar B, Hulse BK, Kerlin AM, Hasseman JP, et al. High-performance calcium sensors for imaging activity in neuronal populations and microcompartments. Nat Methods. 2019;16: 649–657.

54. Zhao Y, Araki S, Wu J, Teramoto T, Chang Y-F, Nakano M, et al. An expanded palette of genetically encoded Ca2+ indicators. Science. 2011;333: 1888–1891.

55. Qian Y, Piatkevich KD, Mc Larney B, Abdelfattah AS, Mehta S, Murdock MH, et al. A genetically encoded near-infrared fluorescent calcium ion indicator. Nat Methods. 2019;16: 171–174.

56. Bruns OT, Bischof TS, Harris DK, Franke D, Shi Y, Riedemann L, et al. Next-generation in vivo optical imaging with short-wave infrared quantum dots. Nat Biomed Eng. 2017;1. doi:10.1038/s41551-017-0056

57. Ntziachristos V. Going deeper than microscopy: the optical imaging frontier in biology. Nat Methods. 2010;7: 603–614.

58. Bi X, Beck C, Gong Y. Genetically Encoded Fluorescent Indicators for Imaging Brain Chemistry. Biosensors. 2021;11. doi:10.3390/bios11040116

59. Hoang H, Sato M-A, Shinomoto S, Tsutsumi S, Hashizume M, Ishikawa T, et al. Improved hyperacuity estimation of spike timing from calcium imaging. Sci Rep. 2020;10: 17844.

60. Pnevmatikakis EA, Merel J, Pakman A, Paninski L. Bayesian spike inference from calcium imaging data. 2013 Asilomar Conference on Signals, Systems and Computers. 2013. pp. 349–353.

61. Vogelstein JT, Watson BO, Packer AM, Yuste R, Jedynak B, Paninski L. Spike Inference from Calcium Imaging Using Sequential Monte Carlo Methods. Biophys J. 2009;97: 636–655.

62. Pachitariu M, Stringer C, Harris KD. Robustness of Spike Deconvolution for Neuronal Calcium Imaging. J Neurosci. 2018;38: 7976–7985.

63. Li X, Zhang G, Wu J, Zhang Y, Zhao Z, Lin X, et al. Reinforcing neuron extraction and spike inference in calcium imaging using deep self-supervised denoising. Nat Methods. 2021;18: 1395–1400.

64. Rupprecht P, Carta S, Hoffmann A, Echizen M, Blot A, Kwan AC, et al. A database and deep learning toolbox for noise-optimized, generalized spike inference from calcium imaging. Nat Neurosci. 2021;24: 1324–1337.

65. Hyder F, Rothman DL, Bennett MR. Cortical energy demands of signaling and nonsignaling components in brain are conserved across mammalian species and activity levels. Proc Natl Acad Sci U S A. 2013;110: 3549–3554.

66. Shulman RG, Hyder F, Rothman DL. Cerebral energetics and the glycogen shunt: Neurochemical basis of functional imaging. Proc Natl Acad Sci U S A. 2001;98: 6417–6422.

67. Harris JJ, Jolivet R, Attwell D. Synaptic energy use and supply. Neuron. 2012;75: 762–777.

68. Magistretti PJ, Pellerin L. Cellular mechanisms of brain energy metabolism and their relevance to functional brain imaging. Philos Trans R Soc Lond B Biol Sci. 1999;354: 1155–1163.

69. Roy CS, Sherrington CS. On the Regulation of the Blood-supply of the Brain. J Physiol. 1890;11: 85–158.17.

70. Watts ME, Pocock R, Claudianos C. Brain Energy and Oxygen Metabolism: Emerging Role in Normal Function and Disease. Front Mol Neurosci. 2018;11: 216.

71. Miki N, Kawabe Y, Kuriyama K. Activation of cerebral guanylate cyclase by nitric oxide. Biochem Biophys Res Commun. 1977;75: 851–856.

72. Peppiatt CM, Howarth C, Mobbs P, Attwell D. Bidirectional control of CNS capillary diameter by pericytes. Nature. 2006;443: 700–704.

73. Lindquist MA, Meng Loh J, Atlas LY, Wager TD. Modeling the hemodynamic response function in fMRI: efficiency, bias and mis-modeling. Neuroimage. 2009;45: S187–98.

74. Taylor AJ, Kim JH, Ress D. Characterization of the hemodynamic response function across the majority of human cerebral cortex. Neuroimage. 2018;173: 322–331.

75. West KL, Zuppichini MD, Turner MP, Sivakolundu DK, Zhao Y, Abdelkarim D, et al. BOLD hemodynamic response function changes significantly with healthy aging. Neuroimage. 2019;188: 198–207.

76. Iannetti GD, Wise RG. BOLD functional MRI in disease and pharmacological studies: room for improvement? Magn Reson Imaging. 2007;25: 978–988.

77. Tuovinen T, Kananen J, Rajna Z, Lieslehto J, Korhonen V, Rytty R, et al. The variability of functional MRI brain signal increases in Alzheimer's disease at cardiorespiratory frequencies. Sci Rep. 2020;10: 1–11.

78. Peng S-L, Chen C-M, Huang C-Y, Shih C-T, Huang C-W, Chiu S-C, et al. Effects of Hemodynamic Response Function Selection on Rat fMRI Statistical Analyses. Front Neurosci. 2019;13: 400.

79. You T, Im GH, Kim S-G. Characterization of brain-wide somatosensory BOLD fMRI in mice under dexmedetomidine/isoflurane and ketamine/xylazine. Sci Rep. 2021;11: 1–13.

80. Schroeter A, Schlegel F, Seuwen A, Grandjean J, Rudin M. Specificity of stimulus-evoked fMRI responses in the mouse: the influence of systemic physiological changes associated with innocuous stimulation under four different anesthetics. Neuroimage. 2014;94: 372–384.

81. Logothetis NK. What we can do and what we cannot do with fMRI. Nature. 2008;453: 869–878.

82. Taylor JG, Krause B, Shah NJ, Horwitz B, Mueller-Gaertner HW. On the relation between brain images and brain neural networks. Hum Brain Mapp. 2000;9: 165–182.

83. Arthurs OJ, Boniface S. How well do we understand the neural origins of the fMRI BOLD signal? Trends Neurosci. 2002;25: 27–31.

84. Ogawa S, Lee TM, Kay AR, Tank DW. Brain magnetic resonance imaging with contrast dependent on blood oxygenation. Proc Natl Acad Sci U S A. 1990;87: 9868–9872.

85. Ogawa S, Tank DW, Menon R, Ellermann JM, Kim SG, Merkle H, et al. Intrinsic signal changes accompanying sensory stimulation: functional brain mapping with magnetic resonance imaging. Proc Natl Acad Sci U S A. 1992;89: 5951–5955.

86. Plesnila N, Putz C, Rinecker M, Wiezorrek J, Schleinkofer L, Goetz AE, et al. Measurement of absolute values of hemoglobin oxygenation in the brain of small rodents by

near infrared reflection spectrophotometry. J Neurosci Methods. 2002;114: 107–117.

87. Kim S-G, Ogawa S. Biophysical and physiological origins of blood oxygenation level-dependent fMRI signals. J Cereb Blood Flow Metab. 2012;32: 1188–1206.

88. Aiello M, Cavaliere C, Salvatore M. Hybrid PET/MR Imaging and Brain Connectivity. Front Neurosci. 2016;10: 64.

89. Moeller F, Siniatchkin M, Gotman J. Simultaneous EEG and fMRI Recordings (EEG–fMRI). In: Ulmer S, Jansen O, editors. fMRI: Basics and Clinical Applications. Cham: Springer International Publishing; 2020. pp. 175–191.

90. Scarapicchia V, Brown C, Mayo C, Gawryluk JR. Functional Magnetic Resonance Imaging and Functional Near-Infrared Spectroscopy: Insights from Combined Recording Studies. Front Hum Neurosci. 2017;11: 419.

91. Schwalm M, Schmid F, Wachsmuth L, Backhaus H, Kronfeld A, Aedo Jury F, et al. Cortex-wide BOLD fMRI activity reflects locally-recorded slow oscillation-associated calcium waves. Elife. 2017;6. doi:10.7554/eLife.27602

92. Lake EMR, Ge X, Shen X, Herman P, Hyder F, Cardin JA, et al. Simultaneous cortex-wide fluorescence Ca2+ imaging and whole-brain fMRI. Nat Methods. 2020. doi:10.1038/s41592-020-00984-6

93. Chen X, Tong C, Han Z, Zhang K, Bo B, Feng Y, et al. Sensory evoked fMRI paradigms in awake mice. Neuroimage. 2020;204: 116242.

94. Chang P-C, Procissi D, Bao Q, Centeno MV, Baria A, Apkarian AV. Novel method for functional brain imaging in awake minimally restrained rats. J Neurophysiol. 2016;116: 61–80.

95. Chen G, Wang F, Dillenburger BC, Friedman RM, Chen LM, Gore JC, et al. Functional magnetic resonance imaging of awake monkeys: some approaches for improving imaging quality. Magn Reson Imaging. 2012;30: 36–47.

96. Yu X, Qian C, Chen D-Y, Dodd SJ, Koretsky AP. Deciphering laminar-specific neural inputs with line-scanning fMRI. Nat Methods. 2014;11: 55–58.

97. Albers F, Schmid F, Wachsmuth L, Faber C. Line scanning fMRI reveals earlier onset of optogenetically evoked BOLD response in rat somatosensory cortex as compared to sensory stimulation. Neuroimage. 2018;164: 144–154.

98. Bubic A, von Cramon DY, Schubotz RI. Prediction, cognition and the brain. Front Hum Neurosci. 2010;4: 25.

99. Qiao Y, Gumin J, MacLellan CJ, Gao F, Bouchard R, Lang FF, et al. Magnetic resonance and photoacoustic imaging of brain tumor mediated by mesenchymal stem cell labeled with multifunctional nanoparticle introduced via carotid artery injection. Nanotechnology.

2018;29: 165101.

100. Carr JA, Franke D, Caram JR, Perkinson CF, Saif M, Askoxylakis V, et al. Shortwave infrared fluorescence imaging with the clinically approved near-infrared dye indocyanine green. Proc Natl Acad Sci U S A. 2018;115: 4465–4470.

101. Pardridge WM. The blood-brain barrier: bottleneck in brain drug development. NeuroRx. 2005;2: 3–14.

102. Abbott NJ, Romero IA. Transporting therapeutics across the blood-brain barrier. Mol Med Today. 1996;2: 106–113.

103. Chen K-T, Wei K-C, Liu H-L. Theranostic Strategy of Focused Ultrasound Induced Blood-Brain Barrier Opening for CNS Disease Treatment. Front Pharmacol. 2019;10: 86.

104. Cetin A, Komai S, Eliava M, Seeburg PH, Osten P. Stereotaxic gene delivery in the rodent brain. Nat Protoc. 2006;1: 3166–3173.

105. Sung YK, Kim SW. Recent advances in the development of gene delivery systems. Biomater Res. 2019;23: 8.

106. O'Brien JA, Lummis SCR. Biolistic transfection of neuronal cultures using a hand-held gene gun. Nat Protoc. 2006;1: 977–981.

107. Sjulson L, Cassataro D, DasGupta S, Miesenböck G. Cell-Specific Targeting of Genetically Encoded Tools for Neuroscience. Annu Rev Genet. 2016;50: 571–594.

108. Vargas JE, Chicaybam L, Stein RT, Tanuri A, Delgado-Cañedo A, Bonamino MH. Retroviral vectors and transposons for stable gene therapy: advances, current challenges and perspectives. J Transl Med. 2016;14: 288.

109. Haggerty DL, Grecco GG, Reeves KC, Atwood B. Adeno-Associated Viral Vectors in Neuroscience Research. Mol Ther Methods Clin Dev. 2020;17: 69–82.

110. Manfredsson FP, Rising AC, Mandel RJ. AAV9: a potential blood-brain barrier buster. Mol Ther. 2009;17: 403–405.

111. Challis RC, Ravindra Kumar S, Chan KY, Challis C, Beadle K, Jang MJ, et al. Systemic AAV vectors for widespread and targeted gene delivery in rodents. Nat Protoc. 2019;14: 379–414.

112. Foust KD, Nurre E, Montgomery CL, Hernandez A, Chan CM, Kaspar BK. Intravascular AAV9 preferentially targets neonatal neurons and adult astrocytes. Nat Biotechnol. 2009;27: 59–65.

113. Michelson NJ, Vanni MP, Murphy TH. Comparison between transgenic and AAV-PHP.eB-mediated expression of GCaMP6s using in vivo wide-field functional imaging of brain activity. Neurophotonics. 2019;6: 025014.

114. Gordon JW, Ruddle FH. Integration and stable germ line transmission of genes

injected into mouse pronuclei. Science. 1981;214: 1244–1246.

115. Goodwin LO, Splinter E, Davis TL, Urban R, He H, Braun RE, et al. Large-scale discovery of mouse transgenic integration sites reveals frequent structural variation and insertional mutagenesis. Genome Res. 2019;29: 494–505.

116. Shizuya H, Kouros-Mehr H. The development and applications of the bacterial artificial chromosome cloning system. Keio J Med. 2001;50: 26–30.

117. Laboulaye MA, Duan X, Qiao M, Whitney IE, Sanes JR. Mapping Transgene Insertion Sites Reveals Complex Interactions Between Mouse Transgenes and Neighboring Endogenous Genes. Front Mol Neurosci. 2018;11: 385.

118. Madisen L, Garner AR, Shimaoka D, Chuong AS, Klapoetke NC, Li L, et al. Transgenic mice for intersectional targeting of neural sensors and effectors with high specificity and performance. Neuron. 2015;85: 942–958.

119. Ormö M, Cubitt AB, Kallio K, Gross LA, Tsien RY, Remington SJ. Crystal structure of the Aequorea victoria green fluorescent protein. Science. 1996;273: 1392–1395.

120. Steinmetz NA, Buetfering C, Lecoq J, Lee CR, Peters AJ, Jacobs EAK, et al. Aberrant Cortical Activity in Multiple GCaMP6-Expressing Transgenic Mouse Lines. eNeuro. 2017;4. doi:10.1523/ENEURO.0207-17.2017

121. Denk W, Strickler JH, Webb WW. Two-photon laser scanning fluorescence microscopy. Science. 1990;248: 73–76.

122. Svoboda K, Yasuda R. Principles of Two-Photon Excitation Microscopy and Its Applications to Neuroscience. Neuron. 2006;50: 823–839.

123. Dana H, Chen T-W, Hu A, Shields BC, Guo C, Looger LL, et al. Thy1-GCaMP6 transgenic mice for neuronal population imaging in vivo. PLoS One. 2014;9: e108697.

124. Wekselblatt JB, Flister ED, Piscopo DM, Niell CM. Large-scale imaging of cortical dynamics during sensory perception and behavior. J Neurophysiol. 2016;115: 2852–2866.

125. Orbach HS, Cohen LB, Grinvald A. Optical mapping of electrical activity in rat somatosensory and visual cortex. J Neurosci. 1985;5: 1886–1895.

126. Akemann W, Mutoh H, Perron A, Rossier J, Knöpfel T. Imaging brain electric signals with genetically targeted voltage-sensitive fluorescent proteins. Nat Methods. 2010;7: 643–649.

127. Homma R, Baker BJ, Jin L, Garaschuk O, Konnerth A, Cohen LB, et al. Wide-field and two-photon imaging of brain activity with voltage- and calcium-sensitive dyes. Methods Mol Biol. 2009;489: 43–79.

128. Akemann W, Mutoh H, Perron A, Park YK, Iwamoto Y, Knöpfel T. Imaging neural circuit dynamics with a voltage-sensitive fluorescent protein. J Neurophysiol. 2012;108:

2323–2337.

129. Grinvald A, Lieke E, Frostig RD, Gilbert CD, Wiesel TN. Functional architecture of cortex revealed by optical imaging of intrinsic signals. Nature. 1986;324: 361–364.

130. Roggan A, Friebel M, Do Rschel K, Hahn A, Mu Ller G. Optical Properties of Circulating Human Blood in the Wavelength Range 400-2500 nm. J Biomed Opt. 1999;4: 36–46.

131. Kura S, Xie H, Fu B, Ayata C, Boas DA, Sakadžić S. Intrinsic optical signal imaging of the blood volume changes is sufficient for mapping the resting state functional connectivity in the rodent cortex. J Neural Eng. 2018;15: 035003.

132. Valley MT, Moore MG, Zhuang J, Mesa N, Castelli D, Sullivan D, et al. Separation of hemodynamic signals from GCaMP fluorescence measured with wide-field imaging. J Neurophysiol. 2020;123: 356–366.

133. Beier HT, Ibey BL. Experimental comparison of the high-speed imaging performance of an EM-CCD and sCMOS camera in a dynamic live-cell imaging test case. PLoS One. 2014;9: e84614.

134. Janesick J, Putnam G. DEVELOPMENTS AND APPLICATIONS OF HIGH-PERFORMANCE CCD AND CMOS IMAGING ARRAYS. Annu Rev Nucl Part Sci. 2003;53: 263–300.

135. Ren C, Komiyama T. Characterizing Cortex-Wide Dynamics with Wide-Field Calcium Imaging. J Neurosci. 2021;41: 4160–4168.

136. Ma Y, Shaik MA, Kim SH, Kozberg MG, Thibodeaux DN, Zhao HT, et al. Wide-field optical mapping of neural activity and brain haemodynamics: considerations and novel approaches. Philos Trans R Soc Lond B Biol Sci. 2016;371. doi:10.1098/rstb.2015.0360

137. Allen WE, Kauvar IV, Chen MZ, Richman EB, Yang SJ, Chan K, et al. Global Representations of Goal-Directed Behavior in Distinct Cell Types of Mouse Neocortex. Neuron. 2017;94: 891–907.e6.

138. Barson D, Hamodi AS, Shen X, Lur G, Constable RT, Cardin JA, et al. Simultaneous mesoscopic and two-photon imaging of neuronal activity in cortical circuits. Nat Methods. 2019;17: 107–113.

139. Vesuna S, Kauvar IV, Richman E, Gore F, Oskotsky T, Sava-Segal C, et al. Deep posteromedial cortical rhythm in dissociation. Nature. 2020;586: 87–94.

140. Kozberg MG, Ma Y, Shaik MA, Kim SH, Hillman EMC. Rapid Postnatal Expansion of Neural Networks Occurs in an Environment of Altered Neurovascular and Neurometabolic Coupling. J Neurosci. 2016;36: 6704–6717.

141. Musall S, Kaufman MT, Juavinett AL, Gluf S, Churchland AK. Single-trial neural

dynamics are dominated by richly varied movements. Nat Neurosci. 2019;22: 1677–1686.

142. Pinto L, Rajan K, DePasquale B, Thiberge SY, Tank DW, Brody CD. Task-Dependent Changes in the Large-Scale Dynamics and Necessity of Cortical Regions. Neuron. 2019;104: 810–824.e9.

143. Salkoff DB, Zagha E, McCarthy E, McCormick DA. Movement and Performance Explain Widespread Cortical Activity in a Visual Detection Task. Cereb Cortex. 2020;30: 421–437.

144. Jacobs EAK, Steinmetz NA, Peters AJ, Carandini M, Harris KD. Cortical State Fluctuations during Sensory Decision Making. Curr Biol. 2020;30: 4944–4955.e7.

145. Gilad A, Gallero-Salas Y, Groos D, Helmchen F. Behavioral Strategy Determines Frontal or Posterior Location of Short-Term Memory in Neocortex. Neuron. 2018;99: 814–828.e7.

146. West SL, Aronson JD, Popa LS, Feller KD, Carter RE, Chiesl WM, et al. Wide-Field Calcium Imaging of Dynamic Cortical Networks during Locomotion. Cereb Cortex. 2021. doi:10.1093/cercor/bhab373

147. Mitra A, Kraft A, Wright P, Acland B, Snyder AZ, Rosenthal Z, et al. Spontaneous Infra-slow Brain Activity Has Unique Spatiotemporal Dynamics and Laminar Structure. Neuron. 2018;98: 297–305.e6.

148. Cramer JV, Gesierich B, Roth S, Dichgans M, Düring M, Liesz A. In vivo widefield calcium imaging of the mouse cortex for analysis of network connectivity in health and brain disease. Neuroimage. 2019;199: 570–584.

149. Brier LM, Landsness EC, Snyder AZ, Wright PW, Baxter GA, Bauer AQ, et al. Separability of calcium slow waves and functional connectivity during wake, sleep, and anesthesia. NPh. 2019;6: 035002.

150. Busche MA, Kekuš M, Adelsberger H, Noda T, Förstl H, Nelken I, et al. Rescue of long-range circuit dysfunction in Alzheimer's disease models. Nat Neurosci. 2015;18: 1623–1630.

151. Doostdar N, Airey J, Radulescu CI, Melgosa-Ecenarro L, Zabouri N, Pavlidi P, et al. Multi-scale network imaging in a mouse model of amyloidosis. Cell Calcium. 2021;95: 102365.

152. Carandini M, Shimaoka D, Rossi LF, Sato TK, Benucci A, Knöpfel T. Imaging the awake visual cortex with a genetically encoded voltage indicator. J Neurosci. 2015;35: 53–63.

153. Zhu MH, Jang J, Milosevic MM, Antic SD. Population imaging discrepancies between a genetically-encoded calcium indicator (GECI) versus a genetically-encoded voltage

indicator (GEVI). Sci Rep. 2021;11: 5295.

154. Xiao D, Vanni MP, Mitelut CC, Chan AW, LeDue JM, Xie Y, et al. Mapping cortical mesoscopic networks of single spiking cortical or sub-cortical neurons. Elife. 2017;6: e19976.

155. Clancy KB, Orsolic I, Mrsic-Flogel TD. Locomotion-dependent remapping of distributed cortical networks. Nat Neurosci. 2019;22: 778–786.

156. Liu X, Ren C, Lu Y, Liu Y, Kim J-H, Leutgeb S, et al. Multimodal neural recordings with Neuro-FITM uncover diverse patterns of cortical–hippocampal interactions. Nat Neurosci. 2021;24: 886–896.

157. Peters AJ, Fabre JMJ, Steinmetz NA, Harris KD, Carandini M. Striatal activity topographically reflects cortical activity. Nature. 2021;591: 420–425.

158. Crick FH. Thinking about the brain. Sci Am. 1979;241: 219–232.

159. Soliman GSH, Trüper HG. Halobacterium pharaonis sp. nov., a New, Extremely Haloalkaliphilic Archaebacterium with Low Magnesium Requirement. Zentralblatt für Bakteriologie Mikrobiologie und Hygiene: I Abt Originale C: Allgemeine, angewandte und ökologische Mikrobiologie. 1982;3: 318–329.

160. Mukohata Y, Sugiyama Y, Ihara K, Yoshida M. An Australian halobacterium contains a novel proton pump retinal protein: archaerhodopsin. Biochem Biophys Res Commun. 1988;151: 1339–1345.

161. Boyden ES, Zhang F, Bamberg E, Nagel G, Deisseroth K. Millisecond-timescale, genetically targeted optical control of neural activity. Nat Neurosci. 2005;8: 1263–1268.

162. Nagel G, Szellas T, Huhn W, Kateriya S, Adeishvili N, Berthold P, et al. Channelrhodopsin-2, a directly light-gated cation-selective membrane channel. Proc Natl Acad Sci U S A. 2003;100: 13940–13945.

163. Zhang F, Wang L-P, Brauner M, Liewald JF, Kay K, Watzke N, et al. Multimodal fast optical interrogation of neural circuitry. Nature. 2007;446: 633–639.

164. Chen I-W, Papagiakoumou E, Emiliani V. Towards circuit optogenetics. Curr Opin Neurobiol. 2018;50: 179–189.

165. Yona G, Meitav N, Kahn I, Shoham S. Realistic Numerical and Analytical Modeling of Light Scattering in Brain Tissue for Optogenetic Applications(1,2,3). eNeuro. 2016;3. doi:10.1523/ENEURO.0059-15.2015

166. Haleh S, Hirac G, Frédéric P. Optical properties of mice skull bone in the 455- to 705-nm range. J Biomed Opt. 2017;22: 10503.

167. Hu J, Adebali O, Adar S, Sancar A. Dynamic maps of UV damage formation and repair for the human genome. Proc Natl Acad Sci U S A. 2017;114: 6758–6763.

168. Lehtinen K, Nokia MS, Takala H. Red Light Optogenetics in Neuroscience. Front Cell Neurosci. 2021;15: 778900.

169. Peirson SN, Brown LA, Pothecary CA, Benson LA, Fisk AS. Light and the laboratory mouse. J Neurosci Methods. 2018;300: 26–36.

170. Lin JY, Knutsen PM, Muller A, Kleinfeld D, Tsien RY. ReaChR: a red-shifted variant of channelrhodopsin enables deep transcranial optogenetic excitation. Nat Neurosci. 2013;16: 1499–1508.

171. Klapoetke NC, Murata Y, Kim SS, Pulver SR, Birdsey-Benson A, Cho YK, et al. Independent optical excitation of distinct neural populations. Nat Methods. 2014;11: 338–346.

172. Guru A, Post RJ, Ho Y-Y, Warden MR. Making Sense of Optogenetics. Int J Neuropsychopharmacol. 2015;18: yv079.

173. Lee C, Lavoie A, Liu J, Chen SX, Liu B-H. Light Up the Brain: The Application of Optogenetics in Cell-Type Specific Dissection of Mouse Brain Circuits. Front Neural Circuits. 2020;14: 18.

174. Deubner J, Coulon P, Diester I. Optogenetic approaches to study the mammalian brain. Curr Opin Struct Biol. 2019;57: 157–163.

175. Friston KJ, Frith CD, Frackowiak RSJ. Time-dependent changes in effective connectivity measured with PET. Hum Brain Mapp. 1993;1: 69–79.

176. Petkov CI, Kikuchi Y, Milne AE, Mishkin M, Rauschecker JP, Logothetis NK. Different forms of effective connectivity in primate frontotemporal pathways. Nat Commun. 2015;6: 6000.

177. Bauer AQ, Kraft AW, Baxter GA, Wright PW, Reisman MD, Bice AR, et al. Effective Connectivity Measured Using Optogenetically Evoked Hemodynamic Signals Exhibits Topography Distinct from Resting State Functional Connectivity in the Mouse. Cereb Cortex. 2018;28: 370–386.

178. Kastanenka KV, Hou SS, Shakerdge N, Logan R, Feng D, Wegmann S, et al. Optogenetic Restoration of Disrupted Slow Oscillations Halts Amyloid Deposition and Restores Calcium Homeostasis in an Animal Model of Alzheimer's Disease. PLoS One. 2017;12: e0170275.

179. Hobson JA. Sleeping, Waking, and Dreaming. In: Koob GF, Moal ML, Thompson RF, editors. Encyclopedia of Behavioral Neuroscience. Oxford: Academic Press; 2010. pp. 237–256.

180. Deco G, Cruzat J, Cabral J, Tagliazucchi E, Laufs H, Logothetis NK, et al. Awakening: Predicting external stimulation to force transitions between different brain states. Proc

Natl Acad Sci U S A. 2019;116: 18088–18097.

181. Deco G, Jirsa VK, McIntosh AR. Resting brains never rest: computational insights into potential cognitive architectures. Trends Neurosci. 2013;36: 268–274.

182. Tanke N, Borst JGG, Houweling AR. Single-Cell Stimulation in Barrel Cortex Influences Psychophysical Detection Performance. J Neurosci. 2018;38: 2057–2068.

183. Poulet JFA, Crochet S. The Cortical States of Wakefulness. Front Syst Neurosci. 2018;12: 64.

184. Vyazovskiy VV, Olcese U, Hanlon EC, Nir Y, Cirelli C, Tononi G. Local sleep in awake rats. Nature. 2011;472: 443–447.

185. Bergmann TO. Brain State-Dependent Brain Stimulation. Front Psychol. 2018;9: 2108.

186. Constantinople CM, Bruno RM. Effects and mechanisms of wakefulness on local cortical networks. Neuron. 2011;69: 1061–1068.

187. Bharioke A, Munz M, Brignall A, Kosche G, Eizinger MF, Ledergerber N, et al. General anesthesia globally synchronizes activity selectively in layer 5 cortical pyramidal neurons. Neuron. 2022. doi:10.1016/j.neuron.2022.03.032

188. Sörnmo L, Laguna P. Chapter 2 - The Electroencephalogram—A Brief Background. In: Sörnmo L, Laguna P, editors. Bioelectrical Signal Processing in Cardiac and Neurological Applications. Burlington: Academic Press; 2005. pp. 25–53.

189. Fries P. A mechanism for cognitive dynamics: neuronal communication through neuronal coherence. Trends Cogn Sci. 2005;9: 474–480.

190. Munia TTK, Aviyente S. Time-Frequency Based Phase-Amplitude Coupling Measure For Neuronal Oscillations. Sci Rep. 2019;9: 1–15.

191. Chamadia S, Pedemonte JC, Hahm EY, Mekonnen J, Ibala R, Gitlin J, et al. Delta oscillations phase limit neural activity during sevoflurane anesthesia. Communications Biology. 2019;2: 1–10.

192. Biswal B, Yetkin FZ, Haughton VM, Hyde JS. Functional connectivity in the motor cortex of resting human brain using echo-planar MRI. Magn Reson Med. 1995;34: 537–541.

193. Buckner RL, Andrews-Hanna JR, Schacter DL. The brain's default network: anatomy, function, and relevance to disease. Ann N Y Acad Sci. 2008;1124: 1–38.

194. Spreng RN, Mar RA, Kim ASN. The common neural basis of autobiographical memory, prospection, navigation, theory of mind, and the default mode: a quantitative meta-analysis. J Cogn Neurosci. 2009;21: 489–510.

195. Fomina T, Hohmann M, Scholkopf B, Grosse-Wentrup M. Identification of the Default Mode Network with electroencephalography. Conf Proc IEEE Eng Med Biol Soc.

2015;2015: 7566–7569.

196. Prestel M, Steinfath TP, Tremmel M, Stark R, Ott U. fMRI BOLD Correlates of EEG Independent Components: Spatial Correspondence With the Default Mode Network. Front Hum Neurosci. 2018;12: 478.

197. Vincent JL, Patel GH, Fox MD, Snyder AZ, Baker JT, Van Essen DC, et al. Intrinsic functional architecture in the anaesthetized monkey brain. Nature. 2007;447: 83–86.

198. Lu H, Zou Q, Gu H, Raichle ME, Stein EA, Yang Y. Rat brains also have a default mode network. Proc Natl Acad Sci U S A. 2012;109: 3979–3984.

199. Barttfeld P, Uhrig L, Sitt JD, Sigman M, Jarraya B, Dehaene S. Signature of consciousness in the dynamics of resting-state brain activity. Proc Natl Acad Sci U S A. 2015;112: 887–892.

200. Deco G, McIntosh AR, Shen K, Hutchison RM, Menon RS, Everling S, et al. Identification of optimal structural connectivity using functional connectivity and neural modeling. J Neurosci. 2014;34: 7910–7916.

201. Raichle ME, MacLeod AM, Snyder AZ, Powers WJ, Gusnard DA, Shulman GL. A default mode of brain function. Proc Natl Acad Sci U S A. 2001;98: 676–682.

202. Alves PN, Foulon C, Karolis V, Bzdok D, Margulies DS, Volle E, et al. An improved neuroanatomical model of the default-mode network reconciles previous neuroimaging and neuropathological findings. Commun Biol. 2019;2: 370.

203. Mantini D, Gerits A, Nelissen K, Durand J-B, Joly O, Simone L, et al. Default mode of brain function in monkeys. J Neurosci. 2011;31: 12954–12962.

204. Barks SK, Parr LA, Rilling JK. The default mode network in chimpanzees (Pan troglodytes) is similar to that of humans. Cereb Cortex. 2015;25: 538–544.

205. Arsenault JT, Caspari N, Vandenberghe R, Vanduffel W. Attention Shifts Recruit the Monkey Default Mode Network. J Neurosci. 2018;38: 1202–1217.

206. Stafford JM, Jarrett BR, Miranda-Dominguez O, Mills BD, Cain N, Mihalas S, et al. Large-scale topology and the default mode network in the mouse connectome. Proc Natl Acad Sci U S A. 2014;111: 18745–18750.

207. Grandjean J, Canella C, Anckaerts C, Ayrancı G, Bougacha S, Bienert T, et al. Common functional networks in the mouse brain revealed by multi-centre resting-state fMRI analysis. Neuroimage. 2020;205: 116278.

208. Gozzi A, Schwarz AJ. Large-scale functional connectivity networks in the rodent brain. Neuroimage. 2016;127: 496–509.

209. Geng X, Hu Y, Gu H, Salmeron BJ, Adinoff B, Stein EA, et al. Salience and default mode network dysregulation in chronic cocaine users predict treatment outcome. Brain.

2017;140: 1513–1524.

210. Tessitore A, Esposito F, Vitale C, Santangelo G, Amboni M, Russo A, et al. Default-mode network connectivity in cognitively unimpaired patients with Parkinson disease. Neurology. 2012;79: 2226–2232.

211. Voets NL, Beckmann CF, Cole DM, Hong S, Bernasconi A, Bernasconi N. Structural substrates for resting network disruption in temporal lobe epilepsy. Brain. 2012;135: 2350–2357.

212. Whitfield-Gabrieli S, Ford JM. Default mode network activity and connectivity in psychopathology. Annu Rev Clin Psychol. 2012;8: 49–76.

213. Zhang L, Zuo X-N, Ng KK, Chong JSX, Shim HY, Ong MQW, et al. Distinct BOLD variability changes in the default mode and salience networks in Alzheimer's disease spectrum and associations with cognitive decline. Sci Rep. 2020;10: 6457.

214. Hunt MJ, Kopell NJ, Traub RD, Whittington MA. Aberrant Network Activity in Schizophrenia. Trends Neurosci. 2017;40: 371–382.

215. Blayney MR. Procedural sedation for adult patients: an overview. Continuing Education in Anaesthesia Critical Care Pain. 2012;12: 176–180.

216. Brown EN, Purdon PL, Van Dort CJ. General anesthesia and altered states of arousal: a systems neuroscience analysis. Annu Rev Neurosci. 2011;34: 601–628.

217. Gerlach AT, Dasta JF. Dexmedetomidine: an updated review. Ann Pharmacother. 2007;41: 245–252.

218. Mizobe T, Maghsoudi K, Sitwala K, Tianzhi G, Ou J, Maze M. Antisense technology reveals the alpha2A adrenoceptor to be the subtype mediating the hypnotic response to the highly selective agonist, dexmedetomidine, in the locus coeruleus of the rat. J Clin Invest. 1996;98: 1076–1080.

219. Nelson LE, Lu J, Guo T, Saper CB, Franks NP, Maze M. The alpha2-adrenoceptor agonist dexmedetomidine converges on an endogenous sleep-promoting pathway to exert its sedative effects. Anesthesiology. 2003;98: 428–436.

220. Akeju O, Pavone KJ, Westover MB, Vazquez R, Prerau MJ, Harrell PG, et al. A comparison of propofol- and dexmedetomidine-induced electroencephalogram dynamics using spectral and coherence analysis. Anesthesiology. 2014;121: 978–989.

221. Huupponen E, Maksimow A, Lapinlampi P, Särkelä M, Saastamoinen A, Snapir A, et al. Electroencephalogram spindle activity during dexmedetomidine sedation and physiological sleep. Acta Anaesthesiol Scand. 2008;52: 289–294.

222. Pawela CP, Biswal BB, Hudetz AG, Schulte ML, Li R, Jones SR, et al. A protocol for use of medetomidine anesthesia in rats for extended studies using task-induced BOLD

contrast and resting-state functional connectivity. Neuroimage. 2009;46: 1137–1147.

223. Greicius MD, Kiviniemi V, Tervonen O, Vainionpää V, Alahuhta S, Reiss AL, et al. Persistent default-mode network connectivity during light sedation. Hum Brain Mapp. 2008;29: 839–847.

224. Paasonen J, Stenroos P, Salo RA, Kiviniemi V, Gröhn O. Functional connectivity under six anesthesia protocols and the awake condition in rat brain. Neuroimage. 2018;172: 9–20.

225. Bukhari Q, Schroeter A, Cole DM, Rudin M. Resting State fMRI in Mice Reveals Anesthesia Specific Signatures of Brain Functional Networks and Their Interactions. Front Neural Circuits. 2017;11: 5.

226. Jung WB, Shim H-J, Kim S-G. Mouse BOLD fMRI at ultrahigh field detects somatosensory networks including thalamic nuclei. Neuroimage. 2019;195: 203–214.

227. Adamczak JM, Farr TD, Seehafer JU, Kalthoff D, Hoehn M. High field BOLD response to forepaw stimulation in the mouse. Neuroimage. 2010;51: 704–712.

228. Brown EN, Lydic R, Schiff ND. General anesthesia, sleep, and coma. N Engl J Med. 2010;363: 2638–2650.

229. Robinson DH, Toledo AH. Historical development of modern anesthesia. J Invest Surg. 2012;25: 141–149.

230. Guidera JA, Taylor NE, Lee JT, Vlasov KY, Pei J, Stephen EP, et al. Sevoflurane Induces Coherent Slow-Delta Oscillations in Rats. Front Neural Circuits. 2017;11: 36.

231. Ranft A, Golkowski D, Kiel T, Riedl V, Kohl P, Rohrer G, et al. Neural Correlates of Sevoflurane-induced Unconsciousness Identified by Simultaneous Functional Magnetic Resonance Imaging and Electroencephalography. Anesthesiology. 2016;125: 861–872.

232. Campagna JA, Miller KW, Forman SA. Mechanisms of actions of inhaled anesthetics. N Engl J Med. 2003;348: 2110–2124.

233. Garcia PS, Kolesky SE, Jenkins A. General anesthetic actions on GABA(A) receptors. Curr Neuropharmacol. 2010;8: 2–9.

234. Brosnan RJ, Thiesen R. Increased NMDA receptor inhibition at an increased Sevoflurane MAC. BMC Anesthesiol. 2012;12: 9.

235. Petrenko AB, Yamakura T, Sakimura K, Baba H. Defining the role of NMDA receptors in anesthesia: are we there yet? Eur J Pharmacol. 2014;723: 29–37.

236. Rehberg B, Xiao YH, Duch DS. Central nervous system sodium channels are significantly suppressed at clinical concentrations of volatile anesthetics. Anesthesiology. 1996;84: 1223–33; discussion 27A.

237. Friederich P, Benzenberg D, Trellakis S, Urban BW. Interaction of volatile anesthet-

ics with human Kv channels in relation to clinical concentrations. Anesthesiology. 2001;95: 954–958.

238. Sirois JE, Lei Q, Talley EM, Lynch C 3rd, Bayliss DA. The TASK-1 two-pore domain K+ channel is a molecular substrate for neuronal effects of inhalation anesthetics. J Neurosci. 2000;20: 6347–6354.

239. Lynch MA. Long-term potentiation and memory. Physiol Rev. 2004;84: 87–136.

240. Mapelli J, Gandolfi D, Giuliani E, Casali S, Congi L, Barbieri A, et al. The effects of the general anesthetic sevoflurane on neurotransmission: an experimental and computational study. Sci Rep. 2021;11: 4335.

241. Steriade M, Nuñez A, Amzica F. A novel slow (< 1 Hz) oscillation of neocortical neurons in vivo: depolarizing and hyperpolarizing components. J Neurosci. 1993;13: 3252–3265.

242. Steriade M, Timofeev I, Grenier F. Natural waking and sleep states: a view from inside neocortical neurons. J Neurophysiol. 2001;85: 1969–1985.

243. Steriade M, Contreras D, Curró Dossi R, Nuñez A. The slow (< 1 Hz) oscillation in reticular thalamic and thalamocortical neurons: scenario of sleep rhythm generation in interacting thalamic and neocortical networks. J Neurosci. 1993;13: 3284–3299.

244. Timofeev I, Steriade M. Low-frequency rhythms in the thalamus of intact-cortex and decorticated cats. J Neurophysiol. 1996;76: 4152–4168.

245. Shu Y, Hasenstaub A, McCormick DA. Turning on and off recurrent balanced cortical activity. Nature. 2003;423: 288–293.

246. Rampil IJ. A primer for EEG signal processing in anesthesia. Anesthesiology. 1998;89: 980–1002.

247. Akeju O, Westover MB, Pavone KJ, Sampson AL, Hartnack KE, Brown EN, et al. Effects of sevoflurane and propofol on frontal electroencephalogram power and coherence. Anesthesiology. 2014;121: 990–998.

248. Massimini M, Huber R, Ferrarelli F, Hill S, Tononi G. The Sleep Slow Oscillation as a Traveling Wave. J Neurosci. 2004;24: 6862–6870.

249. Metherate R, Ashe JH. Ionic flux contributions to neocortical slow waves and nucleus basalis-mediated activation: whole-cell recordings in vivo. J Neurosci. 1993;13: 5312–5323.

250. Timofeev I, Grenier F, Bazhenov M, Sejnowski TJ, Steriade M. Origin of slow cortical oscillations in deafferented cortical slabs. Cereb Cortex. 2000;10: 1185–1199.

251. Haider B, Duque A, Hasenstaub AR, McCormick DA. Neocortical network activity in vivo is generated through a dynamic balance of excitation and inhibition. J Neurosci.

2006;26: 4535–4545.

252. Stroh A, Adelsberger H, Groh A, Rühlmann C, Fischer S, Schierloh A, et al. Making waves: initiation and propagation of corticothalamic Ca2+ waves in vivo. Neuron. 2013;77: 1136–1150.

253. Chauvette S, Crochet S, Volgushev M, Timofeev I. Properties of slow oscillation during slow-wave sleep and anesthesia in cats. J Neurosci. 2011;31: 14998–15008.

254. Gao L, Meng X, Ye C, Zhang H, Liu C, Dan Y, et al. Entrainment of slow oscillations of auditory thalamic neurons by repetitive sound stimuli. J Neurosci. 2009;29: 6013–6021.

255. Sakata S, Harris KD. Laminar structure of spontaneous and sensory-evoked population activity in auditory cortex. Neuron. 2009;64: 404–418.

256. Zingg B, Dong H-W, Tao HW, Zhang LI. Input-output organization of the mouse claustrum. J Comp Neurol. 2018;526: 2428–2443.

257. Wang Q, Ng L, Harris JA, Feng D, Li Y, Royall JJ, et al. Organization of the connections between claustrum and cortex in the mouse. J Comp Neurol. 2017;525: 1317–1346.

258. Narikiyo K, Mizuguchi R, Ajima A, Shiozaki M, Hamanaka H, Johansen JP, et al. The claustrum coordinates cortical slow-wave activity. Nat Neurosci. 2020;23: 741–753.

259. Hudetz AG. General anesthesia and human brain connectivity. Brain Connect. 2012;2: 291–302.

260. Wu T-L, Mishra A, Wang F, Yang P-F, Gore JC, Chen LM. Effects of isoflurane anesthesia on resting-state fMRI signals and functional connectivity within primary somatosensory cortex of monkeys. Brain Behav. 2016;6: e00591.

261. Liu X, Zhu X-H, Zhang Y, Chen W. Neural origin of spontaneous hemodynamic fluctuations in rats under burst-suppression anesthesia condition. Cereb Cortex. 2011;21: 374–384.

262. Bukhari Q, Schroeter A, Rudin M. Increasing isoflurane dose reduces homotopic correlation and functional segregation of brain networks in mice as revealed by resting-state fMRI. Sci Rep. 2018;8: 1–12.

263. Schlegel F, Sych Y, Schroeter A, Stobart J, Weber B, Helmchen F, et al. Fiber-optic implant for simultaneous fluorescence-based calcium recordings and BOLD fMRI in mice. Nat Protoc. 2018;13: 840–855.

264. Purdon PL, Pierce ET, Mukamel EA, Prerau MJ, Walsh JL, Wong KFK, et al. Electroencephalogram signatures of loss and recovery of consciousness from propofol. Proc Natl Acad Sci U S A. 2013;110: E1142–E1151.

265. Rudolph U, Antkowiak B. Molecular and neuronal substrates for general anaesthetics. Nat Rev Neurosci. 2004;5: 709–720.

266. American Psychiatric Association. Diagnostic and Statistical Manual of Mental Disorders. American Psychiatric Association; 2013.

267. Bergman SA. Ketamine: review of its pharmacology and its use in pediatric anesthesia. Anesth Prog. 1999;46: 10–20.

268. Kohrs R, Durieux ME. Ketamine: teaching an old drug new tricks. Anesth Analg. 1998;87: 1186–1193.

269. Olney JW, Newcomer JW, Farber NB. NMDA receptor hypofunction model of schizophrenia. J Psychiatr Res. 1999;33: 523–533.

270. Morgan CJA, Curran HV, Independent Scientific Committee on Drugs. Ketamine use: a review. Addiction. 2012;107: 27–38.

271. Lee K-H, Williams LM, Breakspear M, Gordon E. Synchronous gamma activity: a review and contribution to an integrative neuroscience model of schizophrenia. Brain Res Brain Res Rev. 2003;41: 57–78.

272. Oye I, Paulsen O, Maurset A. Effects of ketamine on sensory perception: evidence for a role of N-methyl-D-aspartate receptors. J Pharmacol Exp Ther. 1992;260: 1209–1213.

273. Purdon PL, Sampson A, Pavone KJ, Brown EN. Clinical Electroencephalography for Anesthesiologists: Part I: Background and Basic Signatures. Anesthesiology. 2015;123: 937–960.

274. Seamans J. Losing inhibition with ketamine. Nat Chem Biol. 2008;4: 91–93.

275. Akeju O, Song AH, Hamilos AE, Pavone KJ, Flores FJ, Brown EN, et al. Electroencephalogram signatures of ketamine anesthesia-induced unconsciousness. Clin Neurophysiol. 2016;127: 2414–2422.

276. Pinault D. N-methyl d-aspartate receptor antagonists ketamine and MK-801 induce wake-related aberrant gamma oscillations in the rat neocortex. Biol Psychiatry. 2008;63: 730–735.

277. Qi R, Li J, Wu X, Geng X, Chen N, Yu H. Effects of Ketamine on Basal Gamma Band Oscillation and Sensory Gating in Prefrontal Cortex of Awake Rats. Neurosci Bull. 2018;34: 457–464.

278. de la Salle S, Choueiry J, Shah D, Bowers H, McIntosh J, Ilivitsky V, et al. Effects of Ketamine on Resting-State EEG Activity and Their Relationship to Perceptual/Dissociative Symptoms in Healthy Humans. Front Pharmacol. 2016;7: 348.

279. Grent-'t-Jong T, Melloni L, Uhlhaas PJ. Dissociation and Brain Rhythms: Pitfalls and Promises. Front Psychiatry. 2021;12: 790372.

280. Liang Z, Wang Y, Sun X, Li D, Voss LJ, Sleigh JW, et al. EEG entropy measures in anesthesia. Front Comput Neurosci. 2015;9: 16.

281. Myles PS, Leslie K, McNeil J, Forbes A, Chan MTV. Bispectral index monitoring to prevent awareness during anaesthesia: the B-Aware randomised controlled trial. Lancet. 2004;363: 1757–1763.

282. Seth AK, Dienes Z, Cleeremans A, Overgaard M, Pessoa L. Measuring consciousness: relating behavioural and neurophysiological approaches. Trends Cogn Sci. 2008;12: 314–321.

283. Deco G, Cruzat J, Kringelbach ML. Brain songs framework used for discovering the relevant timescale of the human brain. Nat Commun. 2019;10: 583.

284. Breakspear M, Jirsa V, Deco G. Computational models of the brain: from structure to function. Neuroimage. 2010;52: 727–730.

285. Hansen ECA, Battaglia D, Spiegler A, Deco G, Jirsa VK. Functional connectivity dynamics: modeling the switching behavior of the resting state. Neuroimage. 2015;105: 525–535.

286. Tognoli E, Kelso JAS. The metastable brain. Neuron. 2014;81: 35–48.

287. Breakspear M. Dynamic models of large-scale brain activity. Nat Neurosci. 2017;20: 340–352.

288. Deco G, Kringelbach ML, Jirsa VK, Ritter P. The dynamics of resting fluctuations in the brain: metastability and its dynamical cortical core. Sci Rep. 2017;7: 3095.

289. Cabral J, Vidaurre D, Marques P, Magalhães R, Silva Moreira P, Miguel Soares J, et al. Cognitive performance in healthy older adults relates to spontaneous switching between states of functional connectivity during rest. Sci Rep. 2017;7: 5135.

290. Stark EA, Cabral J, Riem MME, Van IJzendoorn MH, Stein A, Kringelbach ML. The Power of Smiling: The Adult Brain Networks Underlying Learned Infant Emotionality. Cereb Cortex. 2020;30: 2019–2029.

291. Lord L-D, Expert P, Atasoy S, Roseman L, Rapuano K, Lambiotte R, et al. Dynamical exploration of the repertoire of brain networks at rest is modulated by psilocybin. Neuroimage. 2019;199: 127–142.

292. Shannon CE. The mathematical theory of communication. 1963. MD Comput. 1997;14: 306–317.

293. Tononi G. An information integration theory of consciousness. BMC Neurosci. 2004;5: 42.

294. Oizumi M, Albantakis L, Tononi G. From the phenomenology to the mechanisms of consciousness: Integrated Information Theory 3.0. PLoS Comput Biol. 2014;10: e1003588.

295. Ay N. Information Geometry on Complexity and Stochastic Interaction. Entropy . 2015;17: 2432–2458.

296. Toker D, Sommer FT. Information integration in large brain networks. PLoS Comput Biol. 2019;15: e1006807.

297. Cerullo MA. The Problem with Phi: A Critique of Integrated Information Theory. PLoS Comput Biol. 2015;11: e1004286.

298. Bayne T. On the axiomatic foundations of the integrated information theory of consciousness. Neurosci Conscious. 2018;2018: niy007.

299. Doerig A, Schurger A, Hess K, Herzog MH. The unfolding argument: Why IIT and other causal structure theories cannot explain consciousness. Conscious Cogn. 2019;72: 49–59.

300. Casali AG, Gosseries O, Rosanova M, Boly M, Sarasso S, Casali KR, et al. A theoretically based index of consciousness independent of sensory processing and behavior. Sci Transl Med. 2013;5: 198ra105.

301. Comolatti R, Pigorini A, Casarotto S, Fecchio M, Faria G, Sarasso S, et al. A fast and general method to empirically estimate the complexity of brain responses to transcranial and intracranial stimulations. Brain Stimul. 2019;12: 1280–1289.

302. Caputi L, Pidnebesna A, Hlinka J. Promises and pitfalls of topological data analysis for brain connectivity analysis. Neuroimage. 2021;238: 118245.

303. Rieck B, Yates T, Bock C, Borgwardt K, Wolf G, Turk-Browne N, et al. Uncovering the Topology of Time-Varying fMRI Data using Cubical Persistence. In: Larochelle H, Ranzato M, Hadsell R, Balcan MF, Lin H, editors. Advances in Neural Information Processing Systems. Curran Associates, Inc.; 2020. pp. 6900–6912.

304. Wang Q, Ding S-L, Li Y, Royall J, Feng D, Lesnar P, et al. The Allen Mouse Brain Common Coordinate Framework: A 3D Reference Atlas. Cell. 2020;181: 936–953.e20.

305. Behrens TEJ, Woolrich MW, Jenkinson M, Johansen-Berg H, Nunes RG, Clare S, et al. Characterization and propagation of uncertainty in diffusion-weighted MR imaging. Magn Reson Med. 2003;50: 1077–1088.

306. Renier N, Wu Z, Simon DJ, Yang J, Ariel P, Tessier-Lavigne M. iDISCO: A Simple, Rapid Method to Immunolabel Large Tissue Samples for Volume Imaging. Cell. 2014;159: 896–910.

307. Chung K, Deisseroth K. CLARITY for mapping the nervous system. Nat Methods. 2013;10: 508–513.

308. Kasthuri N, Hayworth KJ, Berger DR, Schalek RL, Conchello JA, Knowles-Barley S, et al. Saturated Reconstruction of a Volume of Neocortex. Cell. 2015;162: 648–661.

309. Adam Y. All-optical electrophysiology in behaving animals. J Neurosci Methods. 2021;353: 109101.

310. Melozzi F, Woodman MM, Jirsa VK, Bernard C. The Virtual Mouse Brain: A Computational Neuroinformatics Platform to Study Whole Mouse Brain Dynamics. eNeuro. 2017;4. doi:10.1523/ENEURO.0111-17.2017

311. Mendez MA, Balabane M, Buchlin J-M. Multi-scale proper orthogonal decomposition of complex fluid flows. J Fluid Mech. 2019;870: 988–1036.

312. Schmid PJ. Dynamic mode decomposition of numerical and experimental data. J Fluid Mech. 2010;656: 5–28.

313. Kunert-Graf JM, Eschenburg KM, Galas DJ, Kutz JN, Rane SD, Brunton BW. Extracting Reproducible Time-Resolved Resting State Networks Using Dynamic Mode Decomposition. Front Comput Neurosci. 2019;13: 75.

314. Grossmann A, Morlet J. Decomposition of Hardy Functions into Square Integrable Wavelets of Constant Shape. SIAM J Math Anal. 1984;15: 723–736.

315. Kiebel S, Kilner J, Friston K. CHAPTER 16 - Hierarchical models for EEG and MEG. In: Friston K, Ashburner J, Kiebel S, Nichols T, Penny W, editors. Statistical Parametric Mapping. London: Academic Press; 2007. pp. 211–220.

316. Wallisch P, Lusignan ME, Benayoun MD, Baker TI, Dickey AS, Hatsopoulos NG. Chapter 13 - Wavelets. In: Wallisch P, Lusignan ME, Benayoun MD, Baker TI, Dickey AS, Hatsopoulos NG, editors. MATLAB for Neuroscientists (Second Edition). San Diego: Academic Press; 2014. pp. 245–252.

317. McInnes L, Healy J, Melville J. UMAP: Uniform Manifold Approximation and Projection for Dimension Reduction. arXiv [stat.ML]. 2018. Available: http://arxiv.org/abs/1802.03426

318. Del Giudice M. Effective Dimensionality: A Tutorial. Multivariate Behav Res. 2021;56: 527–542.

319. Liu JS. Metropolized independent sampling with comparisons to rejection sampling and importance sampling. Stat Comput. 1996;6: 113–119.

320. Martino L, Elvira V, Louzada F. Effective sample size for importance sampling based on discrepancy measures. Signal Processing. 2017;131: 386–401.

321. Seamari Y, Narváez JA, Vico FJ, Lobo D, Sanchez-Vives MV. Robust off- and online separation of intracellularly recorded up and down cortical states. PLoS One. 2007;2: e888.

322. Hoyer C, Gass N, Weber-Fahr W, Sartorius A. Advantages and challenges of small animal magnetic resonance imaging as a translational tool. Neuropsychobiology. 2014;69: 187–201.

323. Genove G, DeMarco U, Xu H, Goins WF, Ahrens ET. A new transgene reporter for in vivo magnetic resonance imaging. Nat Med. 2005;11: 450–454.

324. Gabashvili AN, Chmelyuk NS, Efremova MV, Malinovskaya JA, Semkina AS, Abakumov MA. Encapsulins-Bacterial Protein Nanocompartments: Structure, Properties, and Application. Biomolecules. 2020;10. doi:10.3390/biom10060966

325. Sigmund F, Massner C, Erdmann P, Stelzl A, Rolbieski H, Desai M, et al. Bacterial encapsulins as orthogonal compartments for mammalian cell engineering. Nat Commun. 2018;9: 1–14.

326. Nichols RJ, Cassidy-Amstutz C, Chaijarasphong T, Savage DF. Encapsulins: molecular biology of the shell. Crit Rev Biochem Mol Biol. 2017;52: 583–594.

327. Efremova MV, Bodea S-V, Sigmund F, Semkina A, Westmeyer GG, Abakumov MA. Genetically Encoded Self-Assembling Iron Oxide Nanoparticles as a Possible Platform for Cancer-Cell Tracking. Pharmaceutics. 2021;13. doi:10.3390/pharmaceutics13030397

328. Ki S, Sugihara F, Kasahara K, Tochio H, Shirakawa M, Kokubo T. Magnetic resonance-based visualization of gene expression in mammalian cells using a bacterial polyphosphate kinase reporter gene. Biotechniques. 2007;42: 209–215.

329. Ho D, Zhao X, Gao S, Hong C, Vatner DE, Vatner SF. Heart Rate and Electrocardiography Monitoring in Mice. Curr Protoc Mouse Biol. 2011;1: 123–139.

330. Deco G, Tagliazucchi E, Laufs H, Sanjuán A, Kringelbach ML. Novel Intrinsic Ignition Method Measuring Local-Global Integration Characterizes Wakefulness and Deep Sleep. eNeuro. 2017;4. doi:10.1523/ENEURO.0106-17.2017

331. Jiang Y, Johnson GA. Microscopic diffusion tensor imaging of the mouse brain. Neuroimage. 2010;50: 465–471.

332. Allen BD, Singer AC, Boyden ES. Principles of designing interpretable optogenetic behavior experiments. Learn Mem. 2015;22: 232–238.

333. Alonso Martínez S, Deco G, Ter Horst GJ, Cabral J. The Dynamics of Functional Brain Networks Associated With Depressive Symptoms in a Nonclinical Sample. Front Neural Circuits. 2020;14: 570583.

334. Steinberg DA. Cerebral localization in the nineteenth century–the birth of a science and its modern consequences. J Hist Neurosci. 2009;18: 254–261.

335. Walker SF. A brief history of connectionism and its psychological implications. AI Soc. 1990;4: 17–38.

336. Masamoto K, Kanno I. Anesthesia and the quantitative evaluation of neurovascular coupling. J Cereb Blood Flow Metab. 2012;32: 1233–1247.

337. Busche MA, Kekuš M, Adelsberger H, Noda T, Förstl H, Nelken I, et al. Rescue of long-range circuit dysfunction in Alzheimer's disease models. Nat Neurosci. 2015;18: 1623–1630.

338. Chen P, Hong W. Neural Circuit Mechanisms of Social Behavior. Neuron. 2018;98: 16–30.

339. Massimini M, Ferrarelli F, Esser SK, Riedner BA, Huber R, Murphy M, et al. Triggering sleep slow waves by transcranial magnetic stimulation. Proc Natl Acad Sci U S A. 2007;104: 8496–8501.

340. Schmid F, Wachsmuth L, Schwalm M, Prouvot P-H, Jubal ER, Fois C, et al. Assessing sensory versus optogenetic network activation by combining (o)fMRI with optical Ca2+ recordings. J Cereb Blood Flow Metab. 2016;36: 1885–1900.

341. Shmuel R, Secundo L, Haddad R. Strong, weak and neuron type dependent lateral inhibition in the olfactory bulb. Sci Rep. 2019;9: 1–11.

342. Buckmaster PS, Jongen-Rêlo AL. Highly Specific Neuron Loss Preserves Lateral Inhibitory Circuits in the Dentate Gyrus of Kainate-Induced Epileptic Rats. J Neurosci. 1999;19: 9519–9529.

343. Destexhe A, Hughes SW, Rudolph M, Crunelli V. Are corticothalamic “up” states fragments of wakefulness? Trends Neurosci. 2007;30: 334–342.

344. Murphy M, Bruno M-A, Riedner BA, Boveroux P, Noirhomme Q, Landsness EC, et al. Propofol anesthesia and sleep: a high-density EEG study. Sleep. 2011;34: 283–91A.

345. Ballard ED, Zarate CA Jr. The role of dissociation in ketamine’s antidepressant effects. Nat Commun. 2020;11: 6431.

346. Tervo AE, Nieminen JO, Lioumis P, Metsomaa J, Souza VH, Sinisalo H, et al. Closed-loop optimization of transcranial magnetic stimulation with electroencephalography feedback. Brain Stimul. 2022;15: 523–531.

347. Pais-Roldán P, Takahashi K, Sobczak F, Chen Y, Zhao X, Zeng H, et al. Indexing brain state-dependent pupil dynamics with simultaneous fMRI and optical fiber calcium recording. Proceedings of the National Academy of Sciences. 2020;117: 6875–6882.

348. Du Y, Fu Z, Calhoun VD. Classification and Prediction of Brain Disorders Using Functional Connectivity: Promising but Challenging. Front Neurosci. 2018;12: 525.

349. Ringli M, Souissi S, Kurth S, Brandeis D, Jenni OG, Huber R. Topography of sleep slow wave activity in children with attention-deficit/hyperactivity disorder. Cortex. 2013;49: 340–347.

350. Goldenberg D, Galván A. The use of functional and effective connectivity techniques to understand the developing brain. Dev Cogn Neurosci. 2015;12: 155–164.

351. Scherr M, Utz L, Tahmasian M, Pasquini L, Grothe MJ, Rauschecker JP, et al. Effective connectivity in the default mode network is distinctively disrupted in Alzheimer’s disease-A simultaneous resting-state FDG-PET/fMRI study. Hum Brain Mapp. 2021;42:

4134–4143.

352. Fleischer V, Muthuraman M, Anwar AR, Gonzalez-Escamilla G, Radetz A, Gracien R-M, et al. Continuous reorganization of cortical information flow in multiple sclerosis: A longitudinal fMRI effective connectivity study. Sci Rep. 2020;10: 1–11.

353. Durand DM. What is Neural Engineering? J Neural Eng. 2006;4. doi:10.1088/1741-2560/4/4/e01

354. Lee YF, Gerashchenko D, Timofeev I, Bacskai BJ, Kastanenka KV. Slow Wave Sleep Is a Promising Intervention Target for Alzheimer's Disease. Front Neurosci. 2020;14: 705.

355. Lehoux T, Carrier J, Godbout R. NREM sleep EEG slow waves in autistic and typically developing children: Morphological characteristics and scalp distribution. J Sleep Res. 2019;28: e12775.

356. Deco G, Kringelbach ML. Great expectations: using whole-brain computational connectomics for understanding neuropsychiatric disorders. Neuron. 2014;84: 892–905.

357. Pangalos MN, Schechter LE, Hurko O. Drug development for CNS disorders: strategies for balancing risk and reducing attrition. Nat Rev Drug Discov. 2007;6: 521–532.